INFORMATION TO USERS

This manuscript has been reproduced from the microfilm master. UMI films the text directly from the original or copy submitted. Thus, some thesis and dissertation copies are in typewriter face, while others may be from any type of computer printer.

The quality of this reproduction is dependent upon the quality of the copy submitted. Broken or indistinct print, colored or poor quality illustrations and photographs, print bleedthrough, substandard margins, and improper alignment can adversely affect reproduction.

In the unlikely event that the author did not send UMI a complete manuscript and there are missing pages, these will be noted. Also, if unauthorized copyright material had to be removed, a note will indicate the deletion.

Oversize materials (e.g., maps, drawings, charts) are reproduced by sectioning the original, beginning at the upper left-hand corner and continuing from left to right in equal sections with small overlaps.

Photographs included in the original manuscript have been reproduced xerographically in this copy. Higher quality 6" x 9" black and white photographic prints are available for any photographs or illustrations appearing in this copy for an additional charge. Contact UMI directly to order.

University of Alberta

Development and Application of Scanning Force Microscopy for the Analysis of Non-Specific Protein Adsorption

By

Truong Chi Ta   ©

A thesis submitted to the faculty of Graduate Studies and Research in partial

fulfillment of the requirements for the degree of Doctor of Philosophy

Department of Chemistry

Edmonton, Alberta, Canada

Spring 2001

0-612-60351-2

Canada

University of Alberta

Library Release Form

Name of Author: Truong Chi Ta

Title of Thesis: Development and Application of Scanning Force Microscopy for the Analysis of Non-Specific Protein Adsorption.

Degree: Doctor of Philosophy

Year this Degree Granted: 2001

Permission is hereby granted to the University of Alberta Library to reproduce single copies of this thesis and to lend or sell such copies for private, scholarly or scientific research purposes only.

The author reserves all other publication and other rights in association with the copyright in the thesis, and except as herein before provided, neither the thesis nor any substantial portion thereof may be printed or otherwise reproduced in any material form whatever without the author's prior written permission.

#404, 10818 – 81 Ave
Edmonton, Alberta
Canada T6E 1Y4

January 3 /, 2001
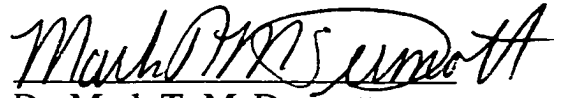
"Set your course by the lights of the stars,

not by the lights of every passing ship"

Unknown

University of Alberta

Faculty of Graduate Studies and Research

The undersigned certify that they have read, and recommend to the Faculty of Graduate Studies and Research for acceptance, a thesis entitled "Development and Application of Scanning Force Microscopy for the Analysis of Non-specific Protein Adsorption" in partial fulfillment of the requirements for the degree of Doctor of Philosophy.

Dr. Mark T. McDermott

Dr. Norman J. Dovichi

Dr. Charles A. Lucy

Dr. Glen R. Loppnow

Dr. Hasan Uludag

Dr. Vladimir Hlady, External
Examiner, University of Utah

04 DEC 2000
Date

This thesis is dedicated to my father, Quang Son Ta. Your strength, guidance and encouragement have been invaluable. Without you, this accomplishment would not be possible.

ABSTRACT

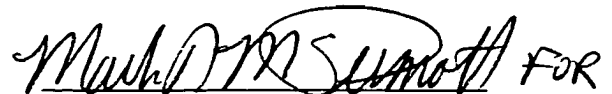In this work, a novel method was developed to map different protein conformations in adsorbed films. Surface chemistry of a substrate can control the amount of protein adsorbed and dictate surface bound protein conformation. In medical devices, the conformation of the adsorbed protein layer is a key variable determining whether the device will be biocompatible. We propose that films on biomaterials can now be probed with scanning force microscopy (SFM). In addition, we believe that it is possible to use SFM imaging to identify individual components in multi-protein films.

We have demonstrated for the first time that SFM can distinguish relative differences in bovine and human fibrinogen conformations adsorbed on gold substrates patterned with octadecanethiol (ODT, $HS(CH_2)_{17}CH_3$) and mercaptohexadecaneoic acid (MHA, $HS(CH_2)_{15}CO_2H$) self-assembled thiolate monolayers (SAMs). Antibody binding studies confirmed this conclusion. The capability of compositionally mapping protein films was further demonstrated in a more complex situation. Fibrinogen films formed on graphite surfaces pre-adsorbed with a partial layer of albumin proteins revealed that fibrinogen adsorbed on top of the BSA layer and in the voids were adsorbed in different conformations. These exciting findings demonstrate a method capable of providing direct conformational information of protein films at nanoscopic lengthscales. Variations in conformation are commonly determined via antibody labeling,

surfactant elution or platelet adhesion studies are indirect techniques. Spectroscopic methods such as infrared and circular dichroism have providing quantitative secondary information, however they require complex deconvolution.

Results included in this presentation are a product of our continuing efforts to utilize SFM in friction force mode to detect protein conformation and demonstrated that it can be applied to a wider range of proteins. This work will also present SFM results obtained for albumin, lysozyme, fibronectin and IgG under similar conditions as those used in the fibrinogen studies on SAMs.

Imaging performed under flow conditions provided real-time details into the early stages of protein adsorption. This setup can provide some information to ascertain the mechanism of adsorption. Real-time imaging provided additional information that fibrinogen adsorbed on ODT and MHA were conformationally distinct. Overall, SFM was shown to be a versatile tool capable of provide information of protein films not obtainable via any other methods.

ACKNOWLEDGEMENTS

What a journey it has been...and now that I have reached the end of this road, I would like to take this opportunity to sincerely thank those that have made my time as a graduate student a wonderful and successful experience. There are so many people I would like to thank, and if I forget to mention anyone, I hope you will accept my apologies.

First and foremost, I would like to thank my graduate supervisor Mark McDermott. You have gone way beyond the call of duty. You are a true friend and I hope we will always stay in touch. Without getting to mushy, I am very honored to have worked with you for the last five years. You have taught me many things about life inside and outside the lab. You saw something in me when few others did five years ago. Thank you for the your confidence and trust. Thank you for providing me the opportunity to perform cutting edge research. I hope that the McDermott group continues to grow and achieve even greater success in the future. I wish you and your family (Christie, Jordan and Quentin) all the best that life has to offer.

To the boys currently in the McDermott group, what can I say but hehe...I am done and you guys are not! All joking aside, James and Gregory, along with Michael (former McDermott group member) you guys were all there from the beginning. You were there when Mark laid down the hammer, twice. You were there when we had to move our offices three times in four years. It was an honor and privilege to work along side you guys. I will miss you all when we go our separate ways. Greg and James, remember I still intend to come to Kenya one day. Michael, I hope your stocks will make you a rich man and remember to pass along any info! Vishal, Mirwais, Aaron, Solomon and Francis, it was a pleasure working with you guys. Each one of you has a completely different personality, making life much more interesting in the lab. I have only fond memories of you all, and because of you guys, graduate school was a pleasant and fun experience.

I would like to assert my heartfelt gratitude to my dad, who has sacrifice so much to afford me the opportunity to educate myself. Since I can remember, you continually emphasize the importance of an education and I believe it is for that reason that I have gone this far. You are the hardest working person I know. You exemplify all the positive qualities that a parent should have when raising a child. You are a pillar of strength and continue to be a shining example in my life. For all of the above reasons, I cannot sincerely say thank you enough. I hope that I have made you proud and love you very much.

To my auntie Lan and family, auntie Long, and the rest of the family in Viet Nam, I know that I am always in your hearts. Thank you for all your support. Especially to my mom, we have not seen one another for more than twenty years and I promise to rectify this problem very soon. I know you have not forgotten me. Your love and devotion continues to uplift my spirits. To the Pham family, and especially Khanh, I thank you for all your words of encouragement. Thanks for all the love and warm thoughts. To May Phan, thank you for being a very good friend.

To all my friends, thanks for giving me a life outside of the lab. I look forward to playing volleyball with you guys each Sunday. Stephanie and Don, thanks for celebrating this accomplishment with me at Characters. Priscilla, you have been a very loving friend and have always been supportive of my academic endeavors. I wish nothing but the best for you; all the happiness, joy and success in the future.

I would like to sincerely thank the University of Alberta for cultivating an environment of the highest quality for learning. I would also like to thank the Department of Chemistry for all their financial support and providing a place for graduate students to perform world class research. I also acknowledge the Natural Science and Engineering Research Council (NSERC) of Canada for funding our

research efforts. Without their support, my research would not be possible. It was money well spent!

Lastly, I would like to acknowledge some collaborators that have helped progress my academic career. I would like to thank Professor Marc Porter (AMES lab, Iowa State University) for providing our lab with research materials such as PDMS stamps, MHA and more. I would like to acknowledge Professor George Whitesides (Harvard, MA) for the gift of the poly(ethylene glycol) terminated thiols, Professor Paul Hansma (University of California, Santa Barbara) for useful discussions with regards to real-time imaging with scanning force microscopy, and Dr. Authur Moore (Advanced Ceramics) for the generous gift of HOPG. I would like to acknowledge Micralyne (formerly Alberta Microelectronic Center) for providing metal-coated substrates. Last, but not least, I would like to Professor Liang Li (PDF supervisor, University of Alberta) for allowing me to finish writing up my thesis and at the same time working in his lab. I appreciate very much your support and the opportunity to perform future research in your lab.

TABLE OF CONTENTS

CHAPTER VII: CONCLUSIONS AND FUTURE WORKS

APPENDIX A: VOLTAMMETRIC AND SCANNING FORCE MICROSCOPIC INVESTIGATION OF ANTHRAQUINONE FILMS SPONTANEOUSLY ADSORBED ON ORDERED GRAPHITE

LIST OF TABLES

LIST OF FIGURES

DDT and ODT SAMs.

LIST OF SYMBOLS

F_N Force applied in the normal direction to the surface

k Spring force constant

x Distance away from a spring's equilibrium state

f Friction force

μ Friction coefficient

R Radius of the SFM tip

γ^* Interfacial energy

$\overset{\circ}{A}$ A distance unit (angstroms)

$\Delta\theta(\lambda)$ Change in resonance angle as a function of wavelength

A Constant calculated from Fresnel optics

B Constant calculated from Fresnel optics

Δn Change in refractive index

Δd Change in thickness of adsorbed layer

λ Wavelength

A_{aI} Absorbance value of amide I band

A_{aII} Absorbance value of amide II band

v_{aI} Wavenumbers (cm^{-1}) of amide I band

v_{aII} Wavenumbers (cm^{-1}) of amide II band

Δ The difference in SPR response for anti-HFG and bIgG binding to adsorbed HFG

δ	SPR response from non-specific binding of bIgG to adsorbed HFG
Si_3N_4	Silicon nitride
ν_a	Wavenumber (cm^{-1}) for the asymmetric C-H stretch
ν_s	Wavenumber (cm^{-1}) for the symmetric C-H stretch
ω_{ts}	Work of adhesion between tip and sample
r	Correlation coefficient
C/cm^2	Charge in Coulombs per cm^2

LIST OF ABBREVIATIONS

μCP	Microcontact printing
ΔE_p	Cathodic-anodic peak separation
AFM	Atomic force microscopy
Ag	Silver
AgCl	Silver chloride
Anti-HFG	Antibody to human fibrinogen
2,6-AQDS	2,6 - anthraquinone disulfonate
Au	Gold
BSA	Bovine serum albumin
bIgG	Bovine immunoglobulin G
CD	Circular dichroism
Cr	Chromium
CV	Cyclic voltammetry
DDT	Dodecanethiol
$E_{1/2}$	Potential at half maximum
EET	Ethyl esterified mercaptoundecanoic acid
EFM	Electric force microscopy
F_{ab}	Binding fragment of antibodies
F_c	Crystallizable fragment of antibodies

FFM	Friction force microscopy
FG	Fibrinogen
FTIR	Fourier transform infrared
FWHM	Full width at half maximum
GC	Glassy carbon
GIXD	Grazing angle X-ray diffraction
HFG	Human fibrinogen
HFN	Human fibronectin
Hg	Mercury
HOPG	Highly oriented pyrolytic graphite
HT	Hexanethiol
IDC-BSA	Intermolecular disulfide crosslinked BSA
IgA	Immunoglobulin A
IgD	Immunoglobulin D
IgE	Immunoglobulin E
IgG	Immunoglobulin G
IgM	Immunoglobulin M
IR	Infrared
IRRAS	Infrared reflectance absorbance spectroscopy
LTIC	Low temperature isotropic carbon
LYS	Lysozyme

MCT	Mercury-Cadmium-Telluride
MET	Methyl esterified mercaptoundecanoic acid
MFM	Magnetic force microscopy
MHA	Mercaptohexadecanoic acid
MPC	Macromolecular protein complexes
MUA	Mercaptoundecanoic acid
MW	Molecular weight
NEXAFS	Near edge X-ray absorption fine structure spectroscopy
NSOM	Near-field scanning optical microscopy
NT	Nonanethiol
ODT	Octadecanethiol
PB	Phosphate buffer
PBS	Phosphate buffer saline
PDMS	Poly(dimethyl) siloxane
PG	Pyrolytic graphite
PSD	Position sensitive photodiode detector
RGD	Arginine-glycine-aspartic acid
RMS	Root means square
RU	Response unit
SAMs	Self-assembled monolayers
SCM	Scanning capacitance microscopy

SDS	Sodium dodecyl sulfate
SEM	Scanning electron microscopy
SPM	Scanning probe microscopy
SPR	Surface plasmon resonance
SSA	Solution self assembly
STM	Scanning tunneling microscopy
TEM	Tunneling electron microscopy
Ti	Titanium
TIRF	Total internal reflectance fluorescence
TM-SFM	Tapping-mode scanning force microscopy
XPS	X-ray photoelectron spectroscopy

CHAPTER I

INTRODUCTION

Scanning Probe Microscopy

Since its inception in the mid-1980's, the growth of scanning probe microscopy (SPM) has been exponential. Today, included in the SPM family of techniques are scanning tunneling microscopy (STM), atomic force microscopy (AFM) or scanning force microscopy (SFM), electric force microscopy (EFM), magnetic force microscopy (MFM), friction force microscopy (FFM), and scanning capacitance microscopy (SCM). Even though each technique generates images of a substrate surface from contrasting fundamental properties or forces, the seminal idea behind these techniques has roots dating back to the early 1970s with the work of Russell Young, Ward and Scire (1). Their development of an instrument called the "topografiner" which contained many elements of the current SPM instrumentation, including a piezoelectric scanner or positioner and feedback systems to control tip-sample distances. The topografiner had low resolution, approximately 3 nm in the vertical direction, and 400 nm in the horizontal direction. Today's instrument can achieve vertical resolution of 0.01 nm and horizontal resolution of 0.1 nm under certain conditions. For some reasons, development of the topografiner stopped, and interest in the work did not reappear until the earlier 1980s. Gerd Binning, Heinrich Rohrer and Christoph Gerber at IBM research (Zurich) refined the topografiner by developing methods to control small tunneling currents and coined the term scanning tunneling microscopy (2, 3). They successfully obtained an atomically resolved image of a Si (111) surface and were awarded the Nobel Prize in physics for the development of STM in 1983. Today, STM has gained wide use as a tool with which to obtain two-dimensional images of surfaces with atomic resolution, and has demonstrated the

ability to fashion novel arrangements of atoms through the selective placement of atoms on surfaces (4-6). STM was, however, limited by the requirement that the sample must be conductive or semi-conductive.

To surmount this shortcoming of STM, Binnig, Quate and Gerber (7) introduced the AFM in 1986 as a tool to map nonconductive surfaces such as polymeric materials and biological specimens. AFM or SFM has become a tool used by researchers from many disciplines ranging from biology, chemistry and engineering. In SFM (Figure 1.01), a sharp tip mounted on a cantilever scans a substrate surface in a raster pattern. SFM generates topographic maps of surfaces by maintaining a constant force between the tip and sample. A feedback system, similar to that used for STM, maintains the user-defined interaction load (force) by either raising or lowering the sample. The magnitude of the feedback signal is used to raise or lower the sample to keep the force constant and is proportional to the topography of the surface. For example, a voltage required to raise the sample indicates that the surface was depressed at that location, and the magnitude of the applied voltage is proportional to the depth of the depression. A laser beam reflected off the back of the cantilever and directed onto a position sensitive photodiode detector (PSD) is most often used to monitor cantilever deflection in order to control the applied force in the normal direction.

Force applied by the probe tip on the sample (F_N) can be calculated by modeling the cantilever as a spring and Equation 1 is a quantitative description of the normal force (F_N), whereby k is the spring constant and x is the distance of cantilever deflection in the normal direction.

$$F_N = kx \qquad \{1\}$$

In practice, the distance the cantilever is bent can be calculated from parameters determined experimentally in a force-distance curve. Figure 1.02A is an example of a raw force-distance plot monitoring laser signal (in Volts) as a surface approaches the tip (i.e. top trace moving from right to left) and then subsequently
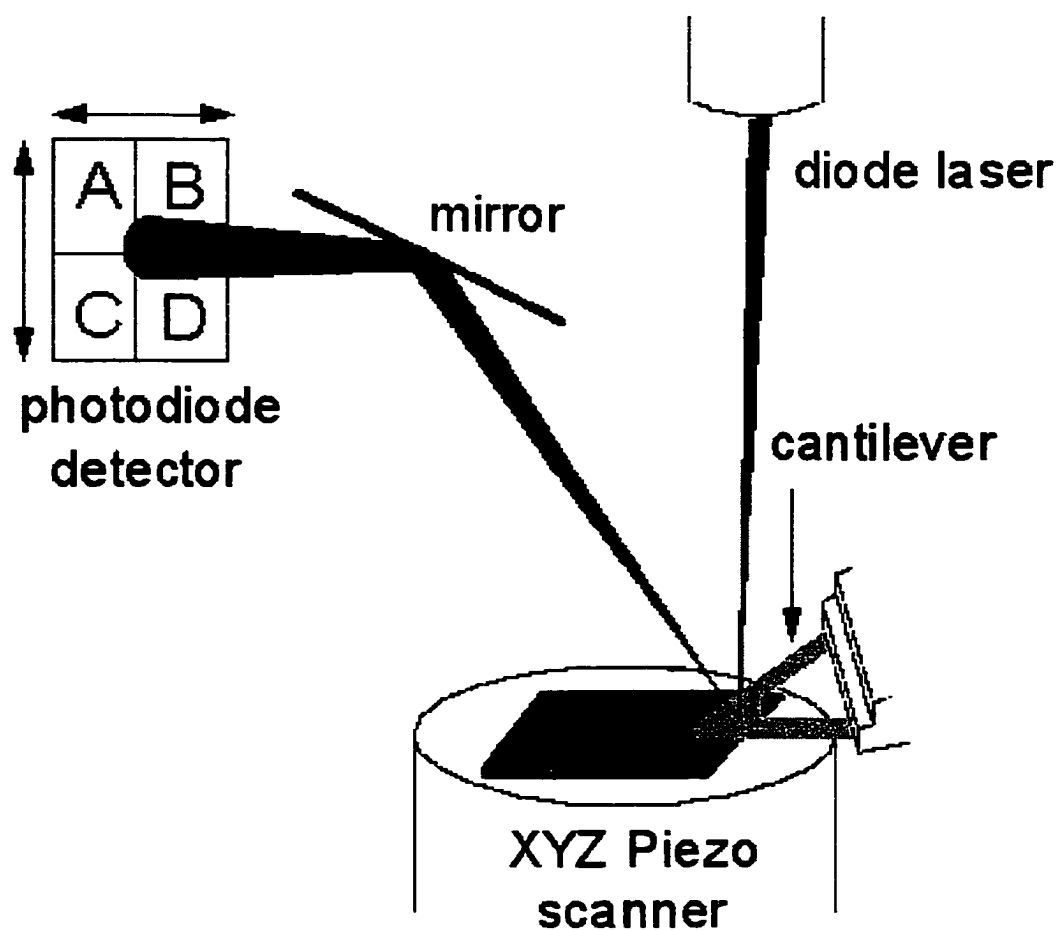
Figure 1.01. Diagramming the principle operations of atomic or scanning force microscope. The probe tip mounted on the bottom side of the cantilever at its apex cannot be seen in this figure.

slope = sensitivity

setpoint (Volts)

breakaway (Volts)

Detector signal (Volts)

A

B
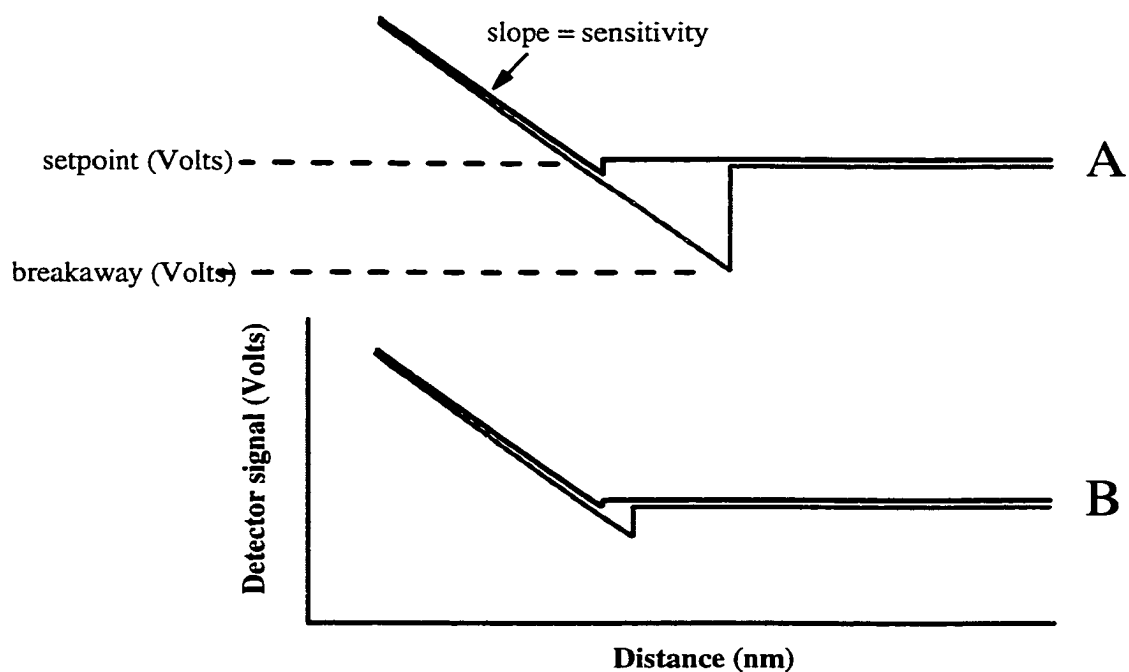
Distance (nm)

Figure 1.02. Examples of force-distance curves obtained in (A) air and (B) in aqueous media. Blue section of the curves is the forward (approach) and red section is the reversal (retraction) of sample movement from the tip.

retracted (bottom trace moving left to right). By following the top curve, one initially observed a flat line indicating no cantilever deflection when the tip is above the surface. As the surface continues to approach the tip, forces acting between the tip and surface pull the tip into contact. Further upper movement of the sample surface results in a repulsive tip-sample interaction causing the cantilever to bend. The slope of this region is the detector sensitivity (Volts/nm) to cantilever bending in the normal direction. During the reverse scan, in some cases the sample has to be retracted further to pull the tip off the surface (adhesion hysteresis). The point where the tip is pulled off the surface is referred to as the breakaway point (Volts). Once the tip is pulled off the surface, the laser signal springs back to the level seen at the start of the approach. In a typical experiment, a user can define the setpoint (Volts) at which an image is to be captured and F_N can be calculated from Equation 2 after sensitivity and breakaway voltage have been determined. Equation 1 can be rewritten as

$$F_N = \frac{\text{Setpoint voltage - Breakaway voltage}}{\text{Sensitivity}} \, (k) \qquad \{2\}$$

whereby k is the cantilever spring constant in the normal direction.

When imaging in air, both the tip and sample surfaces are coated with a thin layer of water and other impurities. When these water covered surfaces come into contact, capillary forces are the dominant contributors to tip adhesion and increase hysteresis (Figure 1.02A). Large capillary forces make it difficult to control the applied F_N. Capillary forces are eliminated when imaging under aqueous conditions (Figure 1.02B). This is extremely important for studies on delicate biological samples. By removing the capillary forces, the surface tension responsible for pulling the tip toward the surface contributing to F_N are eliminated. Furthermore, one can gain greater control over applied forces because the breakaway point and thus F_N can be more accurately determined. Thus, by

selecting cantilevers with appropriate force constant (k), proper selection of setpoint and imaging in aqueous environment, delicate samples can be imaged in contact mode SFM.

The ability to map a surface topographically afforded researchers a technique for analyzing biological samples at the microscopic to nanoscopic scale without staining, as is necessary for scanning electron microscopy (SEM) or transmission electron microscopy (TEM). As optical microscopes are limited by the diffraction limit of light; nanoscopic resolution is impossible. However, a technique called near-field scanning optical microscopy (NSOM) can now deliver two-dimensional resolution comparable to SFM. However, SFM is the able to image biological samples at near physiological conditions (*i.e.*, in solutions with controlled of pH and ionic strength) (8) and therefore concerns regarding the effect of drying the biological sample are removed.

The desire to map not only surface topography but also surface composition (*i.e.*, chemistry) and other material properties such as electric and magnetic fields has led to development of numerous imaging modes. Of importance for the research presented in this thesis are modes with the ability to map surface chemistry. Two compositionally sensitive imaging modes routinely employed in our lab are friction imaging in contact mode SFM and phase imaging in Tapping mode SFM. The work presented here involves the application of friction force imaging to protein films.

At macroscopic contacts, friction force depends only on normal force (F_N) or load via Coulomb's equation

$$f = \mu F_N \qquad \qquad \{3\}$$

where μ is a proportionality constant commonly called the friction coefficient. For a microscopic contact between an SFM tip and a surface, a number of other parameters become important. Kendall (9) has described the friction (f) between a sphere (SFM tip) and a flat surface as,

$$f = \mu F_N + 3\pi R\gamma^*\mu + \mu(6\pi R\gamma^* F_N + 9\pi^2 R^2\gamma^{*2})^{\frac{1}{2}} \qquad \{4\}$$

whereby μ is now a microscopic coefficient of friction, F_N is the normal force, R is the radius of the sphere or tip and γ^* is the interfacial free energy of the tip-sample contact. γ^* depend on the surface-solvent (SL), tip-solvent (TL) and tip-surface (TS) free energies via $\gamma^* = \gamma_{SL} + \gamma_{TL} - \gamma_{TS}$. Inspection of equation 4 reveals that the SFM measured friction depends on normal forces (via F_N), surface chemistry (γ^*) and tip-sample contact area (via R^2). During SFM imaging, F_N and radius of the tip were kept constant, then a friction image corresponds to a map of surface composition.

Equation 4 theoretically suggests that friction SFM can be used to compositionally map surfaces. In practice, the amount of friction between a SFM tip and surface is monitored by observing the amount of torsional bending or twisting of the cantilever. In order to measure the friction between a probe tip and a surface, a four-quadrant photodiode detector was devised (10, 11) as shown in Figure 1.03. Normal deflection is monitored as the total signal intensity of quadrant A plus B minus total signal intensity from quadrant C plus D. Torsional bending is monitored as the sum of signal from quadrants A and C minus the signal sum of quadrant B and D. Schwarz, *et al.* have described in detail quantitative analysis of friction measured by SFM (12).

Friction SFM became a tool that was intended to map surfaces based on properties other than surface topography. Overney, *et al.* (13) were the first to demonstrate this ability. Frisbie, *et al.* (14) and Green, *et al.* (15) also showed that friction imaging was capable of mapping a surface based on surface composition (*i.e.*, chemistry). Both groups used self-assembled monolayers of alkylthiolates on gold to control substrate surface chemistry. It was demonstrated that even without topographic changes, a surface could be mapped based on chemical variation in two- dimensional space. Therefore, the development of friction-SFM allowed for investigations into the relationship between surface chemistry and friction at the
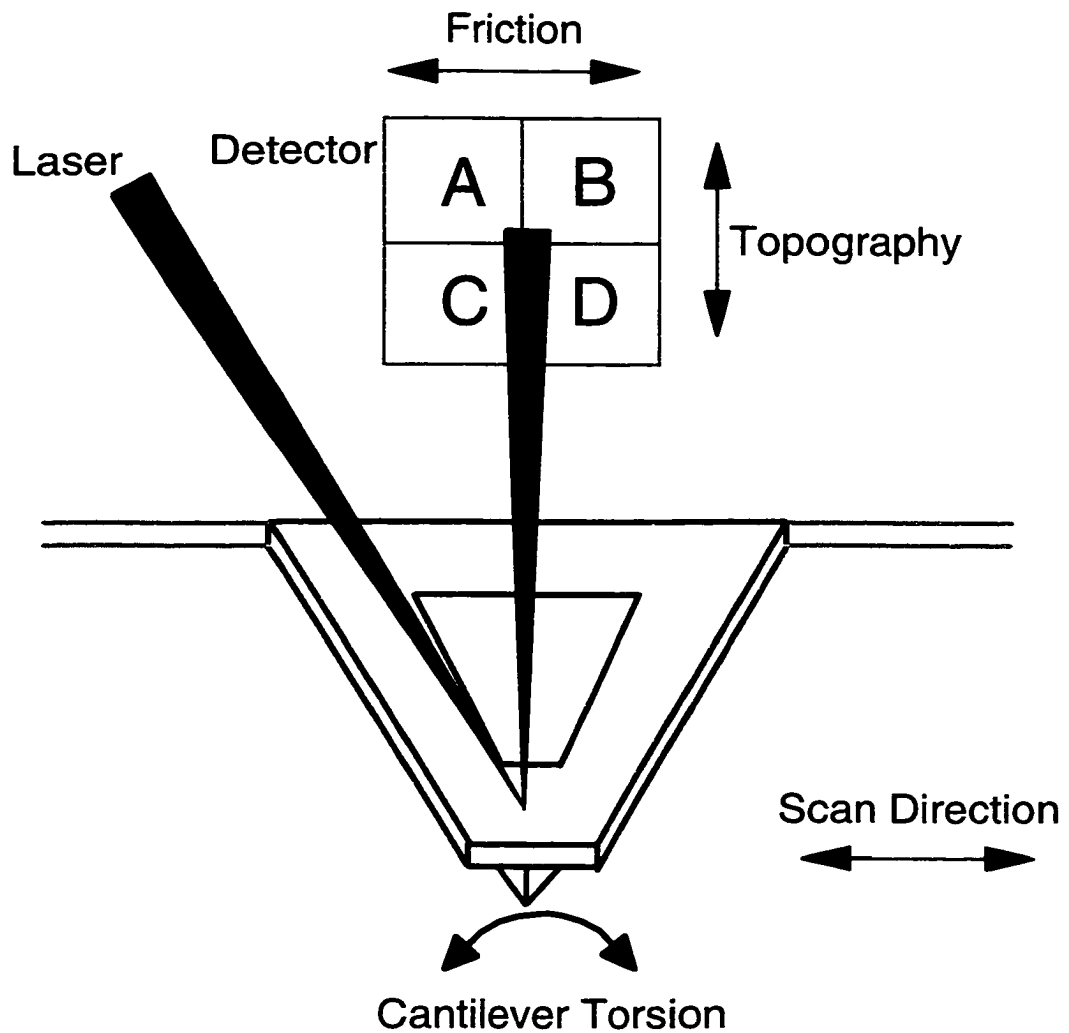
Figure 1.03. Mechanism responsible for generation of LFM images. Torsional bending of the cantilever resulting in lateral motion of the laser; the four-quadrant photodiode detector detects the deflection. LFM measured friction correlates with surface chemistry at the microscopic level.

microscopic scale. More importantly, an image of a surface could be generated from differences in surface chemistry.

Protein Adsorption

Proteins are molecules composed of long chains of amino acids strung together in specific sequences by peptide bonds (polypeptide chain). The linear arrangement of the amino acids is referred to as the protein's primary structure. There are twenty amino acids that are commonly found in proteins, making the number of possible primary structures enormous. Amino acids are distinguished by their side chain groups, and interaction of these side chains causes localized folding of the linear sequence into regular structures such as α helices and β sheets, forming the proteins' secondary structure. Also steric repulsion from the side chains influence the phi and psi angles and thus contributing to proteins secondary structure. Folding of the regions between the α helices and β sheets creates a compact structure referred to as the protein's tertiary structure. The driving force behind protein tertiary folding result mainly from non-covalent interactions via hydrogen bonding, electrostatic and van der Waals forces. In general, denatured proteins will lose their activity because the non-covalent interactions are broken or obstructed resulting in polypeptide chain unfolding and lost of secondary and tertiary conformations. Protein denaturation may be induced by exposure of protein solution to heating, increase ionic strength of the electrolyte, use of surfactant or by protein adsorption onto a surface.

The tendency of proteins to adsorb to surfaces stem from their molecular properties. Protein size, charge, structure and various other chemical properties influence protein surface activity. In terms of size, larger proteins may have greater surface affinity due to increase number of contact points. Proteins that have ionizable amino acid groups on the outer regions of their structure may bind to charged surfaces more readily, especially when protein molecules have an overall charge opposite to the surface charge. Structural stability may determine

protein surface activity. Less structurally stable proteins will unfold to a greater extent when adsorbed on surfaces, increasing surface affinity through increasing in contact area. Increasing the number of sulfur-sulfur bonds improves protein stability and inhibits surface activity. In addition, proteins that have many hydrophobic amino acid groups may exhibit higher surface activity at hydrophobic surfaces. Less soluble proteins may also be more surface active.

Protein-substrate interactions are important in a number of scientific fields. The development of biological sensors, chromatographic separations, and biocompatible implant materials is impacted by protein adsorption. Biocompatibility is a general term defining how well a host accepts an implant. Indicators of incompatibility may be blood clot formation (thrombosis), reduced binding, spreading and growth of cells, and/or formation of a protein encapsulation shell around the implant. The formation of blood vessels and cell growth on the implant suggests successful integration. To improve the biocompatibility of an implant, researchers have focused on the implants' surface chemistry and its effects on the adsorbed protein film. Polyethylene oxide polymer and polyethylene glycol terminated alkyl thiolate monolayers on Au have shown a propensity to resist protein adsorption (16-18). It is not whether proteins adsorb to a surface that will influence biocompatibility, but the more important factor is that the conformation or orientation of the adsorbed protein film facilitating cell binding and growth. Thus, interest in determining how surface chemistry influence protein conformation and developing tools capable of direct analysis of protein conformation or orientation is high.

In combination with protein properties, the chemical nature of the substrate has a direct impact on the characteristics of the adsorbed protein film that finally forms on the surface. Figure 1.04A illustrates how protein molecules may interact with a surface, starting from the solution-state and then possible transitions that it may go through during the adsorption process. At the surface, short and long
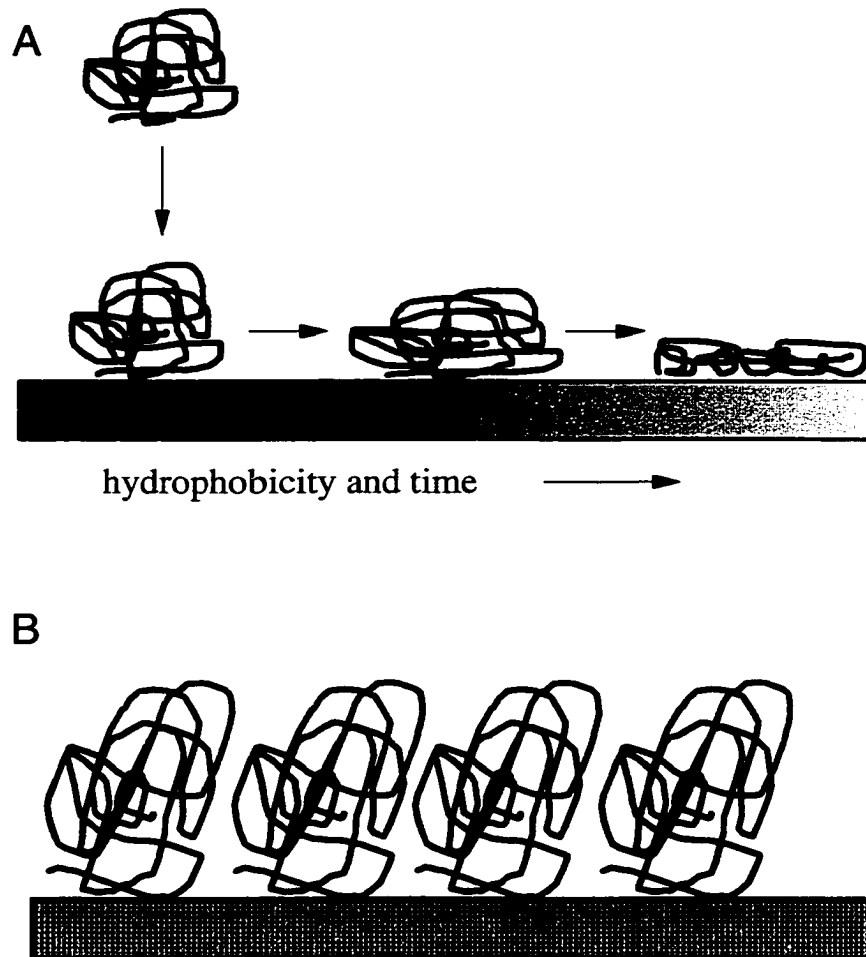
Figure 1.04. (A) Possible steps involved with protein adsorption onto surfaces. Surfaces with greater hydrophobicity incite greater conformational change. (B) Surface properties may also permit proteins to preferentially adsorb in defined orientations.

range intermolecular forces and also hydrophobic forces will likely determine the fate of the protein molecule. Under the appropriate solution conditions, proteins can retain their original conformations. However, more generally the state of the adsorbed protein (conformation/orientation) and strength of binding will be determined by protein and surface composition.

In the initial stages of protein adsorption, protein conformation most likely resembles that in solution. Over a period of time, protein molecules may begin to unfold to enhance interactions with the substrate surface through the amino acids, which were once buried within the folded protein structure. Hydrophobic surfaces tend to induce greater unfolding and conformational change by increasing interaction of hydrophobic amino acids with the surface. For example, the amount of fibrinogen and albumin eluted by surfactants from various polymer surfaces decreased as the time from adsorption to elution was increased (19). Surface composition may not only induce different protein conformations, but can also influence molecular orientation as shown in Figure 1.04B. The chemical properties of the interface created after protein adsorption are a function of adsorbed protein conformation or orientation and thus guide future interactions at the surface.

Plasma Proteins

Fibrinogen, albumin, fibronectin, lysozyme and IgG are proteins that can be found circulating in blood and each have different functions. These proteins were utilized for experiments presented in the following chapters and thus warrant some discussion. Their structures are presented in Figure 1.05. My research interest has focused mostly on fibrinogen because of its importance in the blood-clotting (thrombosis) process that prevents blood loss after an injury. Fibrinogen is a relatively large dimeric protein (~340 kDa), consisting of three pairs of non-identical polypeptide chains. Each half of the dimer contains one Aα, Bβ and γ chain and the halves are held together by disulfide linkages near the N-termini of

the polypeptide chains. Fibrinogen also contains two pairs of oligosaccharides, which are bound to the γ chains. Four major domains have been identified for fibrinogen, with each having different chemical properties (Figure 1.05A) and 6 platelet binding sites per molecule. The D and E domains are more hydrophobic than the αC and αM domains, but are comparable to each other. αC domains (last third of the Aα chains from the C-terminus) demonstrate greater hydrophilicity. However, αM domains (middle third of the Aα chains) are the regions of highest hydrophilicity. In terms of overall charge, fibrinogen is negatively charged (-10) at physiological pH. D and E domains are negatively charged while αC and αM domains are net positive. Because of its large size, distribution of charge and hydrophobic amino acid groups, fibrinogen is capable of adsorbing to a variety of surface (20).

Fibrinogen adsorption has raised concerns because it is a key component in thrombosis. Normally, a blood clot results from the conversion of fibrinogen to fibrin by the enzyme thrombin, allowing the fibrin monomers to aggregate. Aggregation is facilitated by cleavage of the negatively charged fibrinopeptides found at the N-termini of the Aα and Bβ chains. This effectively lowers the net negative charge of the E domain, allowing it to interact with the D domain of adjacent fibrin molecules. From these interactions a mesh like structure forms that can trap platelets and the presence of thrombin can activate the platelets. Once activated, platelets can bind to fibrin monomers and fibrinogen, and continue to release granules containing Ca^{2+} and adenosine diphosphate (ADP) that further stimulate platelet aggregation and platelet activation. The combination of fibrin and platelets results in a stable clot (21).

Conformationally perturbed fibrinogen can bind unactivated platelets (22, 23), and promote platelet aggregation. Thus, fibrinogen adsorbed on surfaces may denature into a stable conformation for surface binding, however, formation of surface-induced blood clots may occur. The adverse effects of these clots include

A
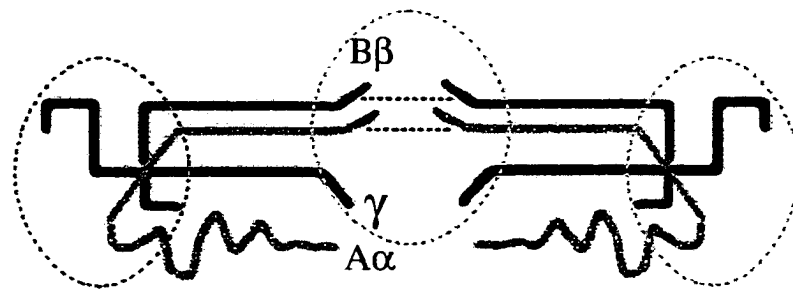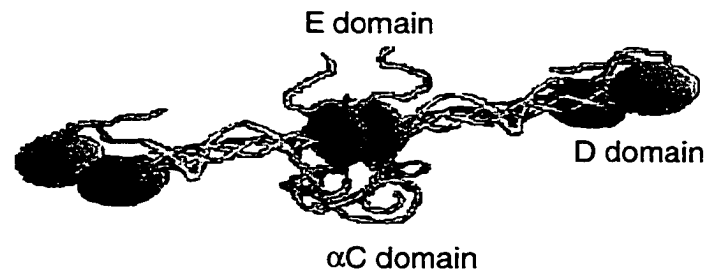
B
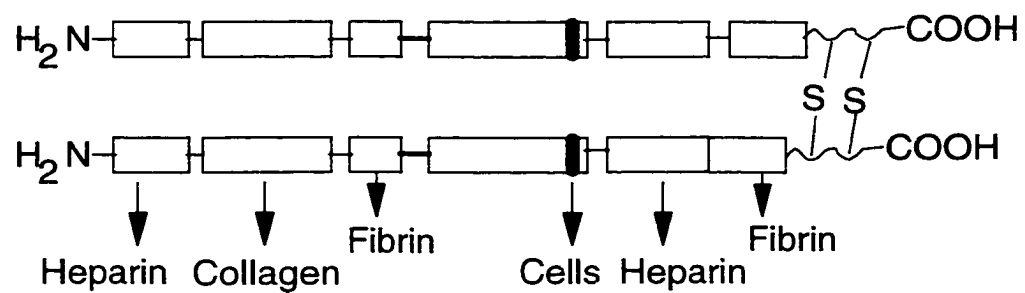
Figure 1.05. (A) Structure of fibrinogen (MW ~340 kDa) and (B) Fibronectin (MW ~550 kDa). Fibrinogen is a dimer, containing 6 polypeptide chains and three domains reported here (E, D and αC). Dimensions of fibrinogen is ~47 nm in length and thickness of ~4-6 nm. Fibronectin has 2 polypeptide chains, and each chain has regions capable of binding specific molecules. Fibronectin used was the monomer.

C
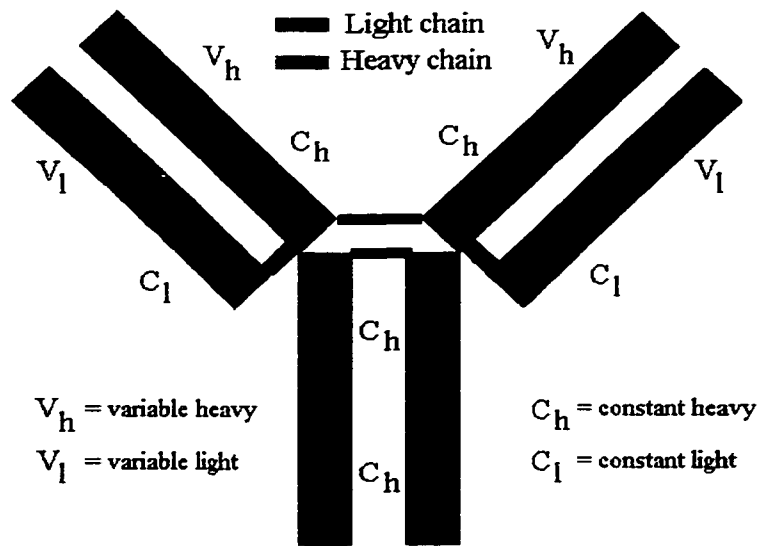
D

Figure 1.05. continued. (C) Illustrated structure of IgG and (D) lysozyme. IgG (MW ~150 kDa) measures approximately ~9 nm tall and specificity of binding is due to the composition of the variable regions. Lysozyme (MW ~14 kDa) has dimensions of approximately 14 nm × 9 nm × 4 nm.

E
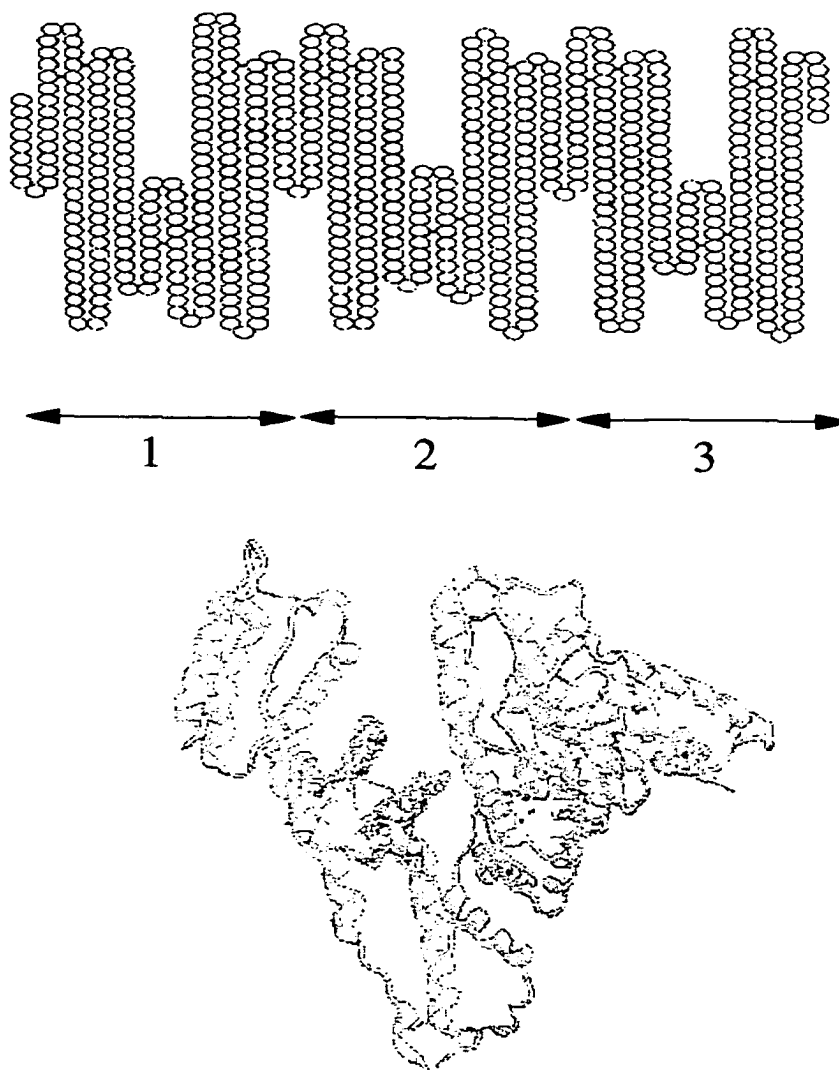
Figure 1.05. continued. (E) Structure of bovine serum albumin (BSA). MW ~66 kDa, single polypeptide consisting of three domains (top) and folding into a heart-shape structure (bottom). Dimension of BSA is ~ 9 nm × 3 nm.

reduction of flow through blood vessel, total vessel blockage as a result dislodged clots flowing in the blood stream, formation of capsules around implants and decreased motility of implants (*i.e.*, heart valves).

Fibronectin is a high molecular weight (~550 kDa), dimeric glycoprotein found in plasma and the extracellular matrix. It consists of two polypeptide chains linked at the C-termini by two disulphide linkages (Figure 1.05B). Fibronectin contains an arginine-glycine-aspartic acid (RGD) sequence that is known to promote cell binding through an integrin protein found in cell membranes (24, 25). Fibronectin have domains capable of binding fibrinogen, collagen and heparin (26-28). Heparin is a polysaccharide with anti-thrombogenic properties. Thus the function of fibronectin is to mediate cell attachment to surfaces and to bind other extracellular proteins.

Immunoglobulin (IgG) describes a class of antibody proteins that act as markers for immune system response to foreign substances (antigens). Each antibody molecule contains four polypeptide chains, two heavy and two light chains, forming a Y-shaped structure as illustrated in Figure 1.05C. The IgG structure is stabilized by four intermolecular disulfide bonds and has a MW of ~150 kDa. Secondary structural content determined from X-ray spectroscopy (29, 30) and circular dichroism (CD) (31) indicated β-sheet (76%), β-turn (14%) and random coil (10%). Proteolytic cleavage of an immunoglobulin molecule produces two fragment pieces, F_c (crystallizable domain) and F_{ab} (antibody binding domain). F_{ab} domains are responsible for recognition specificity of target antigens. In immunoassays and affinity chromatography, the F_c domains are covalent linked to a substrate or physisorbed to a layer of protein A. This procedure is believed to arrange the active portion of the antibody to face the solution interface for binding antigen.

Lysozyme (LYS) shown in Figure 1.05D is an enzyme protein that can be found abundantly in egg whites and in mammal circulatory systems at lower

levels. Although the function in eggs is still unknown, LYS can act to inhibit bacterial growth through weakening of bacterial cell wall in mammals. Lysozyme can break down N-acetyl glucosamine (NAG) and N-acetyl muramic acid (NAM) polysaccharides that are important components in bacterial cell walls, leading to osmotic lysis. Lysozyme is a small, spherically shaped protein with molecular weight of ~14.5 kDa. It is a single polypeptide chain, containing mainly α-helix structures and regions of β-sheet conformations. Lysozyme has an isoelectric point of approximately 10.9 and is therefore categorized as a cationic protein. Because of its compact structure, some (32) have suggested that lysozyme may resist conformational changes as a result of adsorption onto various surfaces.

Albumin is the most abundant plasma protein (~50 mg/mL) in human blood. Its primary function is as a transport vehicle for fatty acid molecules that display low solubility in aqueous media. Its structure, as shown in Figure 1.05E, indicates the presence of three domains (I, II and III) and previous studies have indicated that bovine serum albumin (BSA) contains mostly α-helix (55%) and random conformations (45%). NMR (33) and X-ray crystallography (34) have determined albumin to be a heart-shaped protein with measurements of approximately 3 nm × 9 nm. Albumin has been found to undergo reversible conformational changes as a function of pH. At neutral pH, albumin has an overall negative charge of −18. The study of albumin adsorption is important because it is often used to passivate surfaces to prevent non-specific adsorption to active sites. In addition, adsorption phenomena such as competitive adsorption and the Vroman effect (35) are likely influenced by albumin because it is present at higher concentration than most proteins.

Self-assembled Alkylthiolate Monolayers on Gold

Self-assembled monolayers (SAMs) are collections of molecules that form spontaneously at a substrate surface. The arrangement of the molecules produces a thin film on the substrate, altering the chemistry of its surface. Formation of

SAMs on gold surfaces involves the chemisorption of organosulfur compounds. Nuzzo and Allara (36) were the first to demonstrate that dialkyl-disulfides (R_1-S-S-R_2) form monolayers that were structurally ordered and crystalline. Shortly thereafter, it was discovered that SAMs formation on Au can be derived from thiol (R-SH) compounds (37-39). Preparation of SAMs involves immersion of a clean Au substrate in a dilute (sub-millimolar) organosulfur solution. Immersion times can vary, from several minutes to days depending upon the solution concentration and the organosulfur species.

In this work, SAMs were formed by immersion of clean gold substrates in millimolar ethanolic alkylthiol solution for a period of time as indicated in the following chapters. Thiols were used because of unequivocal evidence indicating that the resultant monolayers are structurally stable, ordered and crystalline (37, 38). The surface composition and structural characteristics of a thiolate monolayer are determined by the structure of the thiol molecule. Figure 1.06 is a generic representation of a thiol molecule. Its structure can be broken into three parts, the sulfur head group, aliphatic body and a tail group. The sulfur head group is used to anchor the molecule to the surface. Chemisorption likely occurs from cleavage of S-H bonds and formation of S-Au bonds. The energy associated with this exothermic process is approximately 40-45 kcal/mole (40). Energetic arguments suggest that there will be competition for binding sites and thus most sites will likely be occupied, causing formation of close-packed monolayers. There are still pin-hole defects in the monolayer and less ordered packing at domain boundaries (41, 42). Formation of thiolate monolayers is an equilibrium process, whereby surface bound thiolate can interchange with thiol molecules in solution. This dynamic process has been found to "heal" monolayers containing defects over time.

Porter, *et al.* (37) have studied the effects of chain length (number of methylene units) on film thickness. For shorter chains (n<9), they observed by
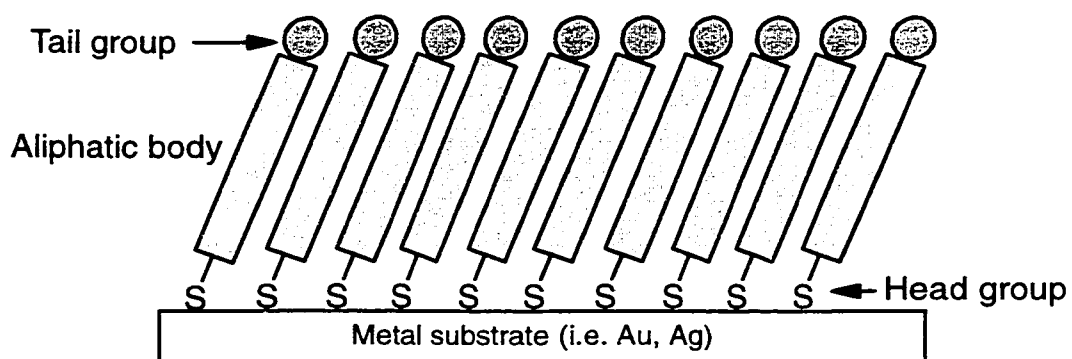
Figure 1.06. Self-assembled monolayers formed from alkylthiol chemisorption on Au substrates. The chains are oriented 20-30° away from the normal direction, enhancing van der Waals interactions between the methylene units. Tail groups included in the work are CO_2H, CH_3, OCH_2CH_3, and OCH_3.

ellipsometric measurements increases in thickness of 0.56 Å per -CH$_2$ group. For n>9, values of 1.5 Å/CH$_2$ were observed. Theoretical calculation for all-trans, fully extended alkanethiol bound normal to the surface show that the measured heights/thickness should increase ~1.3 Å/CH$_2$. Calculations from FTIR (43) analysis suggest that the molecules were not bound perpendicular to the surface, but tilted 20-30° from normal. Tilting of the chains is believed to maximize van der Waals interactions between the chains, and energies associated with these interactions are on the order of a few kcal/mol (<10) (44). After tilt was taken into account, the slope expected was only 1.1 Å/CH$_2$. The discrepancy of measured and calculated slopes may be the result of three different factors. The first two factors are the accuracy of the refractive index of the gold substrate and that of the adsorbed film, and the third factor is surface coverage. Infrared studies have shown that short chain (n<9) form fluid-like monolayers, while longer chains form crystalline monolayers (37). There will more discussion of chain length effects and the quality of microcontact-printed SAMs in Chapter IV.

The tail or functional end of the thiol molecule determines the chemistry of the interface that is generated upon chemisorption. A non-exhaustive list of functional groups that have appeared in literature includes -NH$_2$, -CO$_2$H, -OH, -CH$_3$, esters, and various polyethylene glycols (-OCH$_2$CH$_2$-X) (14, 17, 18, 37, 44, 45). Thus, surface parameters that can be modulated include surface free energy and charge. Because alkylthiolate self-assembled monolayers exhibit similar crystallinity and packing at longer chain length, variation in monolayer structure can be ignored, thus affording studies on the influence of surface chemistry on protein adsorption, lubrication, friction and wear. Thiolate self-assembled monolayer systems are extensively used to simulate surfaces with different chemistry because of their ease of preparation, stability, and favorable structural properties.

Research Objectives

Protein adsorption at solid surfaces has been shown to affect the biocompatibility of implants. Only by understanding the mechanisms of protein adsorption and developing a thorough knowledge of how surface properties influence protein adsorption can biocompatibility concerns be addressed. Most studies of adsorbed protein films are studied by macroscopic techniques, which provided a great deal of information. However such techniques, including infrared spectroscopy, circular dichroism and ellipsometry only provide an average representation of the surface. Electron microscopic studies can provide details of protein films at higher resolution, however, the samples must be dried and stained. SPM techniques permit investigation of biological specimens on scales comparable to electron microscopy without staining or modification to the specimens. The work to be presented stems from three motivations.

The first motivation derives from the need to develop protocols and methods for studying protein adsorption in situ. Imaging in solution allows the samples to be kept near physiological conditions; however, many difficulties arise regarding instrumental set up, and as of 1996, many research groups were still imaging biological samples in ambient conditions (i.e. room conditions). The objective is to evolve methods for mechanistic studies of protein film formation. Experimentation by flowing protein into the microscope's fluid cell will provide insight into the initial stages of adsorption. Studies will be performed on atomically smooth surfaces of highly-oriented pyrolytic graphite (HOPG) and mica.

The second objective is to determine how surface chemistry influences protein adsorption. Interests in the biomaterial research field lie not in detection of single protein structures, but in the study of protein films. Gold surfaces tailored to exhibit specific chemistry will be prepared from alkylthiols. Octadecanethiol ($HS(CH_2)_{17}CH_3$) and mercaptohexadecanoic acid ($HS(CH_2)_{15}CO_2H$) were chosen

because the resultant surfaces are vastly different in chemistry. Other functional groups to be studied include -OCH$_3$ and -OCH$_2$CH$_3$. Parameters such as protein coverage and adsorbed protein states will be areas of focus.

Contact mode SFM operated in friction force mode has shown the ability to map surfaces compositionally (14, 15). The last motivation is to determine whether friction imaging can be applied to map adsorbed protein states. Microcontact printing of ODT and MHA surfaces will serve to prepare substrates for these studies. Antibody binding studies will provide further verification of results.

References

(1)   Young, R.; Ward, J.; Scire, F. *Phys. Rev. Lett.* **1971,** *27,* 922.

(2)   Binning, G.; Rohrer, H.; Gerber, C.; Weibel, E. *Phys. Rev. Lett.* **1982,** *49,* 57.

(3)   Binning, G.; Rohrer, H.; Gerber, C.; Weibel, E. *Phys. Rev. Lett.* **1983,** *50,* 120.

(4)   Eigler, D. M.; Schweizer, E. K. *Nature* **1990,** *344,* 524.

(5)   Heller, E. J.; Crommie, M. F.; Lutz, C. P.; Eigler, D. M. *Nature* **1994,** *369,* 464.

(6)   Crommie, M.; Lutz, C. P.; Eigler, D. M. *Science* **1993,** *262,* 218.

(7)   Binnig, G.; Quate, C. F.; Gerber, C. *Phys. Rev. Lett.* **1986,** *12,* 930.

(8)   Drake, B.; Prater, C. B.; Weisenhorn, A. L.; Gould, S. A. C.; Albrecht, T. R.; Quate, C. F.; Cannell, D. S.; Hansma, H. G.; Hansma, P. K. *Science* **1989,** *243,* 1586-1589.

(9)   Kendall, K. *Nature* **1986,** *319,* 203-205.

(10)   Meyer, G.; Amer, N. M. *Appl. Phys. Lett.* **1990,** *57,* 2089.

(11)   Marti, O.; Colchero, J.; Mlynek, J. *Nanotechnol.* **1990,** *1,* 141.

(12)   Schwarz, U. D.; Koster, P.; Wiesendanger, R. *Rev. Sci. Instrum.* **1996,** *67,* 2560.

(13)   Overney, R. M.; Meyer, E.; Frommer, J.; Brodbeck, D.; Luthi, R.; Howald, L.; Guntherodt, H.-J.; Fujihira, M.; Takano, H.; Gotoh, H. *Nature* **1992,** *359,* 133 - 135.

(14)   Frisbie, C. D.; Rozsnyai, L. F.; Noy, A.; Wrighton, M. S.; Lieber, C. M. *Science* **1994,** *265,* 2071.

(15)   Green, J. B. D.; McDermott, M. T.; Porter, M. D.; Siperko, L. M. *J. Phys. Chem.* **1995,** *99,* 10960 - 10965.

(16)   Pale-Grosdemange, C.; Simon, E. S.; Prime, K. L.; Whitesides, G. M. *J. Am. Chem. Soc.* **1991,** *113,* 12 - 20.

(17)   Prime, K. L.; Whitesides, G. M. *Science* **1991,** *252,* 1164 - 1167.

(18)   Prime, K. L.; Whitesides, G. M. *J. Am. Chem. Soc.* **1993,** *115,* 10714 - 10721.

(19)   Bohnert, J. A.; Horbett, T. A. *J. Colloid Interface Sci.* **1986,** *111,* 363-380.

(20)   Feng, L.; Andrade, J. D. In *Proteins at Interfaces II: Fundamentals and Applications*; Horbett, T. A., Brash, J. L., Eds.; American Chemical Society: Washington, DC, 1995, pp 66 - 79.

(21)   Campbell, N. A. *Biology,* Third Edition ed.; The Benjamin/Cummings Publishing Company, Inc.: Redwood City, 1993.

(22)   Shiba, E. *Am. J. Physiol.* **1991,** *260.*

(23)   Ugarova, T. P. *J. Biol. Chem.* **1993,** *268,* 21080.

(24)   Rouslahti, E.; Pierschbacher, M. D. *Cell* **1986,** *44,* 517.

(25)   McClary, K. B.; Grainger, D. W.; Ugarova, T. *J. Biom. Mater. Res.* **2000,** *50,* 428-439.

(26)   Mosher, D. F. *Ann. Rev. Med.* **1984,** *35,* 561.

(27) Hynes, R. O. *Ann. Rev. Cell Biol.* **1985**, *1*, 67.

(28) Rouslahti, E. *Ann. Rev. Biochem.* **1988**, *57*, 375.

(29) Marquart, M.; Deisenhofer, J.; Huber, R.; Palm, W. *J. Mol. Biol.* **1980**, *141*, 369-391.

(30) Deisenhofer, J. *Biochemistry* **1981**, *20*, 2361-2370.

(31) Vermeer, A. W. P.; Bremer, M. G. E. G.; Norde, W. *Biochim. Biophys. Acta.* **1998**, *1425*, 1-12.

(32) Cullen, D. C.; Lowe, C. R. *J. Colloid Interface Sci.* **1994**, *166*, 102-108.

(33) Bos, O. J. M.; Labro, J. F. A.; Fischer, M. J. E.; Witling, J.; Janssen, L. H. M. *J. Biol. Chem.* **1989**, *264*, 953-959.

(34) Carter, D. C.; He, X. M.; Munson, S. H.; Twigg, P. D.; Gernert, K. M.; Broom, M. B.; Miller, T. Y. *Science* **1989**, *244*, 1195-1198.

(35) Vroman, L.; Adams, A. L. *J. Biomed. Mater. Res.* **1969**, *3*, 43.

(36) Nuzzo, R.; Allara, D. L. *J. Am. Chem. Soc.* **1983**, *105*, 4481.

(37) Porter, M. D.; Bright, T. B.; Allara, D. L.; Chidsey, C. E. D. *J. Am. Chem. Soc.* **1987**, *109*, 3559-3568.

(38) Bain, C. D.; Troughton, E. B.; Tao, Y.-T.; Evall, J.; Whitesides, G. M.; Nuzzo, R. G. *J. Am. Chem. Soc.* **1989**, *111*, 321 - 335.

(39) Nuzzo, R. G.; Dubois, L. H.; Allara, D. L. *J. Am. Chem. Soc* **1990**, *112*, 558 - 569.

(40) Dubois, L. H.; Zegarski, B. R.; Nuzzo, R. G. *J. Am. Chem. Soc.* **1990**, *112*, 570.

(41) McDermott, C. A.; McDermott, M. T.; Green, J.-B.; Porter, M. D. *J. Phys. Chem.* **1995**, *99*, 13257.

(42) Yamada, R.; Wano, H.; Uosaki, K. *Langmuir* **2000**, *16*, 5523-5525.

(43) Allara, D. L.; Nuzzo, R. G. *Langmuir* **1985**, *1*, 52-66.

(44)   Ulman, A. *An Introduction to Ultrathin Organic Films: From Langmuir-Blodgett to Self-Assembly*; Academic Press: San Diego, 1991.

(45)   Sinniah, S. K.; Steel, A. B.; Miller, C. J.; Reutt-Robey, J. E. *J. Am. Chem. Soc.* **1996,** *118*, 8925 - 8931.

CHAPTER II

REAL-TIME OBSERVATION OF PROTEIN FILM FORMATION ON WELL-DEFINED SURFACES WITH SCANNING FORCE MICROSCOPY*

Introduction

The work presented in this chapter will demonstrate the main advantages of scanning force microscopy for obtaining two-dimensional images of biological specimens. The ability to obtain a clear and accurate representation of a sample under electrolyte solution is a non-trivial task. There are many technical challenges to overcome and thus, the learning curve is initially very steep. Experiments carried out in this chapter allowed me to develop and fine-tune the skills necessary to be a proficient probe microscopist.

The importance of adsorbed protein films to areas such as implant medicine, biosensor design, food processing and chromatographic separations has provided the incentive for researchers from a broad range of disciplines to focus studies on protein-surface interactions [1]. When a foreign material comes into contact with blood, it is generally accepted that a complex biomolecular film forms rapidly at the interface. Important components of this film include plasma proteins, which are involved in the blood clotting cascade and have also been shown to modify the interaction of various blood components at the blood-biomaterial interface [2]. Numerous studies have lead to the general understanding that the type, amount and the conformation of surface bound plasma proteins are all crucial in determining the biocompatibility of materials [1, 3, 4].

Fibrinogen (FG) is one plasma protein that has received much attention due to its dual functionality in thrombosis (formation of a blood clot). The conversion

---

of FG to fibrin and the subsequent polymerization of fibrin are key steps in blood clot formation. Fibrinogen also serves as an adhesive agent in the aggregation of platelets that occurs simultaneously with fibrin polymerization in the development of a hemostatic blood clot [5]. A variety of techniques have been employed to probe the interfacial properties of FG including ellipsometry [6], infrared spectroscopy [7], radio labeling [8], surface plasmon resonance [9] and X-ray photoelectron spectroscopy [10]. These methodologies have provided a wealth of macroscopic information reflecting behavior averaged over the entire surface. The structure of single FG proteins [11] and the architecture of FG films [12] have also been probed at microscopic length scales using scanning electron microscopy (SEM) investigations. Recently, immunogold labeling combined with SEM imaging has been utilized to probe the architecture of adsorbed FG films [13]. The results of both macroscopic and microscopic studies to date have shown that FG binds strongly and in high amounts to most surfaces and competes efficiently with other proteins for adsorption sites [4]. Although this knowledge has provided some insights into the factors affecting blood biocompatibility, the nature of the high surface activity of FG is not completely understood.

Relative to other proteins, the amount of FG adsorbed is less sensitive to substrate composition [4]. Because of this relatively low substrate influence, the presence of a dense FG film at the solution-biomaterial interface is not an absolute indicator of the material's biocompatibility. A factor which is likely important in determining thrombosis resistance is the conformation of the surface-bound FG. For example, platelet adhesion correlates with factors other than the total amount of FG adsorbed, suggesting that the orientation of the adsorbed FG is significant [14]. A number of parameters have been shown to influence the conformation of adsorbed FG including the nature of the substrate [12c, 15] and the concentration of FG in solution before adsorption [15c, 16]. There is also evidence for post-adsorptive transitions in FG structure [17], highlighting the complexity of FG

interfacial interactions. Common methods employed to probe the conformation of FG in adsorbed films are generally indirect, involving observation of the protein's ability to bind platelets [14, 17a] and antibodies [14a,b,d, 17a, 18] or measuring the amount of protein that is eluted from the surface by a surfactant such as sodium dodecylsulfate (SDS) [19]. Spectroscopic techniques such as infrared [7] and circular dichroism [20] have also been utilized to probe conformational changes in protein layers. These techniques have advanced understandings of the factors that affect pre-formed FG films; however, little information exists on the initial growth process of FG layers and the influence of the substrate on growth mechanisms. The mechanism of FG film formation is of interest because the manner in which an adsorbed layer forms directly influences the structure and properties of the completed film.

Early studies focused on the initial growth of FG layers generally involved measuring the amount of FG adsorbed as a function of time or solution concentration (adsorption isotherms) [8, 21]. These investigations have shown that FG adsorption is rapid and yield isotherms that generally exhibit a saturation plateau reflecting a closely packed monolayer. The saturation coverage varies slightly from surface to surface, implying surface-induced conformational changes or varying amounts of protein-protein interactions [21]. Microscopic studies of the initial stages of FG adsorption have been carried out by SEM imaging of films adsorbed from solutions of varying concentration [12e] or of samples where film formation had been interrupted at various times (quenched films) [12c]. These investigations also involved staining of the quenched films to provide contrast for SEM imaging. The uncertainty in the relationship between a stained, quenched film and the actual layer forming in solution has led us to believe that an in situ, real-time observation of film growth will provide additional insights into the structure of adsorbed FG.

Scanning force microscopy (SFM) has recently found widespread use in probing biological materials [22]. The dramatic increase in popularity of SFM for examining biological systems stems from its ability to image in buffer solutions where environmental conditions such as pH, ionic strength and temperature can be adjusted to simulate physiological conditions. This capability has prompted the SFM observation of several biological processes in real-time. For example, a fascinating early demonstration was the real-time observation of the transformation of FG to fibrin [23]. Other examples of biological processes that have been examined in real-time include protein crystal growth [24] and the dynamic release of protein from a biodegrading polymer [25]. Individual protein dynamics have also been observed [26].

The adsorption of plasma proteins has been probed with SFM in both static [27-29] and dynamic modes [30]. Individual FG molecules [27a] and FG films [27-29] have been imaged after the substrate had reached equilibrium with the protein solution. The real-time examination of immunoglobulin G (IgG) adsorption to mica [30a] and graphite [30b] has appeared in separate reports. The mechanism of IgG adsorption appears to vary with each substrate, providing a basis for further SFM investigations aimed at unraveling the effect of substrate on protein film growth. However, to my knowledge, SFM imaging has not been exploited to probe the initial stages of FG film growth or in the investigation of surface induced variations of FG film structure.

This chapter reports results of an SFM investigation focused on the influence of substrate on the assembly of FG films. Images detailing both pre-formed layers and the real-time assembly of FG films on highly oriented pyrolytic graphite (HOPG) and mica surfaces are presented. Although these are well-defined substrates, they effectively serve as models for more complex hydrophobic and hydrophilic surfaces. Graphitic substrates are also directly relevant to biocompatibility studies due to the use of pyrolytic carbon in prosthetic heart

valves. A series of studies has recently appeared highlighting the adsorption of FG at low temperature isotropic carbon (LTIC) surfaces [31, 32]. Also, in this study, frictional contrast was developed to give insights into the structure of adsorbed protein [30b]. The results show that the growth process observed with each substrate governs the final film properties. Details of my observations provided a structural basis for substrate dependent differences in bovine fibrinogen (BFG) adsorption.

Experimental

Reagents and Materials. Fraction I bovine fibrinogen (BFG) with 89% clottable protein was obtained from Sigma (St. Louis, MO) and used as received. Water from a Nanopure (Barnstead, Dubuque, IA) purification system was used in all solution preparations. BFG solutions (50 μg/mL) were made in 10 mM sodium phosphate buffer (PB) at pH = 7.4. Fibrinogen and protein free PB solutions were filtered using a 0.22 μm millex-GV, low protein binding filter (Millipore, Bedford, MA) before adsorption experiments. Elution of proteins was performed with 3% w/v SDS (SERVA) in water. Fresh surfaces of highly oriented pyrolytic graphite (HOPG) (Advanced Ceramic Materials, Lakewood, OH) were generated by cleaving with adhesive tape before each experiment. Mica (Asheville Schoonmaker Mica Co., Newport News, VA) was cleaved with a razor blade to generate a clean surface.

SFM Imaging. SFM images were obtained with a Nanoscope III (Digital Instruments, Santa Barbara, CA) equipped with a fluid cell. Silicon nitride cantilevers (Digital Instruments) with nominal spring constants of 0.06 N/m were used. For all experiments discussed here, the imaging force was ≤1 nN. Images are presented without filtering. A software planefit was used where necessary to reduce image distortions as a result of the non-linearity of the tube piezo scanner.

Each experiment began with the introduction of phosphate buffer into the fluid cell that was then allowed to equilibrate for 30 to 60 min to reduce drift.

Images of the substrate in buffer were collected in order to compare the surface before and after the addition of BFG. Imaging was performed under static solution or with solution flowing through the fluid cell. For static imaging, after equilibration of the cell in PB, BFG solution was introduced into the fluid cell by a negative pressure gradient. Adsorption times were approximately 30 min. Images were taken with BFG solution in the cell and after the cell was further flushed with phosphate buffer with no apparent differences observed. As a result, the assumption was made that protein adsorption to the probe tip does not influence the quality of the images obtained at the resolution employed here (micron scale).

The setup for flowing solution through the SFM fluid cell is similar to that described in a previous report [33] and illustrated in Figure 2.01. A 5 mL syringe body served as a reservoir for buffer and BFG solutions to be gravity fed into the fluid cell. Images were taken with the buffer solution flowing at 0.1–0.2 mL/min. When the images appeared stable, PB was allowed to flow into the fluid cell until the syringe reservoir approached empty. A 50 μg/mL BFG solution was then added to the syringe reservoir and BFG was carried into the cell by a continuous flow. Images were captured continuously at a scan rate of 10.2 Hz.

Elution experiments. The SDS elution experiments were performed on pre-formed BFG films on HOPG as described for the static imaging conditions above. The BFG was equilibrated with the surface for 30 min. The 3% SDS solution was then flowed through the fluid cell for 60 minutes at a flow rate of ~1 mL/min. After this time, the cell was flushed with PB. Flow was then stopped and images were taken in static buffer.

Results and Discussion

The following sections details in situ topographic and lateral force SFM studies of BFG films on HOPG and mica surfaces. Initially, images of BFG films pre-formed from 50 μg/mL solutions in PB will be discussed. These types of BFG layers were designated as equilibrium films given that the surface bound species
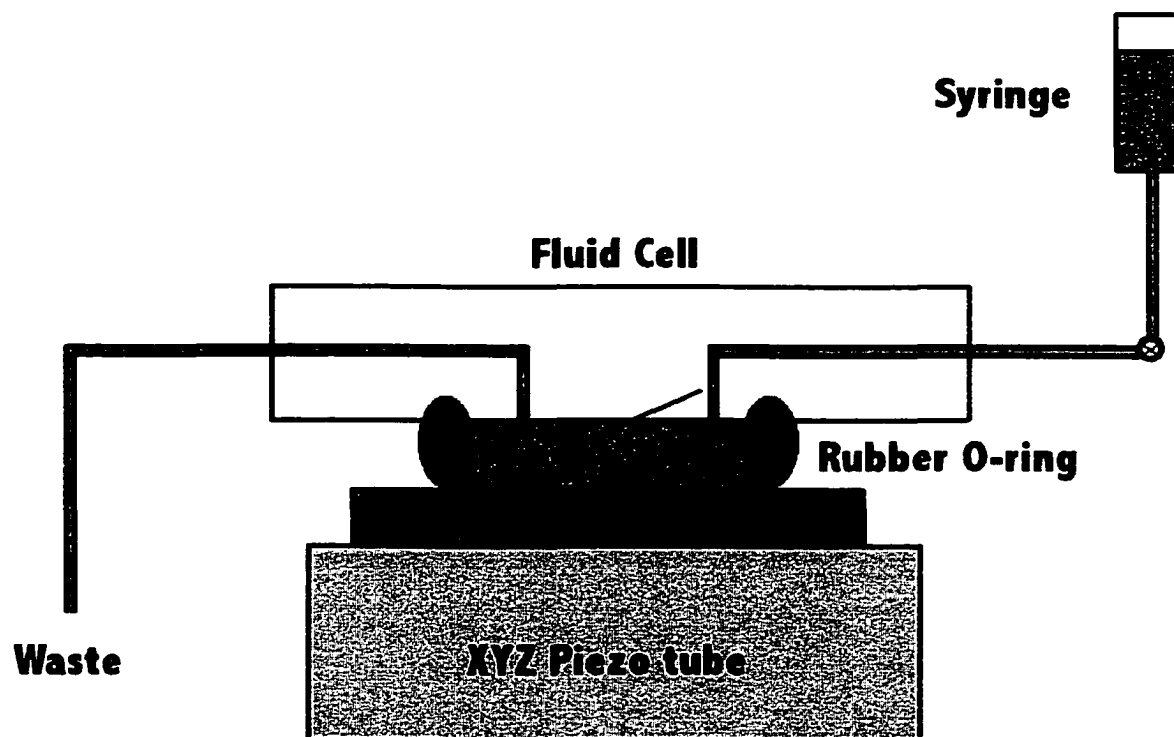
Figure 2.01. SFM fluid cell used for imaging substrates under solution conditions. Syringe reservoir used containment of buffer and protein solution. Plunger was removed for real-time flow experiments and a stopcock was used to control flow rate.

has reached equilibrium with the solution. Then, results of real-time exploration of BFG film growth on the different surfaces will be presented. Lastly, insights into surface induced variations in final film structure through the SFM analysis of SDS elution experiments and a detailed model of BFG binding based on structural considerations will be rendered.

Equilibrium BFG film structure. An illustration of the utility of SFM for probing surface-induced variations in adsorbed BFG film structure is provided by in situ images of pre-formed layers. The substrates utilized in the present study were thoroughly characterized before protein adsorption because a previous study had reported substrate features that appeared to be similar to biological molecules [34]. Parts A and B of Figure 2.02 are respective 4×4 μm^2 topographic and lateral force images representative of cleaved HOPG collected in PB solution. The topographic features in Figure 2.02A are similar to those noted in numerous SPM studies of HOPG [35, 36]. The majority of the image consists of atomically flat basal plane graphite, which exhibits a relatively constant lateral force signal in Figure 2.02B [36]. A cleavage step is apparent in the lower portion of the image, exhibiting a lateral force signature consistent with "tripping" of the tip over the face of the step [36, 37]. Generally, the surface structure of HOPG imaged during this study consisted of atomically flat basal plane and some cleavage step defects.

Exposure of cleaved basal plane HOPG to 50 $\mu g/mL$ BFG solution resulted in a surface such as that depicted in Figure 2.02C and D. Part C of Figure 2.02 is a 4×4 μm^2 topographic image collected in the BFG/PB solution after 30 min of equilibration time. Figure 2.02D is the corresponding lateral force image. These images are clearly distinct from the images of unmodified HOPG in PB. The topography consists of uniformly dispersed spherical structures exhibiting a range of heights between 6 and 13 nm at a density of 24 ± 2 structures/μm^2 [38]. Spherical structures with heights up to 60 nm have been observed and continuing investigations have revealed that both the density and height of these structures are
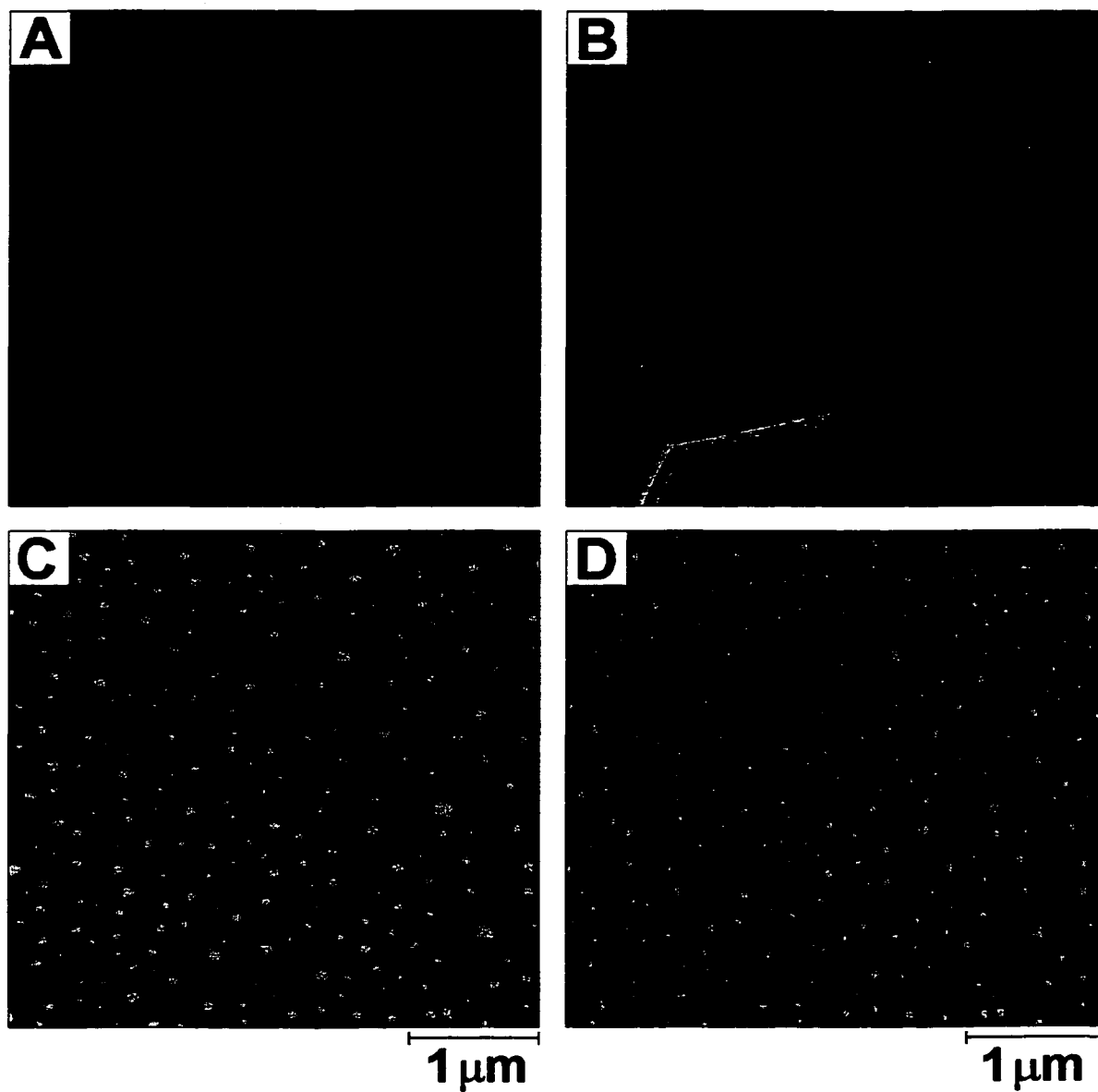
Figure 2.02. In situ SFM images of an unmodified HOPG substrate and a BFG film on HOPG. (A) 4 × 4 μm^2 topographic SFM image of cleaved HOPG in phosphate buffer (Z-scale = 5 nm) and (B) the corresponding lateral force image (Z-scale = 0.1 V). (C) 4 × 4 μm^2 topographic image of a BFG film on HOPG adsorbed from a 50 μg/ml BFG solution for 30 min (Z-scale = 20 nm) and (D) the corresponding lateral force image (Z-scale = 0.1 V).

concentration and flow-rate dependent [39]. Concentration dependent spherical structures in adsorbed BFG films have also been previously observed in SEM images [12a, d, e]. These reports interpret the spheres as fibrinogen aggregates and are discussed further in Chapter V. The aggregates observed here are stable to imaging for an extended period of time (at least 5 h), implying a robust structure. Upon initial inspection, the lower background region appears to be molecularly flat and could be interpreted as the HOPG substrate. However, as detailed below, images collected during BFG adsorption show that the background consists of a well-packed BFG monolayer. It is not clear from Figure 2.02C and D, however, whether the aggregates form on top of the initial BFG monolayer or if they are bound to the substrate surface and are embedded in the BFG monolayer.

An identical experiment was performed on a cleaved mica surface. Parts A and B of Figure 2.03 are representative topographic and lateral force images of freshly cleaved mica in PB. The topography of mica is atomically smooth and the friction is constant over the surface. The structure of a BFG film formed on mica from a 50 μg/mL solution is illustrated in parts C and D of Figure 2.03. Although subtle, the presence of adsorbed BFG is indicated by an increase in the RMS roughness of the surface from 0.087 nm for unmodified mica to 0.618 nm for Figure 2.03C. The BFG film exhibits a uniform topography and friction. With the imaging forces used here (≤ 1 nN), tip induced displacement of the BFG was noted as has been illustrated previously [28a]. Unlike the film structure on hydrophobic HOPG, however, spherical aggregates do not exist in BFG films adsorbed onto mica. It is clear from Figures 2.02 and 2.03 that the SFM observed morphology of BFG films is influenced by the nature of the substrate.

Real-time BFG film formation. To monitor the adsorption of BFG in real-time, experiments were performed while either PB or BFG solution were flowing through the SFM fluid cell at a rate of 0.1-0.2 mL/min. Images collected during such an experiment at a cleaved HOPG surface are shown in Figure 2.04. Each
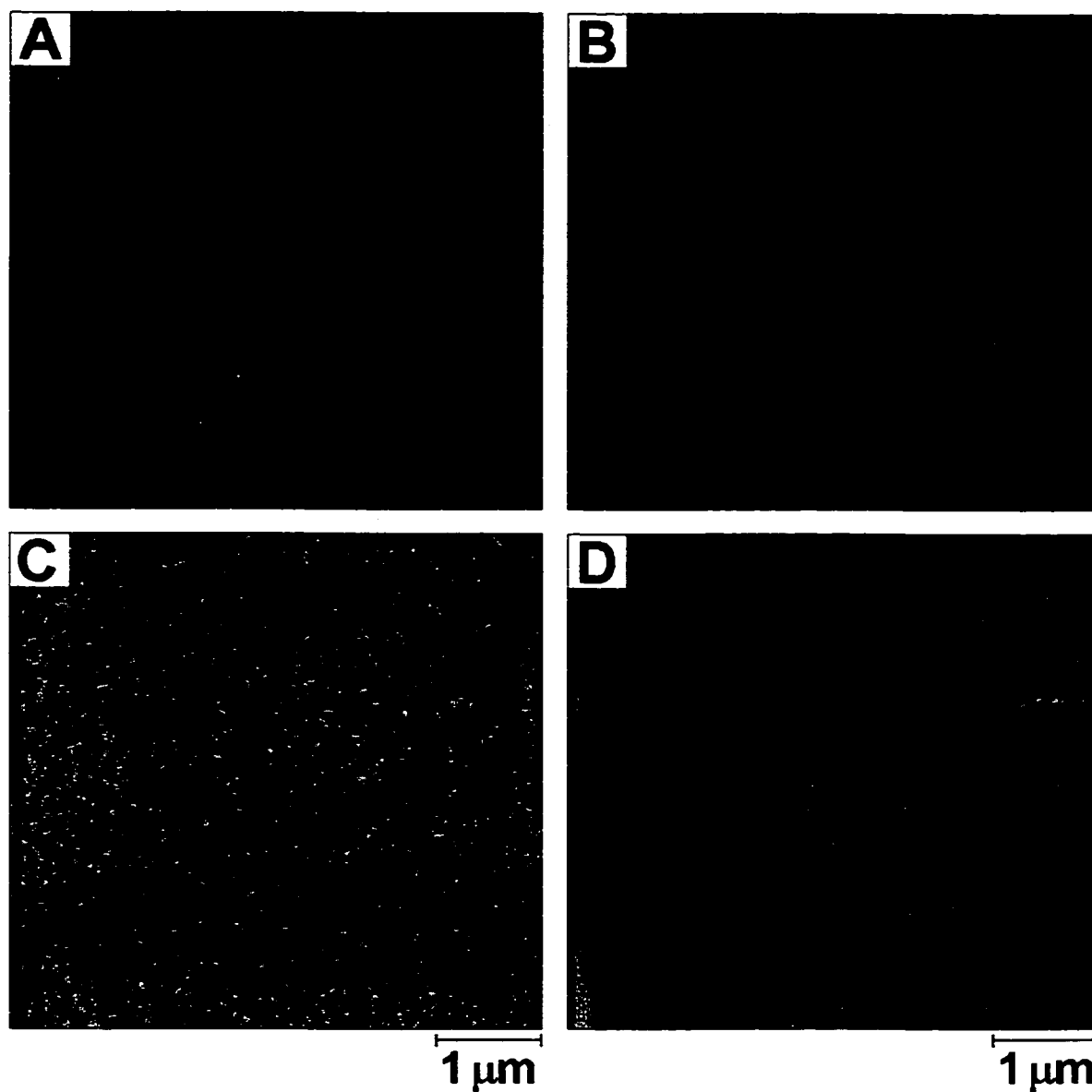
Figure 2.03. In situ SFM images of an unmodified mica substrate and a BFG film on mica. (a) 5 × 5 μm^2 topographic SFM image of cleaved mica in phosphate buffer (Z-scale = 5 nm) and (B) the corresponding lateral force image (Z-scale = 0.1 V). (C) 5 × 5 μm^2 topographic image of a BFG film on mica adsorbed from a 50 $\mu g/ml$ BFG solution for 30 min (Z-scale = 5 nm) and (D) the corresponding lateral force image (Z-scale = 0.1 V).

image represents consecutive scans requiring ~50 s to complete. This is a sufficiently long time scale that the development of the BFG film can be monitored during a single image as well as through image to image comparisons. Figure 2.04A is the topographic image of the initial HOPG substrate collected in flowing PB. This image remained constant for ~4 min prior to the addition of BFG, illustrating the stability of imaging under flow conditions. Bovine fibrinogen solution was then added to the buffer reservoir and allowed to flow through the SFM fluid cell. Part B of Figure 2.04 is a topographic image collected as the slow scan axis advanced from bottom to top. Because the BFG has not yet reached the fluid cell, the lower portion of the image resembles the original substrate.

The initial stages of BFG adsorption are observed in the top half of Figure 2.04B and appear as 3-4 nm increases in topography [38]. Although the accepted rod-like structure of BFG is not resolved in the images, this does not preclude that the initial adsorbed structures in Figure 2.04B are individual BFG molecules. However, because the SFM tip can artificially broaden the lateral dimensions of small structures, the actual size of these features is uncertain and it would be risky to identify them as single molecules. Thus, these structures are designated as clusters. The height of the clusters is inconsistent with any of the known dimensions of BFG (45 nm long × 6 nm wide) but is similar to the SFM measured height of individual fibrinogen molecules adsorbed at a hydrophobic surface [27a]. The measured height either reflects a tip-induced compression of the surface-bound BFG or a diminished molecular dimension resulting from protein denaturation upon adsorption. The structure in the top right corner marked with arrow **a** is the nucleation of a BFG strand. For adsorption timing purposes, t = 0 was defined as approximately halfway through Figure 2.04B with the image being complete at t = 25 s. The time scale is listed here simply as a means to track BFG film formation and no kinetic information was extracted from these data.
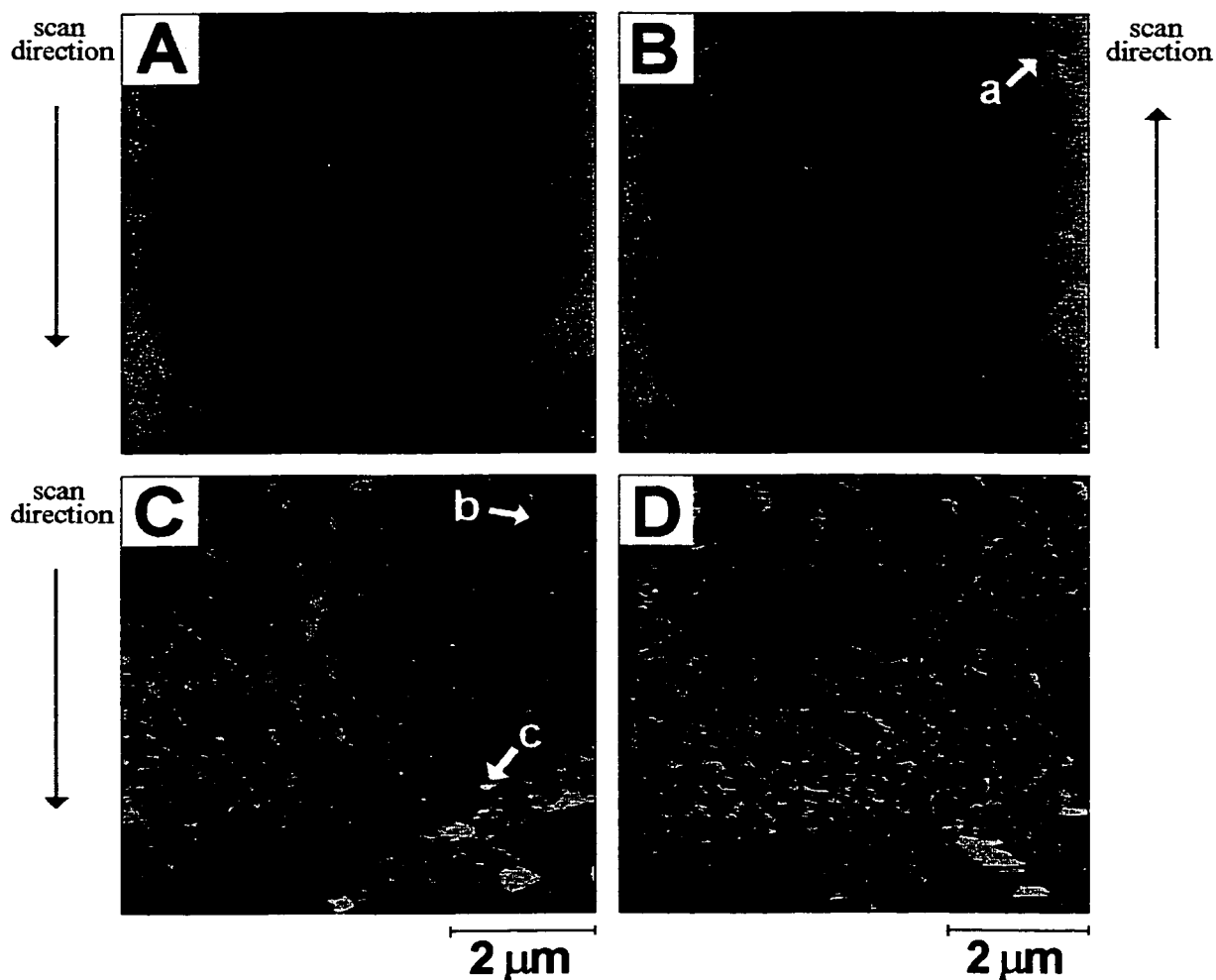
Figure 2.04. 6.6 × 6.6 μm² consecutive SFM images of BFG film growth on HOPG monitored in real-time with continuous flow. Parts A and B are topographic images (Z-scale = 10 nm). Parts C, E, and G are topographic images (Z-scale = 10 nm) while parts D, F and H are their corresponding lateral force images (Z-scale = 0.2 V). For timing purposes the center of the scan in part B is defined as t = 0, as this is the point initial adsorption is observed. C and D were captured 75 s after initial adsorption. Parts E and F correspond to 125 s, parts and G and H correspond to 225 s. Figure 2.04 continues on the next page.
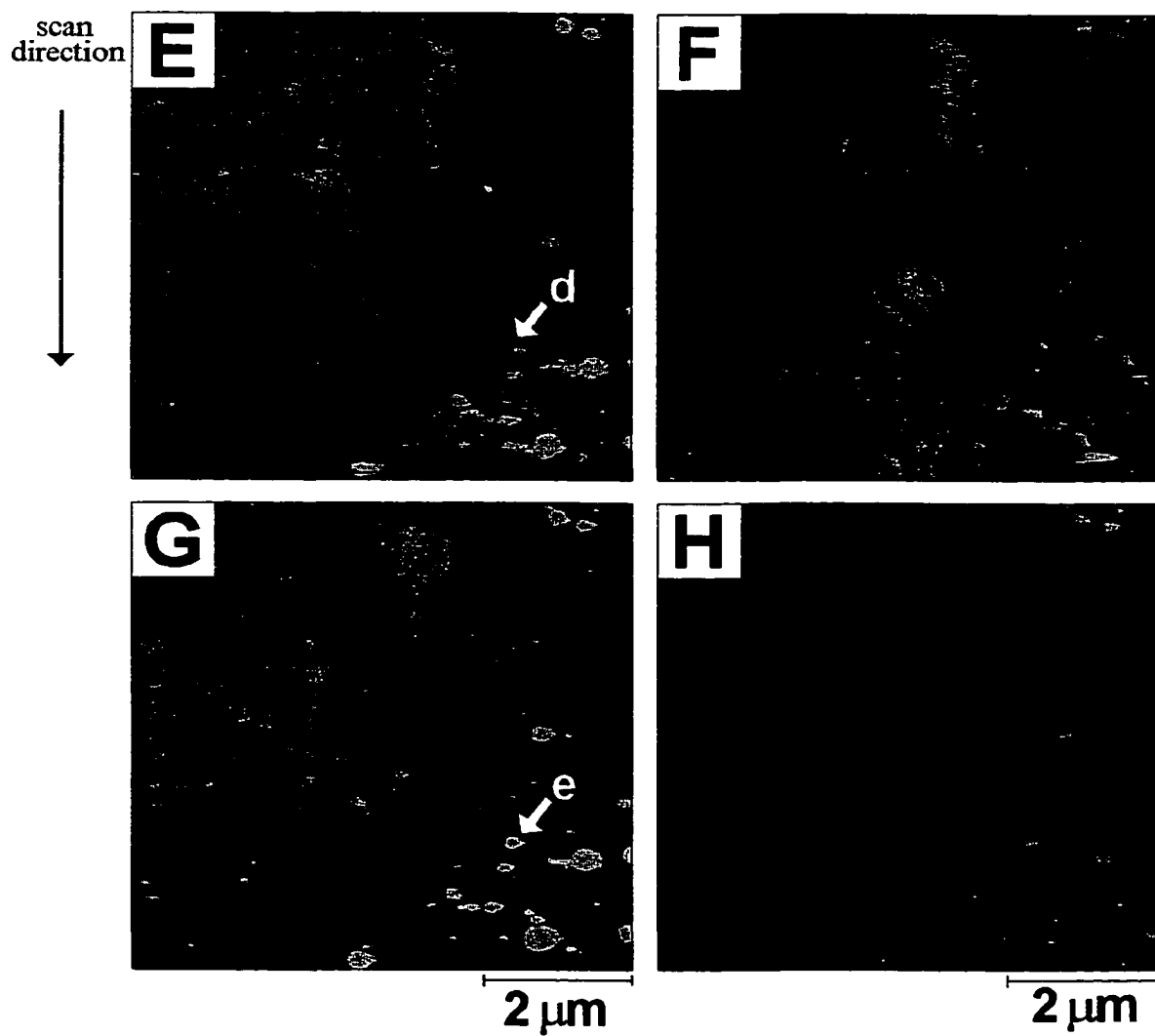
Figure 2.04. Continued. Note that parts G and H are 2 scans after parts E and F.

Parts C and D in Figure 2.04 are topographic and lateral force images, respectively of the ensuing downward scan. A higher density of larger clusters relative to Figure 2.04B are observed early, at the top of the image. A number of these clusters have lengthened into strands and indeed the strand highlighted in Figure 2.04B (arrow **a**) appears to have grown in length and formed a branching point (arrow **b**). The "streaks" apparent in Figure 2.04C and 2.04D imply that some tip-induced displacement of the protein strands is occurring at these early stages [30]. Within a few seconds, a denser network of strands has formed in the center portion of the images. This network finally merges to become a nearly completed BFG monolayer in the bottom region of Figure 2.04C and 2.04D. This is shown more clearly in Figure 2.05, which is a 4×4 μm^2 expanded view (software zoom) of the lower left corner of Figure 2.04C and 2.04D. Note that the streaking is less significant as the network becomes more densely packed. Several strands are oriented perpendicular to the fast scan direction, indicating that the probe tip is not preferentially aligning the fully formed strands with the direction of the scan. The structure of the monolayer in the bottom portion of the images appears to be relatively densely packed with a few small defects apparent as depressions in the topography (Figures 2.04C and 2.05A). The low and constant frictional signal of the near-complete film that is observed in the bottom left corner of Figure 2.05B (and Figure 2.04D) implies a robust, crystalline-like architecture [37]. A tripping signal in the lateral force images is observed as the tip scans over the topographic defects in the near-complete monolayer. Also apparent in the bottom right corner of parts B and C of Figure 2.04 are several spherical aggregates similar to those observed in equilibrium films (Figure 2.02C and D).

A fibrinogen network has previously been observed in SEM images [12c, f]. Recent SFM studies have also noted the formation of a network structure on hydrophobic silicon and poly(tetrafluoroethylene) [27]. The observation of a
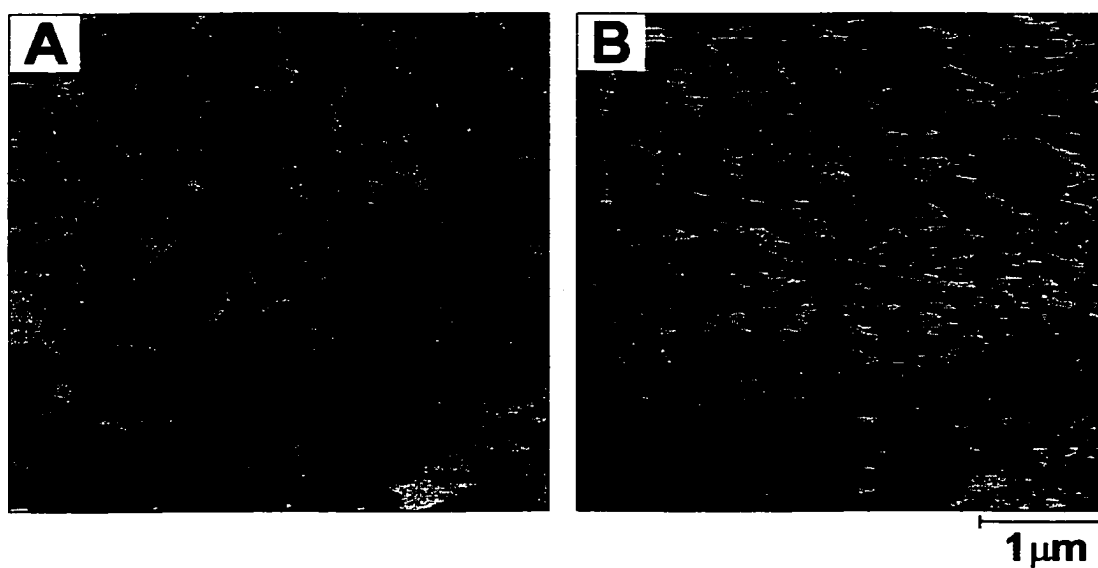
Figure 2.05. 4 × 4 μm² (A) topographic and (B) lateral force images from a software zoom of the lower left corner of Figure 2.04C and 2.04D.

network early in the growth process in this work argues that significant intermolecular interactions are involved in BFG film formation on HOPG. Branched strands were observed in SFM investigations of equilibrium BFG films on HOPG assembled from lower concentration solutions (Figure 2.06) [39]. SFM topographic image shown in Figure 2.06 was generated after 30 min exposure of 1 μg/mL BFG solution to HOPG, rinsed with phosphate buffer, and imaged in buffer. The image shows incomplete coverage at this low concentration and adsorption time. Areas darker in color are indicative of the HOPG surface, and the lighter areas are strand-like structures of BFG. A growth process driven by intermolecular interactions is consistent with an island mechanism whereby a monolayer forms via accretion of adsorbate at island edges via migration across the substrate surface. However, in contrast to the island growth mechanism, the BFG monolayer appears to develop via an increase in the density of the network strands through additional branching (Figure 2.05). Importantly, protein-protein interactions that develop during film formation will be retained and contribute to a robust final film structure.

There are no observable differences in the formation or final structure of the BFG layer near the location of the step defect at the lower right corner of the image area in Figure 2.05. The differences in reactivity between edge plane and basal plane HOPG are well documented [40]. For example, the adsorption for quinones [40b] and dye molecules [41] is enhanced at defect sites relative to the basal plane due to the exposure of the higher reactivity edge plane at a step. Carbon biomaterials such as LTIC, which are utilized in prosthetic heart valves, exhibit a complex surface microstructure containing nanometer-sized domains of both edge plane and basal plane [42]. It is noted that there is no preferential nucleation or growth at step defects implying that BFG adsorption is not sensitive to the graphite microstructure. Thus, the well-defined surface of HOPG can be
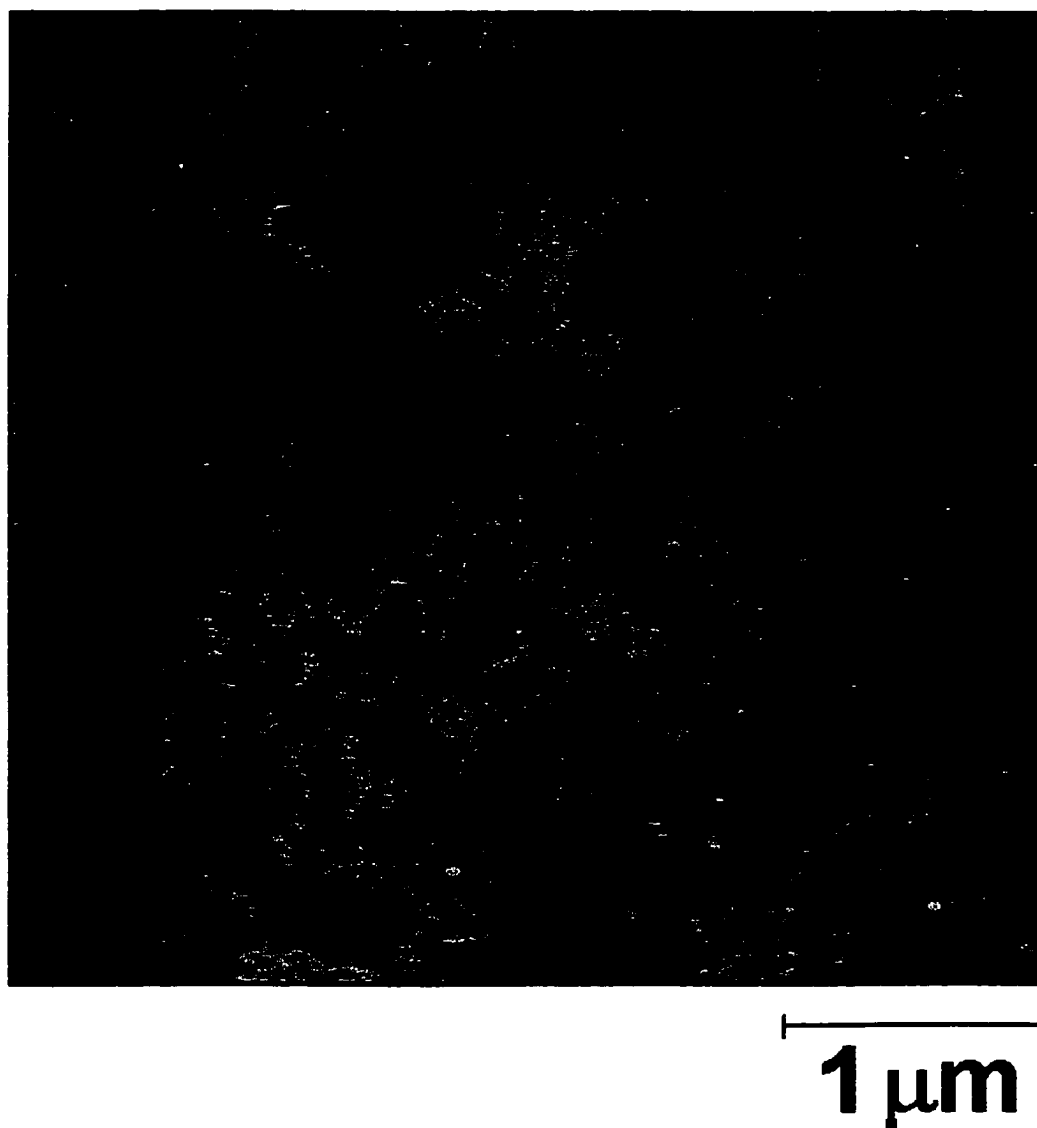
Figure 2.06. 4 × 4 μm² SFM Tographic image (Z scale = 10 nm) after 30 min adsorption of 1 μg/ml of BFG on HOPG. Image was obtained in phosphate buffer revealing strand-like structures. Darker regions are areas with no BFG.

considered a model for the surface of less ordered carbon biomaterials such as LTIC.

Further progress of the film formation is detailed in parts E-H of Figure 2.04. The topography and lateral force images of Figure 2.04E and 2.04F are the upward scan collected subsequent to Figure 2.04C and 2.04D and represent the film structure after 125 s. The basal plane surface is near completely covered with a well-packed layer of BFG, as is illustrated by a low and constant frictional response over the majority of the image in Figure 2.04F. Some pinhole defects in the film structure are observed in the topography and appear as localized increases in the lateral force. Two large defects are also apparent in the center and at the top of the images. A gradient in the density of the pinholes is evident with more defects present early in the scan. As time progresses, the defect sites either become occupied by solution-bound BFG molecules or the monolayer reorganizes to "heal" the defects resulting in a lower defect density near the top of Figure 2.04E and 2.04F. The initial aggregates formed in the bottom portion of the image remain stable to imaging while aggregates have also formed coincident with the fully developed monolayer in the center and top of the image.

Parts G and H of Figure 2.04 are the topographic and lateral force images after 225 s and represent complete film formation. No significant changes in film structure were noted after this point and multilayer adsorption was not observed. The pinhole defects observed in previous images have been completely "healed". Interestingly, the BFG molecules that have adsorbed in the larger defects observed in Figure 2.04E and 2.04F have apparently adopted a different conformation from the surrounding area, as indicated by a higher topography in Figure 2.04G and slightly higher friction in Figure 2.04H at these areas. These larger defects are believed to be the result of the probe-tip interfering with monolayer formation as there have been no observations of these variations in topography and friction apparent in parts G and H of Figure 2.04 in pre-formed films. It is noted that the

tip also hinders the formation of the aggregates. While some spherical structures are apparent in Figure 2.04G, the density is much lower than that in Figure 2.02C. Subsequent imaging of the region outside the scan area in Figure 2.04 revealed aggregates at a density similar to that observed in Figure 2.02C. Although there were some tip interferences during BFG film formation, the topography and friction of the monolayer in Parts G and H of Figure 2.04 are identical to that of pre-formed films. Thus, it is believed that the images in Figure 2.04 accurately reflect the actual film formation.

Careful inspection of the images in Figure 2.04 shows that aggregates initially form at the basal plane surface and become embedded in the surrounding close-packed monolayer. Arrow c in Figure 2.04C highlights the nascent growth of a single aggregate which is fully formed in Figure 2.04G (arrow e). In Figure 2.04C this aggregate appears to be located in a region where the monolayer is incomplete. Thus, a fully packed layer is not required for nucleation of the aggregates. In Figure 2.04E, the surrounding monolayer is more fully formed; however, a defect site remains apparent around the aggregate (arrow d), strongly arguing that the aggregate is associated with the basal plane substrate. In Figure 2.04G the monolayer is fully formed and has completely surrounded the aggregate (arrow e) [43]. These observations thus support a model where a single BFG molecule (or a small group of BFG molecules) initially binds to the basal plane surface in a conformation that induces aggregation. Aggregation of BFG molecules may have occurred in solution. The aggregates and monolayer adsorbed simultaneously and the aggregates are ultimately embedded in a well-packed film.

In summary, real-time observation of BFG film formation from single-component solutions indicates a mechanism involving the nucleation of small molecular clusters that assemble into strands with branching like appearance. The branching of the two-dimensional network continues until a densely packed

monolayer film results. Concurrently, localized three-dimensional growth occurs, leading to a dispersed array of aggregates that become embedded in the BFG monolayer.

Figure 2.07 shows the topographic images tracking BFG film formation at the mica-buffer interface. The lateral force images do not provide any additional information and are not included in this case. Figure 2.07A is the upward scan after PB containing BFG begins to flow through the cell. Initially, individual clusters adsorb randomly across the mica surface. The height of these structures ranges from 4 to 6 nm, similar to the initial structures seen at HOPG. Parts B-E are consecutive scans following the initial adsorption noted in Figure 2.07A. The image resulting from the ensuing downward scan (Figure 2.07B) shows a homogeneous increase in density of dispersed clusters especially near the bottom of the image where more time has elapsed. This trend continues throughout the intermediate stages of film growth until the bottom of Figure 2.07D, where the monolayer appears nearly complete. In some cases, larger clusters are observed but in general, the film growth on mica can be described by a uniform increase in the density of adsorbed BFG molecules or clusters. The formation of a network of strands on mica is not observed. The growth process observed in Figure 2.07 implies that the driving force for adsorbate-substrate nucleation is greater than that for the formation of protein-protein interactions. The lack of evidence for lateral interactions during film formation is in marked contrast to the growth process on HOPG. The film is completely formed in approximately 5 min, and is defect-free and appears to be well packed. Multilayers or aggregates were not observed. The region outside the scan appears identical to the image area of Figure 2.07, indicating little interference of the tip.

Surfactant-induced elution studies. It is clear from the observations presented above that BFG can form complete monolayers on both HOPG and mica. This is not surprising considering that several studies have shown that the
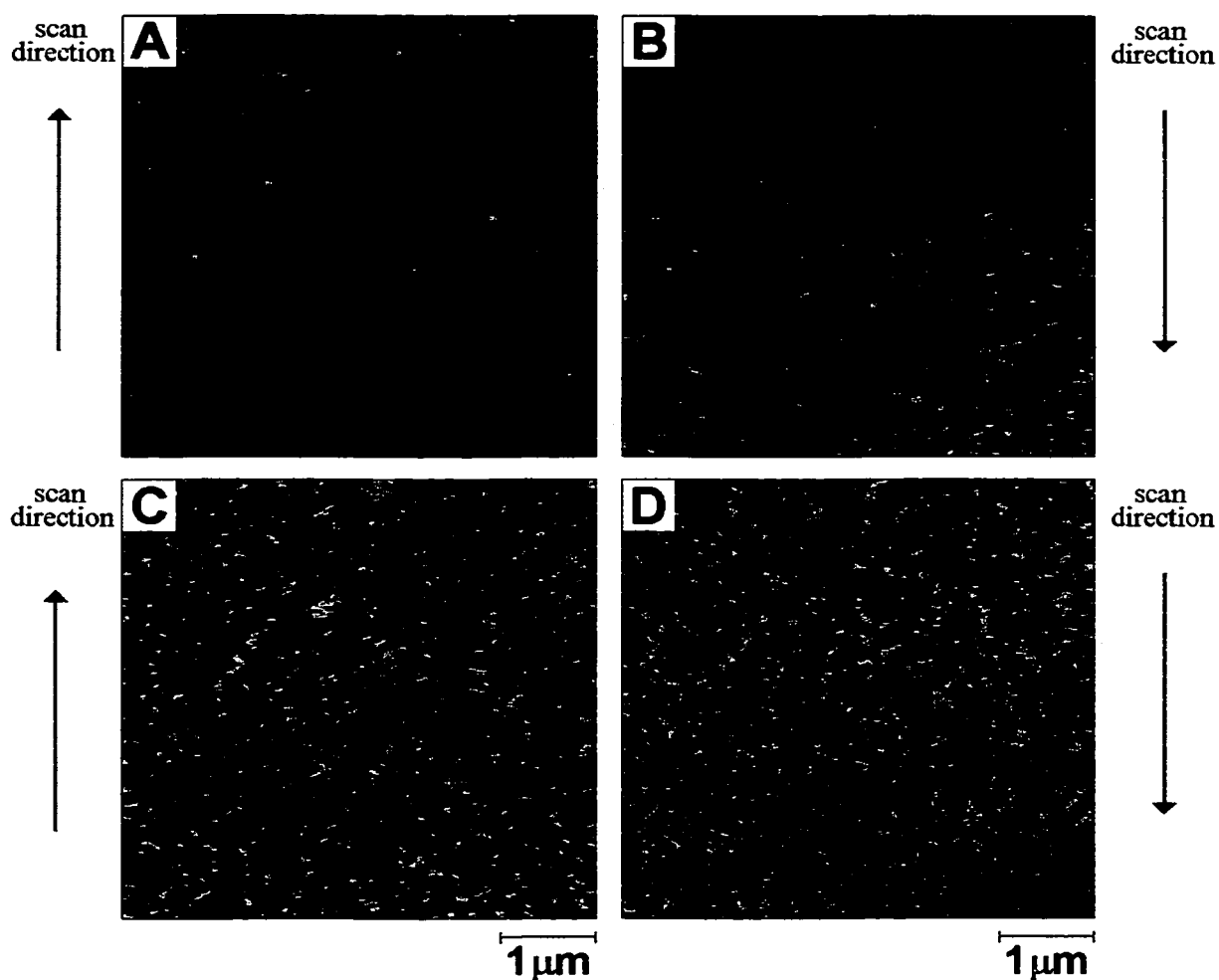
Figure 2.07. 5 × 5 μm² SFM images of BFG film growth on mica monitored in real-time with continuous flow. All images are topographic with a z-scale=10 nm except for (A) where the z-scale= 5 nm. (A) Upward scan whereby we define t = 0 s as halfway through the scan. (B) Successive downward scan, with an elapsed time of 75 s. (C) Successive upward scan with an elapsed time was 125 s. (D) Successive downward with an elapsed time was 175 s.
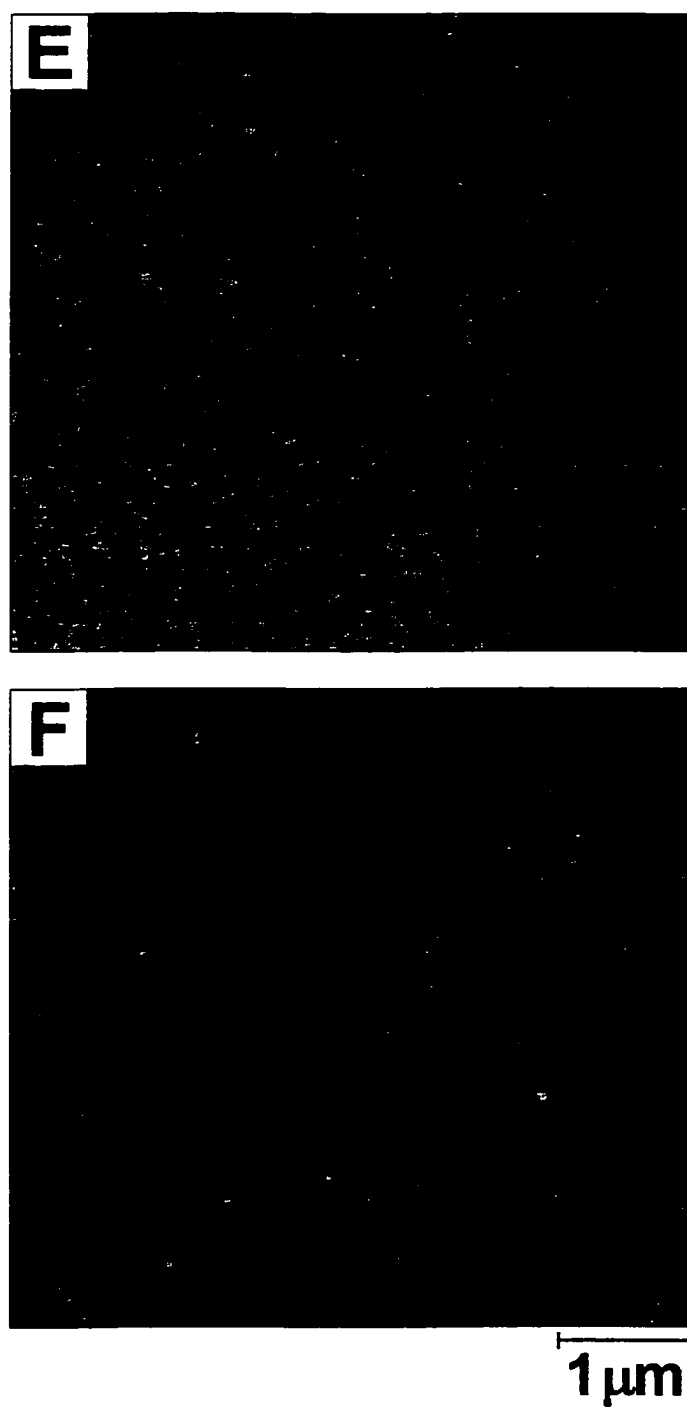
Figure 2.07. Continued. (E) Successive upward scan with an elapsed time was 225 s. (F) An upward scan and elapsed time was 325 s.

nature of the substrate has little influence on the quantity of fibrinogen adsorbed [5]. In contrast, Figures 2.04 and 2.07 illustrate different growth mechanisms at each substrate. Differences in the formation of an adsorbed layer will likely be manifested in variations in the final film properties. One variation that is readily apparent is the film morphology on each substrate depicted in Figures 2.02 and 2.03. Another final film property that was evaluated was how tightly the BFG layer was bound to each substrate. The elution of surface-bound proteins by surfactant solutions is a well-accepted method for gauging adsorbate-substrate binding [14d, 44]. It is suspected that the BFG film would be more robust on HOPG compared to mica based on the higher degree of intermolecular interactions involved in film formation.

Figure 2.08 presents the images of pre-formed films before and after exposure to a flowing SDS solution. Figure 2.08A is a $10 \times 10 \ \mu m^2$ topographic image in PB of a BFG film formed at HOPG. Figure 2.08B is the corresponding topographic image in PB after the SDS solution was allowed to flow through the fluid cell [45]. The monolayer and aggregates are present in both images implying that SDS has little affect on the film adsorbed at HOPG. This observation is consistent with recent results indicating a low susceptibility of fibrinogen adsorbed on LTIC to SDS elution [31, 32]. Parts C and D of Figure 2.08 are $9 \times 9 \ \mu m^2$ before and after images for an identical experiment on mica. As illustrated in Figure 2.08D, the SDS significantly displaces the monolayer from the mica surface. The large structure apparent on the right-hand side of Figure 2.08D is not related to the protein monolayer and is likely an impurity. These experiments provide compelling evidence that BFG monolayers are tightly bound to HOPG surfaces and only weakly interact with mica as was predicted based on the observed growth patterns. The significance of this result stems from a previous report which correlated the amount of fibrinogen eluted with SDS with platelet binding [14d]. For example, fibrinogen that was more tightly bound to polymer
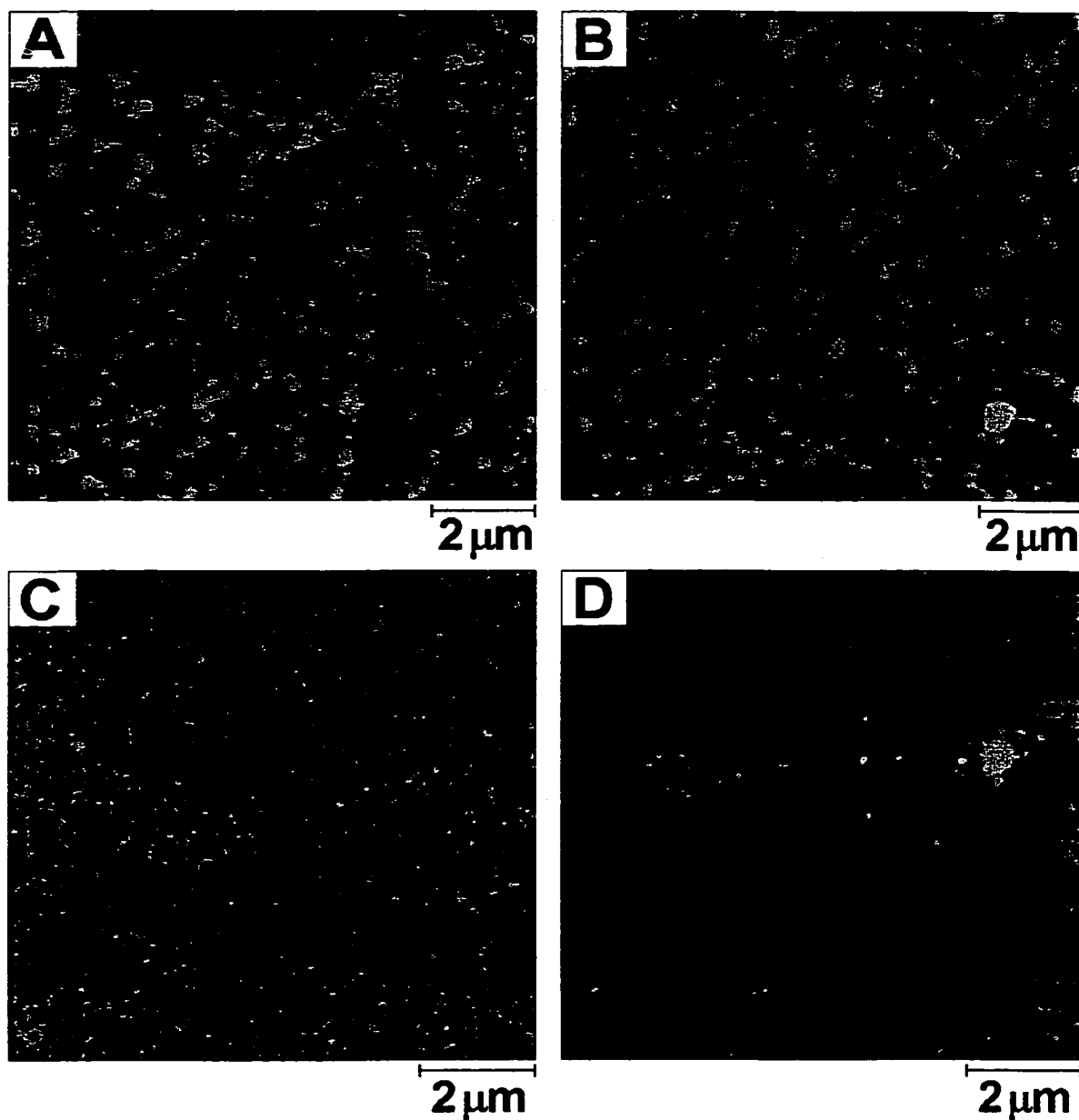
Figure 2.08. 10 × 10 μm² SFM images. (A) Topographic (Z-scale = 30 nm) image in PB of BFG film pre-formed on HOPG. (B) Topographic (Z-scale = 25 nm) image in PB of BFG film on HOPG after 60 min elution with 3% w/v SDS at a flow rate of 1 mL/min. (C) Topographic (Z-scale = 5 nm) image in PB of BFG film pre-formed on mica. (D) Topographic (Z-scale = 7 nm) image of BFG film on mica after 60 min elution with 3% w/v SDS at a flow rate of 1 mL/min.

surfaces exhibited a lower affinity for platelets than a loosely bound layer. Thus, because interfacial platelet aggregation is a key step in the formation of a blood clot, the biocompatibility of a surface may be influenced by how tightly it binds fibrinogen.

Structural basis for different film growth mechanisms. Fibrinogen is a large protein (MW ~340,000 Dalton) which exists as a dimer with several molecular domains. Figure 2.09A shows a schematic of a BFG molecule highlighting the structural regions pertinent to the following discussion. A detailed discussion on the structure of each domain and the corresponding effect on adsorption has recently appeared [4]. The distal D domains are known to be hydrophobic with lower structural stability allowing these regions to deform and maximize their contact area upon adsorption to hydrophobic surfaces. These domains also carry a –4 net charge. Two αC domains extend from each D domain and consist of the C termini of one of the three pairs of polypeptide chains that comprise BFG (*i.e.*, the Aα chain). This domain contains both hydrophobic and hydrophilic regions and carries a net +2 charge. The αC domain is not directly involved in the polymerization of BFG to fibrin but may be involved in the branching and stabilization of fibrin [4].

The results presented above point to a tightly bound BFG film on HOPG that features significant lateral interactions. A mechanism involving adsorbate-substrate binding through the D domain and intermolecular coupling through the αC domains is consistent with experimental observations. The hydrophobic D domains likely interact with the HOPG in a similar manner to that proposed for hydrophobic binding of FG to LTIC [31a]. This situation is depicted in Figure 2.09A. Another possibility resulting in an identical final outcome involves an initial relatively weak hydrophobic interaction between the graphite surface with the hydrophobic region of the αC domain. This mechanism is attractive based on the high flexibility of this domain that permits high collision frequencies [4]. A
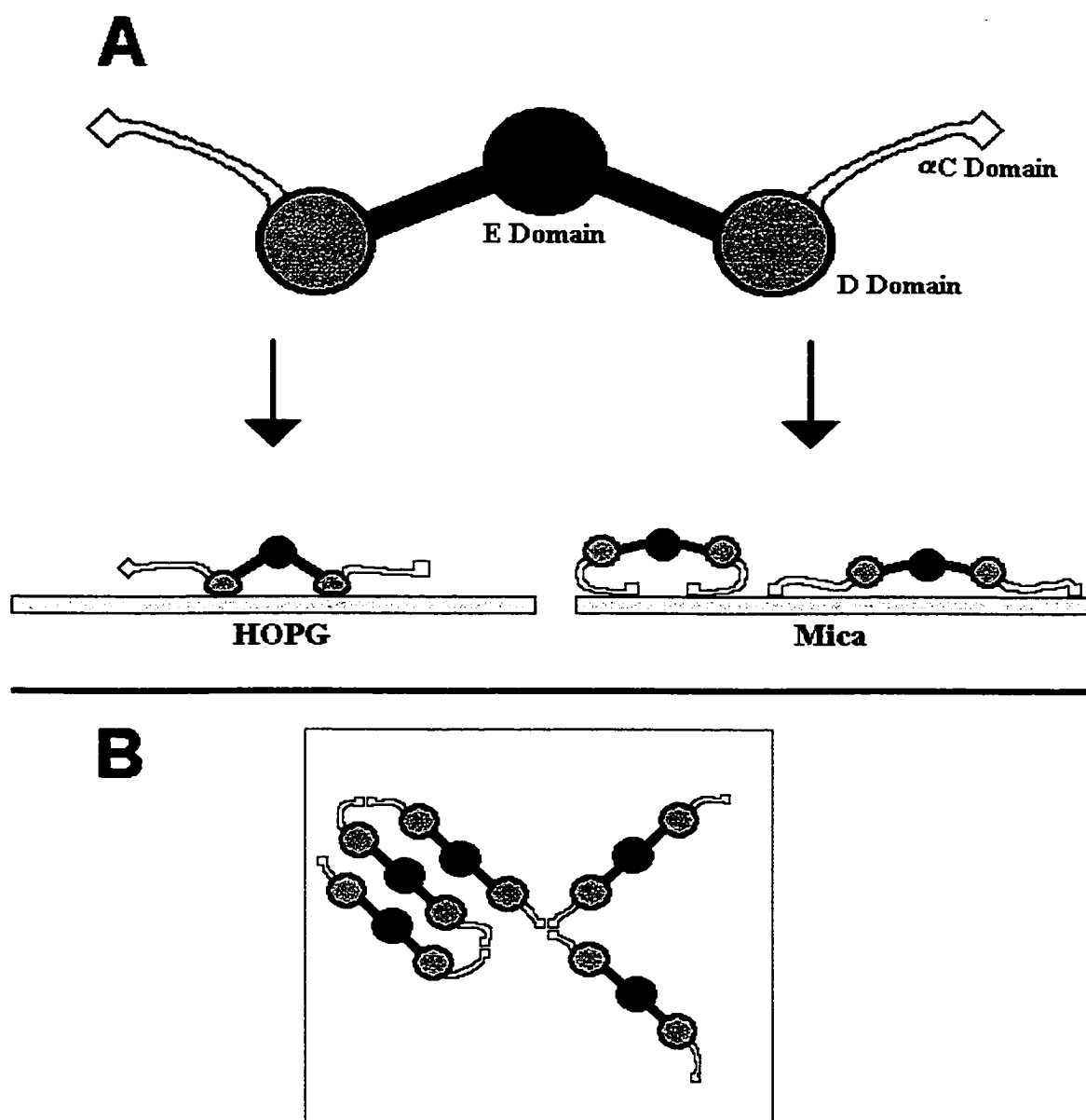
Figure 2.09. (A) Schematic representation of a proposed model for fibrinogen adsorption onto HOPG and mica surfaces. (B) Fibrinogen network formation on HOPG showing intermolecular interactions of αC domains.

stronger hydrophobic binding between the D domains and surface follows the initial interaction, thus freeing the αC domains to interact elsewhere.

Results from several studies point to a strong tendency of the αC domain to interact with other αC domains both intra- and intermolecularly [5]. Several reports have provided evidence that the αC domains contain complementary sites which bind intramolecularly to form a super domain [46] observed by SEM [47]. These sites also provide the pathway for enhanced intermolecular interactions. It is proposed that the surface-bound BFG network observed here and elsewhere [12c, 12f, 27] forms from the coupling of αC domains on adjacent molecules. Branching would occur via interactions between multiple αC domains as illustrated in Figure 2.09B. The combined effect of hydrophobic adsorbate-substrate binding through the D domain and strong lateral interactions results in a crystalline-like monolayer which is tenaciously bound to carbon materials. It is noted that interactions between αC domains on adjacent proteins also provide a viable pathway for aggregate formation.

The relatively weak adsorption of BFG to mica surfaces as evidenced by SDS elution implies a much different binding mechanism relative to HOPG. The hydrophilic mica surface is unlikely to induce significant hydrophobic interactions with domains on BFG. Following the arguments presented above, the lack of any significant evidence for intermolecular interactions in the images detailing film growth in Figure 2.07 suggests little coupling of αC domains in adjacent molecules. The isoelectric point of mica ranges between 3 and 3.5 [48]. Thus in addition to being hydrophilic, the surface of mica is negatively charged at a pH of 7.4 and could interact electrostatically with the positively charged αC domains of BFG. These domains would then be unavailable to form lateral intermolecular interactions. It has recently been predicted that interactions between the αC domains and a surface should not be strong based on a low degree of

hydrophobicity and a low net charge [4]. Electrostatic interactions are also expected to be mediated by ionic species in the solution [31b]. In addition, adsorbed BFG has been readily eluted with SDS when bound to a surface only through its αC domain [5]. Thus, a mechanism involving the electrostatic binding of BFG to mica through the αC domains as depicted in Figure 2.09A is consistent with my observations.

Conclusions

I have shown that the morphology of fibrinogen films depends on the nature of the substrate. Fibrinogen films adsorbed to HOPG are composed of uniformly distributed aggregates embedded in a well-packed monolayer. A fully formed monolayer is observed on mica with no evidence of aggregates. SFM real-time monitoring of fibrinogen film formation has provided insights into the growth mechanism at each surface. The growth of BFG films on HOPG proceeds via network formation and propagation, and involves lateral interactions between adsorbates. The final film structure is the result of strong intermolecular interactions and tight binding to the surface. These properties are reflected in a high resistance to SDS elution. I propose that BFG binds to the graphite hydrophobically through the D domains and lateral interactions form through the αC domains. On mica surfaces, BFG film growth involves a homogeneous increase in nucleation sites, indicating that mica-BFG interactions are stronger than any intermolecular interactions. SDS can easily elute the resulting film. An electrostatic interaction between the positively charged αC domains and the negatively charged mica is consistent with my observations.

The overall conclusion from the results presented in this chapter is that fibrinogen film formation processes are influenced by surface composition. Even though the substrates used (HOPG and mica) were excellent for SFM analysis because they are atomically smooth, their surface chemistry is not completely homogenous and difficult to control. In the forthcoming chapters (chapter III and

IV), studies will focus on surfaces with well-controlled chemistry. This was achieved through self-assembled thiolate monolayers on Au substrates (discussed in chapter I).

References

1. (a) Brash, J. L; Horbett, T. A.; Eds. Proteins at Interfaces: *Physiochemical and Biochemical Studies*; ACS Symposium Series No. 343; American Chemical Society: Washington, **1986**. (b) Horbett, T. A.; Brash, J. L. Eds. *Proteins at Interfaces II: Fundamentals and Applications*; ACS Symposium Series, No. 602, American Chemical Society: Washington, **1995**.

2. Morrissey, B. W. *Ann. N.Y. Acad. Sci.* **1977**, 283, 50-64.

3. (a) Andrade, J. D.; Hlady, V. *Ann. N.Y. Acad. Sci.* **1987**, 516, 158-72. (b) Horbett, T.A. *Cardiovascular Pathology* **1993**, 2, 137S-148S.

4. Feng, L.; Andrade, J. D. *In Proteins at Interfaces II: Fundamentals and Applications*; Brash, J. L, Horbett, T. A., Eds.; ACS Symposium Series No. 602; American Chemical Society: Washington, **1995**; Chapter 5.

5. See [4] and references there in.

6. See, for example: (a) Andrade, J. D., Ed. *Surface and Interfacial Aspects of Biomedical Polymers*; Plenum Press: New York, **1985**; Vols. 1 and 2. (b) Prime, K. L.; Whitesides, G. M. *Science* **1991**, 252, 1164-7.

7. (a) Lenk, T. J.; Chittur, K. K.; Ratner, B. D. *Trans. Soc. Biomater.* **1989**, 15, 134. (b) Chittur, K. K.; Fink, D. J.; Hutson, T. B.; Gendreau, R. M.; Jakobsen, R. J.; Leininger, R. I.; *In. Proteins at Interfaces: Physiochemical and Biochemical Studies*; Brash, J. L; Horbett, T. A.; Eds.; ACS Symposium Series No. 343; American Chemical Society: Washington, **1986**, Chapter 23.

8. See, for example: (a) Ward, C. A.; Stanga, D. J. *Colloid Interface Sci.* **1986**, 114, 323-29. (b) Lahav, J. *J. Colloid Interface Sci.* **1987**, 119, 262-74. (c) Young, B. R.; Pitt, W. G.; Cooper, S. L. *J. Colloid Interface Sci.* **1988**, 125, 246-60.

9.   (a) Mrksich, M.; Sigal, G. B.; Whitesides, G. M. *Langmuir* **1995**, 11, 4383-5. (b) Green, R. J.; Davies, J.; Davies, M. C. Roberts, C. J.; Tendler, S. J. B. *Biomaterials* **1997**, 18, 405-13.

10.   (a) Ratner, B. D.; McElroy, B. J. *In Spectroscopy in the Biomedical Sciences*; Gendreau, R. M., Ed.; CRC Press Inc.; Boca Raton, FL, **1986**;107-140.

11.   (a) Hall, C. E.; Slayter, H. S. J. *Biophysic. Biochem. Cytol.* **1959**, 5, 11. (b) Gorman, R. R.; Stoner, G. E. Catlin, A. *J. Phys. Chem.* **1971**, 75, 2103-7. (c) Fowler, W. E.; Erickson, H. P. *J. Mol. Biol.* **1979**, 134, 241-9.

12.   (a) Köppel, G. Z. *Zellforschung* **1967**, 77, 443-517. (b) Stoner, G. E.; Srinivasan, S.; Gileadi, E. *J. Phys. Chem.* **1971**, 75, 2107-11. (c) Rudee, M. L.; Price, Y. M. *J. Biomed. Mater. Res.* **1985**, 19, 57-66. (d) Brynda, E.; Houska, M.; Lednocky, F. *J. Colloid Interface Sci.* **1986**, 113, 164-71. (e) Nygren, H.; Stenberg, M. *J. Biomed. Mater. Res.* **1988**, 22, 1-11. (f) Eberhart, R. C.; Munro, M. S.; Frautschi, J. R.; Sevastianov, V. I.; *In Proteins at Interfaces: Physiochemical and Biochemical Studies*; Brash, J. L; Horbett, T. A.; Eds.; ACS Symposium Series No. 343; American Chemical Society: Washington, **1986**, Chapter 24.

13.   (a) Park, K.; Albrecht, R. M.; Simmons, S. R.; Cooper, S. L. *J. Colloid Interface Sci.* **1986**, 111, 197-212. (b) Murthy, K. D.; Diwan, A. R.; Simmons, S. R.; Albrecht, R. M.; Cooper, S. L. *Scanning Microsc.* **1987**, 1, 765-73. (c) Pankowsky, D. A.; Ziats, N. P.; Topham, N. S.; Ratnoff, O. D.; Anderson, J. M. *J. Vasc. Sur.* **1990**, 11, 599-606.

14.   (a) Lindon, J. N.; McManama, G.; Kushner, L.,; Merrill, E. W.; Salzman, E. W. *Blood* **1986**, 68, 355-62. (b) Salzman, E. W.; Lindon, J.; McNamana, G.; Ware, J. W.; *Ann. N.Y. Acad. Sci.* **1987**, 516, 184-95. (c) Chinn, J. A.; Horbett, T. A.; Ratner, B. D. *Thromb. Haemost.* **1991**, 65, 608-17. (d) Kiaei, D.; Hoffman, A. S.; Horbett, T. A.; Lew, K. R. *Biomater.* **1995**, 29, 729-39.

15.   (a) Horbett, T. A J. *Biomed. Mater. Res.* **1981**, 15, 673-95. (b) Uniyal, S.; Brash, J. L. *Thromb. Haemostas.* **1982**, 47, 285-90. (c) Slack, S. M.; Horbett, T. A. *J. Colloid Interface Sci.* **1989**, 13, 148-65.

16.   Slack, S. M.; Horbett, T. A. *J. Colloid Interface Sci.* **1988**, 124, 535-551.

17. (a) Chinn, J. A.; Posso, S. E.; Horbett, T. A.; Ratner, B. D. *J. Biomed. Mater. Res.* **1991**, 25, 535-55. (b) Rapoza, R. J.; Horbett, T. A *J. Biomed. Mater. Res.* **1990**, 24, 1263-87.

18. See, for example, Horbett, T.A., and K.R. Lew. *J. Biomat. Sci., Polym. Edn.* **1994**, 6, 15-33.

19. (a) Bohnert, J. A.; Horbett, T. A. *J. Colloid Interface Sci.* **1986**, 111, 363-80. (b) Rapoza, R. J.; Horbett, T. A. *J. Biomater. Sci.* **1989**, 1, 69-80.

20. McMillin, C. R.; Walton, A. G.; J. Colloid Interface Sci. 1974, 48, 345-349.

21. Brash, J. L.; *In Proteins at Interfaces: Physiochemical and Biochemical Studies*; Brash, J. L, Horbett, T. A., Eds.; ACS Symposium Series No. 343; American Chemical Society: Washington, **1986**, Chapter 30.

22. For a recent review see, Hansma, H.; Hoh, J. H. *Annu. Rev. Biophys. Biomol. Struct.* **1994**, 23, 115-39.

23. Drake, B.; Prater, C. B.; Weisenhorn, A. L.; Gould, S. A.; Albrect, T. R.; Quate, C. F.; Cannell, D. S.; Hansma, H. G.; Hansma, P. K. *Science* **1989**, 243, 1586-9.

24. (a) Land, T. A.; Malkin, A. J.; Kuznetsov, Y. G.; McPherson, A.; Yoreo, J. J. *Phys. Rev. Lett.* **1995**, 75, 2774-7. (b) Malkin, A. J.; Land, T. A.; Kuznetsov, Y. G.; McPherson, A.; Yoreo, J. *J. Phys. Rev. Lett.* **1995**, 75, 2778-81.

25. Shakesheff, K. M.; Davies, M. C.; Heller, J.; Roberts, C. J.; Tendler, S. J. B.; Williams, P. M. *Langmuir* **1995**, 11, 2547-53.

26. (a) Radmacher, M.; Fritz, M.; Hansma, H. G.; Hansma, P. K. *Science* **1994**, 265, 1577-9. (b) Lewis, A.; Rousso, I.; Khachatryan, E.; Brodsky, I.; Lieberman, K.; Sheves, M. *Biophys. J.* **1996**, 70, 2380-4.

27. (a) Wigren, R.; Elwing, H.; Erlandsson, R.; Welin, S.; Lundström, I. *FEBS* **1991**, 280, 225-8. (b) Rasmusson, J. R.; Erlandson, R.; Salaneck, W. R.; Schott, M.; Clark, D. T.; Lundström, I. *Scanning Microsc.* **1994**, 8, 481-90.

28. (a) Lea, A. S.; Pungor, A.; Hlady, V.; Andrade, J. D.; Herron, J. N. and Voss Jr., E. W. *Langmuir* **1992**, 8, 68-73. (b) Warkentin, P.; Wälivaara, B.; Lundström, I.; Tengvall, P. *Biomater.* **1994**, 15, 786-795.

29. (a) Eppell, S. J.; Zypman, F. R.; Marchant, R. E. *Langmuir* **1993**, 9, 2281-9. (b) Siedlecki, C. A.; Eppell, S. J.; Marchant, R. E. *J. Biomed. Mater. Res.* **1994**, 28, 971-80. (c) Eppel, S. J.; Simmons, S. R.; Albrecht, R. M.; Marchant, R. E. *Biophys. J.* **1995**, 68, 671-80.

30. (a) Lin, J. N.; Lea, A. S.; Hansma, P. K.; Andrade, J. D. *Langmuir* **1990**, 509-11. (b) Cullen, D. C.; Lowe, C. R. *J. Colloid Interface Sci.* **1994**, 166, 102-8.

31. (a) Feng, L.; Andrade, J. D. *J. Biomed. Mater. Res.* **1994**, 28, 735. (b) Feng, L.; Andrade, J. D. *J. Colloid Interface Sci.* **1994**, 166, 419-26. (c) Feng, L.; Andrade, J. D. *Biomaterials* **1994**, 15, 323-33.

32. Chinn, J. A.; Phillips Jr., R. E.; Lew, K. R.; Horbett, T. A. *J. Colloid Interface Sci.* **1996**, 184, 11-19.

33. Thomson, N.H., Kasas, S., Smith, B., Hansma, H.G., Hansma, P.K., *Langmuir* **1996**, 12, 5905-8.

34. Clemmer, C. R.; Beebe, T. P. Jr. *Science* **1991**, 251, 640-2.

35. See, for example: (a) Chang, H.; Bard, A. J. *Langmuir* **1991**, 7, 1143-53. (b) McDermott, M. T.; McCreery, R. L. *Langmuir* **1994**, 10, 4307-14.

36. Baselt, D. R.; Baldeschwieler, J. D. *J. Vac. Sci. Technol. B* **1992**, 10, 2316-22.

37. McDermott, M. T.; Green, J.B.; Porter, M. D. *Langmuir* **1997**, 13, 2504-10.

38. The lateral dimensions of any observed structures was not here because of the well known broadening effect of the SFM tip renders these measurements questionable.

39. Ta, T. C.; McDermott, M. T. *J.Colloid Interface Sci.*, submitted.

40.   (a) McCreery, R. L. *In Electroanalytical Chemistry*, Bard, A. J.; Ed.; Marcel Dekker: New York, **1991**; Vol. 17. (b) McDermott, M. T.; Kneten, K. R.; McCreery, R. L. *J. Phys. Chem.* **1992**, 96, 3124-30.

41.   Ray III, K.; McCreery, R. L. *Anal. Chem.* **1997**, 69, 4680 - 4687.

42.   Bokros, J. C.; Lagrange, L. D.; Shoen, F. J. *In Chemistry and Physics of Carbon*; Walker Jr., P. L.; Thrower, P. E., Eds.; Dekker: New York, NY, **1973**, 103-262.

43.   Chapter V in this thesis [39].

44.   Bohnert, J. L.; Horbett, T. A. *J. Colloid Interface Sci.* **1986**, 111, 363-77.

45.   There was no evidence to indicate that any SDS was adsorbed to the probe tip after flushing the cell with PB.

46.   (a) Doolittle, R. F. *In BFG, thrombosis, coagulation and BFGrinolysis*; Liu, C. I.; Chien, S. Eds.; Plenum Press: New York, **1990**; p. 25. (b) Medved, L. V.; Gorkun, O. V.; Privalov, P. L. *FEBS* **1983**, 160, 291-5.

47.   Rao, S. P. S. *J. Mol. Bio.* **1991**, 222, 89.

48   Reynders, P.; personal communication.

CHAPTER III

FIBRINOGEN ADSORPTION ON SINGLE COMPONENT ALKYL THIOLATE SELF-ASSEMBLED MONOLAYERS ON GOLD SUBSTRATES*

Introduction

In Chapter II, protocols and skills were developed for studying protein adsorption with SFM under aqueous conditions. More importantly, discoveries were made that film characteristics, such as morphology and packing, are dependent upon the properties of the substrates upon which these films were formed. HOPG and mica are topographically ideal for SFM adsorption studies at solid/liquid and solid/gas interfaces. However, my interest lies in how substrate interfacial chemistry influences the conformation/orientation of the adsorbed protein molecules, and thus the overall properties of the films. Even though HOPG and mica are model surfaces, their surface chemistry was not well defined or controllable. In this chapter, studies of fibrinogen adsorption on chemically controlled substrates using scanning force microscopy (SFM) will be presented. In addition, to corroborate and support conclusions derived from SFM, other important surface characterization tools such as reflectance infrared spectrometry and surface plasmon resonance will be applied detect antibody binding.

The ability to control non-specific protein adsorption at interfaces is a key issue in the design of biosensors, assays, chromatographic separations and implant materials. In comparison to receptor-ligand binding which involves a particular site on the biomolecule, non-specific adsorption generally involves the interaction of a large fraction of the amino acid sequence with the surface. Because of the participation of a significant portion of the protein, adsorption often induces

---

* Certain sections of this chapter were published as "Ta, T. C. and McDermott, M. T. *Anal. Chem.* **2000**, 72, 2627-2634".

conformational changes from the solution state (1). Also, in some situations, a single binding mode will be favored over the many possible modes, producing a protein film with a preferred orientation of molecules (2, 3). It is well accepted that the properties of surfaces will govern both the degree of conformational change and the orientation of non-specifically adsorbed proteins (1, 4). In addition, our understanding of the mechanistic details governing the effect that the surface properties have on the structure of adsorbed protein layers has advanced significantly over the last several years. However, the ability to rationally design interfaces for biosensors, implants, etc., with predefined control over protein adsorption will only be realized with the aid of techniques that can rapidly analyze surface induced variations in protein conformation and orientation.

Common methods used to study protein states are procedures that quantify the amount of bound protein or the strength of binding on different surfaces. A common method involves tagging of the protein with a radioactive label (5, 6). Variations in conformation/orientation are inferred based on the amount of adsorbed protein detected at different surfaces or based on the amount detected after elution by a surfactant (5, 7). The second group is spectroscopic techniques that directly provide some structural information. These techniques include infrared (IR) (8-12), linear and circular dichroism (12-14), total internal reflection fluorescence (TIRF) (15) and electron spin resonance coupled with spin labeling (16). The advantages of fourier transform infrared spectrometry (FTIR) will be explored to gain insight on the relative amounts of protein adsorbed to our surfaces. Because the focus is to investigate protein adsorbed at an interface, a non-conventional IR setup was used. Figure 3.01 shows the sample-IR interaction for infrared reflectance absorbance spectroscopy (IRRAS). A p-polarized IR beam is directed onto a surface at a grazing angle. This angle is approximately 80° from the surface normal for Au substrates. At this angle, there is an optimum enhancement of the IR electric field in the direction normal to the surface (17).
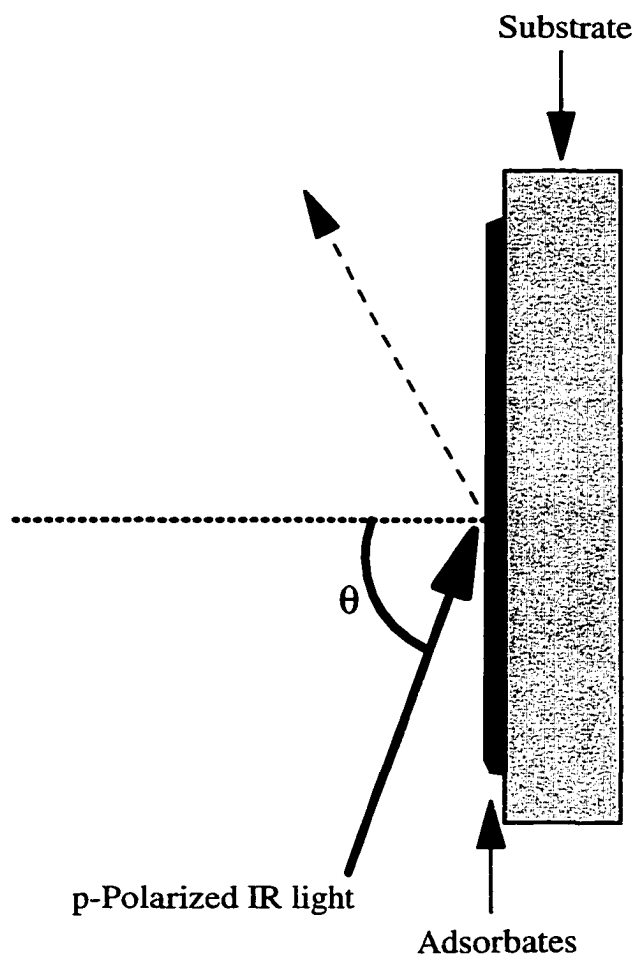
Figure 3.01. Sample-IR beam interaction for infrared absorbance reflectance spectroscopy (IRRAS). A p-polarized IR light is directed at a grazing angle onto a substrate (i.e., Au, $\theta \sim 80°$). Adsorbates on the substrate surface that are IR active with a dipole component in the normal direction will absorb the IR radiation. Chemical groups may be determined by their characteristic adsorption energies.

Therefore, molecules on the surface that contain transition dipoles with components perpendicular to the surface are able to absorb IR energy. IRRAS is able to identify chemical groups and is sensitive to the orientation of functional groups at the interface. IRRAS is employed here as a means of quantifying protein adsorption.

The third type of analysis involves the evaluation of antibody or platelet binding to the adsorbed protein film (5, 18, 19). Antibodies are often used in immunoassays to detect the presence of specific antigens. Antibodies are proteins that function as markers for the immune response by binding selectively and with high affinity to various molecules that are to be excreted. Antibodies contain four polypeptide chains per molecule, 2 heavy and 2 light chains that are bridged through disulfide bonds (20). Both inter- and intra-chain bridging are present. IgM, IgE, IgA, IgD and IgG are five classes of antibody that are classified according to the type of heavy chains that they contain. Antibody molecules are "Y"-shaped structures, in which the open end of the "Y" is the variable region that determines an antibody's selectivity and binding affinity. The region on an antigen that antibodies bind to is called the epitope. Since antibodies are produced to bind to a particular epitope, any change in epitope structure (*i.e.*, surface induced denaturation) will influence the degree of antibody binding.

Also of note are sensor techniques based on acoustic wave devices (21) and surface plasmon resonance (SPR) which have been used to probe specific binding and non-specific protein adsorption (22). Extensive discussion of both fundamental and applied aspects of SPR has appeared in numerous reports (23-25) and therefore only a brief and simplified overview of SPR is discussed here. Figure 3.02A shows the basic operating units found in an SPR instrument. The heart of this instrument includes a light source, an array detector, and a prism to help couple the electric light wave vector to the surface plasmon frequency. Surface plasmons are waves generated by electrons that oscillate at certain

A
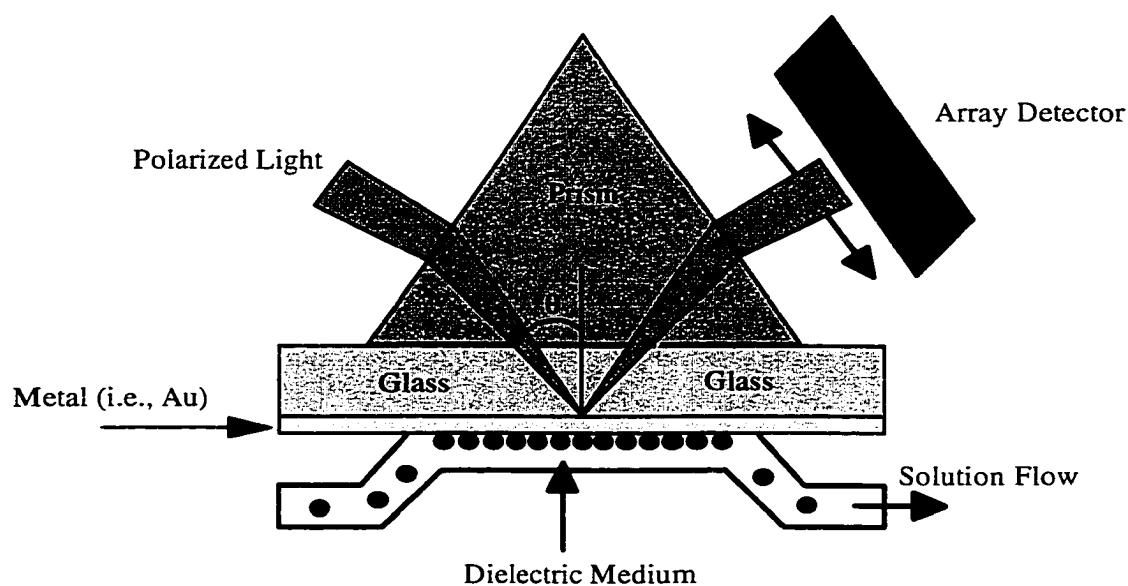
B
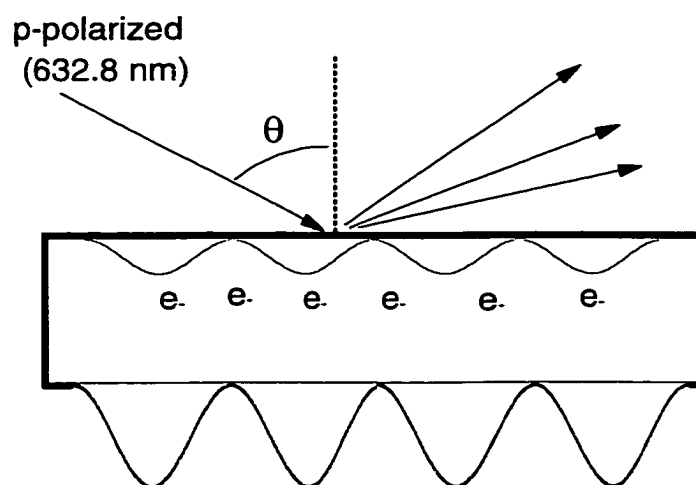
Figure 3.02. A) Surface plasmon resonance (SPR) detection system. "●" represent adsorbates, ranging from organic molecules (i.e., alkylthiols) to biomolecules (i.e., proteins) which change the reflective index (n). B) At a specific θ, polarized light wavevectors are able to couple to plasmon wavevectors, leading to a minimum reflectance.

frequency within the metal (Figure 3.02B). When a focused laser source interacts with the metal surface at a grazing angle, internal reflectance occurs. At a specific angle light energy will be able to couple with plasmons at the metal surface, propagating an electromagnetic field on the opposite side of the metal surface, resulting in a decrease in reflectance. This is often referred to as surface plasmon resonance or angle of resonance. This angle of reduced reflectance is dependent upon the metal (*i.e.*, Ag or Au), the wavelength of the laser source, and the dielectric properties of the interface on the opposite side of the prism. Therefore, any change in dielectric property results in a shift in the angle of resonance, leading to an increase in reflectance and detector response. Equation 6 relates the change in resonance angle as a function of excitation wavelength $\Delta\theta$ (λ) to the change in refractive index (Δn) and average thickness of an adsorbed layer (Δd)(26).

$$\Delta\theta \, (\lambda) = A \, \Delta n \, (\lambda) + B \, \Delta d \qquad \{6\}$$

$\Delta\theta$ is the change in resonance angle, λ is the wavelength of light used for excitation, Δn is the change of refractive index on the sensing side of the metal surface, Δd is the change in thickness of adsorbed layer, A and B can be calculated based on Fresnel optics as detailed by Hansen (27).

Since the electromagnetic field decays exponentially from the metal surface, any dielectric fluctuation within ~100 nm of the metal is detectable. Modification schemes for changing the dielectric characteristics include covalent attachment of molecules such as alkanethiols on Au, antibody-antigen coupling where either one is covalently attached to a polymer coating on a metal surface, or non-specific adsorption. Experiments performed here involve the non-specific adsorption of fibrinogen to alkylthiol-modified Au substrates. Antibody binding will be used to monitor adsorbed fibrinogen states.

Related to the work in this chapter, topographic SFM imaging has been employed to gain insights on adsorbed protein orientation and conformation (28, 29). In these studies, the heights of proteins adsorbed on different substrates were correlated with their adsorbed state. In Chapter II, it was demonstrated that real-time monitoring of fibrinogen adsorption on different substrates could be useful in establishing the mode of binding (30). Results and conclusions to be presented in this chapter will focus on applying height measurements and real-time monitoring of protein adsorption to shed some light on protein film properties as a function of substrate chemistry.

Several researchers have exploited functionalized self-assembled monolayer (SAM) films to study the effect of interfacial chemistry on protein adsorption (31-34). Herein, methyl and carboxylate-terminated alkyl thiolate monolayers on gold were employed as substrates for protein adsorption. These functional groups were chosen because each can potentially induce vastly different interactions. Proteins should interact with the hydrophobic, methyl-terminated surface mainly through dispersion or van der Waals interactions. The carboxylate-terminated monolayer can potentially induce electrostatic and dipole-dipole type binding, as well as hydrogen bonding. Films of bovine fibrinogen (BFG) adsorbed on single component monolayers, were examined by infrared reflection absorption spectroscopy (IRRAS) (17) and SFM. The latter half of this chapter will focus on human fibrinogen (HFG) because the antibody for HFG is commercially available. Fibrinogen was chosen because of its high surface affinity and its importance in thrombosis (35).

Experimental

Reagents and Materials: All solutions were prepared using water from a Nanopure (Barnstead, Dubuque, IA) purification system. Phosphate buffered saline (PBS, pH 7.4) was prepared with reagent grade 0.2 mM KH_2PO_4 and 0.8 mM Na_2HPO_4, NaCl (10 mM) and KCl (1 mM). PBS was used to prepare protein

solutions, as the liquid medium for imaging, and for washing steps. Bovine fibrinogen (Fraction I, 95% clottable) and human fibrinogen (Fraction I) were obtained from Sigma (St. Louis, MO). Fibrinogen solution concentrations of 20 µg/mL were freshly prepared by weight just prior to each day of experiments. Goat antiserum to human fibrinogen (anti-HFG) was purchased from ICN Biomedical (Aurora, Ohio), and diluted with PBS to achieve concentrations of 160 µg/mL. Bovine IgG (160 µg/mL, ICN Biomedical) was used for evaluating the quantity of non-specific binding. PBS and protein solutions were filtered with a 22 µm millex-GV, low-protein binding filter (Millipore, Bedford, MA) before they were used in scanning force microscopy (SFM) and SPR experiments. Octadecanethiol, $HS(CH_2)_{17}CH_3$ (ODT) (Aldrich, Milwaukee, WI) was recrystallized twice from ethanol before use. Mercaptohexadecanoic acid, $HS(CH_2)_{15}CO_2H$ (MHA) was a gift from Dr. Marc Porter (Ames Lab, Iowa State). Thiol solutions (10 µM - 1 mM) were prepared in punctilious ethanol (Quantum Chemical Co, Newark, NJ).

Substrate preparation and modification. All gold substrates were prepared by sputtering Au onto a support material. For infrared analysis, 15 nm of Cr and 300 nm of Au were sputtered onto clean glass microscope slides (Au/Cr/glass). For SFM experiments, 300 nm of Au was sputter coated onto 1 cm diameter disks of Tempax (Berliner Glass) glass (Au/Tempax). These substrates were subsequently annealed in a muffle furnace at 300°C for 3 h and then further annealed in a H_2 flame as reported previously (36). This procedure produces a surface with large (1 µm diameter) Au crystallites exhibiting a (111) texture. For surface plasmon resonance (SPR) studies, unmodified Au sensors (Pioneer Chip J1) were purchased from Biacore (Sweden).

All Au substrates were modified with alkanethiol self-assembled monolayers (SAMs). Only homogeneous monolayers (single component monolayers) were prepared. Au/Cr/glass, Au/Tempax and SPR sensor substrates

were immersed into 10 μM to 1 mM ethanolic ODT solutions for at least 24 hr to produce homogeneous methyl (CH_3) and 1 mM ethanolic MHA for 1 hour to form the carboxylate (COO⁻) terminated monolayers.

SPR measurements: Measurements were performed on a BIAcore 2000 instrument (BIAcore, Sweden). ODT and MHA modified sensors were allowed to equilibrate in flowing PBS at a flow rate of 10 μL/min for 30 min. The same flow rate was used for all washing steps, and for antibody binding studies. After equilibration, ODT and MHA modified sensors were monitored to find the baseline response (RU units). The response from each of the four channels was individually recorded and this value was used to compare the response of the same channel obtained after the sensor has been exposed to 20 μg/mL HFG for 1 hour. Differences in RU response indicated the amount of HFG binding to each type of sensor. HFG-modified sensors were used to investigate antibody binding. Two binding procedures were examined. The first involved binding of anti-HFG and non-specific bovine IgG onto different channels. At a flow rate of 10 μL/min, approximately 200 μL of solution was needed to reach saturation. Once saturation was obtained, injection was stopped and the sensors washed with PBS for 15 min. Washing caused partial desorption of weakly bound antibodies, evident by a small (~ 5-10%) decrease in response. After 15 min of washing, the signal stabilizes to achieve a plateau. This plateau level was used to measure the response due to binding. The amount of specific binding was based on the difference in the response of two channels (anti-HFG and bovine IgG). The second method involves addressing only one channel. To an HFG-modified sensor, bovine IgG binding experiments was performed as described above. The premise behind this procedure was that bovine IgG would bind only the non-specific sites. Once the signal stabilized after washing, anti-HFG was added to the same channel and the increase in response, which should reflect only specific binding, was monitored.

SFM Imaging: SFM images were collected using a Nanoscope III (Digital Instruments, Santa Barbara, CA) equipped with a fluid cell for in situ operation. Triangular Si_3N_4 cantilevers (k ≈0.06 nN/nm) were used for all images. Each real-time SFM experiment begins with acquiring images of the substrate in PBS. PBS flow was then started using the procedure previously described in Chapter II. Flow rates of 0.1-0.2 mL/min were used. Images were captured with PBS flowing through the fluid cell. Then 20 μg/mL of BFG solution was added to a near-empty syringe reservoir and allowed to flow into the fluid cell. Images presented here were captured continuously at scan rates of 5 to 10.2 Hz. All images were collected at normal forces below 10 nN.

Infrared Reflectance Absorbance Spectroscopy (IRRAS): IRRAS spectra were collected with a Mattson Infinity FTIR spectrometer (Madison, WI) equipped with a low-noise MCT-A detector. A reflection accessory and a home built sample holder were housed in an external, auxiliary bench. Samples for IRRAS were the modified Au/Cr/glass substrates. For protein adsorption studies, monolayer coated substrates were immersed in 20 μg/mL solutions of BFG or HFG in PBS for 60 min. Substrates were removed from solution, rinsed with PBS and dried in a stream of argon. Spectra were collected using 500 scans with 2 cm^{-1} resolution. Slides modified with HFG were further used to investigate antibody binding. Protein covered slides were exposed to 160 μg/mL anti-HFG or non-specific bovine IgG for 2 h. The slides are removed, rinsed with PBS and dried under argon. The relative quantity of adsorbed protein and bound antibody on ODT and MHA Au surfaces was based on the intensity of the amide II stretching band (~ 1540 cm^{-1})(37, 38).

Results and Discussion

This chapter will present results from our studies of fibrinogen adsorption on surfaces with well-controlled chemistry. Discussion will be centered around SFM, IRRAS and SPR for characterizing fibrinogen films on ODT and MHA

single component SAMs. Antibody binding results will also be presented to further support conclusions that are made. Knowledge obtained from these studies will provide the background for designing experiments carried out in chapter IV.

SFM and IRRAS studies of fibrinogen adsorption on single component monolayers. IRRAS was employed to assess the relative amount of BFG adsorbed on both functional groups. Figures 3.03 and 3.04 contain IRRAS spectra from 2000 to 1000 cm^{-1} of the monolayer-modified gold interfaces before and after exposure to BFG solutions. In this spectral range, proteins and peptides exhibit characteristic bands, which are the direct results of vibrations in the amide linkages. Specifically, the amide I band (C=O stretch) appears in the region from 1650 to 1680 cm^{-1} and the amide II band (combination of C-N stretch and N-H bend) is generally located in the vicinity of 1550 cm^{-1}. These bands typically exhibit high intensity and are useful as a diagnostic indicator for adsorbed proteins (10, 39).

The spectra for the ODT/Au interface are shown in Figure 3.03. Spectrum 1 of Figure 3.03 corresponds to the unmodified ODT monolayer and exhibits no major vibrational bands in this region, as expected for a methyl-terminated alkane-thiolate monolayer. Note the presence of weak bands at 1467 and 1382 cm^{-1} due to CH_2 scissor and CH_3 symmetric deformation modes, respectively (40). Spectrum 2 is observed following exposure of the ODT/Au film to 20 μg/mL BFG in PBS for 1 hour. Strong absorbencies corresponding to amide I (v_{aI} = 1672 cm^{-1}) and amide II bands (v_{aII} = 1545 cm^{-1}) are observed indicating that BFG was absorbed to the CH_3 functional groups. This observation is consistent with previous measurements of fibrinogen adsorption on methyl-terminated monolayers (31) and the generally accepted belief that hydrophobic interactions are important in protein adsorption.

The spectroscopic results describing the interaction of BFG with a carboxylate-terminated monolayer are contained in Figure 3.04. Spectrum 1 of
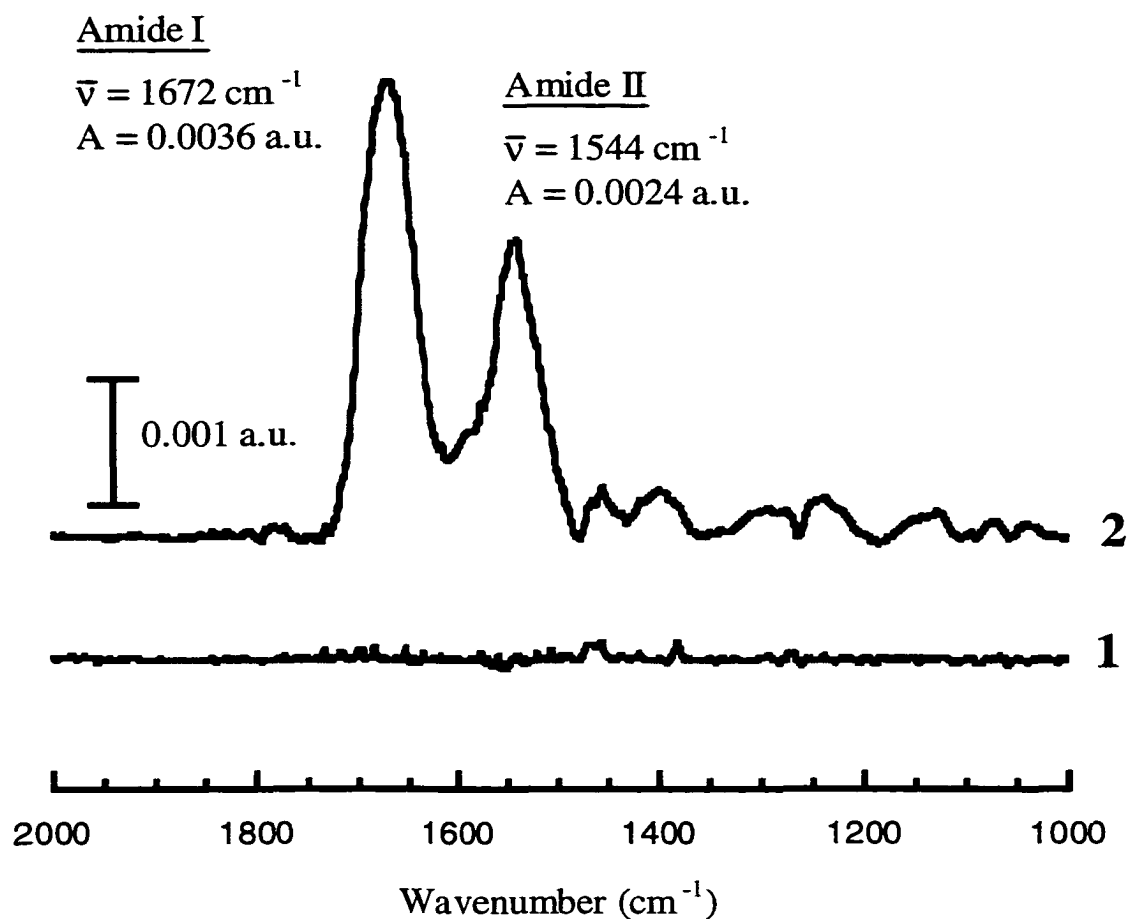
Figure 3.03. IRRAS spectra of ω-functionalized alkanethiolate monolayers bound at gold substrates before and after exposure to 20 µg/mL BFG in PBS for 1 hr. Methyl-terminated monolayer (ODT/Au): spectrum 1 - initial monolayer, spectrum 2 – after adsorption of BFG.
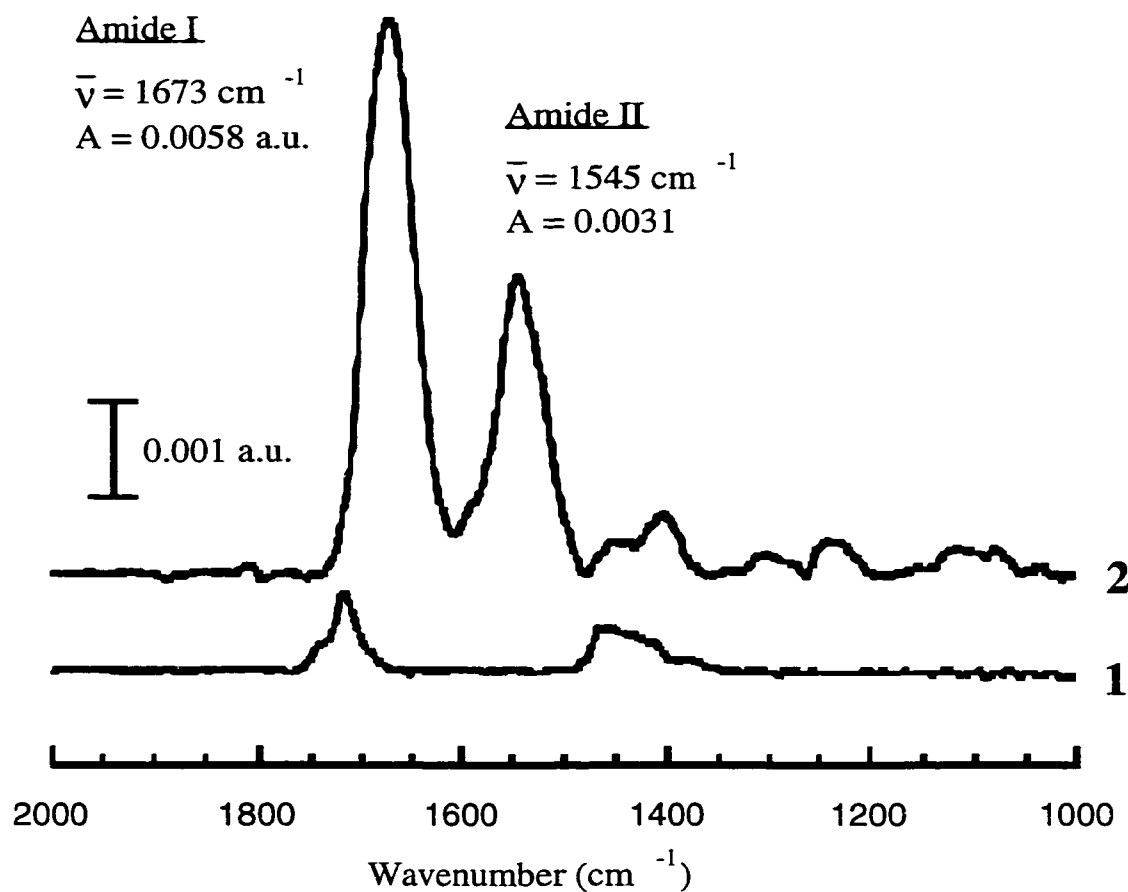
Figure 3.04. IRRAS spectra of ω-functionalized alkanethiolate monolayers bound at gold substrates before and after exposure to 20 μg/mL BFG in PBS for 1 hr. Carboxylate-terminated monolayer (MHA/Au): spectrum 1 - initial monolayer, spectrum 2 – after adsorption of BFG.

Figure 3.04 corresponds to the self-assembled MHA/Au monolayer before exposure to BFG. The C=O stretch consists of a hydrogen bonded component at 1718 cm^{-1} and a non-hydrogen bonded component appearing as a shoulder at 1741 cm^{-1} (40). A broad carboxylate band at 1450 cm^{-1} is also apparent. Based on the reported pKa of 5 - 8 for this monolayer-substrate system (41, 42), the carboxylic acid moieties are partially converted to carboxylate groups upon immersion in pH 7.4 PBS. The presence of the carboxylate peak ($\sim 1450 \text{ cm}^{-1}$) in the infrared spectrum such some degree of deprotonation. The appearance of the amide I and amide II bands in spectrum 2 of Figure 3.04 shows that the carboxylate-terminated surface of the MHA/Au monolayer also exhibits an affinity for BFG.

The absorbance of the amide II band (A_{aII}) is linearly related to the amount of protein bound to the surface (10, 43, 44). The similarity in A_{aII} for the methyl surface in Figure 3.03 ($A_{aII} = 0.0024$ a.u.) and the carboxylate surface in Figure 3.04 ($A_{aII} = 0.0031$ a.u.) that there is implies only a small difference in the amount of BFG is adsorbed at each functional group. In addition, the infrared spectra in Figures 3.03 and 3.04 supply some qualitative details about the state of adsorbed BFG at each functional group. First, the position of the amide I band in both spectra is shifted to higher wavenumbers from its position for BFG in solution or solid ($v_{aI} = 1649 \text{ cm}^{-1}$), implying a degree of adsorption-induced conformation change (10). Secondly, the position and absorbance of the amide I band (A_{aI}) has been correlated with protein conformation (45). In Figure 3.03, $v_{aI} = 1672 \text{ cm}^{-1}$ and $A_{aI} = 0.0036$ a.u., while in Figure 3.04, $v_{aI} = 1673 \text{ cm}^{-1}$ and $A_{aI} = 0.0058$ a.u. The frequency of each band is similar and cannot be used as a basis for assigning a denatured state of the protein. However, the difference in the absorbance values suggests that each functional group induce different adsorbed states of BFG. In summary, the infrared spectra of Figures 3.03 and 3.04 showed that BFG binds to both methyl and carboxylate functional groups at approximately the same

coverage. Also, the details of the spectra begin to build a picture describing the influence of each functional group on the state of adsorbed BFG.

SFM was employed to gain insights into the two dimensional structure of the BFG films adsorbed at each functional group. Figure 3.05 contains 3.0 × 3.0 μm^2 images detailing the adsorption of BFG onto ODT/Au in real time. The images are centered at the same Au crystallite throughout the experiment. Parts A and B of Figure 3.05 are respective topographic and friction force images of the Au supported ODT monolayer in flowing PBS before BFG adsorption. The topography of the crystallite consists of a number of Au (111) steps oriented at 60° angles, consistent with the hexagonal packing of atoms in the Au (111) crystal face. Some of these steps are visible in Figure 3.05B as local increases in the frictional signal due to the tip interacting with the face of the step (*i.e.*, tripping).

As shown in Chapter II, adding BFG solution to the stream of PBS flowing through the fluid cell enables real-time observation of the adsorption process (30). Figure 3.05C and 3.05D are topographic and friction images that capture an intermediate stage of the spontaneous adsorption of BFG to the methyl-terminated ODT layer. The binding of material to the top of the modified Au (111) crystallite is evident in the topography (Figure 3.05C). The height of the adsorbed domains in Figure 3.05C measure 1.0–1.5 nm, consistent with previous SFM measurements of fibrinogen adsorbed to a hydrophobic monolayer (46). This measured height is less than the expected width of a single BFG molecule (4-6 nm) possibly because of structural rearrangement. It is thought that the D-domains of fibrinogen change conformation to maximize hydrophobic interactions (35) and thus would account for the observed heights. The strand-like shape of the adsorbing BFG observed in Figure 3.05C is similar to that observed during real-time adsorption of BFG onto hydrophobic graphite and is characteristic of significant intermolecular interactions (30). It is noted that there appears to be no significant frictional
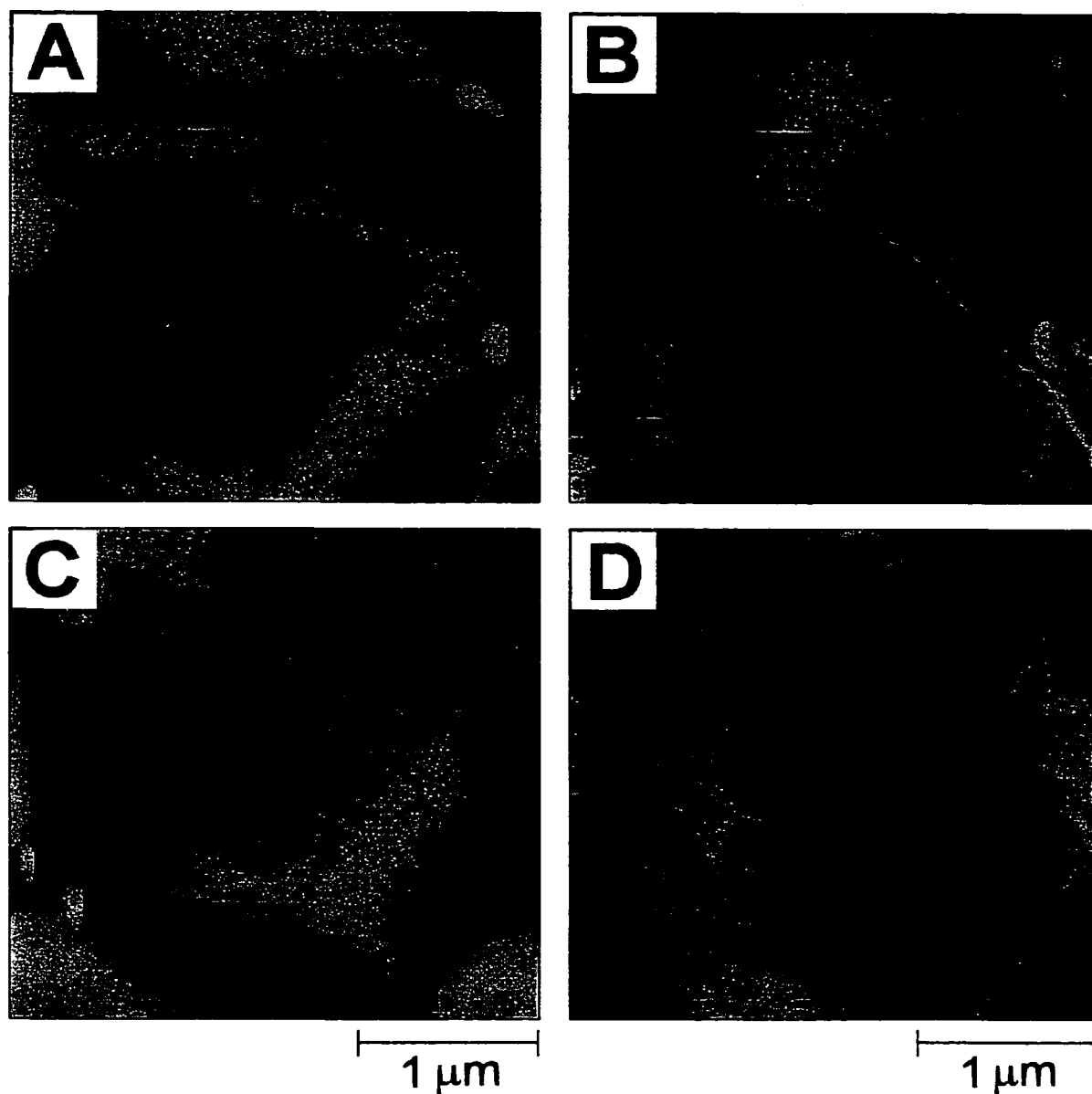
Figure 3.05. 3 × 3 μm² SFM images depicting the real-time time adsorption of BFG to a methyl-terminated monolayer (ODT/Au). Parts A and C (Z-scales = 10 nm) are topographic images and parts B and D (Z-scales = 0.2 V) are the corresponding friction images. All images were collected under flowing solution. (A and B): initial methyl surface under flowing PBS. (C and D): during adsorption of BFG. Figure 3.05 (parts E and F) continues on next page.
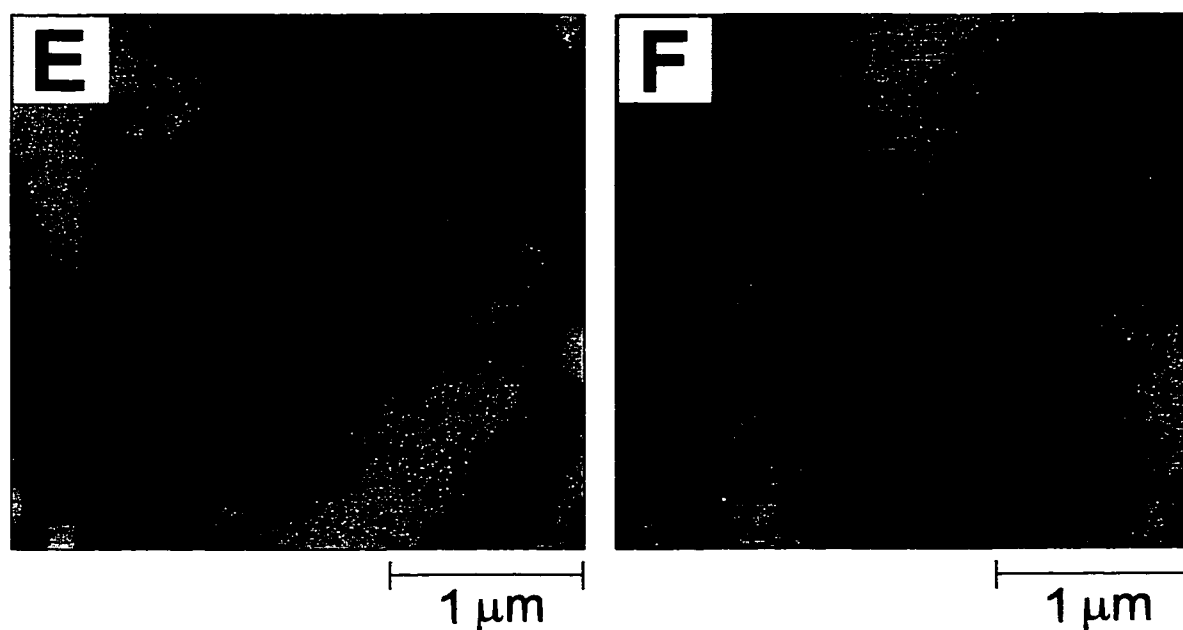
Figure 3.05. Continued. Images E (topography, Z-scale = 15 nm) and F (friction, Z-scale = 0.2 V) were collected 5 minutes after initial addition of BFG to the fluid cell.

difference in Figure 3.05D between the partially formed BFG layer and the underlying ODT monolayer.

Parts E and F are topographic and lateral force SFM images of the same Au crystallite following complete formation of the BFG film. The steps that were prominent in Figure 3.05A are no longer visible in Figure 3.05E. The frictional signal in Figure 3.05F shows little spatial variation across the adsorbed protein layer. These observations are consistent with a uniform, well-packed BFG layer bound to the methyl-modified surface. Although it is evident in Figure 3.05C that the tip displaces BFG during adsorption, the structure of the fully formed BFG film in the area where the tip was scanned is identical to that in a surrounding area. In addition, the layer is stable to imaging at forces of 1-10 nN and at scan rates from 1 to 10 Hz. The adsorbed film can be displaced upon application of sufficient force (>20 nN) between the tip and sample. It is noted that BFG likely adsorbs to the Si_3N_4 probe tip concurrent with the test surface; however, no noticeable decrease in resolution at the micron scales is evident in Figure 3.05.

A similar experiment was performed at the interface of the MHA/Au monolayer and is detailed in Figure 3.06. Images A and B are again the topography and frictional signatures of the initial carboxylate terminated surface in flowing PBS. Interestingly, the frictional signal at the steps in Figure 3.06B is low relative to the surrounding terraces, in contrast to that observed in Figure 3.05B. It is believed that the contrast is due to the tip interacting with lower free energy methylene groups of the chain structure that may be exposed at step edges. An intermediate stage in BFG film formation is shown in parts C and D of Figure 3.06. At the carboxylate-terminated surface, BFG adsorbs in circular, island-like domains that are 4 nm in height. This measurement, which approaches the dimension of the D-domains of fibrinogen, contrasts that observed at the ODT/Au surface (1.0–1.5 nm). The circular islands in Figure 3.06C also differ from the strand-like structures observed on the methyl surface in Figure 3.05C. From a

Figure 3.06. 2.5 × 2.5 μm² SFM images depicting the real-time time adsorption of BFG to a carboxylate-terminated monolayer (MHA/Au). Parts A and C (Z-scales = 10 nm) are topographic images and parts B and D (Z-scale = 0.5 V) are the corresponding friction images. All images were collected under flowing solution. (A and B): initial carboxylate surface under flowing PBS. (C and D): during adsorption of BFG. Parts E and F continue on next page.
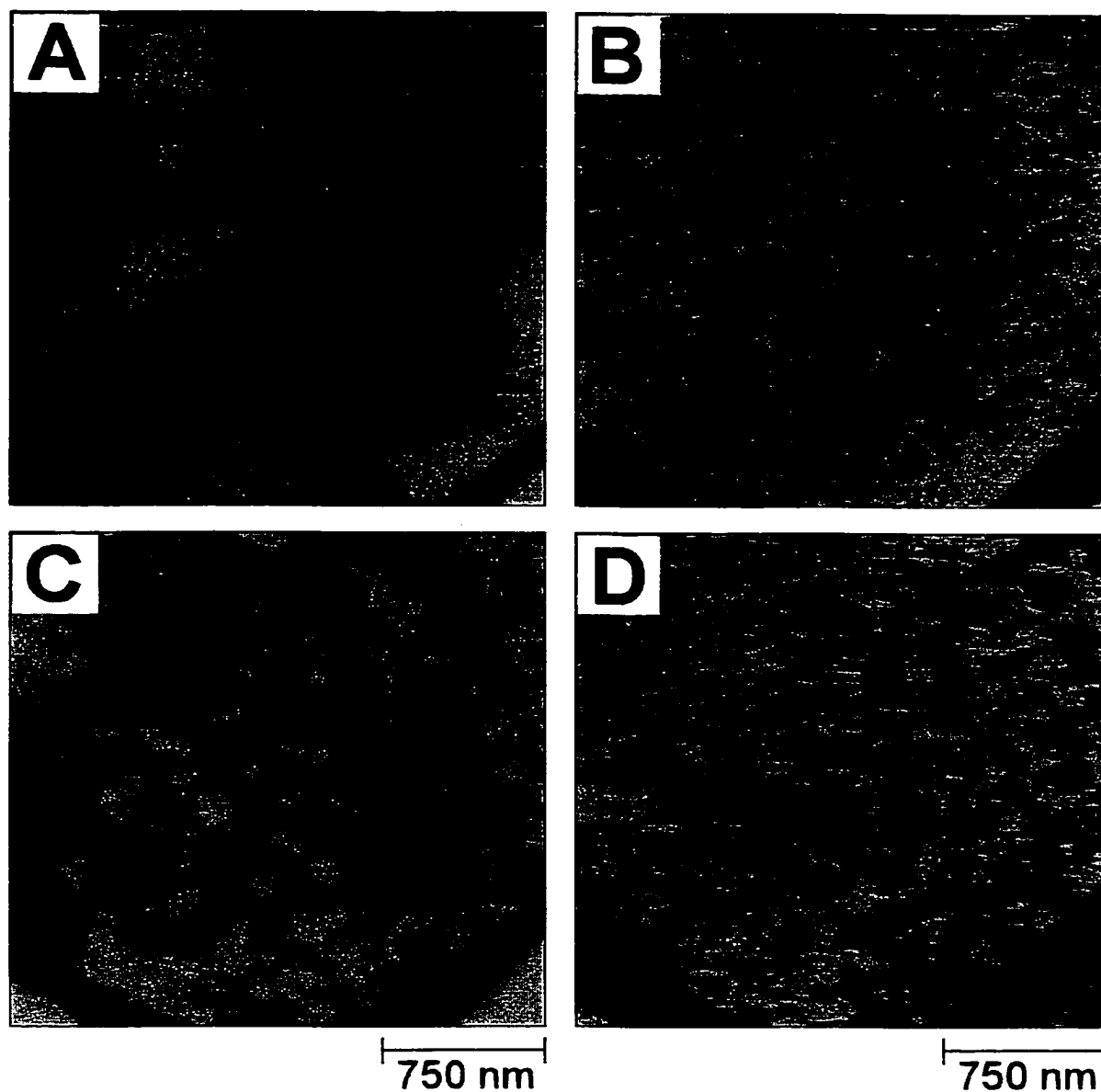
Figure 3.06. Continued. Images E (topography, Z-scale = 15 nm) and F (friction, Z-scale = 0.5 V) were collected 2 minutes after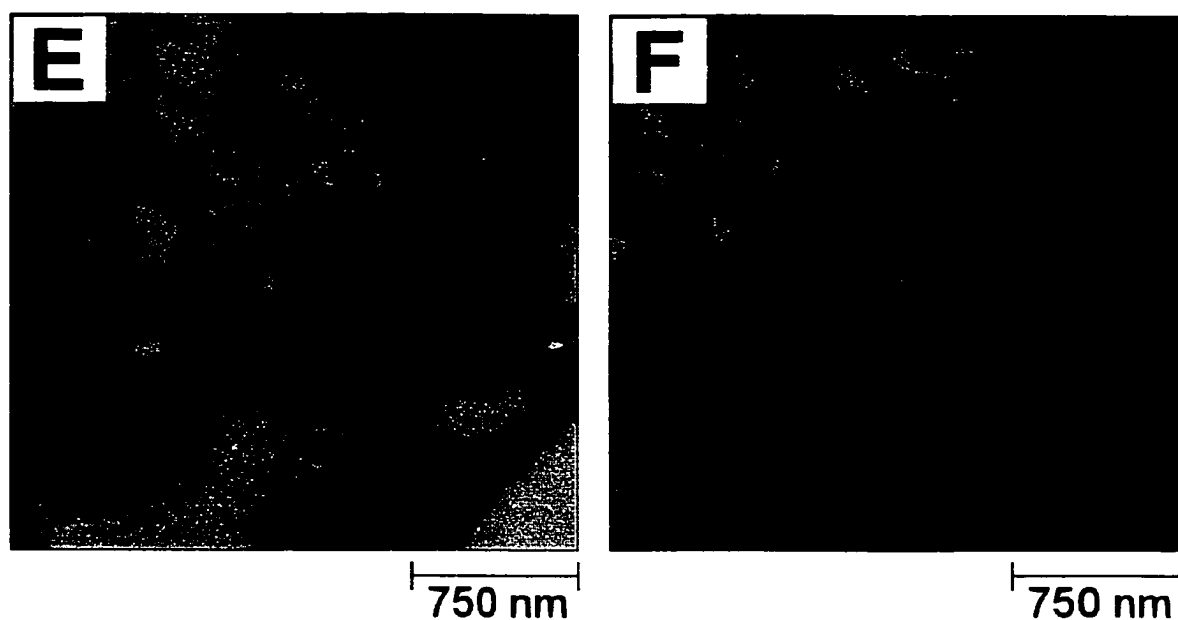 initial addition of BFG to the fluid cell. Images collected after 1 hour adsorption time (equilibrate film) show that the higher friction region "heals" and the friction image is uniform.

strictly topographic standpoint, these two observations suggest that BFG binds by different modes at each functional group.

Upon continual addition of BFG to the fluid cell, a layer exhibiting uniformity in both topography and friction forms, as shown in Figure 3.06E and 3.06F. Several regions of higher friction remain in Figure 3.06F, corresponding to lower topographic areas in Figure 3.06E, where the layer is incomplete due to the scanning of the SFM probe tip. From a collection of images outside the scan area of Figure 3.06, similar to the case for the methyl terminated interface, BFG adsorbs to form a complete, well-packed layer on the carboxylate groups that is stable to imaging for extended periods.

The above SFM studies of BFG adsorption indicate that 20 μg/mL solution is adequate to form a monolayer of protein on both ODT and MHA surfaces with the formation of few protein aggregates. Also, the protein film is closely packed and is sufficiently robust to withstand the forces of the probe tip (< 15 nN). Therefore, the images are reflective of the protein-solution interfaces, and not the underlying monolayer beneath the protein film. IRRAS provides evidence to suggest that the surface chemistry influence binding and conformation of the adsorbed protein. However, the differences in the spectra were small, and a definitive conclusion on the conformation of the adsorbed protein could not be made based on the IRRAS spectra alone.

Antibody binding is an accepted technique for detecting differences in protein conformation (47-50) and will be used here. Commercial access to anti-BFG is limited, and thus efforts shifted towards human fibrinogen (HFG), as polyclonal anti-HFG can be readily purchased. HFG is similar in structure to BFG and therefore the conditions used above for BFG studies will be extended to HFG. Figures 3.07 and 3.08 show HFG adsorption on ODT and MHA single monolayer Au (111) substrates. Panels A and B of Figure 3.07 are typical of an ODT/Au (111) surface imaged by contact mode SFM in PBS. As noted earlier for Figure
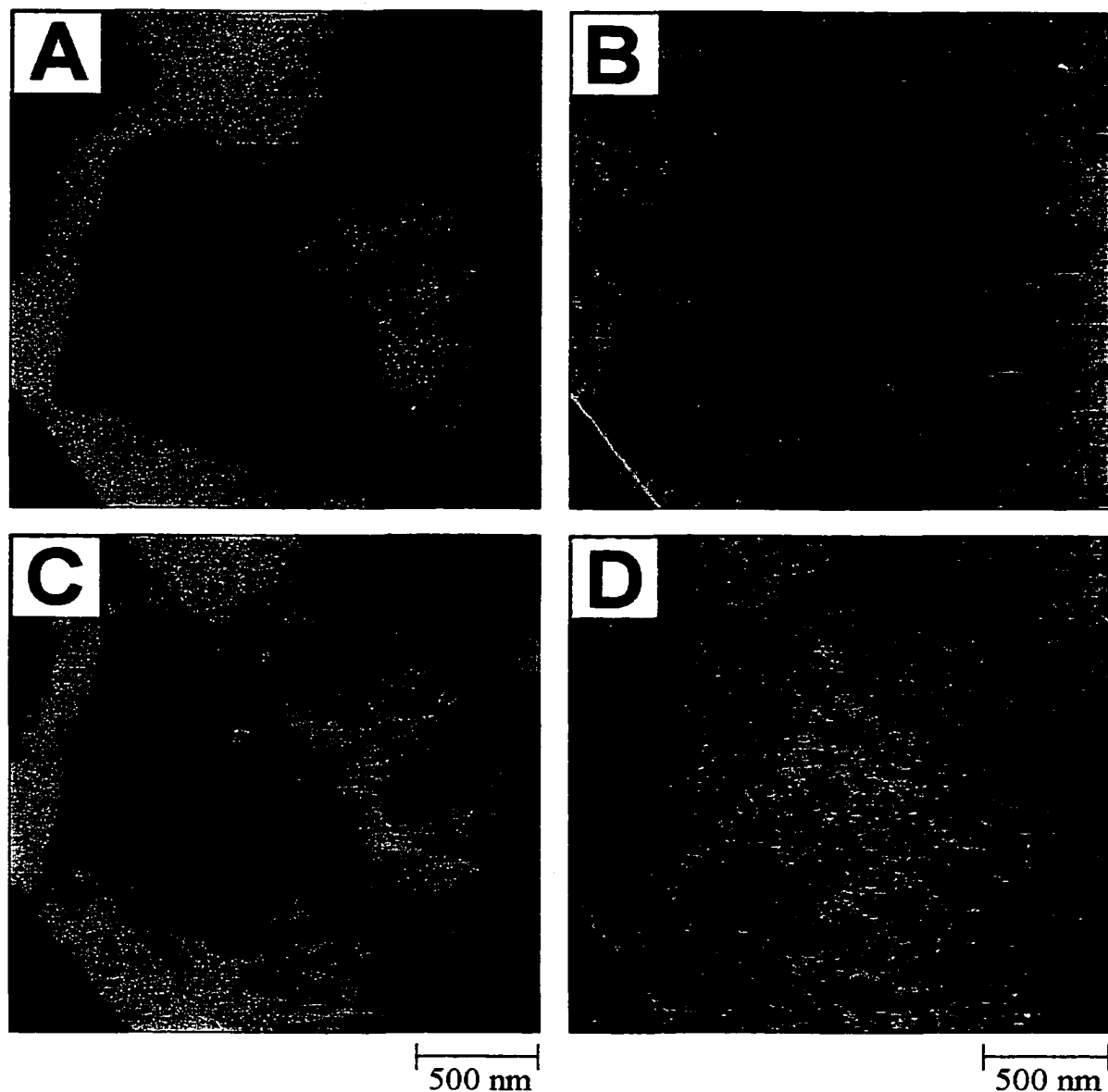
Figure 3.07. 2.2 × 2.2 μm² SFM images depicting the HFG adsorption onto methyl-terminated monolayer (ODT/Au). Parts A and C (Z-scales = 10 nm) are topographic images and parts B and D (Z-scale = 0.1 V) are the corresponding friction images. (A and B): initial methyl terminated surface under PBS. (C and D): 30 min after initial adsorption of HFG.

3.05A, steps between Au terraces can be seen before exposure to HFG (Figure 3.07A). After exposure to HFG solution for 1 h, the step features are no longer observable (Figure 3.07C). The resultant HFG films have covered up these steps, and more importantly a completed film was observed. Figure 3.08 revealed that HFG adsorbs significantly to MHA/Au (111) surfaces. The before (Figure 3.08A and B) and after (Figure 3.08C and D) images indicate a complete film also forms for HFG on MHA-modified Au surface. The conclusion from Figures 3.07 and 3.08 is that 20 µg/mL HFG protein solution does form a robust HFG film, very similar to that of BFG. In both cases, there was no evidence of protein displacement by the probe tip, and SFM images of HFG films formed under these conditions are reflective of the properties of the protein-solution interface and not convoluted by the underlying SAM. The quantity of anti-HFG binding to pre-adsorbed HFG on ODT and MHA modified substrate will serve to indicate the relative adsorbed conformation of HFG and monitored with IRRAS and SPR.

Antibody binding studies by IRRAS: Antibody binding is a widely accepted method for detecting differences in protein conformation (47, 50). However, quantification of bound antibodies usually involves a labeling step, where the antigen or antibody is labeled with fluorescent dyes (51) or radioisotopes (5, 6, 52, 53). Antibodies can be produced to bind only to one epitope on an antigen with high affinity; these antibodies are referred to as monoclonal. On the other hand, polyclonal antibodies can bound to many epitopes, with varying degrees of binding strength. Since little knowledge was available as to which epitopes would be exposed at the interface upon HFG adsorption, it was more prudent to start our investigation using a polyclonal antibody. Therefore a "shot-gun" approach was considered to be most suitable because our goal was not to determine precisely which domain of the protein contributed to the differences in conformation. Rather, the goal was to find evidence that HFG adsorbed onto a particular surface binds a statistically different
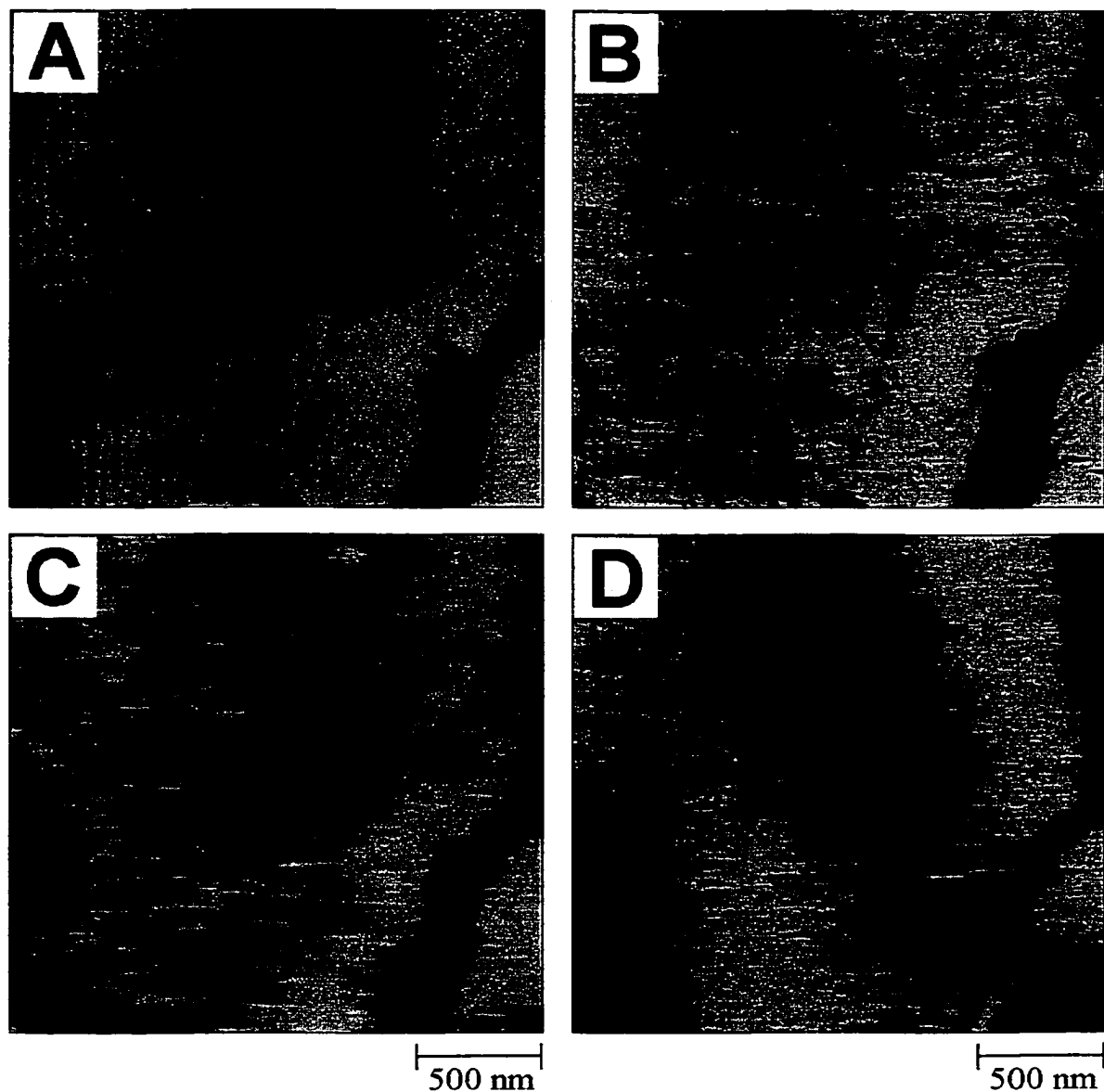
Figure 3.08. 2.2 × 2.2 μm² SFM images depicting the HFG adsorption onto carboxylate-terminated monolayer (MHA/Au). Parts A and C (Z-scales = 10 nm) are topographic images and parts B (Z-scale = 1.0 V) and D (Z-scale = 0.1 V) are the corresponding friction images. (A and B): initial carboxylate terminated surface under PBS. (C and D): 30 min after initial adsorption of HFG. The large dark and light bands in part D is due to the interference pattern of the laser. This is seen on occasion when imaging under solution.

amount of antibodies compared to HFG adsorbed onto another surface. The premise behind the experimental design was based on the assumption that different antigen (protein) conformation will express different binding sites (epitope) that will be communicated as differences in the amount of antibody binding.

Antibodies contain amide backbone linkages that are IR active. As shown earlier in this chapter, IRRAS is capable of quantifying protein at a SAM/Au interface. In addition, protein adsorption obtained by IRRAS requires no labeling procedures. IRRAS will be used to quantify antibody binding to HFG which was pre-adsorbed to ODT and MHA modified Au surfaces. Differences in binding will be attributed to surface-induced conformation/orientational variation in HFG films.

Spectrum A in Figure 3.09 was obtained after 1 h adsorption of HFG. Protein adsorption to ODT-modified Au surfaces is easily discernible by the two major amide bands, amide I at 1671 ± 1 cm^{-1} and amide II at 1546 ± 1 cm^{-1}. Discussion of amide I and II bands were presented earlier for BFG. Amide II bands can be used to gauge the amount of protein, either in solution or adsorbed to a surface. The focus will be on using amide II intensities as a measure of antibody interaction. The intensity of this band after HFG adsorption on ODT surface was 0.0024 ± 0.0001 a.u. Weakly adsorbing amide III bands in the vicinity of 1240 cm^{-1} are due to N-H bending. These peaks are sensitive to hydrogen-bonding interactions, and therefore can be used as a diagnostic tool for assigning adsorbed protein states (37, 54). Because amide III bands are weakly absorbing as compared to amide I and amide II modes, A_{III} will not be used, and thus no further discussion on this band will be presented. Two other peaks are present in the amide region, positioned at ~1455 cm^{-1} and 1405 cm^{-1}. These peaks arise from the functional groups on the protein side chains. The peak at 1455 cm^{-1} is due to the bending of C-H bonds from CH_2 and CH_3 moieties, while the peak at 1405 cm^{-1}

Amide I, ~1671 cm⁻¹

C

B

Amide II, ~1546 cm⁻¹

A

0.002 a.u.

Amide III, ~1240 cm⁻¹

2000   1800   1600   1400   1200   1000

Wavenumber (cm⁻¹)
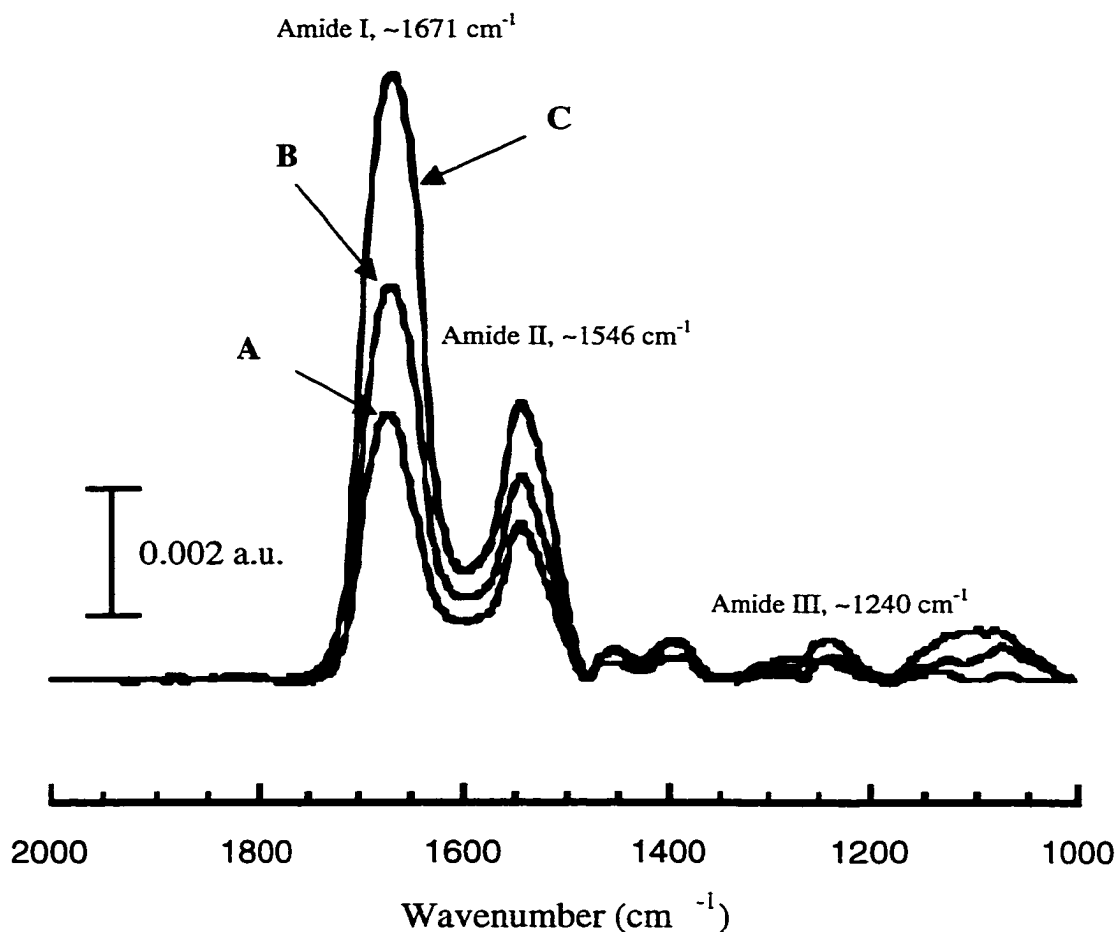
Figure 3.09. IRRAS investigation of HFG films adsorbed onto ODT modified Au surfaces, before and after exposure to anti-HFG and Bovine IgG. (A) Example of an IRRAS spectrum of HFG (20 μg/mL) after 1 h adsorption onto ODT/Au. (B) Representative spectrum obtained after bovine IgG (160 μg/mL, 2 h exposure) binding to a surface similar to that used for spectrum A. Bovine IgG serves as a control to monitor non-specific binding, while anti-HFG was the specific antibody. (C) Spectrum after 2 h exposure of the same substrate used to obtained spectrum A to 160 μg/mL anti-HFG. Amide II intensities were used for quantitation purposes.

results from a symmetric CO_2^- stretching mode (54). Based on the spectrum, it is clear that HFG does adsorb onto methyl (CH_3) terminated surfaces.

Spectrum B in Figure 3.09 was obtained after 2 h exposure of the same substrate that was used to obtain the spectrum A to 160 μg/mL anti-HFG solution. All the amide bands increased in intensity due to antibodies binding at the interface. There are numerous factors that must be considered before determining the amount of specific interaction. These concerns focus on the physisorption of anti-HFG either onto the top of the HFG film and/or onto the underlying monolayer through defect areas in the film. Another concern was the possibility of HFG displacement, and subsequent anti-HFG adsorption to that vacant site. To address these concerns, it was necessary to expose HFG films to another antibody that should interact only through non-specific interactions. Bovine IgG was used in the control studies because it is in the same antibody class as anti-HFG, yet should have low specific affinity for HFG. Spectrum C in Figure 3.09 is the IRRAS spectrum obtained on pre-adsorbed HFG on ODT/Au after 2 h exposure to 160 μg/mL bovine IgG (bIgG). There is an increase in the intensity of the amide bands. However, the increase was smaller than that observed with anti-HFG. The difference of amide II intensities from spectra C and B were assigned as the amount of specific binding based on the assumption that bIgG and anti-HFG are similar in size.

Similar experiments and analyses were performed on MHA surfaces (carboxylate terminated). The IRRAS spectra are shown in Figure 3.10. Spectrum A indicates that HFG adsorbs to MHA surfaces in similar amounts as to ODT surfaces ($A_{II, MHA}$ = 0.0021 ± 0.0001 a.u.). The frequency of the amide absorption bands also are very similar, amide I = 1671 ± 1 cm^{-1} and amide II = 1545 ± 1 cm^{-1}. However, similarities between the peak positions of HFG on the two surfaces do not necessary indicate similar protein conformation. It is possible, under our experimental setup, that the IRRAS absorption frequency does not
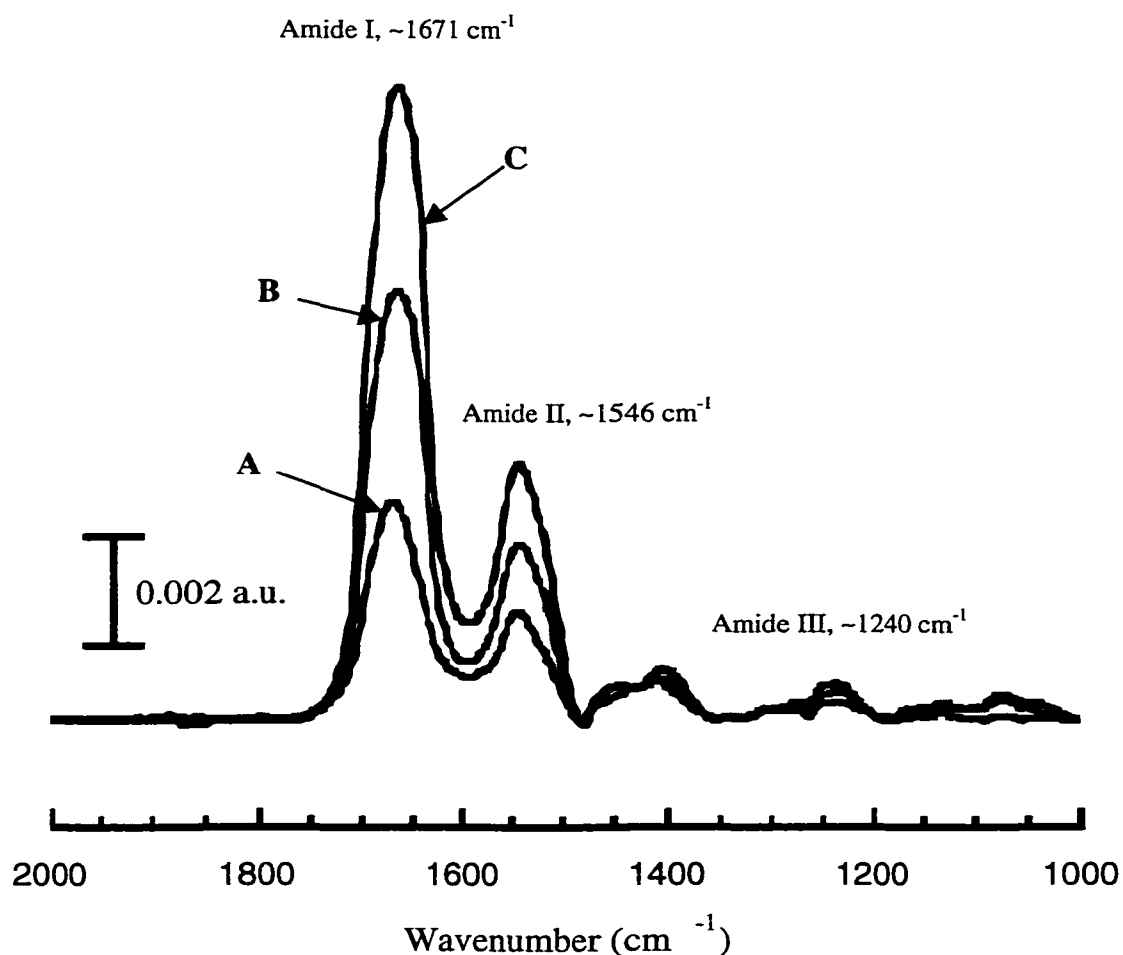
Figure 3.10. IRRAS investigation of HFG films adsorbed onto MHA modified Au surfaces, before and after exposure to anti-HFG and Bovine IgG. (A) Example of an IRRAS spectrum of HFG (20 µg/mL) after 1 h adsorption onto MHA/Au. (B) Representative spectrum obtained after bovine IgG (160 µg/mL, 2 h exposure) binding to a surface similar to that used for spectrum A. Bovine IgG serves as a control to monitor non-specific binding, while anti-HFG was the specific antibody. (C) Spectrum after 2 h exposure of the same substrate used to obtained spectrum A to 160 µg/mL anti-HFG. Amide II intensities were used for quantitation purposes.

correlate with protein secondary structures because the protein films are dried and low spectrometer resolution (2 cm^{-1}), and thus is unable to resolve conformational information. Similar results were reported in other articles whereby proteins were determined to be conformationally different but the amide peak positions did not show significant difference (54). As a result, antibody studies are critical for verifying the conformation of the adsorbed HFG. Spectrum C in Figure 3.10 shows a representative spectrum of anti-HFG and HFG on a MHA/Au substrate, while spectrum B as the control experiments with bIgG. These curves are similar to those obtained on ODT-modified substrates. The amount of specific binding was calculated as the difference in intensities between spectra C and B. In summary, HFG absorbs onto both ODT and MHA surfaces in similar quantities, and IRRAS can detect the presence of the bound antibody. The control experiments allowed us to determine the amount of specific binding.

To determine if HFG molecules on methyl surfaces are conformationally different than those adsorbed on carboxylate surfaces, amide II peak intensities were considered as a measure of antibody binding. Results from the IRRAS studies on antibodies binding are summarized in Figure 3.11. Because there is a small variation in the amount of HFG adsorbed between the two surfaces ($A_{II, ODT}$ = 0.0024 a.u. versus $A_{II,MHA}$ = 0.0021 a.u.), it was necessary to normalize any increase in absorption due to antibody binding. The equation below was used to generate the normalized values used in Figure 3.11, based on amide II intensities.

Percent Increase = $\dfrac{\text{Intensity with antibody/HFG - Intensity with HFG}}{\text{Intensity with HFG}} \times 100\%$ {7}

The percentage increases were compared between the two surface chemistries. On the methyl-terminated surfaces, increase due to anti-HFG bound was 77 ± 8 %, as compared to 130 ± 9 % on carboxylate-terminated surfaces. After taking into
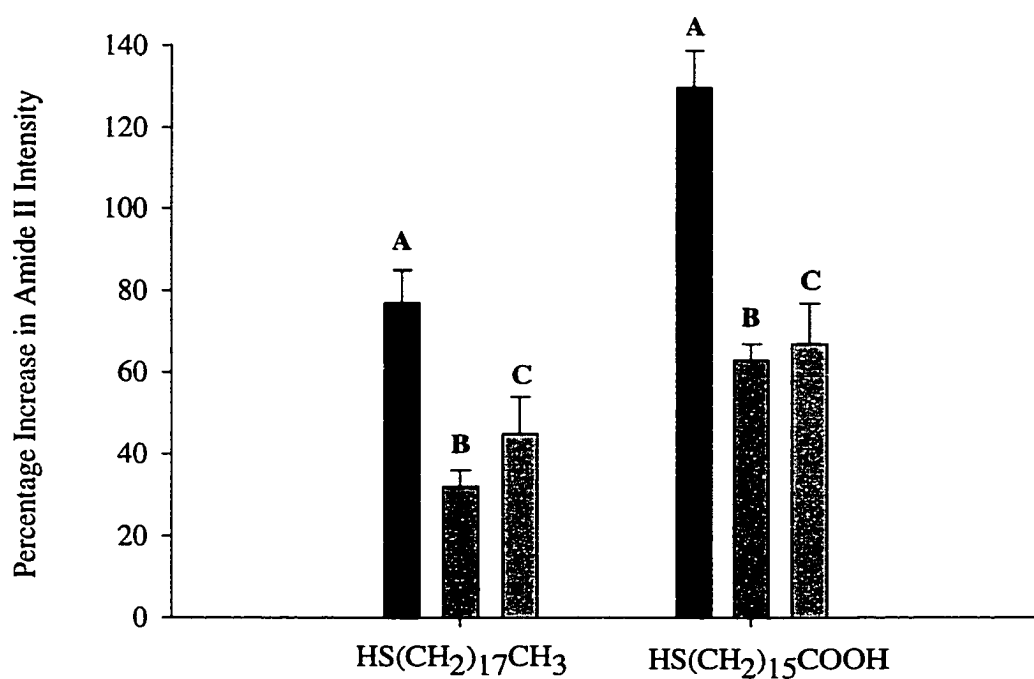
Figure 3.11. Bar graph represention of the percentage increase in intensity of the Amide II band due to bound antibodies compared to Au substrates that were modified with an appropriate alkanethiol, and exposed to 20 μg/mL HFG for 1 h. These surfaces were either then exposed to 160 μg/mL of anti-HFG (A) or bovine IgG (B) for 2 h. (C) Representing the corrected increase in the Amide II band intensity, and thus reflects the amount of specific binding.

account non-specific interactions, these values decrease respectively to 45 ± 9 % and 67 ± 10 %. The difference in anti-HFG binding between ODT and MHA-modified surfaces decreased after taking non-specific interactions into account. The reason is that MHA surfaces showed greater non-specific binding (B-bars), 63 ± 4 % as compared to 32 ± 4 % on the ODT surface. It is not clear why there is more non-specific adsorption onto HFG film adsorbed on MHA surfaces. However, one possibility lies in the fact the HFG films on ODT adsorb very tightly to the surface, forming a tight and compact film. This reduces the number of localized vacant sites, and allows less displacement/exchange of HFG and antibody. IRRAS shows that the amounts of specific binding are different across the two surfaces analyzed. Antibody binding monitored by IRRAS begins to paint a picture that supports data acquired from SFM, indicating that surface chemistry does influence the conformation of the adsorbed fibrinogen. To further substantiate our claim, surface plasmon resonance (SPR) was applied to monitor antibody binding under an aqueous environment.

Surface Plamson Resonance: Surface plasmon resonance is an invaluable tool for probing biomolecular interactions because both the kinetics and quantity of adsorption may be monitored under simulated physiological conditions. Also, no labeling procedures are necessary for detection. Experimental conditions used herein mimic those used in IRRAS investigations. SPR will be used to reveal the relative quantity of adsorbed HFG and the amount of antibody binding. Antibody binding was performed in situ, and therefore eliminates any concerns due to the washing and drying steps that may have cast uncertainties in the IRRAS results. The goal of SPR studies was to determine the quantity of adsorption or binding. BIAcore have stated in their literature that a 1000 RU response approximately corresponds to a surface concentration of 1 ng/mm^2.

SPR detects adsorbates based on the shift in the angle of resonance. The angle of resonance is the angle of lowest reflectivity, which was determined and

locked when the sensor was under buffer. As protein begins to adsorb to the interface, reflectivity increases and a plot of signal detected (RU units) versus time is generated and is referred to as a sensorgram. A greater degree of shifting correlates with a higher quantity of adsorbates. SPR sensors used were Au films (sensors), modified with either ODT or MHA. These sensors were then exposed to 20 μg/mL of HFG for 30 min, rinsed with PBS, dried with argon and placed into the SPR instrument for antibody binding analysis. These sensors will be referred to as either ODT-HFG or MHA-HFG sensors. HFG adsorbed strongly to both surface functional groups as reflected by only a small decrease in signal (~100 RU) as the sensors were washed with buffer. This finding is similar to a previous report (55) in which the authors found that fibrinogen does adsorb to hydrophobic surfaces $[HS(CH_2)_{10}CH_3]$. The quantity of HFG adsorbed was calculated based on the signal observed before the sensors were exposed to HFG and compared to the same channel after HFG exposure.

HFG adsorption caused approximately 4623 ± 512 RU change in response on ODT surfaces, and 5672 ± 233 RU on MHA sensors. The MHA surface adsorbs more HFG. This conclusion is not surprising based on the fact that hydrophobic surfaces have been shown to induce dramatic fibrinogen denaturation, causing proteins to unfold and spread across the surface (30, 56). Therefore, less protein per unit area would adsorb because more binding site would be occupied per molecule of fibrinogen. A hydrophilic MHA surface denatures fibrinogen to a lesser degree, as indicated by the island-like structures seen in Figures 3.05C, D and 3.06C, D.

Figure 3.12 are sensorgrams obtained for the determination of specific anti-HFG binding and non-specific bIgG binding to ODT-HFG sensors. Because each sensor has four flow channels that can be addressed individually, each curve was obtained on the same sensor, but in a different channel. The response signal and times were normalized to zero for illustration purposes. Sensorgram B was
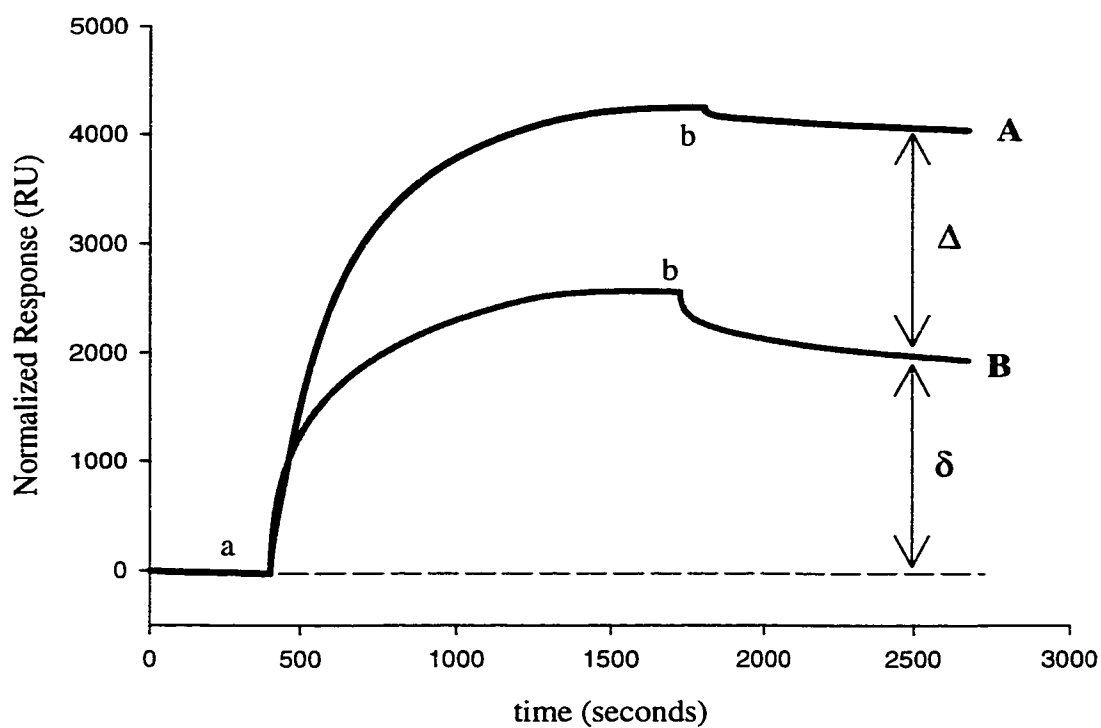
Figure 3.12. (A) SPR sensorgrams of antibody binding (160 μg/mL anti-HFG) and (B) non-specific adsorption (160 μg/mL bovine IgG onto HFG adsorbed to Au sensors modified with ODT. (a) Point of injection of either anti-HFG or IgG into the flow channel. (b) Washing with PBS. (Δ) Quantity of specific binding and (δ) quantity of non-specific adsorption.

obtained after injection of 160 μg/mL bIgG to one flow channel. The increase in response (δ) was 1929 ± 131 RU, measured on the signal plateau after rinsing with PBS. Decrease in signal upon washing with PBS was observed. However, the decrease was small and a plateau was observed after 20 min of washing. This indicates that non-specific binding of bIgG was strong. To a separate channel, 160 μg/mL anti-HFG was added, and sensorgram A was generated. The increase in response was 3582 ± 495 RU. Again there was a small decrease in signal with washing; however, plateau level was achieved quickly, indicating strong binding. The difference in response between the two curves is 1653 ± 512 RU (Δ), and is attributed only to specific binding.

Similar determinations were performed on MHA-HFG sensors. The results of these studies are shown in Figure 3.13. The sensorgram B was obtained after injection of 160 μg/mL IgG and washing with PBS. δ was calculated to be 2403 ± 124 RU. The increase in signal response after addition of anti-HFG (sensorgram B) to a different channel was 6778 ± 487 RU, and the calculated Δ value was 4375 ± 503 RU. The ratio of $\Delta_{MHA}/\Delta_{ODT}$ is 2.6 ± 0.9. Thus, on MHA-HFG surfaces, the amount of specific binding is more than double than that observed on ODT-HFG surfaces.

As noted earlier, MHA surfaces adsorb a greater quantity of HFG. This fact suggests that greater specific antibody binding at MHA surfaces may result merely from more HFG bound at the surface. To address this concern, a ratio was calculated from the intensity of HFG adsorption onto MHA and ODT, and the ratio was determined to be 1.2. If the contrast in specific binding were only the result of the antigen quantity, $\Delta_{MHA}/\Delta_{ODT}$ would be 1.2. However, $\Delta_{MHA}/\Delta_{ODT}$ was 2.6 ± 0.9. Thus, the difference in binding is now believed to be due to differences in HFG conformation. On the MHA surface, HFG conformation exposed more binding sites or epitopes at the interface. Normalized SPR signals caused by the
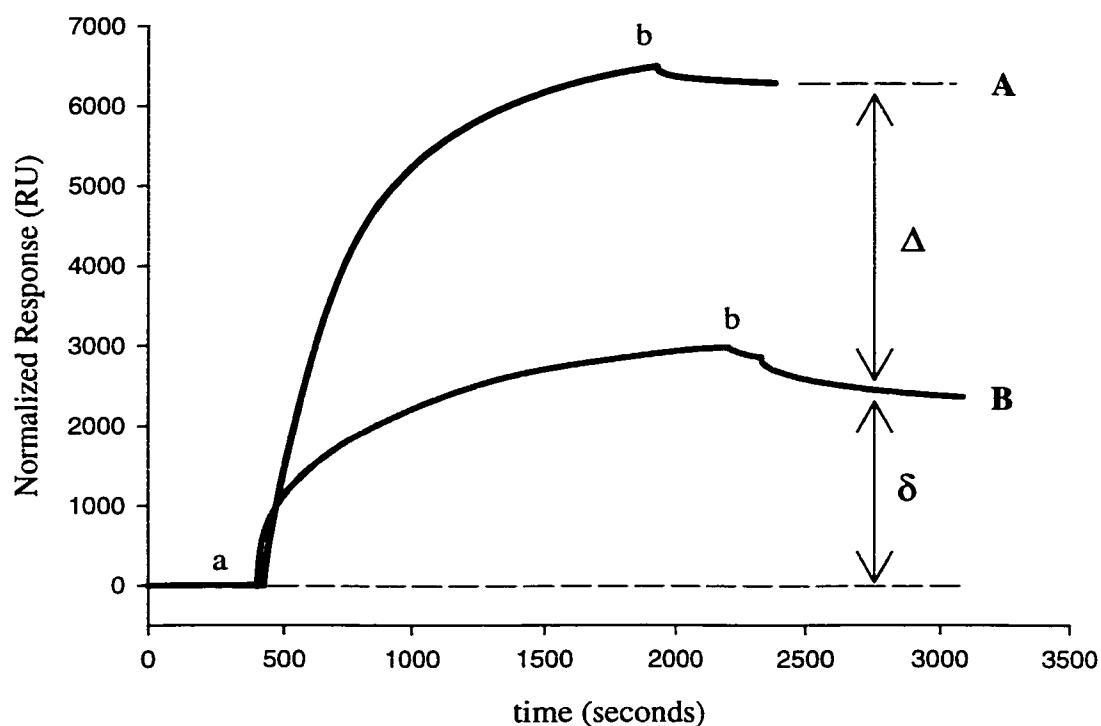
Figure 3.13. (A) SPR sensorgram of antibody binding (160 μg/mL anti-HFG) and (B) non-specific adsorption (160 μg/mL bovine IgG) onto HFG adsorbed to Au sensors modified with MHA. (a) Injection point of either anti-HFG or IgG into the flow channel. (b) Washing with PBS. (Δ) Amount of specific binding and (δ) quantity of non-specific adsorption.

adsorption of HFG to ODT and MHA sensors, and the binding of anti-HFG and bovine IgG onto ODT-HFG and MHA-HFG sensors are summarized in Table 3.1.

The magnitude of the SPR response tracks the change of adsorbed mass at the interface. Thus it is possible to estimate the number of anti-HFG molecules bound per molecule of HFG, by comparing the ratio of SPR response generated by the binding of anti-HFG to the response for HFG adsorption, and the mass ratio of anti-HFG to HFG. The mass ratio is calculated using the average molecular weight of anti-HFG ($\approx$150 kDa) and HFG ($\approx$340 kDa). Shown in Table 3.1, the mass ratio of antibody to HFG was 0.44. On ODT-HFG sensors, the ratio determined from SPR signals revealed a ratio of 0.36. Because these ratios are similar, it indicates that there is only one anti-HFG binds to one molecule of HFG. On MHA-HFG sensors, the SPR signal ratio was 0.77, which is approximately double the value observed on ODT-HFG sensors. Therefore, it is estimated that there are two anti-HFG molecules bound to one molecule of HFG. This finding corroborates conclusions made earlier from FTIR studies, where greater antibody binding to HFG on MHA surfaces (Figure 3.11) was observed. At this time, there is still no information on the specific epitopes involved. However, evidence from FTIR, SFM and SPR does suggest that HFG adsorbed in a different conformation on MHA-modified Au substrates as compared to ODT surfaces.

The control experiments performed using bovine IgG was designed to account for any non-specific interactions that may distort conclusions for specific binding. The desire was to have a better understanding on the location of these non-specific interactions, and whether they were blocking the specific binding epitopes. Experiments involved here were similar to those SPR studies detailed above. In contrast however, we will inject both bovine IgG and anti-HFG sequentially to the same flow channel. The premise behind this design was to see if similar levels of binding would be achieved in comparison to levels that was observed when separate channels were used. If the results are similar, a

Signal due to (RU units)	$HS(CH_2)_{17}CH_3$	$HS(CH_2)_{15}COOH$
Human Fibrinogen (HFG)	4623 ± 512	5672 ± 233
Anti-HFG antibodies	3582 ± 495	6778 ± 487
Bovine IgG (δ)	1929 ± 131	2403 ± 124
Specific Binding (Δ)	1653 ± 512	4375 ± 503
Mass ratio (antibody/HFG)	0.44	0.44
Ratio of Δ signal/HFG signal	0.36 ± 0.12	0.77 ± 0.9
# of anti-HFG molecules bound to HFG	$0.8 \pm 0.2 : 1$	$1.8 \pm 0.2 : 1$

Table 3.1. Signals obtained from SPR investigations. Anti-HFG and bovine IgG were analyzed on separate channels on ODT-HFG and MHA-HFG sensors. Specific binding (Δ) was calculated as the difference in signal for anti-HFG and bovine IgG. Mass ratios were based on approximate molecular weights of antibodies (≈150 kDa) and HFG (≈340 kDa). Approximate molecules of anti-HFG bound to HFG were determined from the ratio of Δ signal/HFG signal and Mass ratio (antibody/HFG).

conclusion could be made that non-specific interactions do not significantly block the specific binding epitopes.

Figure 3.14 are results obtained on ODT-HFG (sensorgram B) and MHA-HFG (Sensorgram A) sensors. Only one channel on each sensor was used. On the ODT-HFG surface, injection of 160 µg/mL bovine IgG (point a) revealed a typical sensorgram in which the response rises to a plateau, and upon washing with PBS (point b), some signal is lost. Washing was continued until a baseline was established, followed by injection of 160 µg/mL anti-HFG to the same channel. The signal increased due to anti-HFG binding to adsorbed HFG until a plateau level was reached. Washing with PBS (point d) showed that there was a strong affinity between HFG and anti-HFG because the loss of signal from washing was limited. On MHA-HFG sensors, similar behaviors were observed. Sensorgram A indicates that there is more non-specific interaction on this sensor, approximately 500 RU. The signal for anti-HFG binding was twice that observed on the ODT-HFG sensors. Because results from the single channel experiments showed similar results to those obtained from separate channels, it is believed that bovine IgG does not block the epitopes that are used by anti-HFG to bind to adsorbed HFG. The magnitude of the signal change upon injection of bovine IgG and anti-HFG are summarized in Table 3.2. Signals for non-specific interactions were 1929 ± 131 and 2403 ± 124 RU on ODT-HFG and MHA-HFG sensor respectively. Signals due to anti-HFG specific binding (Δ) were 2758 ± 15 and 5588 ± 85 RU. By comparing the specific binding/HFG signal ratio to the mass ratio, the approximate number of molecules of anti-HFG bound to one HFG molecule could be estimated. On ODT-HFG, this estimate is 1.4 to 1, which is close to that estimated in Table 3.1. The difference may be the result of the washing procedure (point b) being of insufficient length. On MHA-HFG sensor, the estimate is 2.2 to 1. This value is similar although a little larger than values reported in Table 3.1. Overall, the two methods for determining the number of
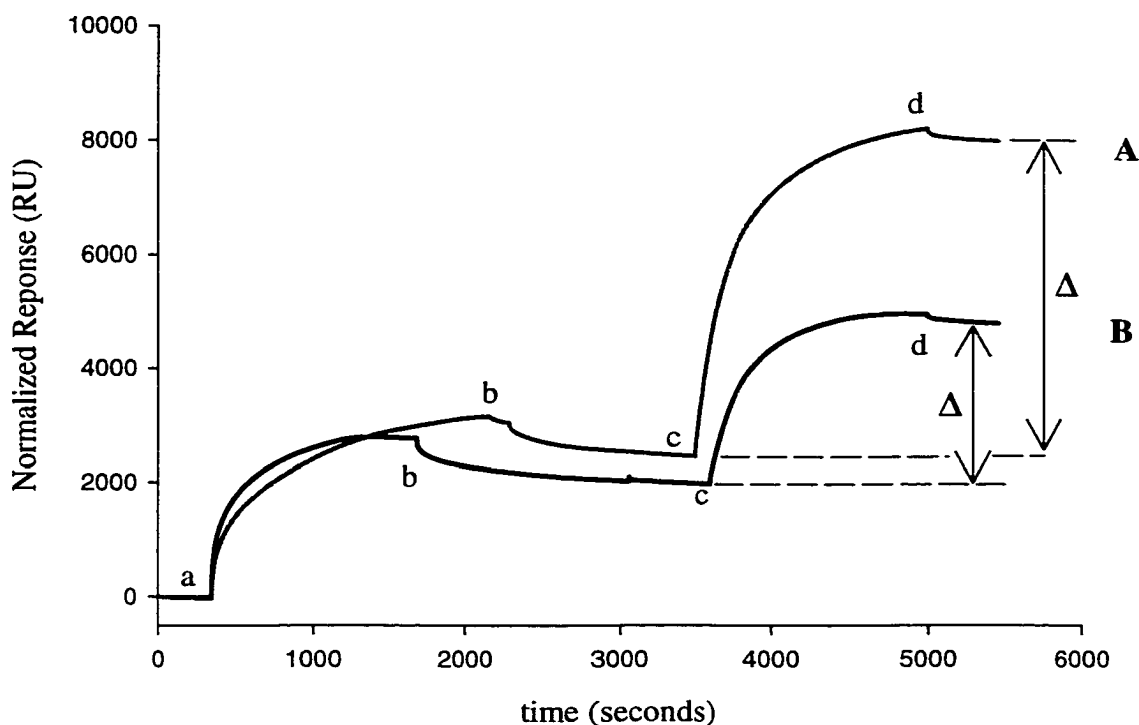
Figure 3.14. SPR sensorgram depicting normalized response (RU units) due to anti-HFG and nonspecific IgG binding. Flow rate was kept constant at 10 μL/min for all experiments. Sensorgram A was obtained on a Au sensor modified with MHA and 1 h adsorption of 20 μg/mL HFG. Sensorgram B was obtained on a Au sensor modified with ODT and 1 h adsorption of 20 μg/mL HFG. (a) Injecting 160 μg/mL bovine IgG (b) PBS wash (c) 160 μg/mL anti-HFG and injection (d) PBS wash to the flow channels. (Δ) Signal due to anti-HFG binding.

Signal due to (RU units)	HS(CH$_2$)$_{17}$CH$_3$	HS(CH$_2$)$_{15}$COOH
Bovine IgG (δ)	1929 ± 131	2403 ± 124
Anti-HFG antibodies (Δ)	2758 ± 15	5588 ± 85
Ratio of Δ signal/HFG signal	0.60 ± 0.04	0.99 ± 0.05
# of anti-HFG molecules bound to HFG	1.4 ± 0.1: 1	2.2 ± 0.1 : 1

Table 3.2. Signals obtained from SPR investigations. Bovine IgG and anti-HFG were sequentially added to the same channel. Since IgG was injected first, non-specific interaction sites would have been taken up by bovine IgG, and therefore signal changes upon addition of anti-HFG were directly due to specific binding. Non-specific interactions were sufficient to withstand PBS washing for 20 min. Approximate molecules of anti-HFG bound to HFG was determined from the ratio of Δ signal/HFG signal and Weight ratio (antibody/HFG).

anti-HFG bound per molecule of HFG arrive at similar relative conclusions. On ODT-HFG sensors, approximately one anti-HFG bound per HFG molecule, while on MHA-HFG this value is two to one. To reiterate, differential binding was attributed to the differences in HFG conformation influenced by substrate surface chemistry, and thus HFG adsorbed on ODT surfaces are conformationally different than HFG on MHA modified surfaces.

Conclusions

In this Chapter, surfaces were tailored to exhibit specific surface chemistries. Self-assembly of alkylthiolates on Au substrates was a simple and quick method for this purpose. ODT created a neutral, hydrophobic surface. In contrast, MHA resulted in a negatively charged (at pH 7.4), and hydrophilic surface. IRRAS investigation showed that similar amounts of fibrinogen adsorbed on both functional groups. Adsorption of bovine fibrinogen monitored via SFM provided subtle hints indicating that a hydrophobic surface has a greater tendency to denature the proteins, causing them to spread out and resulting in reduced topographic features. Bovine fibrinogen (BFG) adsorption on MHA surfaces showed a lesser tendency to denature as seen in our real-time adsorption studies. Therefore, SFM begins to provide the initial hints that surface chemistry affects adsorbed protein states.

To further substantiate this claim, antibody binding to adsorbed human fibrinogen (HFG) was monitored. Films derived from 20 μg/mL HFG solution formed a complete monolayer just like those formed from BFG. Quantity of antibody attachment was detected using IRRAS by monitoring the intensity of the amide II band. Results from IRRAS revealed that anti-HFG was able to bind in greater quantity to HFG adsorbed on MHA as compared to HFG on ODT modified surfaces. This claim was reinforced by SPR data that suggest that two anti-HFG molecules bound per molecule of HFG on MHA-modified surfaces. HFG on ODT surfaces bound in a one to one ratio. Therefore, in this chapter I

have demonstrated conclusively that surface chemistry plays a critical role in defining the conformation of fibrinogen. Because the fibrinogen molecules are in a different conformational state, they most likely will expose variable chemical domains to the liquid interface. Based upon this supposition, I felt that it may be possible to use lateral force (friction) SFM, which has already demonstrated the ability to map a surface compositionally, to detect these differences. Thus, to our knowledge, results to be presented in the next chapter are the first demonstration that friction SFM is able to map differences in protein conformation.

References

(1)   Horbett, T. A.; Brash, J. L. In *Proteins at Interfaces: Physicochemical and Biochemical Studies*; Brash, J. L., Horbett, T. A., Eds.; American Chemical Society: Washington, DC, 1987, pp 1 - 33.

(2)   Lu, D. R.; Lee, S. J.; Park, K. *J. Biomat. Sci. Polymer Edn* **1991**, *3*, 127 - 147.

(3)   Lee, J. E.; Saavedra, S. S. In *Proteins at Interfaces II: Fundamentals and Applications*; Horbet, T. A., Brash, J. L., Eds.; American Chemical Society: Washington, DC, 1995, pp 269 - 279.

(4)   Brash, J. L.; Horbett, T. A. In *Proteins at Interfaces II : Fundamentals and Applications*; Brash, J. L., Horbett, T. A., Eds.; American Chemical Society: Washington, DC, 1995, pp 1 - 23.

(5)   Chinn, J. A.; Posso, S. E.; Horbett, T. A.; Ratner, B. D. *J. Biom. Mat. Res.* **1992**, *26*, 757-778.

(6)   Rapoza, R. J.; Horbett, T. A. *J. Biomater. Sci.* **1989**, *1*, 69-80.

(7)   Sheller, N. B.; Petrash, S.; Foster, M. D.; Tsukruk, V. V. *Langmuir* **1998**, *14*, 4535-4544.

(8)   Sarver, R. W. J.; Krueger, W. C. *Anal. Biochem.* **1993**, *212*, 519 - 525.

(9)   Chittur, K. K. *Biomaterials* **1998**, *19*, 357-369.

(10) Liedberg, B.; Ivarsson, B.; Lundstrom, I. *J. Biochem. Biophys. Met.* **1984,** *9*, 233-243.

(11) Azpiazu, I.; Chapman, D. *Biochim. Biophys. Acta.* **1992,** 268-274.

(12) Sarver, R. W.; Krueger, W. C. *Anal. Biochem.* **1991,** *199*, 61 - 67.

(13) McMillin, C. R.; Walton, A. G. *J. Colloid Interface Sci.* **1974,** *48*, 345-349.

(14) Chittur, K. K.; Fink, D. J.; Hutson, T. B.; Gendreau, R. M.; Jakobsen, R. J.; Leininger, R. I. In *Proteins at Interfaces: Physicochemical and Biochemical Studies*; Brash, J. L., Horbett, T. A., Eds.; American Chemical Society: Washington DC, 1987, pp 362 - 377.

(15) Buijs, J.; Britt, D. W.; Hlady, V. *Langmuir* **1998,** *14*, 335 - 341.

(16) Nicholov, R.; Lum, N.; Veregin, R. P. N.; DiCosmo, F. In *Proteins at Interfaces II: Fundamentals and Applications*; Horbett, T. A., Brash, J. L., Eds.; American Chemical Society: Washington, DC, 1995, pp 280 - 295.

(17) Lipert, R. J.; Lamp, B. D.; Porter, M. D. In *Modern Techniques in Applied Molecular Spectroscopy*; Mirabella, F. M., Ed.; John Wiley & Sons, Inc.: NY, 1998, pp 83 - 126.

(18) Kiaei, D.; Hoffman, A. S.; Horbett, T. A.; Lew, K. R. *J. Biom. Mat. Res.* **1995,** *29*, 729-739.

(19) Welle, A.; Grunze, M.; Tur, D. *J. Colloid Interface Sci.* **1998,** *197*, 263 - 274.

(20) Darnell, J.; Lodish, H.; Baltimore, D. In *Molecular Cell Biology*; Scientific American Books, Inc.: New York, 1986, pp 77 - 80, 1095 - 1097.

(21) Seigel, R. R.; Harder, P.; Dahint, R.; Grunze, M.; Josse, F.; Mrksich, M.; Whitesides, G. M. *Anal. Chem.* **1997,** *69*, 3321 - 3328.

(22) Green, G. J.; Davies, J.; Davies, M. C.; Roberts, C. J.; Tendler, S. J. B. *Biomaterials* **1997,** *18*, 405 - 413.

(23) Löfås, S.; Malmqvist, M.; Rönnberg, I.; Stenberg, E.; Liedberg, B.; Lundström, I. *Sensors and Actuators B* **1991,** *5*, 79 - 84.

(24)   Silin, V.; Plant, A. *Trends in Biotech.* **1997,** *15,* 353 - 359.

(25)   Davies, J. *Nanobiology* **1994,** *3,* 5 - 16.

(26)   Boussaad, S.; Pean, J.; Tao, N. J. *Anal. Chem.* **2000,** *72,* 222-226.

(27)   Hansen, W. N. *J. Opt. Soc. Am.* **1969,** *58,* 380-390.

(28)   Taborelli, M.; Eng, L.; Descouts, P.; Raineri, J. P.; Bellamkonda, R.; Aebischer, P. *J. Biom. Mat. Res.* **1995,** *29,* 707-714.

(29)   Cullen, D. C.; Lowe, C. R. *J. Colloid Interface Sci.* **1994,** *166,* 102-108.

(30)   Ta, T. C.; Sykes, M. T.; McDermott, M. T. *Langmuir* **1998,** *14,* 2435-2443.

(31)   Prime, K. L.; Whitesides, G. M. *Science* **1991,** *252,* 1164 - 1167.

(32)   Lestelius, M.; Biedberg, B.; Tengvall, P. *Langmuir* **1997,** *13,* 5900-5908.

(33)   Patel, N.; Davies, M. C.; Heaton, R. J.; Roberts, C. J.; Tendler, S. J. B.; Williams, P. M. *Appl Phys. A* **1998,** *66,* S569 - S574.

(34)   DiMilla, P. A.; Folkers, J. P.; A., B. H.; Harter, R.; Lopez, G.; Whitesides, G. M. *J. Am. Chem. Soc.* **1994,** *116,* 2225-2226.

(35)   Feng, L.; Andrade, J. D. In *Proteins at Interfaces II: Fundamentals and Applications*; Horbett, T. A., Brash, J. L., Eds.; American Chemical Society: Washington, DC, 1995, pp 66 - 79.

(36)   Finot, M. O.; McDermott, M. T. *J. Am. Chem. Soc.* **1997,** *119,* 8564 - 8565.

(37)   Barbucci, R.; Magnani, A. *Biomaterials* **1994,** *15,* 955-962.

(38)   Caruso, F.; Furlong, D. N.; Ariga, K.; Ichinose, I.; Kunitake, T. *Langmuir* **1998,** *14,* 4559-4565.

(39)   Lenk, T. J.; Horbett, T. A.; Ratner, B. D. *Langmuir* **1991,** *1991,* 1755-1764.

(40)   Nuzzo, R. G.; Dubois, L. H.; Allara, D. L. *J. Am. Chem. Soc* **1990,** *112,* 558 - 569.

(41) Noy, A.; Vezenov, D. V.; Lieber, C. M. *Annu. Rev. Mater. Sci.* **1997,** *27,* 381 - 421.

(42) van der Vegte, E. W.; Hadziioannou, G. *J. Phys. Chem. B* **1997,** *101,* 9563 - 9569.

(43) Jakobsen, R. J.; Brown, L. L.; Winters, S.; Gendreau, R. M. *J. Biomed. Mater. Res.* **1983,** *16,* 199 - 201.

(44) Pitt, W. G.; Spiegelberg, S. H.; Cooper, S. L. In *Proteins at Interfaces: Physicochemical and Biochemical Studies*; Brash, J. L., Horbett, T. A., Eds.; American Chemical Society: Washington DC, 1987, pp 324 - 338.

(45) Jakobsen, R. J.; Wasacz, F. M. In *Proteins at Interfaces: Physicochemical and Biochemical Studies*; Brash, J. L., Horbett, T. A., Eds.; American Chemical Society: Washington DC, 1987, pp 339 - 361.

(46) Marchant, R. E.; Barb, M. D.; Shainoff, J. R.; Eppel, S. J.; Wilson, D. L.; Siedlecki, C. A. *Thromb. Haemost.* **1997,** *77,* 1048-1051.

(47) Egodage, K. L.; S. de Silva, B.; Wilson, G. S. *J. Am. Chem. Soc.* **1997,** *119,* 5295-5301.

(48) Browning-Kelley, M. E.; Wadu-Mesthrige, K.; Hari, V.; Liu, G. Y. *Langmuir* **1997,** *13,* 343-350.

(49) Allen, S.; Chen, X.; Davies, J.; Davies, M. C.; Dawkes, A. C.; Edwards, J. C.; Roberts, C. J.; Sefton, J.; Tendler, S. J. B.; Williams, P. M. *Biochem.* **1997,** *36,* 7457-7463.

(50) Jemmerson, R.; Liu, J.; Hausauer, D.; Lam, K.-P.; Mondino, A.; Nelson, R. D. *Biochem.* **1999,** *38,* 3599-3609.

(51) Craig, D. B.; Dovichi, N. J. *Anal. Chem.* **1998,** *70,* 2493 - 2494.

(52) Bentaleb, A.; Abele, A.; Haikel, Y.; Schaaf, P.; Voegel, J. C. *Langmuir* **1998,** *14,* 6493 - 6500.

(53) Bentaleb, A.; Abele, A.; Haikel, Y.; Schaaf, P.; Voegel, J. C. *Langmuir* **1999**.

(54)   Liedberg, B.; Ivarsson, B.; Lundstrom, I.; Salaneck, W. R. *Prog. Coll. Polym. Sci.* **1985,** *70*, 67 - 75.

(55)   Mrksich, M.; Sigal, G. B.; Whitesides, G. M. *Langmuir* **1995,** *11*, 4383-4385.

(56)   Ta, T. C.; McDermott, M. T. *Anal. Chem.* **2000,** *72*, 2627- 2634.

CHAPTER IV

MAPPING PROTEIN ADSORPTION ON PATTERNED SELF-ASSEMBLED ALKYLTHIOLATE MONOLAYER ON GOLD WITH SFM*

Introduction

Chapter III detailed the investigation of fibrinogen adsorption onto single component monolayers. Initial findings based upon topographic scanning force microscopy (SFM) images led to speculations that the chemical nature of the substrate surface determines the adsorbed conformational state of fibrinogen. On hydrophilic surfaces (MHA), the thickness of the protein clusters from real-time SFM imaging closely reflects the expected thickness (~6 nm) of native fibrinogen molecules and suggests a limited degree of denaturation. On hydrophobic (ODT) surfaces, the measured thickness of the protein clusters were greatly reduced, implying extensive protein unfolding. Antibody binding monitored by FTIR and SPR, further substantiated the claim that adsorbed fibrinogen is conformationally unique on each functional group. In this chapter, compositional sensitive friction force microscopy (FFM) is employed to map differences in the adsorbed fibrinogen conformation on patterned substrates.

The growth of scanning force microscopy (SFM) in both academic and industrial research can be attributed, in part, to its applicability for imaging biological samples. Related to the present work, SFM has enjoyed widespread usage in protein research. Applications range from the imaging of individual protein molecules (1, 2) to the analysis of protein films (3-6). One of the more recent, exciting advances in SFM technology has been the development of contrast mechanisms with the ability to map surfaces based on composition. Several

---

* Certain sections of this chapter were published as "Ta, T. C., and McDermott, M. T. *Anal. Chem.* **2000**, 72, 2627-2634".

groups have demonstrated that contact SFM, operated in lateral (or friction) force mode, can discriminate segregated assemblies of functional groups (7-12).

The friction at a SFM tip-sample junction depends on the normal force (*i.e.*, load), the interfacial free energy (γ^*) and the tip-sample contact area (13) as discussed in Chapter I (equation 4). Since SFM images are collected at constant load, frictional contrast is generated by spatial variations in the chemistry of the surface and/or mechanical properties (e.g., viscoelasticity), which influence contact area. The work presented here combines the compositional sensitivity of FFM with its utility in probing adsorbed proteins. Our assumption is that, due to the dependence of SFM measured friction on surface chemistry and mechanical properties, this imaging mode would also be useful in differentiating the conformation and/or orientation of protein molecules adsorbed on a surface.

Determining protein conformation by FFM adsorbed on single component monolayers is difficult and imprecise. For accurate quantitative comparison, the tip radius and torsional force constant of the cantilever must be known. In Chapter III, our studies characterized fibrinogen adsorption to single component octadecanethiol (ODT) and mercaptohexadecanoic acid (MHA) monolayers. Surface chemistry was shown to induce different adsorbed fibrinogen conformation. The approach used here involves the use of substrates that allow differences in conformation to be observed in a single image. Thus, distinct chemical regions need to be positioned side by side. Microcontact printing (μCP) allowed us to achieve this goal. Surfaces were printed with ODT and the remaining bare gold regions were back-filled via solution self-assembly of MHA.

Self-assembled monolayers (SAM) formed by solution self-assembly (SSA) have been thoroughly investigated (14, 15). Monolayers formed from longer alkyl chain thiols were described to be crystalline and ordered (14). They formed model surfaces, with stable and defined surface chemistry. Monolayers formed by this method result from transportation of thiol molecules to the surface

by solution diffusion in order for a covalent bond to form. In the case of microcontact printing, transferring thiols to the metal surface required physical contact of an "inked" polymer support to the metal surface. The question of whether monolayers formed by μCP are comparable to SSA has arisen and remains unsettled. In the first part of the Results and Discussions section of this chapter, monolayers formed by μCP and SSA will be compared by infrared reflectance absorbance spectroscopy (IRRAS). Numerous papers have appeared recently applying infrared spectroscopy (16), scanning probe methods (including friction force microscopy (16, 17) and scanning tunneling microscopy (18)), wettability (18), near edge x-ray absorption fine structure spectroscopy (NEXAFS) (19), and grazing angle x-ray diffraction (GIXD) (17) to compare the monolayer structures of μCP and SSA monolayers. In addition, the monolayers' ability to protect metal surfaces from chemical etchants (20, 21) can serve as an indicator of monolayer ordering and packing. These studies revealed that under certain stamping conditions, monolayers prepared by the two methods were similar. Conditions such as thiol concentration, method of inking, time of contact between stamp and surface, and alkyl chain lengths were determining factors for monolayer packing, domain size and distribution.

Experimental

Reagents and Materials: All solutions were prepared using water from a Nanopure (Barnstead, Dubuque, IA) purification system. Phosphate buffered saline (1 mM PBS, pH 7.4) was prepared with reagent grade 0.2 mM KH_2PO_4 and 0.8 mM Na_2HPO_4, NaCl (10 mM) and KCl (1 mM). 1 mM PBS was used to prepare protein solutions, and as the liquid medium for imaging and washing steps. Bovine fibrinogen (Fraction I, 95% clottable) and human fibrinogen (Fraction I) were obtained from Sigma (St. Louis, MO). Fibrinogen solution concentrations of 20 μg/mL were prepared. Goat antiserum to human fibrinogen (anti-HFG) and bovine IgG (bIgG) were purchased from ICN Biomedical (Aurora,

Ohio), diluted with PBS to achieve concentrations of 160 μg/mL. Human fibronectin (HFN) was purchased from ICN Biomedical (Ohio), chicken lysozyme (LYS) and bovine serum albumin (BSA)(fraction V, 99% protein) were obtained from Sigma (St. Louis, MO) and were prepared to concentrations of 20 μg/mL, 100 μg/mL, 1 mg/mL respectively. All proteins were used as received without further purification, and protein concentration was calculated from its measured weight. All protein solutions were freshly prepared just prior to each day of experiments. PBS and protein solutions were filtered with a 22 μm millex-GV, low-protein binding filter (Millipore, Bedford, MA) before they were used in scanning force microscopy (SFM).

Hexanethiol [$HS(CH_2)_5CH_3$] (HT), nonanethiol [$HS(CH_2)_8CH_3$] (NT), dodecanethiol [$HS(CH_2)_{11}CH_3$] (DDT), and octadecanethiol [$HS(CH_2)_{17}CH_3$] (ODT) were purchased from Aldrich (Milwaukee, WI) and used as received except for ODT, which was recrystallized twice from ethanol before use. Mercaptohexadecaneoic acid, $HS(CH_2)_{15}CO_2H$ (MHA) was a gift from Dr. Marc Porter (Ames Lab, Iowa State). Millimolar thiol solutions were prepared in punctilious ethanol (Quantum Chemical Co, Newark, NJ). Sylgard 184 poly(dimethyl)siloxane (PDMS) elastomer kit was purchased from Dow Corning (Mississauga, On) for preparation of the featureless polymeric stamp.

Substrates preparation and modification: Substrates for SFM experiments were prepared by sputter coating 40 nm of Au onto Ti primed (2 nm) silicon wafer or mica. Substrates for IRRAS consisted of 300 nm sputter Au films on Ti primed glass microscope slides. Patterned substrates were prepared by μCP following procedures developed by Whitesides' group (22-24). Numerous variations in procedure such as thiol concentration and stamping time (17, 19) have been used, however the overall principle behind μCP is illustrated in Figure 4.01. Typically, an elastomeric stamp was immersed in ethanolic ODT for 1 minute, effectively inking the stamp. The stamp was then removed, rinsed with ethanol and dried
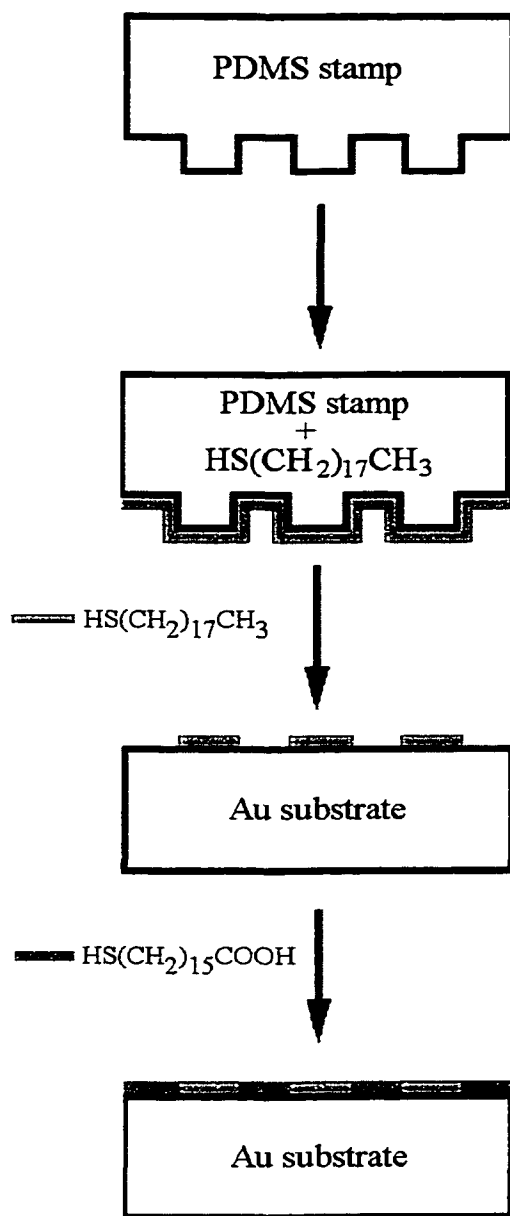
Figure 4.01. Procedures involved in microcontact printing (μCP) of alkylthiols onto Au covered substrates. This simple process allows for patterning of two distinct chemical regions, -CH₃ domains (hydrophobic, neutral) and –COOH domains (hydrophilic, partial negatively charged at pH > 5.5).

under stream of argon. Transfer of thiol molecules required bringing the stamp and Au substrate into contact for a period of time, ranging from 30–60 sec. The partially modified substrate was then immersed into an ethanolic MHA solution for 30 min. The patterned substrate was removed and rinsed with ethanol and dried with argon prior to protein adsorption study by SFM.

Two types of stamps were used. For protein adsorption, the stamps used contained patterned features with recessed regions (gift of Dr. Marc Porter). For infrared reflectance absorbance spectroscopy (IRRAS) comparing solution assembly versus microcontact printing of alkanethiolate monolayers, featureless stamp were used. The stamp was formed by pouring the Sylgard elastomer mixture (10 parts elastomer to 1 part hardener) into a mold with similar dimensions as the glass slides with a piece of silicon wafer as its bottom. This mixture was allowed to cure for 2 days at room temperature and subsequently peeled from the mold, rinse with ethanol and dried. The side facing the silicon was used as the stamping side. For IRRAS, the stamping conditions were similar to that described above. Each Au/Ti/glass substrate was prepared to contain only one component (*i.e.*, one functional group), either by solution assembly or microcontact printing. Au/Ti/glass were immersed in the appropriate thiol solution for 12-24 h for solution self-assembly.

SFM Imaging. SFM images were collected using a Nanoscope III (Digital Instruments, Santa Barbara, CA) equipped with a fluid cell for in situ operation. Triangular Si_3N_4 cantilevers (k~ 0.06 nN/nm) were used for all images. Real-time SFM experiment begins with acquiring images of the substrate in PBS. PBS flow was then started using the procedure previously described (5). Flow rates of 0.1 - 0.2 mL/min were used. Images were captured with PBS flowing through the fluid cell, then 20 μg/mL of BFG solution was added to a near empty syringe reservoir and allowed to flow into the fluid cell. Images presented here were captured continuously at a scan rate of 1 to 10.2 Hz. The scan speed did not affect the

friction contrast. For all other proteins (HFG, HFN, LYS, BSA and bIgG), images were collected at least 1 h after addition of the protein solution into the fluid cell. Before imaging the protein films, the cell was rinsed with PBS and images were obtained with PBS in the cell. Most images were collected at a normal force below 10 nN. Normal forces in the range of 6 to 12 nN were found to be optimal for observing frictional contrast on the protein films. For scratching experiments, a small area (2 - 5 μm^2) on each functional group was selected while imaging with minimal applied load. The load on the tip was gradually increased to 30 nN, and the tip was allowed to scan two full images at a scan rate of 10 Hz. Subsequently, the imaging force was reduced to below 10 nN, and an image was acquired after zooming out to a large scan size.

Infrared Reflectance Absorbance Spectroscopy (IRRAS): IRRAS spectra were collected with a Mattson Infinity FTIR spectrometer (Madison, WI) equipped with a low-noise MCT-A detector cooled with liquid N_2. A reflection accessory and a home built sample holder were housed in an external, auxiliary bench. Samples for IRRAS were Au/Ti/glass substrates modified with HT, NT, DDT and ODT via microcontact printing or solution preparation. Au/Ti/glass substrates with single component ODT or MHA monolayers that was previously incubated with HFN, LYS, BSA and bIgG were also obtained. Spectra were collected using 500 scans with 2 cm^{-1} resolution, with a grazing angle of 78°. Solution self-assembled deuterated octadecanethiol (gift of Prof. Marc Porter, Ames Lab, Iowa) on Au/Ti/glass was used as the background.

Results and Discussion

Equation 4 in Chapter I indicates that SFM measured friction as a function of the load applied by the tip, the contact area and surface chemistry. In this chapter, FFM will be used to map protein interfacial composition. Differences in friction contrast will be attributed to different adsorbed conformations. In order to do so, the contact area must be controlled. Substrates with adjacent regions of

varying chemistry prepared by μCP are to be utilized. The chain structure of the monolayer determines mechanical properties (contact area) and it is known that long chain monolayers prepared by SSA are crystalline and mechanically stable (14). The concern here is whether long chain monolayers printed under our conditions are also crystalline and mechanically stable (*i.e.*, are μCP monolayers comparable to SSA).

Characterization of monolayers prepared by μCP. Monolayers formed by SSA have been characterized by infrared spectroscopy, ellipsometry and electrochemical methods [14]. These studies indicated that these monolayers are crystalline and well-packed. Many characterization tools have been used to evaluate and compare monolayers formed by μCP and SSA (16-19). The findings suggest that under some stamping conditions, surfaces prepared by μCP were indistinguishable from SSA (18). In this chapter, crystallinity of the monolayer prepared by μCP and SSA formed under the conditions applied in our laboratory was evaluated by IRRAS and SFM.

A. *IRRAS of μCP and SSA monolayers*. As indicated earlier in this chapter, conditions used in the μCP process are important factors in controlling monolayer properties. Due to the number of protocols available for μCP, and because our method is slightly different from those used in other laboratories, I felt that it was necessary to determine how monolayers formed by μCP and SSA may differ. To determine whether the monolayers were similar, the positions and shapes of the C-H adsorption bands were monitored. These bands have shown to be sensitive to the packing density of alkyl chains. For example, infrared spectroscopy studies of single crystal polyethylene exhibited methylene C-H asymmetric stretch v_a (CH_2) of 2920 cm^{-1} (25, 26), indicative of a crystalline (highly-ordered) substrate. When polyethylene was heated to its melting point, the same stretching mode increased to 2928 cm^{-1}. Shifting of the v_a (CH_2) band to higher energies is indicative of

decreasing chain interactions, ordering and packing density. Porter, *et al.* (14) observed v_a (CH$_2$) of approximately 2918 cm^{-1} for long chain thiols, indicative of crystalline monolayer. Shorter chain thiols exhibited a blue shift in absorption energies from the case of ODT as a result of lower interchain interactions reflecting greater monolayer disorder.

Figure 4.02 display IRRAS spectra obtained in the C-H stretch region (2800 - 3000 cm^{-1}) for four alkanethiolate monolayers generated either from μCP or SSA. The precursor thiols differed only in the number of methylene units (n = 5, 8, 11, 17). Spectrum 1 of Figure 4.02A is representative of ODT (n = 17) chemisorbed by solution self-assembly on Au substrates. Assignments of the C-H stretching modes are shown in Figure 4.02A. The five diagnostic absorption bands for the C-H stretches are clearly evident; v_a (CH$_3$) due to the asymmetric stretch of the terminal methyl group, v_a (CH$_2$) from the asymmetric stretches of the methylene units; v_s (CH$_3$) from the symmetric stretch of the terminal methyl group, v_s (CH$_2$) for the symmetric stretches originating from the methylene units, and v_s (CH$_3$, FR) is the symmetric C-H stretching resulting Fermi resonance interactions. The absorbance frequencies of these bands are summarized in Table 4.1. μCP of ODT (spectrum 2, Figure 4.02A) produced monolayers that showed similar IR signatures to those produced by SSA. The peak positions are similar, indicating that μCP and SSA of long chain thiols (n = 17) produce similar monolayers. In both case, the position of the v_a (CH$_2$) adsorption bands appears at approximately 2919 cm^{-1}, indicating both type of monolayers were ordered and crystalline (14). The other four peaks were similar in shape, intensity and location, suggesting that ODT monolayers formed were method independent.

Spectra of Figure 4.02B were realized from substrates modified with dodecanethiol (DDT). All characteristic C-H stretches can be observed for both method of preparation. Their intensities are less than ODT due to the shorter
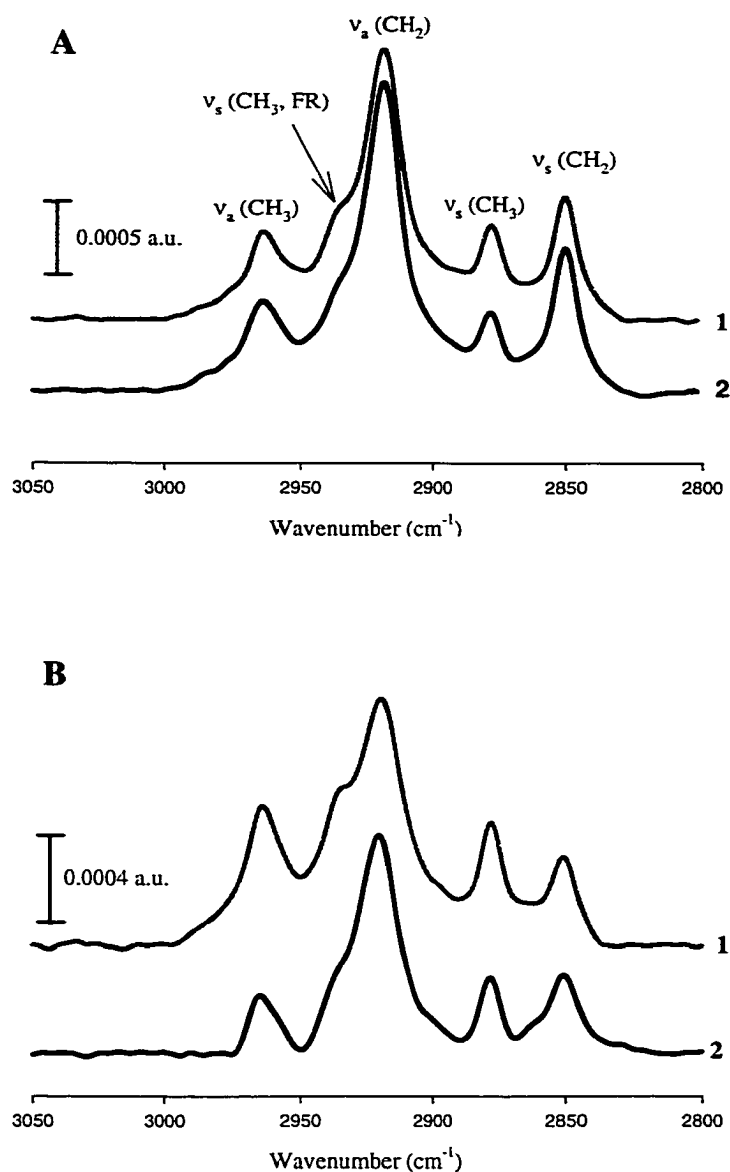
Figure 4.02. FTIR spectra in the C-H stretching region. These spectra were used to compare solution self-assembled (spectra 1) and microcontact printed (spectra 2) monolayers of alkanethiols [HS(CH₂)ₙCH₃] on Au/Ti/glass substrates. The effect of chain length was also evaluated (n = 5, 8, 11, and 17). (A) long chain system (n = 17) and (B) medium chain (n = 11). v_a (CH₃) and v_s(CH₃) are respectively due to assymetric and symmetric C-H stretches of the terminal CH₃ groups. v_a (CH₂) and v_s(CH₂) are respectively due to assymetric and symmetric C-H stretches of the CH₂ units that make up the alkyl chain. v_a (CH₃, FR) is due to Fermi resonance splitting of the an asymmetric CH₃ deformation mode.
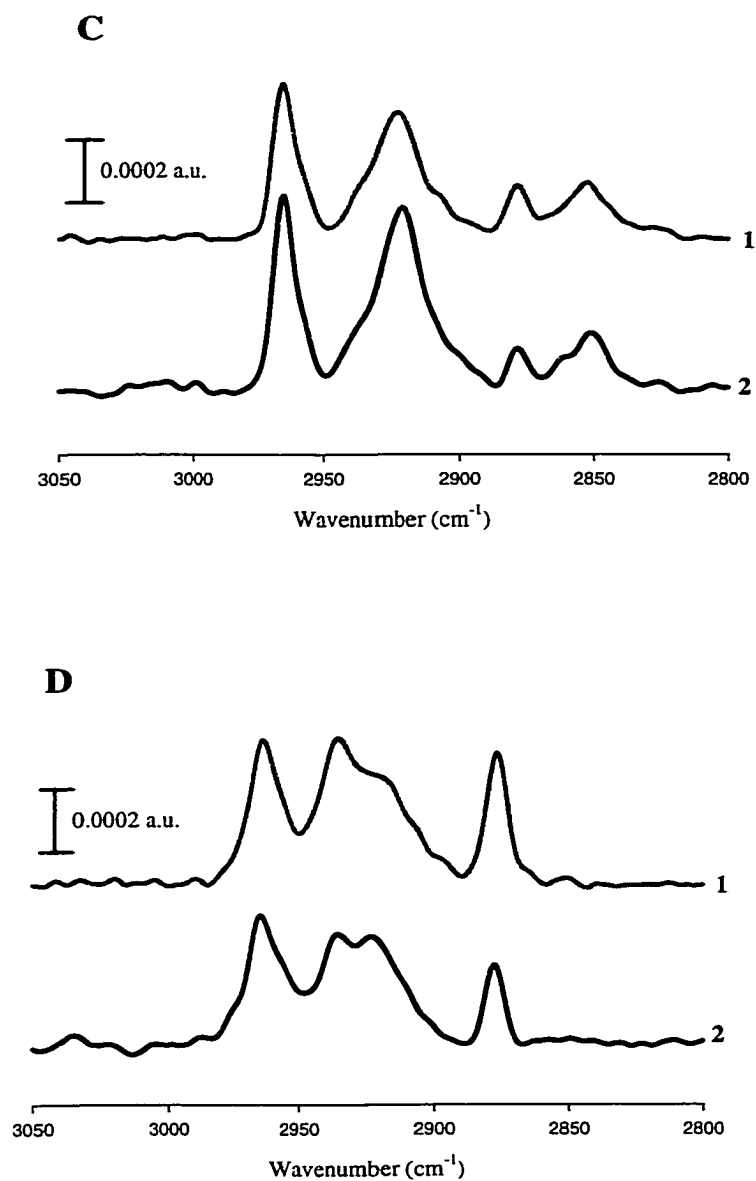
Figure 4.02. Continued. FTIR spectra in the C-H stretching region. (C) Medium chain length (n = 8). (D) Short chain system (n = 5). Spectra 1 were of monolayers formed from solution self-assembly and spectra 2 were of μCP monolayers.

length of the alkyl chain. Peak positions do not differ significantly between μCP (spectrum 2) and SSA (spectrum 1). The peak positions of v_a (CH_2) for μCP and SSA respectively were 2921 cm^{-1} and 2920 cm^{-1}. These frequencies indicate that the monolayers are ordered, however they are less ordered than for ODT. The shape of the four main adsorption peaks is similar to spectra shown in Figure 4.02A of a crystalline monolayer. Therefore, DDT monolayers prepared by either μCP or SSA were indistinguishable by IRRAS.

By decreasing the chain length (n), the peaks in the C-H stretching regions change drastically. For example, the shape of the v_a (CH_2) band becomes distorted and the peak position is shifted to higher energies (Figure 4.02 C, D and Table 4.1). Spectra in Figure 4.02C were obtained from nonanethiol (NT) modified Au substrates. Peak intensities have decreased from the cases of ODT and DDT, however, the peaks are in similar positions. Examination of v_a (CH_2) frequencies showed a small increase from the ODT case, revealing a trend typically observed when the number of methylene units in the alkyl chain is reduced. Reduction in the number of methylene units lowers the availability of van der Waals interactions, and leads to a more liquid-like monolayer (14). A higher v_a (CH_2) frequency is indicative of a disordered, liquid-like environment. Most importantly, the spectrum of NT monolayers formed by μCP (spectrum 2) and SSA (spectrum 1) showed little difference, and therefore the quality of the monolayers derived from NT are method independent.

Spectra of thiolate monolayers obtained from hexanethiol (HT) are shown in Figure 4.02D. Because HT contains only five methylene units, it has been shown to form less ordered monolayers from solution self-assembly (14). This observation suggested that monolayers formed by HT may exhibit greater dependency on the method of preparation. After comparing the spectra in Figure 4.02D, it was concluded that monolayers formed by μCP and SSA of HT were

n	Method	v_s (CH$_2$)	v_a (CH$_2$)	v_s (CH$_3$)	v_a (CH$_3$)	v_s (CH$_3$,FR)
5	C$_6$ (μCP)	N/A	2923	2877	2964	2935
	C$_6$ (SSA)	2852	2922	2878	2964	2935
8	C$_9$ (μCP)	2851	2921	2879	2966	2939
	C$_9$ (SSA)	2851	2922	2879	2966	2936
11	C$_{12}$ (μCP)	2851	2921	2878	2965	2934
	C$_{12}$ (SSA)	2850	2920	2878	2964	2934
17	C$_{18}$ (μCP)	2850	2919	2878	2964	2934
	C$_{18}$ (SSA)	2851	2919	2877	2963	2934

Table 4.1. C-H stretching frequencies of four alkanethiolate monolayers formed either by microcontact printing (μCP) or solution self-assembly (SSA). v_s and v_a represents the symmetric and asymmetric stretches respectively.

similar. Figure 4.02D shows evidence of some deviation in the peak shape of the middle two bands. However, their peak positions were essentially identical. v_a (CH$_2$) observed were higher than in the case of ODT, DDT, and NT monolayers (Table 4.1), indicative of a monolayer with greater disorder.

B. *SFM characterization of μCP monolayers.* To further investigate whether μCP monolayers are structurally different than monolayers formed by SSA, Au/Ti/Si substrates were stamped and back-filled with ODT, resulting in a surface with uniform chemistry but containing areas that were either formed by μCP or SSA. Figure 4.03 contains topographic and friction images of a μCP and SSA prepared ODT substrates. Figures 4.03A (topography, Z-scale = 10 nm) and 4.03B (friction, Z-scale = 2 V) are 90 × 90 μm^2 SFM images captured in air of a Au/Ti/Si substrate stamped with ODT only. The topographic image shows that the stamping process had transferred ODT onto the surface. The height difference between the top of the monolayer and the Au surface was approximately 1.5-2 nm and correlates with the expected length of an extended ODT molecule (1.8 - 2 nm) determine from calculations using van der Waals radii. The friction image showed that the ODT regions were lower in friction than the unmodified Au areas because the ODT regions are lower in surface free energy.

Figures 4.03A and 4.03B were obtained with the fluid cell o-ring in place to ensure subsequent images remained in the same area. This is important because in Figures 4.03C and D, ethanolic ODT solution was introduce in the fluid cell and allowed to equilibrate for 30 min before images were taken while the surfaces was maintain under the same thiol solution. Height and friction contrast in parts C and D of Figure 4.03 disappeared as a result of ODT back-filling. Figure 4.03D shows no friction contrast, which was expected because the stamped and back-filled regions are compositionally identical. Furthermore, the lack of frictional contrast also suggests that the tip-sample contact area remains constant between monolayer prepared by μCP and SSA of ODT.
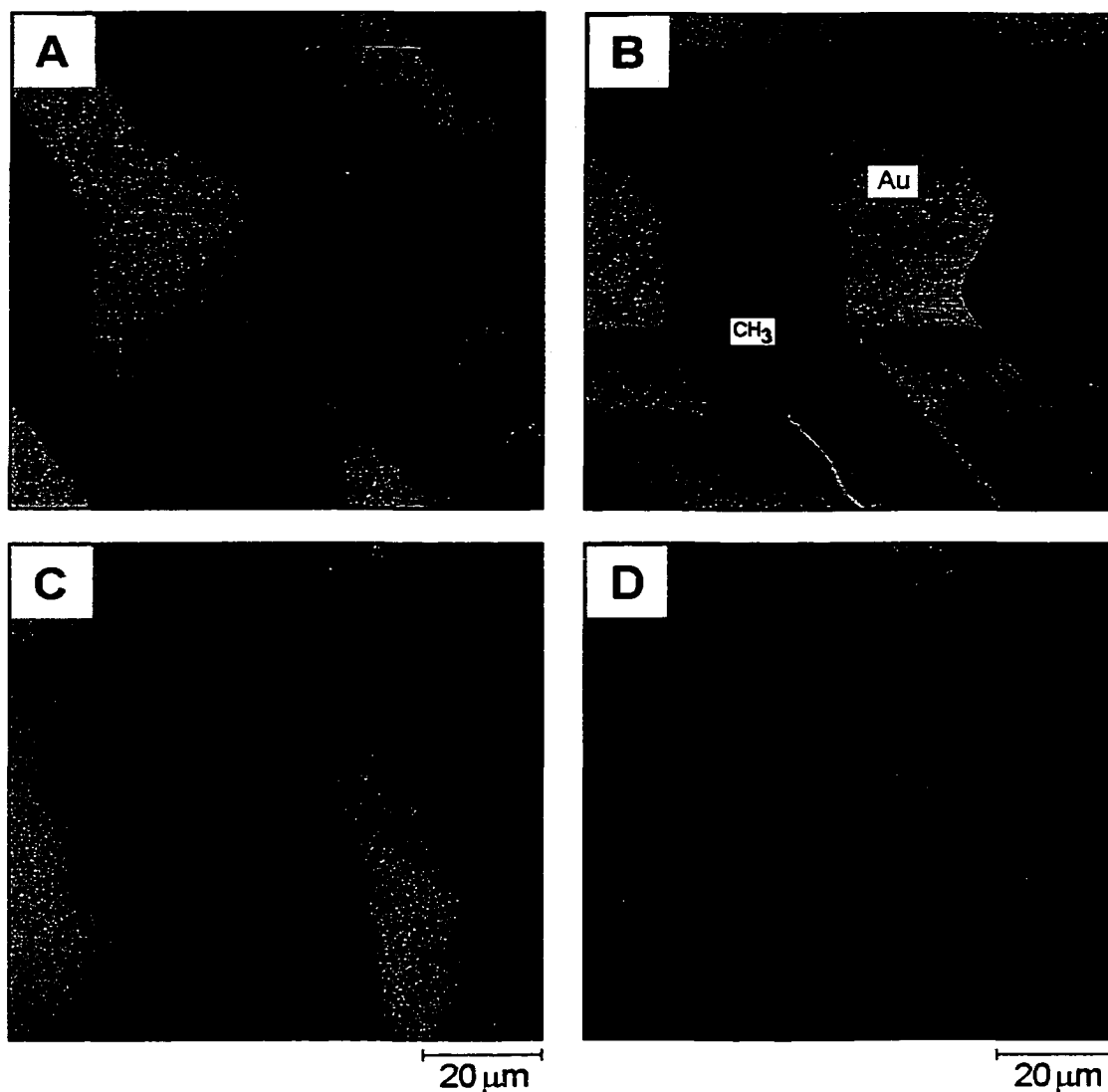
Figure 4.03. 90 × 90 μm^2 SFM images of ODT chemisorbed onto Au/Ti/Si substrates. (A) Topography (Z-scale = 10 nm) and (B) Friction (Z-scale = 2 V) were captured simultaneously after μCP with ODT with no back-filling. The substrate used to obtain images A and B was subsequently exposed to ethanolic ODT solution for 30 min and image captured while ODT solution was in the fluid cell. (C) Topography (Z-scale = 10 nm) and (D) Friction (Z-scale = 0.1 V) reveals that upon backfilling with ODT, both height and friction contrast disappeared.

SFM images, collected in ambient air, of a surface prepared by μCP ODT and back-filling with MHA are shown in Figure 4.04. Part A of Figure 4.04 is the topography of the resultant pattern images under ambient conditions, where only subtle differences in height are observed between the stamped region and the self-assembled region. However, the extreme difference in surface composition at the termini of these two monolayers result in the frictional variations observed in Figure 4.04B. The observed contrast results from the dependence of SFM-measured friction on the interfacial free energy between the tip and sample. In this case, and as has been reported previously, the interaction between the Si_3N_4 tip and the methyl groups is much less than that with the carboxylic acid groups, resulting in a lower observed friction (8).

One advantage of SFM for studies of protein adsorption is the versatility of both the solid-gas interface and the solid-liquid interface. This is important because the native environments of proteins are aqueous based, and therefore investigations under near physiological conditions are highly desirable. Figure 4.04C is a topographic image of a patterned monolayer, similar to that of Figure 4.04A, obtained while the substrate was under PBS solution. Notably, height contrasts were observed between the two chemical regions. The carboxylated regions appear to have higher topography (~ 0.5 nm) than the methyl regions. This phenomenon was often observed, but its origin has not been determined. Two possible explanations are currently being studied. First, it is possible that the heights difference is an artifact due to charge repulsion. At pH 7.4, both the Si_3N_4 probe tip, with an isoelectric point of 6.0 (27), and the carboxylate groups are partially deprotonated. Studies of surface confined carboxylic acid terminated thiolate SAMs reported pKa of ~5 (28, 29) to ~8 (30, 31). A recent report (31) cited that at pH 7, approximately 15% of carboxylic acid monolayers are ionized. The repulsive interaction between the tip and surface is interpreted as an increase in height. The second explanation is that the absorption of water and electrolyte
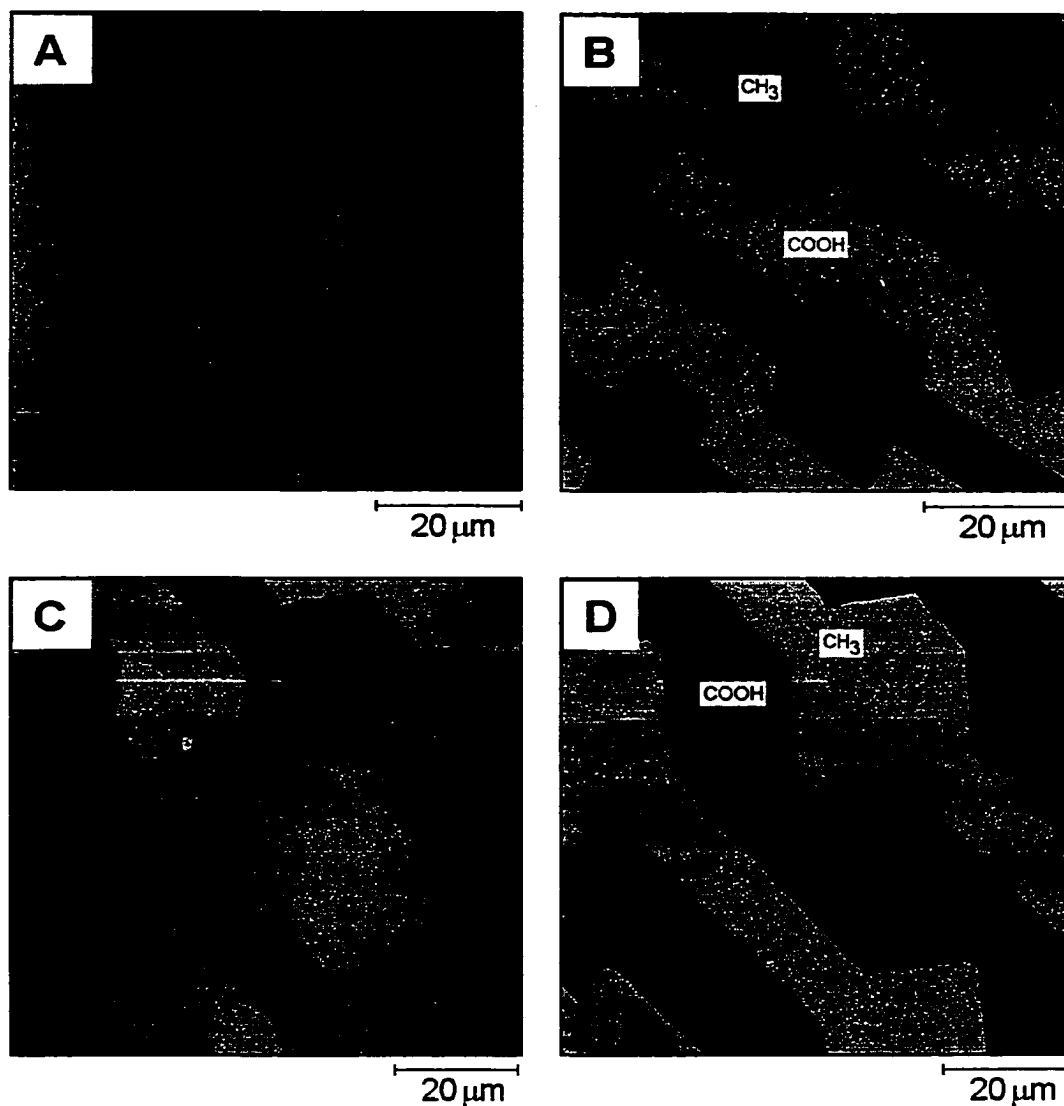
Figure 4.04. SFM images of patterned monolayers prepared by microcontact printing ODT and back-filling with MHA. A (topography, Z-scale = 5 nm) and B (friction, Z-scale = 0.5 V) are 70 × 70 μm^2 images collected simultaneously in ambient air. C (topography, Z-scale = 10 nm) and D (friction, Z-scale = 0.5 V) were collected simultaneously in PBS (pH = 7.2). Changing the imaging medium cause a reversal in friction between the two chemical domain.

ions from the PBS solution into the hydrophilic (MHA) portion of the monolayer, increasing the height of this region. A third explanation is the repulsion of carboxylic acid charges among themselves.

Figure 4.04D is the friction image observed in PBS, captured simultaneously with the topographic image in Figure 4.04C. The ODT regions reveal a higher friction with respect to the MHA regions. The frictional contrast in Figure 4.04D has inverted from that in Figure 4.04B, which was collected in air. In PBS, electrostatic repulsion reduces the interactions between these surfaces and lowering the observed friction at the carboxylate regions relative to the methyl region (10, 11). In addition, the energy for solvent re-organization is much greater for the hydrophobic regions and thus, the tip has greater adhesion with the ODT region when both are immersed in PBS (13). As a result, the tip experiences greater friction on the ODT areas relative to the MHA regions. Also, ordering of water molecules on the ODT regions and therefore the adlayer is more viscous that results in greater friction.

Under the stamping and SSA conditions used in our laboratory, IRRAS was not able to differentiate monolayers prepared by μCP and SSA. Others have reported similar finding using FTIR (16), STM and wettability (18), while others have found some differences. Near-edge X-ray absorption fine structure spectroscopy (NEXAFS) (17) and X-ray photoelectron spectroscopy (XPS) (32) found that monolayers formed by μCP had more defects than SSA. Thus, the issue of whether μCP can form similar monolayers to those of SSA is dependent upon numerous factors, and a simple answer to this question is not possible. From our work with IRRAS, monolayers formed via μCP and SSA were similar. Substrates that were μCP and SSA with ODT reveal no friction contrast. Thus, monolayers formed by both methods are structurally similar. To prepare the surface that contained adjacent areas of different chemistry, ODT was chosen as the preferred alkanethiol for stamping because others (20, 21) have shown that

longer chain thiols are able to form monolayers with greater packing density. MHA will be used as the back-filling constituent. With this protocol, I am confident that variations in SFM measured friction will be due to the protein surface chemistry and not a result of structural artifacts.

Fibrinogen Adsorption to Patterned Monolayers. Examination of each chemically tailored interface separately, as in Chapter III (Figures 3.05 and 3.06), provided excellent details regarding the packing of fibrinogen (both BFG and HFG) and gives some preliminary indications that fibrinogen adsorbs differently to methyl and carboxylate groups. However, it is believed that probing the adsorption of fibrinogen on each functional group simultaneously will allow us to better evaluate the ability of FFM to map functional group driven variations in protein adsorption.

Determining whether protein adsorbs at a surface from just SFM images is difficult with low-resolution imaging. Without IRRAS data from Chapter III, it is not possible to state with confidence that a protein film was present at the surface. High-resolution imaging is possible, however films that are highly compact will appear featureless, and may be confused with the substrate surface. An easy method that can be used to determine whether there are adsorbates on the surface is through scratching experiments using the SFM tip. This method involves purposely disrupting the film by imaging at high applied load. Scanning the tip in a raster pattern at higher normal forces will dislodge the adsorbates, plowing them together and often aligning them in a perpendicular direction to the fast scan axis. Areas where the film was scratched has a topographic signature because the tip had altered the film.

Figure 4.05 is a SFM image after a scratching experiment. Au/Ti/Si substrate was patterned with ODT and MHA by μCP, and incubated for 1 h with 20 μg/mL HFG. Figure 4.05 shows two areas that were scratched one on each functional group. Scratched areas showed higher topographic features than the
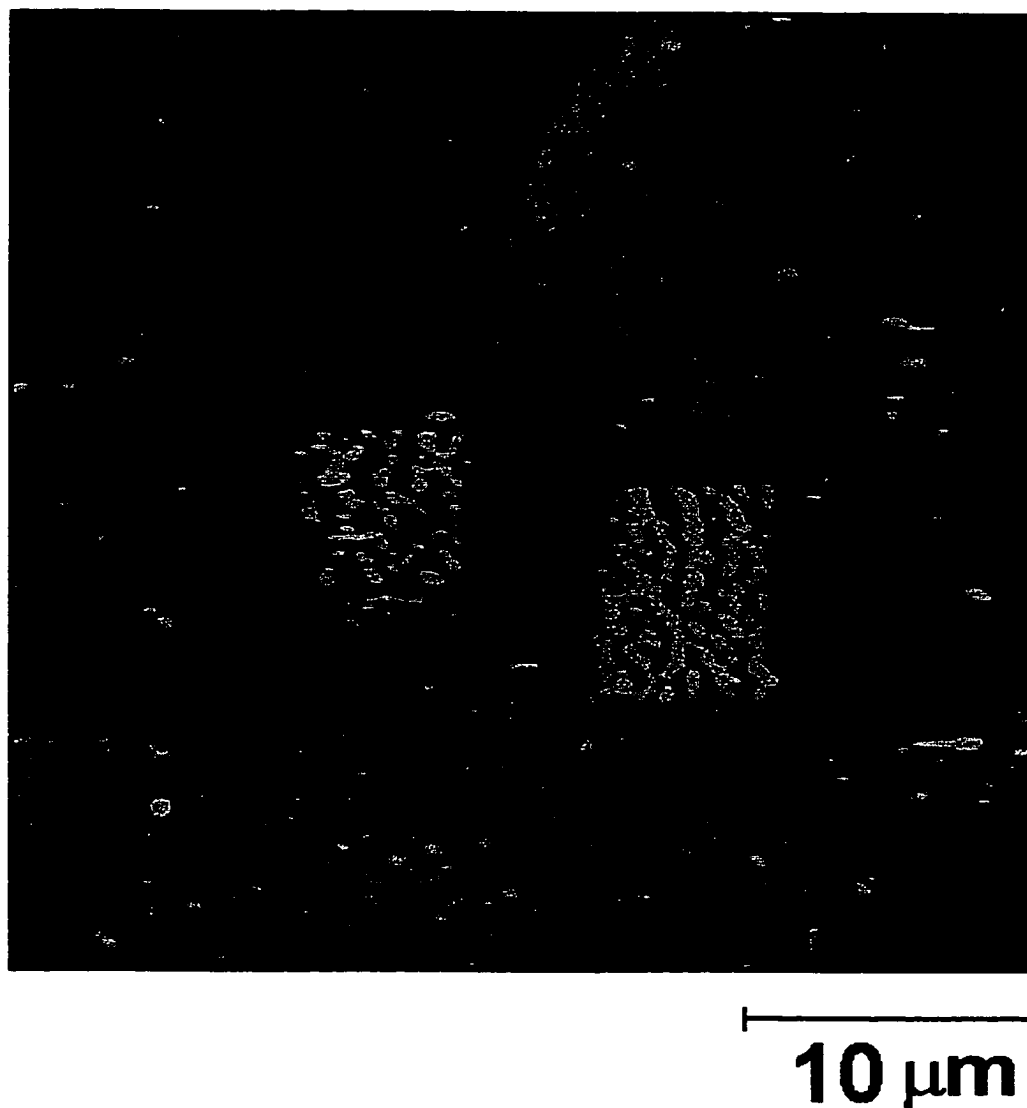
Figure 4.05. 35 × 35 µm² Topographic (Z-scale = 10 nm) SFM image obtained after 1 h incubation of 20 µg/mL HFG on ODT/MHA patterned surface. The squares in the center of each image were generated by applying a greater load to the probe tip (> 25 nN), and scanned repeatedly over the same area. The load was reduced (< 10 nN) to capture images at the larger scan size.

unperturbed surroundings. This is the result of protein aggregation caused by the tip plowing the protein molecules together and aligning them in strands that run perpendicular to the fast scan axis (left-right direction). It was much easier to detect the presence of protein after scratching was performed and it is clearly evident that HFG are adsorbed on both functional groups. The regions surrounding the scratched areas remained smooth in texture and thus adsorbate detection was improved after scratching. The utility of scratching experiments was demonstrated here as a method for protein detection, revealing that HFG adsorbed on ODT and MHA surfaces, as noted earlier by IRRAS (chapter III, Figure 3.09 and 3.10) and high resolution SFM studies (Figure 3.05 and 3.06).

A. *Mapping the conformation of adsorbed fibrinogen.* Due to the sensitivity of SFM measured friction to interfacial composition, frictional imaging should be sensitive to variations in protein adsorption at each functional group. Figure 4.06 contains 40 × 40 μm^2 friction force images detailing the real-time adsorption of BFG to a methyl/carboxylate-patterned surface. Figure 4.06A is the pattern imaged in flowing PBS. Note that the methyl-terminated regions are higher in friction. Parts B-D of Figure 4.06 show the effect of the adsorption of BFG on the frictional contrast of the pattern. As BFG adsorbs (Figure 4.06B and 4.06C), the contrast between the methyl and carboxylate groups diminishes. Following equilibration of the BFG layer with the surface, an inversion in contrast is observed in Figure 4.06D relative to that in Figure 4.06A.

Antibody binding results in Chapter III showed that human fibrinogen (HFG) adsorbs to methyl and carboxylate surfaces in different conformations. Figure 4.07 confirms that HFG adsorbed to a patterned substrate yields a contrast similar to BFG in Figure 4.06D. Figure 4.07 is a representative friction force image (55 × 55 μm^2) of HFG adsorbed from 20 $\mu g/mL$ after 1 h adsorption time. Frictional contrast from the HFG film is clearly evident and the direction of contrast is same as observed with BFG (Figure 4.06D). Based on the friction
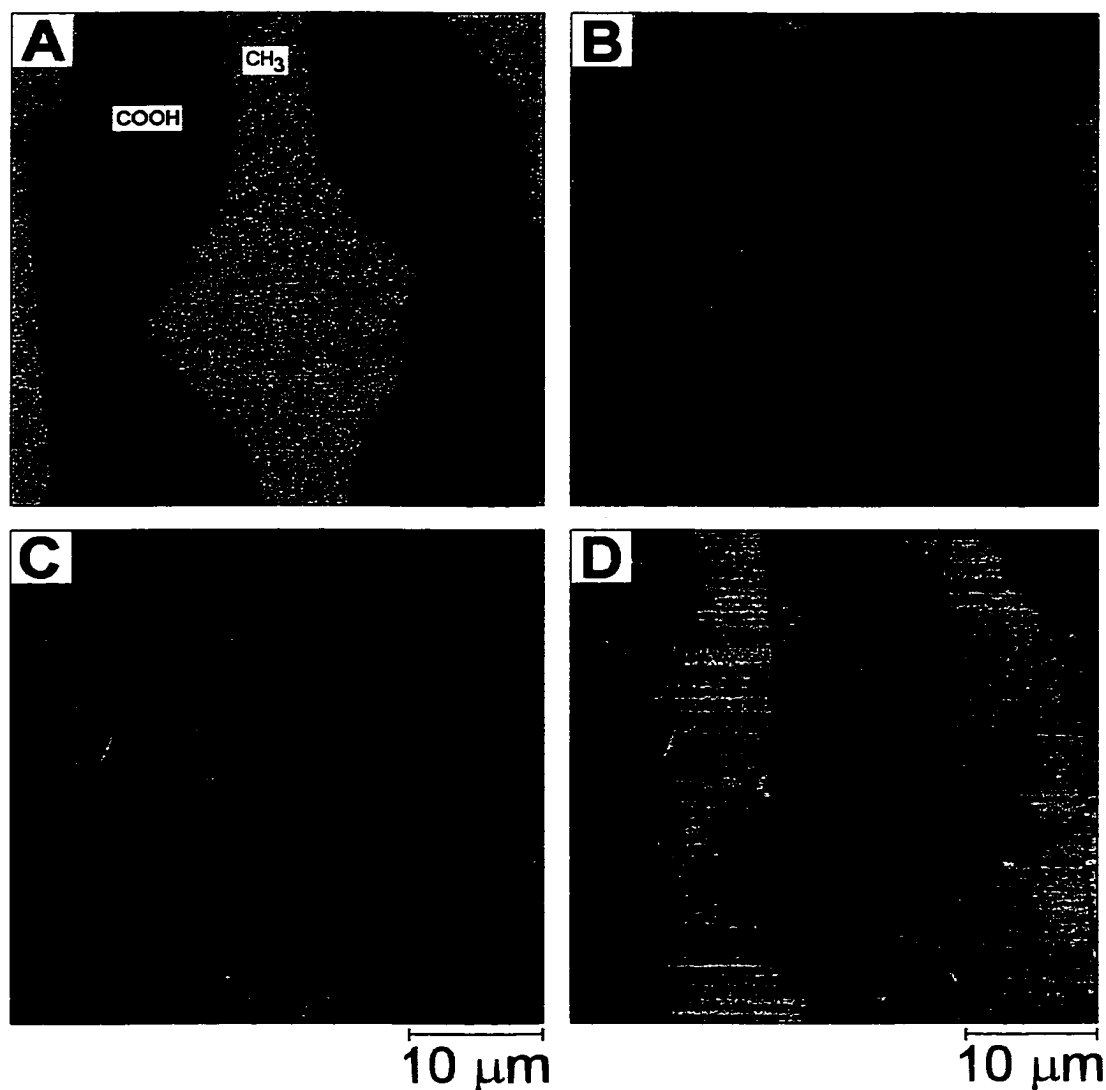
Figure 4.06. Friction images, 40 × 40 μm^2, depicting the real-time adsorption of BFG to a patterned monolayer. All images were collected under flowing solution. (A) Initial surface under flowing PBS. Methyl groups show higher contrast (Z-scale = 0.7 V), B (Z-scale = 0.7 V) and C (Z-scale = 0.4 V) during the adsorption of BFG; (D) completed BFG film (Z-scale = 0.3 V). Image D was collected 22 min after initial addition of BFG to the fluid cell.
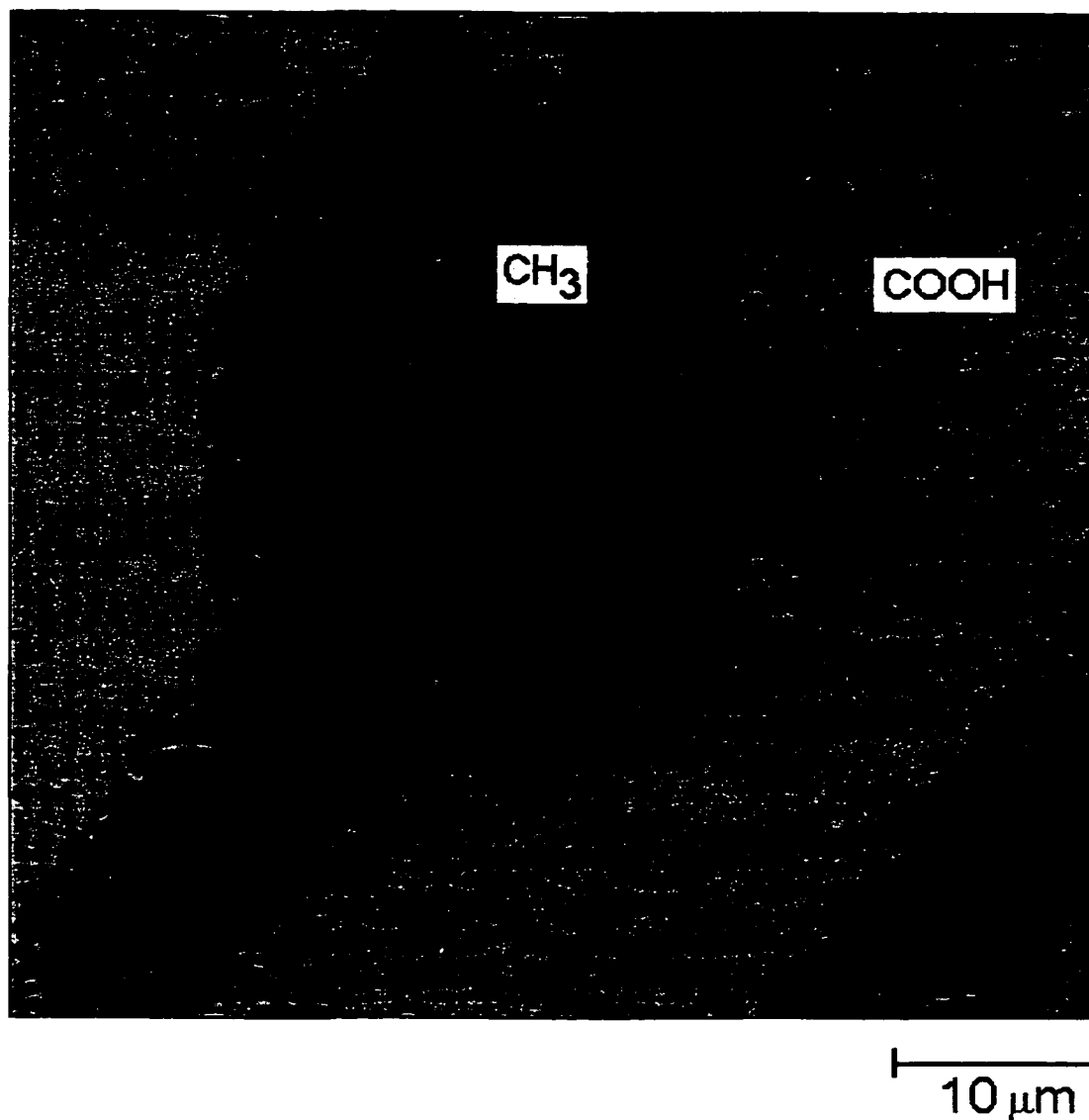
Figure 4.07. 55 × 55 μm² friction image of patterned Au surface (Z-scale = 0.5 V) after 1 h incubation with 20 μg/mL HFG solution. The underlying SAM was stamped with ODT and backfilled with MHA. Contrast of the protein film is due to the functional groups on the protein that are exposed at the interface. Frictional contrast is similar to that observed in the case of BFG (Figure 4.06D).

images in Figures 4.06 and 4.07, combined with the results in Chapter III, we believe that the friction contrast observed illustrates the ability of SFM to map protein conformation. This model is illustrated in Figure 4.08.

B. *Characterization of friction contrast.* Generation of friction contrast may be the result of imaging artifacts. These artifacts include the tip interacting directly with the monolayer underneath the protein film, the tip being influenced by long range electrostatic forces originating from the carboxylic acid groups, proteins adsorbed to the tip, or as a result of printing monolayers. These concerns are addressed below.

IRRAS and SFM experiments characterizing the adsorption of BFG to each functional group separately in Chapter III (Figures 3.03, 3.04, 3.05, and 3.06) showed that BFG adsorbs in similar quantities to both methyl and carboxylate functionalities. In addition, BFG films are complete, well packed, and stable to imaging on each group. Therefore, we believe the tip is not penetrating through the fibrinogen film and interacting directly with the monolayer underneath the protein film.

The contrast in Figure 4.06 and 4.07 may be governed by a long-range electrostatic interaction with the underlying monolayer. However, images collected in a buffer with higher salt concentration (~130 mM) where electrostatic interactions will be better shielded (28) show a similar contrast to Figure 4.06 and 4.07. Thus, the tip is not electrostatically interacting with the underlying monolayer.

Figure 4.08 suggests that proteins are likely to have adsorbed to the tip. We however believe that as long as the composition remains constant as the tip scans across both functional groups, friction contrast is the result of protein film properties not tip composition. An effort toward reducing protein adsorption on the tip was performed. Whitesides' group has shown that poly(ethylene) glycol terminated monolayers are resistant to protein adsorption (33). Tips were first
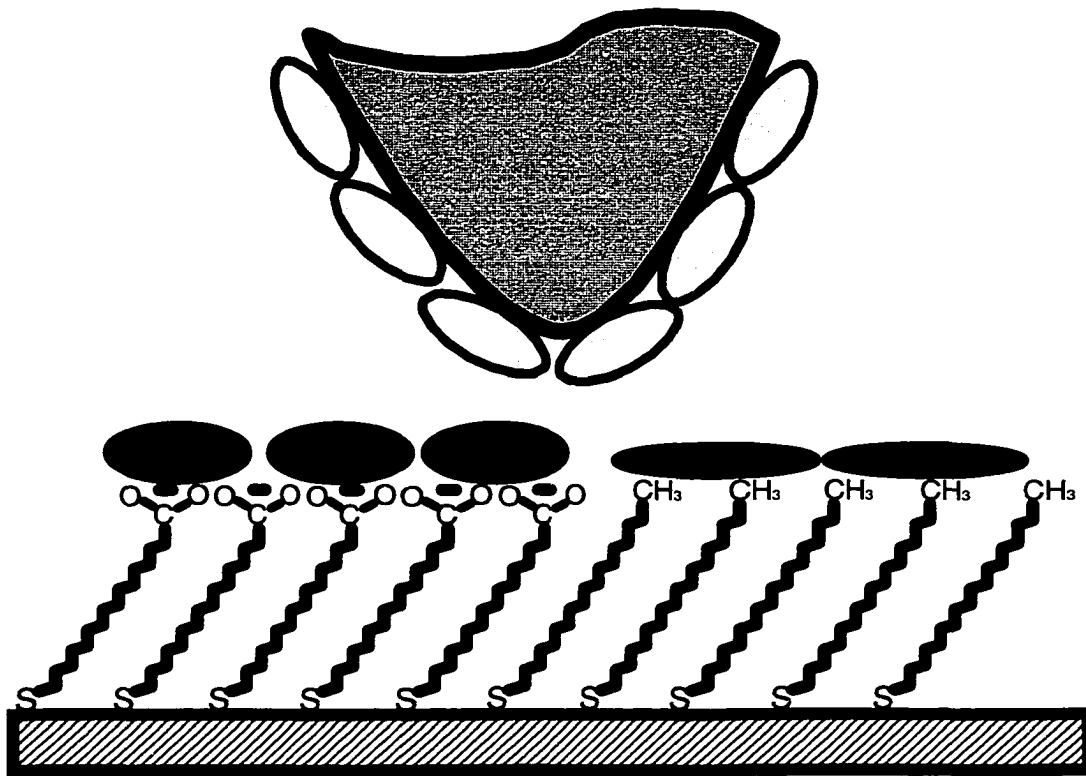
Figure 4.08. Illustration depicting possible effect of functional groups on protein adsorption. Note that the drawings are not to scale. Each functional group induces a distinct conformation, therefore a frictional contrast would be expected.

primed with Cr (2 nm) and sputtered with Au (50 nm). The gold coated tips were then immersed in 1 mM $HS(CH_2)_{11}(OCH_2CH_2)_3OCH_3$ overnight, rinsed with ethanol and used within an hour. Images with these "protein resistant" tips revealed similar contrast as Figures 4.06D and 4.07.

To further investigate the origin of the contrast in Figures 4.06 and 4.07, HFG was adsorbed to a substrate that was printed and back-filled with ODT. The same substrate shown in Figure 4.03 was utilized and the resultant images are shown in Figure 4.09. Parts A and B of Figure 4.09 were obtained in PBS buffer. Both topography (Figure 4.09A) and friction (Figure 4.09B) showed no contrast, similar to Figures 4.03C, D where ethanol was the imaging medium. Subsequent to acquiring the images shown in Figures 4.09A and B, 20 µg/mL HFG solution was added to the cell for 1 h. The fluid cell was rinsed with PBS. Images of the HFG film are shown in Figure 4.09C (topography) and D (friction). Some clustering of HFG molecules was observed on µCP and SSA ODT regions. However, friction contrast like that shown in Figures 4.06D and 4.07 was not observed. Figure 4.09D indicates that monolayers formed by µCP did not bias the frictional contrast and thus surface chemistry is the determining factor for SFM measured friction of adsorbed HFG films. This further cements our conclusion that frictional contrast observed in Figures 4.06D and 4.07 was due to the adsorbed state of the protein.

To summarize, friction force microscopy was demonstrated as a valuable tool for differentiating relative conformation of adsorbed fibrinogen. IRRAS and SPR antibody binding studies from Chapter III substantiate this claim. Possible causes of friction artifacts, such as the tip sensing the monolayer underneath the protein film and also variation in the monolayer structure as a result of the µCP process were addressed. The evidences we have to date suggest that the frictional contrast is due to the differences in the composition at the protein-liquid interface, which is determined by the conformation of the adsorbed protein (34, 35).
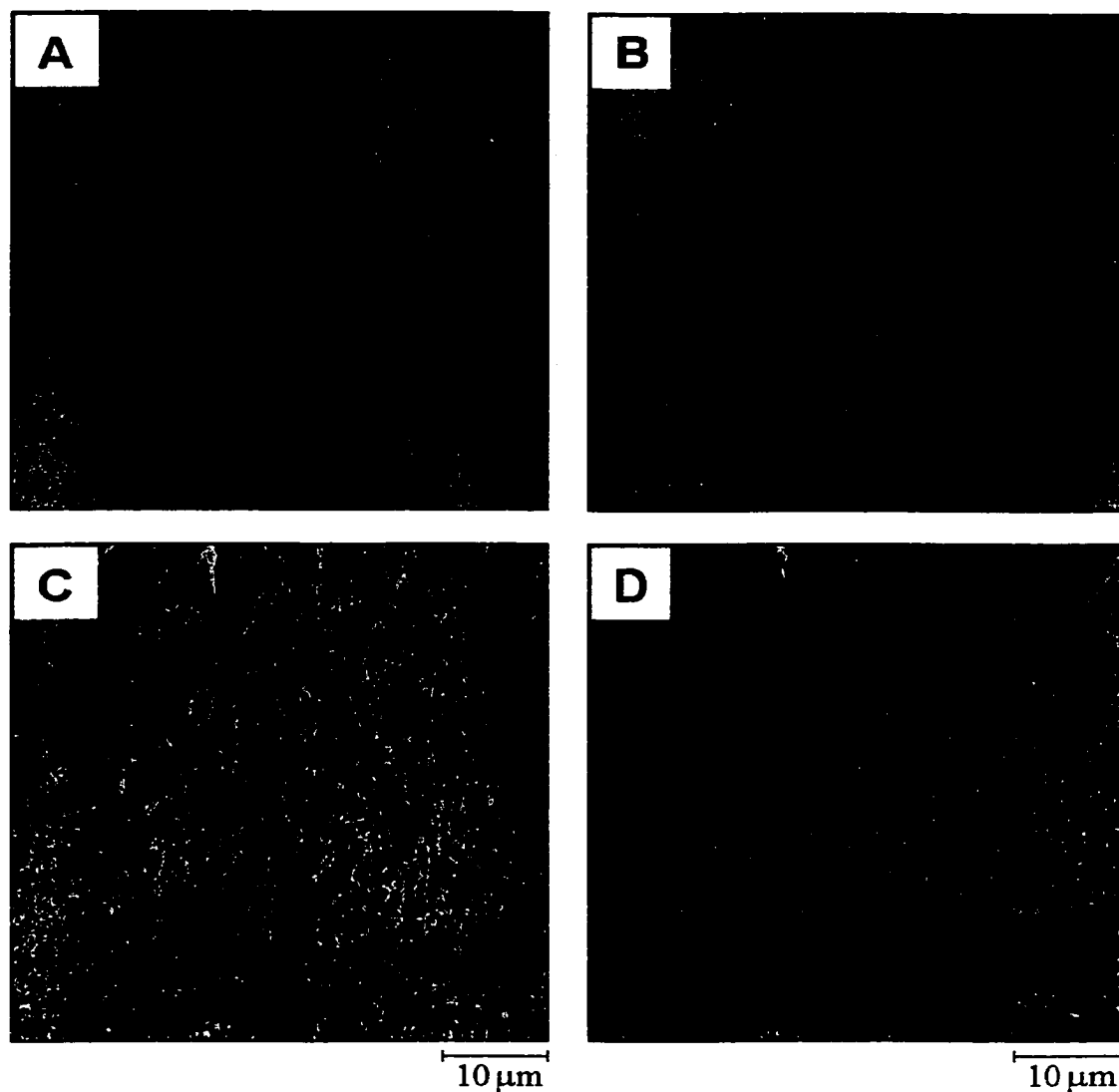
Figure 4.09. All images are 50 × 50 μm². The fluid cell was washed extensively with PBS after panels shown in Figure 4.03C and D were obtained. Parts A (topography, Z-scale = 10 nm) and B (friction, Z-scale = 0.5 V) were obtained in PBS. C (topography, Z-scale = 10 nm) and D (friction, Z-scale = 0.2 V) were obtained after 1 h incubation with 20 μg/mL of HFG.

Conformation or Orientation. Antibody binding studies to HFG adsorbed on ODT and MHA surfaces revealed that HFG adsorbed to MHA were binding greater amount of anti-HFG. There are concerns that the origin of this difference may not be the result of differences in conformation but rather orientation. However, in our opinion, discussion of protein orientation continues to be relevant only if proteins retain their solution conformations as they adsorbed to both ODT and MHA modified surfaces. If there are any evidence of different degree of denaturation at the two surfaces, then orientation is no longer relevant. Discussions would then focus on protein conformation.

Amide I absorption bands from IRRAS studies were shifted to higher energies upon adsorption to the surfaces (Figure 3.03, 3.04, 3.09, and 3.10), indicating protein denaturation upon adsorption. Furthermore, thickness measurement of adsorbed fibrinogen molecules revealed that at ODT surfaces fibrinogen were denaturing more (*i.e.*, lower thickness) than fibrinogen adsorbed on MHA surfaces (Figure 3.05 and 3.06). Combined with IRRAS studies, fibrinogen is denaturing differently at ODT and MHA surfaces, and therefore orientation is not an issue. Thus, differential antibody binding is most likely the result of differences in protein conformation.

FFM mapping of other proteins. To demonstrate further applicability of friction-SFM for detecting protein conformation, similar protocols were used to study various other proteins (HFN, BSA, LYS and bIgG). In the process, concerns regarding frictional bias (*i.e.*, protein on ODT regions always being lower in friction) would also be addressed. Proteins are composed of many amino acids covalently linked and folded into a three-dimensional structure. The properties at the surface of a folded protein are governed by structural factors such as the sequence and type of amino acid, and folding. Environmental factors such as the electrolyte in which the protein is dissolved and, in the case of adsorption, the extent of protein rearrangement to enhance interaction with the surface can

influence the properties at the protein's surface. Because of protein diversity, it may be expected that the direction of frictional contrast may also show variability. For example, a fibronectin film on ODT regions may not exhibit lower friction as observed in the case of fibrinogen. Some proteins will retain the same contrast as the monolayer in PBS (Figure 4.06A), while others will exhibit contrast that are "flipped", as exhibited by fibrinogen (Figure 4.06D and 4.08) and some proteins may exhibit no friction contrast at all.

IRRAS was used to assess whether these four proteins would adsorb onto ODT and MHA surfaces. Figure 4.10 shows IRRAS spectra in the amide region (1800 to 1300 cm^{-1}) of HFN (spectrum 1), BSA (spectrum 2), LYS (spectrum 3), and bIgG (spectrum 4) on ODT modified surfaces. The presence of the amide peaks in the spectra indicates that all four proteins adsorbed onto the hydrophobic surface. Their absorbance intensities and peak positions are also summarized in Figure 4.10. Analysis of amide II intensities reveals that HFN adsorbs in lower abundance than the other proteins and is in agreement with previous work (36). This report was based on fibronectin adsorption from plasma, and thus competition for adsorption sites from other proteins resulted in less fibronectin adsorption. In our case, only single protein solutions were used, and our observations of lower HFN absorbency indicate a sub-monolayer HFN film. Higher resolution SFM imaging to date has not found evidence of partial monolayer formation, and SFM scratching experiments did detect the presence of adsorbed protein. It is possible that HFN is completely unfolded and spread across the substrates as a very thin film.

Figure 4.11 are spectra of HFN, BSA, LYS and bIgG on MHA modified surfaces. Amide absorbance peaks were observed for all four proteins, indicating that each had adsorbed onto the carboxylated surfaces. The intensities and peak positions are summarized in Figure 4.11. Amide II intensities were used to compare the amount of adsorption by each protein on the two surface chemistries.
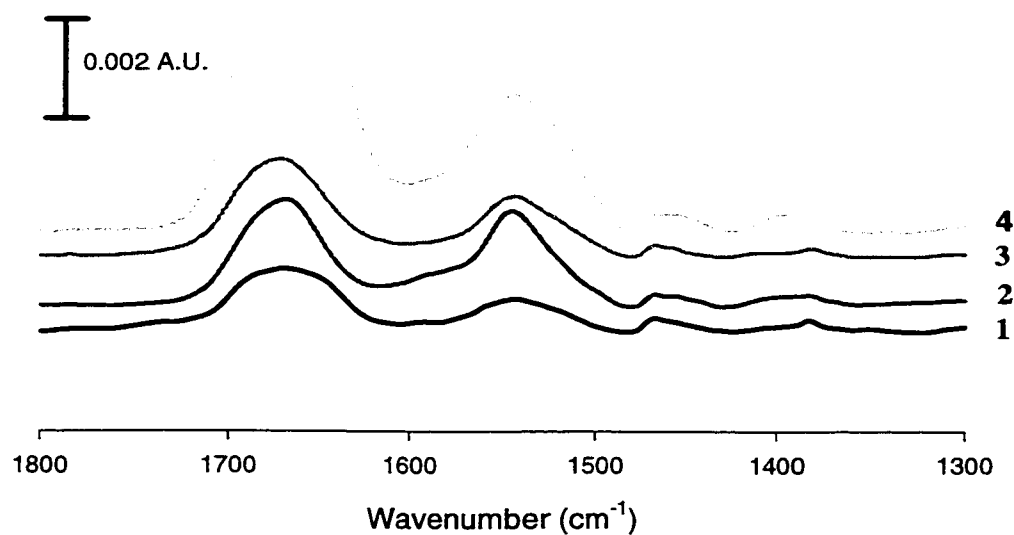
Protein	Amide I Absorbance (a.u.)	Amide II Absorbance (a.u.)	V_{aI} (cm^{-1})	V_{aII} (cm^{-1})
HFN	0.00125	0.00065	1671	1543
BSA	0.00213	0.00192	1670	1545
LYS	0.00194	0.00120	1672	1544
bIgG	0.00640	0.00278	1660	1543

Figure 4.10. Spectra obtained by IRRAS of human fibronectin (20 µg/mL HFN, spectrum 1), bovine albumin (1 mg/mL BSA, spectrum 2), chicken lysozyme (100 µg/mL LYS, spectrum 3) and bovine IgG (100 µg/mL bIgG, spectrum 4) after 1.5 - 2 h adsorption time on ODT modified Au/Ti/Si substrates. The presence of amide peaks in each spectrum indicate that all four proteins did adsorb to ODT surfaces. Absorbance and frequency of amide II and I bands are summarize in the table shown.
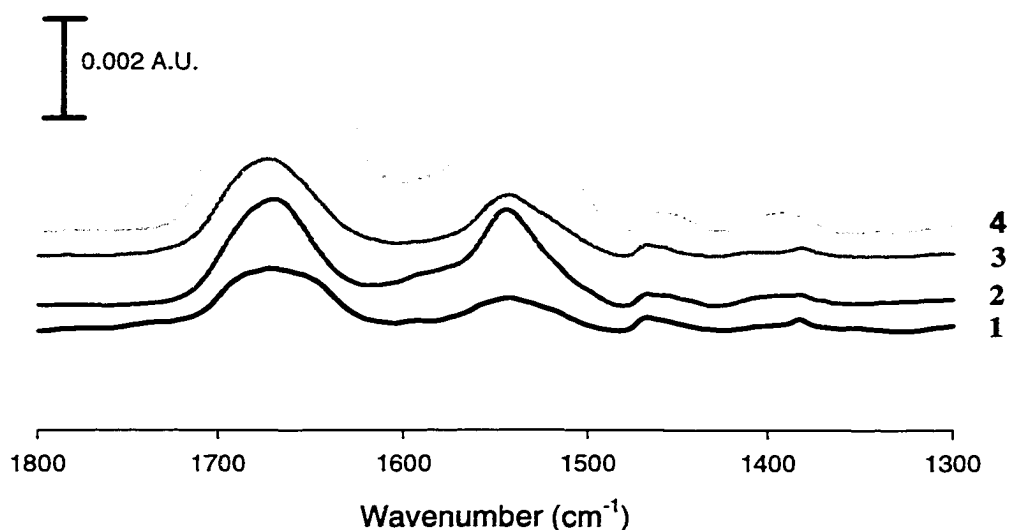
Protein	Amide I Absorbance (a.u.)	Amide II Absorbance (a.u.)	V_{aI} (cm^{-1})	V_{aII} (cm^{-1})
HFN	0.00148	0.00068	1675	1542
BSA	0.00264	0.00167	1671	1544
LYS	0.00433	0.00174	1674	1542
bIgG	0.00634	0.00258	1659	1542

Figure 4.11. Spectra obtained by IRRAS of human fibronectin (20 μg/mL HFN, spectrum 1), bovine albumin (1 mg/mL BSA, spectrum 2), chicken lysozyme (100 μg/mL LYS, spectrum 3) and bovine IgG (100 μg/mL bIgG, spectrum 4) after 1.5 - 2 h adsorption time on MHA modified Au/Ti/Si substrates. The presence of amide peaks in each spectrum indicated that all four proteins did adsorb to MHA surfaces. Absorbance and frequency of amide II and I bands are summarized in the table shown. The absorption frequency of amide bands for each protein on the two surface types did not differ significantly. IRRAS resolution used was 2 cm^{-1}.

With the exception of LYS, each protein adsorbed in similar amount at both surface chemistries. In the case of LYS, a larger deviation was observed, indicating LYS had greater affinity toward a carboxylate terminated surface. In all cases, protein concentrations were chosen to allow formation of a complete protein film after 1 h of incubation. Figure 4.10 and 4.11 indicate that all four proteins adsorb onto ODT and MHA surfaces, and therefore I proceeded to image their respective films on patterned monolayers.

Figure 4.12 are frictional SFM images of these four proteins on pattern ODT and MHA surfaces. Figure 4.12A is an 85 × 85 μm^2 image after incubation in 20 μg/mL HFN solution. HFN also exhibited a frictional contrast at a pattern of methyl and carboxylate functional groups. The contrast observed at the adsorbed HFN layer was identical to that of the initial contrast observed for the patterned monolayers imaged in PBS (Figure 4.06A). Recent studies on cell spreading and fibronectin adsorption on similar methyl and carboxylate terminated monolayers showed, via antibody binding, that fibronectin binds in a distinct conformation on each of these surface chemistry (37). Combining these findings with our results observed in Figure 4.12A provides compelling evidence that SFM-based friction is sensitive to adsorbed protein states.

Figure 4.12B is an image after incubation with 1 mg/mL BSA solution. The image indicates the presence of frictional contrast. However, in comparison to the contrast observed in Figure 4.06A of a patterned substrate without protein, an inversion of contrast was observed. Figure 4.12C was obtained after incubation with 100 μg/mL of lysozyme. The contrast direction remained similar to the SAM observed in Figure 4.06A. Thus, some proteins generate the same contrast, while others invert the frictional contrast relative to our baseline image of a patterned ODT/MHA surface with no protein incubation (Figure 4.06A). To date, we have discovered that HFG, BFG, and BSA invert the frictional contrast, while HFN and lysozyme maintain the same frictional contrast. The direction of contrast is not
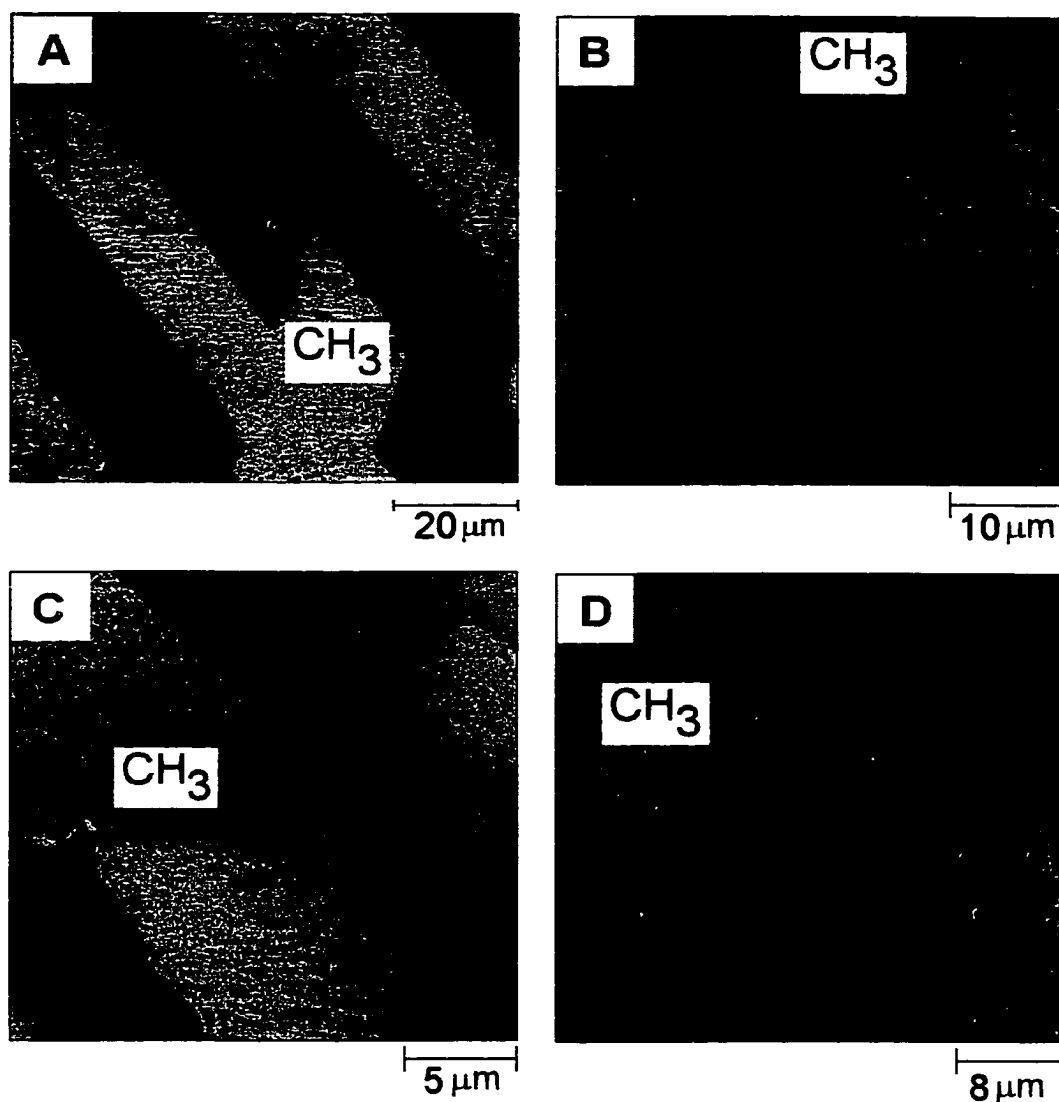
Figure 4.12. SFM friction images obtained in 1 mM PBS (10 mM NaCl, 1 mM KCl) after 1 h incubation of proteins on Au substrates patterned with ODT/MHA. (A) 20 µg/mL human fibronectin (HFN), 85 × 85 µm^2, Z - scale = 0.1 V. (B) 1 mg/mL bovine albumin (BSA), 45 × 45 µm^2, Z - scale = 0.1 V. (C) 100 µg/mL chicken lysozyme (LYS), 22 × 22 µm^2, Z - scale = 0.2 V. (D) 160 µg/mL bovine IgG, 38 × 38 µm^2, Z - scale = 0.1 V. Normal force applied in the range of 6-10 nN.

important, it is the fact that a contrast was observed at all which is the important finding.

In our ongoing work surveying other proteins, we have discovered that bIgG adsorbed onto ODT and MHA patterned surfaces shows indistinguishable frictional signal between the two chemical regions (Figure 4.12D). Based on our earlier supposition linking friction contrast to protein adsorbed states, it is believed that bIgG films on methyl and carboxylate surfaces display similar conformation, and thus FFM was not able to detect any small differences that may have been present. Because all three friction contrast scenarios were observed, friction contrast generated was not the result of an imaging artifact, but the result of composition of the protein film.

Antibody Binding Monitored by SFM. To develop SFM as an analytical tool or as an instrument for biomaterials research, Jones, *et al.* (38) recently demonstrated the application of topographic SFM for monitoring immunoassay systems on a microscopic scale. They observed an increase in height ~ 4 nm as rabbit IgG was linked to the surface, and a further increase of ~ 4 nm was observed as a result of anti-rabbit IgG binding. Their height measurements for IgG molecules were half the height expected from X-ray crystallography (39, 40). The ability to spatially examine antibody binding provided a means to determine the presence of an antigen on a surface, or protein adsorbed state induced by the surface. Topographic SFM was used here to detect antibody binding and provide additional evidence to support that HFG adsorbed on ODT and MHA surfaces were conformationally distinct.

Results from SFM antibody binding studies are contained in Figure 4.13. Figures 4.13A-C are 45 × 45 μm^2 topographic images of Au/Ti/Si substrates patterned with ODT and MHA. Figure 4.13A was obtained after 1 h exposure to 20 μg/mL of HFG and rinsed with PBS. HFG films formed on MHA regions were thicker than that on ODT regions. A cross section shows that the film on MHA is
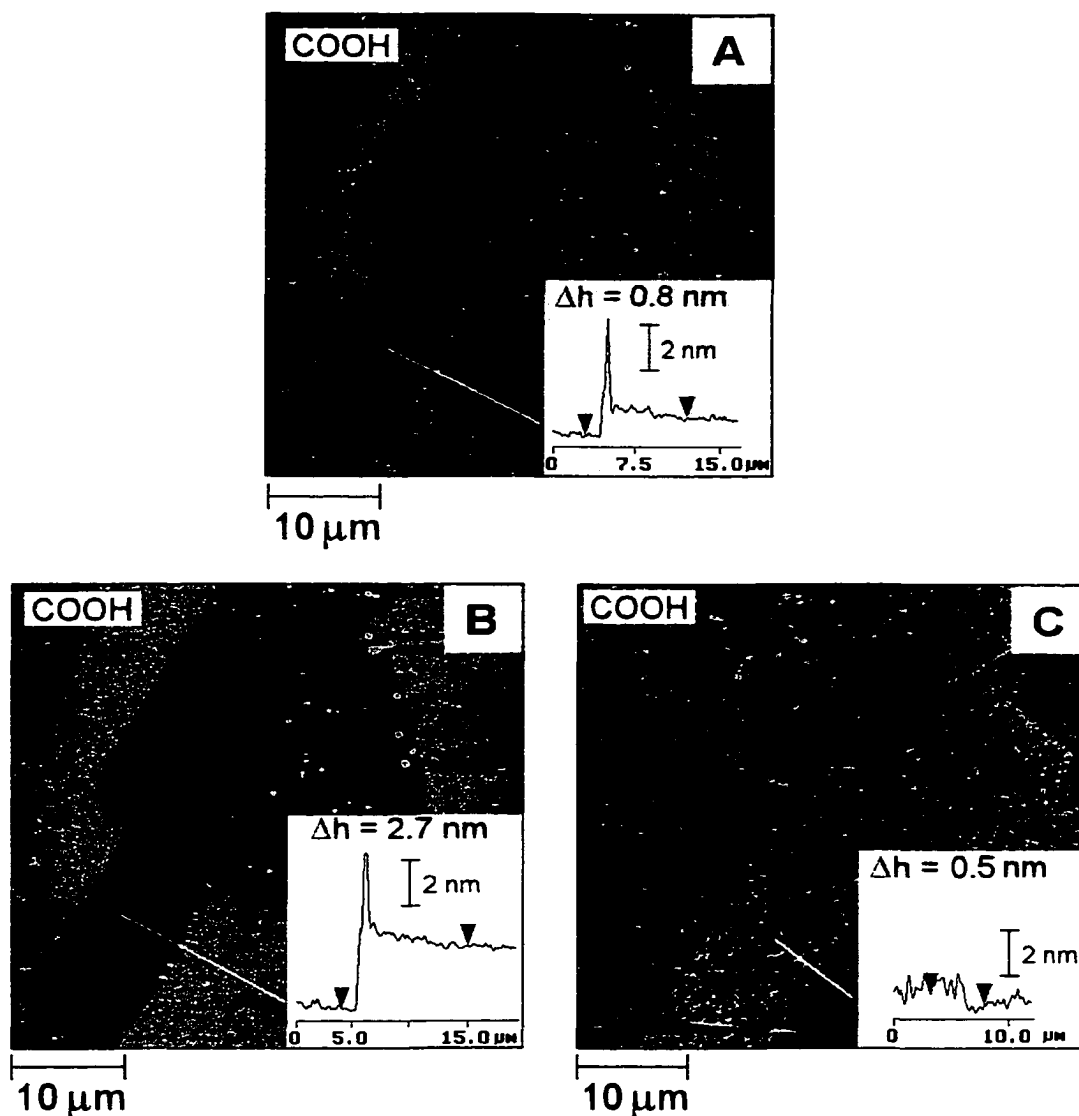
Figure 4.13. All topographic images, 45 × 45 μm². (A) 20 μg/mL HFG adsorbed on ODT and MHA patterned surfaces (Z - scale = 10 nm). (B) 160 μg/mL anti-HFG bound to adsorbed HFG in (A) (Z-scale = 10 nm). (C) 160 μg/mL bovine IgG binding to adsorbed HFG (Z -scale = 10 nm). The white line in each image indicates the location where the cross sectional profile was taken. After HFG adsorption, a small height difference was observed between the protein films adsorbed on ODT and MHA regions (~0.8 nm). This difference was elevated to ~2.7 nm after anti-HFG binding. Our control experiments showed no such increase because there is only nonspecific adsorption (panel C).

~ 0.8 nm thicker. Topography contrast reflects different degrees of denaturation. ODT surfaces induce greater protein unfolding driven by hydrophobic interactions. To the surface shown in Figure 4.13A, 160 µg/mL of anti-HFG was added to the fluid cell and allowed to interact for 2 h, after which PBS rinsing was performed and images were captured in PBS. A cross-section of the topography image showed that the relative height measurement between the two regions had increased to ~2.7 nm, an increase of approximately 2 nm above the same region measured in Figure 4.13A. The increase in topographic contrast was a result of differential binding. It was assumed that if antibody binding were similar on both surface functional groups, the height contrast would be expected to remain unchanged. Therefore, differential increase in film thickness provide further evidence that HFG molecules adsorbed at ODT and MHA are in a different conformational state. Bovine IgG (bIgG) was used to assess the degree of non-specific adsorption and served as a control study. Figure 4.13C is a topographic image of a patterned ODT and MHA surface after incubation with 20 µg/mL HFG (1 h) and 160 µg/mL of bIgG for 2 h. Topographic contrast between ODT and MHA regions obtained with bIgG does not reproduce Figure 4.13B. Thus, bIgG shows no preferential binding to HFG on either chemical region.

To provide one possible explanation of our SFM observations (Figure 4.13), Figure 4.14 shows an artistic representation depicting the possible molecular layering. Figure 4.14 was constructed also using the SPR results presented in Chapter III which concluded that on MHA surfaces, two molecules of anti-HFG are bound per molecule of HFG while on ODT surfaces the ratio is one to one. From Figure 4.13B, no height contrast matching the crystallographically measured dimensions of approximately 8-9 nm (41, 42) was observed. Jones, et al. (38) reported SFM height for IgG to be ~4 nm, but the increase observed in Figure 4.14B was only 2 nm. Coupled with SPR results, it is clear that anti-HFG binds to HFG adsorbed on both functional groups. It is believed that the epitopes
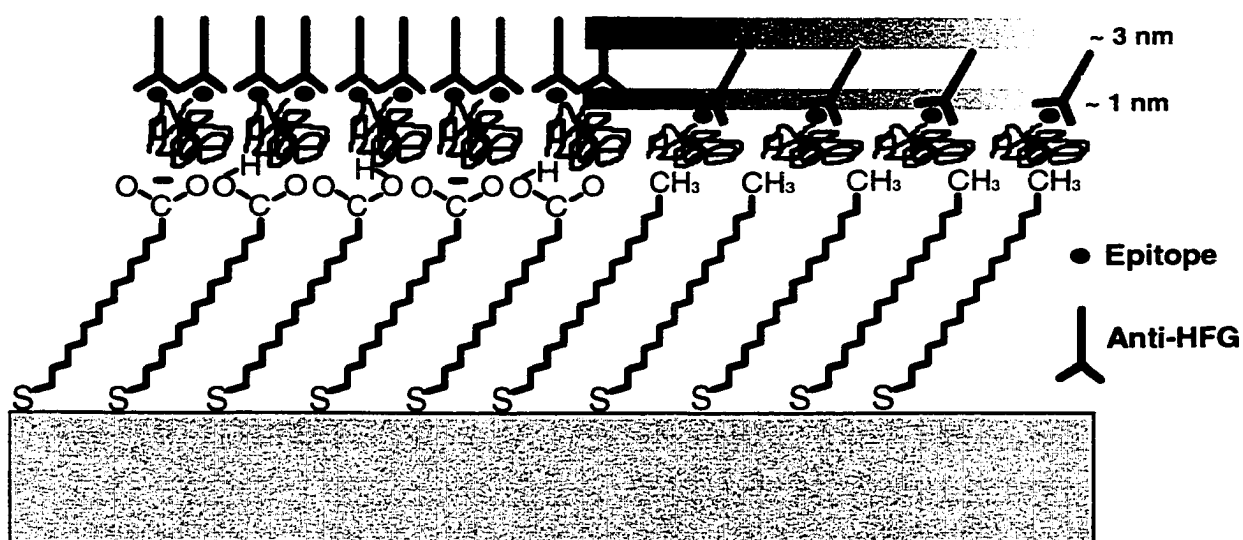
Figure 4.14. An illustration (not to scale) showing one possible explanation for the topographic contrasts observed in Figure 4.09. The number of epitopes and anti-HFG molecules bound per HFG molecule adsorbed on ODT and MHA regions are based upon SPR results discussed in chapter III. The thickness of the HFG film was ~1 nm higher on the MHA regions. Upon incubation of anti-HFG to the HFG films, the height contrast on the protein layers across the two chemical domains increased to ~3 nm. We hypothesize that the epitopes of HFG adsorbed on ODT regions were exposed to the liquid interface in a manner that allowed antibodies to bind at a tilted angle, resulting in an increase in height contrast between the two chemical regions. Variations of epitope location and availability suggest that the surface chemistry has influenced the adsorbed state of HFG.

found on HFG at the surface likely aligns the bound antibodies differently in the normal direction, producing topographic contrast. The ability to detect antibody by SFM may allow for detection of various antigens located in a sea of matrix. As an example, it may be possible to detect one specific protein component in a complex protein film at a localized level.

From antibody binding evidences that have been gathered using IRRAS, SPR and now SFM, it can be concluded with some confidence that the adsorbed state of HFG is influenced by chemical properties of the surface. The origin of friction contrast of HFG films adsorbed on ODT and MHA patterned substrates show that FFM was detecting relative differences in protein conformation (Figures 4.06D and 4.08). To our knowledge, results presented in this chapter have demonstrated for the first time the utility of friction force microscopy for detecting protein conformation.

Conclusions

This chapter demonstrated convincingly for the first time that SFM operated in the friction force mode could differentiate relative adsorbed fibrinogen conformation. Supporting this conclusion were SPR and IRRAS results from Chapter III, and SFM antibody binding analysis in this chapter. In the future, attaching an antibody to a probe tip may enhance frictional contrast (43). Protocols developed here for monitoring relative protein conformation was applied to other proteins that include fibronectin, albumin, lysozyme and IgG. Friction contrast observed after incubation of patterned surfaces with protein was not the result of various imaging artifacts such as the tip sensing the monolayer underneath the protein film or differences in SAM monolayer structure. In the next chapter, a continuing demonstration of the utility of SFM for probing biological films further promotes friction force microscopy's ability to compositionally map these films.

References

(1)   Fritz, M.; Radmacher, M.; Cleveland, J. P.; Allersma, M. W.; Stewart, R. J.; Gieselmann, R.; Janmey, P.; Schmidt, C. F.; Hansma, P. K. *Langmuir* **1995,** *11,* 3529-3535.

(2)   Marchant, R. E.; Barb, M. D.; Shainoff, J. R.; Eppel, S. J.; Wilson, D. L.; Siedlecki, C. A. *Thromb. Haemost.* **1997,** *77,* 1048-1051.

(3)   Rasmusson, J. R.; Erlandsson, R.; Salaneck, W. R.; Schott, M.; Clark, D. T.; Lundstrom, I. *Scanning Microsc.* **1994,** *8,* 481-490.

(4)   Baty, A. M.; leavitt, P. K.; Siedlecki, C. A.; Tyler, B. J.; Suci, P. A.; Marchant, R. E.; Geesey, G. G. *Langmuir* **1997,** *13,* 5702 - 5710.

(5)   Ta, T. C.; Sykes, M. T.; McDermott, M. T. *Langmuir* **1998,** *14,* 2435-2443.

(6)   Gunning, A. P.; Mackie, A. R.; Wilde, P. J.; Morris, V. *Langmuir* **1999,** *15,* 4636-4640.

(7)   Frisbie, C. D.; Rozsnyai, L. F.; Noy, A.; Wrighton, M. S.; Lieber, C. M. *Science* **1994,** *265,* 2071.

(8)   Green, J. B. D.; McDermott, M. T.; Porter, M. D.; Siperko, L. M. *J. Phys. Chem.* **1995,** *99,* 10960 - 10965.

(9)   van der Vegte, E. W.; Hadziioannou, G. *J. Phys. Chem. B* **1997,** *101,* 9563 - 9569.

(10)   van der Vegte, E. W.; Hadziioannou, G. *Langmuir* **1997,** *13,* 4357 - 4368.

(11)   Noy, A.; Vezenov, D. V.; Lieber, C. M. *Annu. Rev. Mater. Sci.* **1997,** *27,* 381 - 421.

(12)   Takano, H.; Kenseth, J. R.; Wong, S.-S.; O'Brien, J. C.; Porter, M. D. *Chem. Rev.* **1999,** *99,* 2845 - 2890.

(13)   Sinniah, S. K.; Steel, A. B.; Miller, C. J.; Reutt-Robey, J. E. *J. Am. Chem. Soc.* **1996,** *118,* 8925 - 8931.

(14)   Porter, M. D.; Bright, T. B.; Allara, D. L.; Chidsey, C. E. D. *J. Am. Chem. Soc.* **1987,** *109,* 3559-3568.

(15) Bain, C. D.; Troughton, E. B.; Tao, Y.-T.; Evall, J.; Whitesides, G. M.; Nuzzo, R. G. *J. Am. Chem. Soc.* **1989,** *111,* 321 - 335.

(16) Bar, G.; Rubin, S.; Parikh, A. N.; Swanson, B. I.; Sawodzinski, T. A. J.; Whangbo, M.-H. *Langmuir* **1997,** *13,* 373 - 377.

(17) Eberhardt, A. S.; Nyquist, R. M.; Parikh, A. N.; Zawodzinski, T.; Swanson, B. I. *Langmuir* **1999,** *15,* 1595 - 1598.

(18) Larsen, N. B.; Biebuyck, H.; Delamarche, E.; Michel, B. *J. am. Chem. Soc.* **1997,** *119,* 3017 - 3026.

(19) Fischer, D.; Marti, A.; Hahner, G. *J. Vac. Sci. Technol. A* **1997,** *15,* 2173 - 2180.

(20) Delamarche, E.; Schmid, H.; Bietsch, A.; B., L. N.; Rothuizen, H.; Michel, B.; Biebuyck, H. *J. Phys. Chem. B* **1998,** *102,* 3324 - 3334.

(21) Libioulle, L.; Bietsch, A.; Schmid, H.; Michel, B.; Delamarche, E. *Langmuir* **1999,** *15,* 300 - 304.

(22) Kumar, A.; Whitesides, G. M. *Appl. Phys. Lett.* **1993,** *63,* 2002.

(23) Kumar, A.; Biebuyck, H. A.; Whitesides, G. M. *Langmuir* **1994,** *10,* 1498 - 1511.

(24) Xia, Y.; Tien, J.; Qin, D.; Whitesides, G. M. *Langmuir* **1996,** *12,* 4033-4038.

(25) Synder, R. G.; Strauss, H. L.; Elliger, C. A. *J. Phys. Chem.* **1982,** *86,* 5145 - 5150.

(26) Synder, R. G.; Maroncelli, M.; Strauss, H. L.; Hallmark, V. M. *J. Phys. Chem.* **1986,** *90,* 5623 - 5630.

(27) Lin, X. Y.; Creuzet, F.; Arribart, H. *J. Phys. Chem.* **1993,** *97,* 7272 - 7276.

(28) Vezenov, D. V.; Noy, A.; Rozsnyai, L. F.; Lieber, C. M. *J. Am. Chem. Soc.* **1997,** *119,* 2006 - 2015.

(29)   Smalley, J. F.; Chalfant, K.; Feldberg, S. W.; Nhair, T. M.; Bowden, E. F.
        J. Phys. Chem. B **1999,** *103*, 1676-1685.

(30)   Hu, K.; Bard, A. J. *Langmuir* **1997,** *13*, 5114-5119.

(31)   Ashby, P. D.; Chen, L.; Lieber, C. M. *J. Am. Chem. Soc.* **2000,** *122*, 9467-9472.

(32)   Evans, S. D.; Cooper, S. D.; Johnson, S. R.; Flynn, T. M.; Ulman, A.
        Supramol. Sci. **1997,** *4*, 247 - 252.

(33)   Prime, K. L.; Whitesides, G. M. *J. Am. Chem. Soc.* **1993,** *115*, 10714 -
        10721.

(34)   Egodage, K. L.; S. de Silva, B.; Wilson, G. S. *J. Am. Chem. Soc.* **1997,** *119*,
        5295-5301.

(35)   Jemmerson, R.; Liu, J.; Hausauer, D.; Lam, K.-P.; Mondino, A.; Nelson, R.
        D. *Biochem.* **1999,** *38*, 3599-3609.

(36)   Tidwell, C. D.; Ertel, S. I.; Ratner, B. D. *Langmuir* **1997,** *13*, 3404-3413.

(37)   McClary, K. B.; Grainger, D. W.; Ugarova, T. *J. Biom. Mater. Res.* **2000,**
        50, 428-439.

(38)   Jones, V. W.; Kenseth, J. R.; Porter, M. D.; Mosher, C. L.; Hendersen, E.
        Anal. Chem. **1998,** *70*, 1233-1241.

(39)   Marquart, M.; Deisenhofer, J.; Huber, R.; Palm, W. *J. Mol. Biol.* **1980,** *141*,
        369-391.

(40)   Deisenhofer, J. *Biochemistry* **1981,** *20*, 2361-2370.

(41)   Silverton, E. W.; Navia, M. A.; Davies, D. R. *Proc. Natl. Acad. Sci.* **1977,**
        74, 5140-5144.

(42)   Browning-Kelley, M. E.; Wadu-Mesthrige, K.; Hari, V.; Liu, G. Y.
        Langmuir **1997,** *13*, 343-350.

(43)   Allen, S.; Chen, X.; Davies, J.; Davies, M. C.; Dawkes, A. C.; Edwards, J.
        C.; Roberts, C. J.; Sefton, J.; Tendler, S. J. B.; Williams, P. M. *Biochem.*
        1997, *36*, 7457-7463.

CHAPTER V

INVESTIGATION OF DUAL COMPONENT PROTEIN FILMS ON GRAPHITE WITH SCANNING FORCE MICROSCOPY*

Introduction

In Chapter III and IV, protocols were developed to utilize the compositional mapping ability of friction force microscopy (FFM) for analysis of protein films. Fibrinogen was shown to adsorb in similar coverage to methyl and carboxylate terminated surface single-component monolayers. Fibrinogen films formed on patterned surfaces containing segregated chemical regions showed frictional contrast and antibody binding studies by IRRAS and SPR revealed that the conformation of adsorbed fibrinogen was influenced by surface chemistry. Thus, it was proposed that the frictional contrast in FFM could be used to detect relative differences in adsorbed protein state. This chapter describes the novel application of FFM as a method to characterize biofilms.

Scanning force microscopy (SFM) has become a useful tool for the analysis of adsorbed protein layers. The two-dimensional structure of protein films (1-7) as well as the nature (8, 9) and conformation (10, 11) of the adsorbed proteins have been probed by SFM. Typically, films consisting of one type of protein are studied by SFM. However, when an artificial material contacts a biological fluid, the final structure of the resulting biofilm will depend on the interactions of many proteins with each other as well as with the surface (12). Although this situation is much more complex, the interest in phenomena such as the blood compatibility of medical devices has driven researchers to consider multi-protein solutions. In this chapter, I attempt to extend the use of FFM to the analysis of a dual component protein film.

When a multi-protein solution such as blood plasma interacts with a surface, the competition between different proteins for adsorption sites must be considered. The Vroman effect describes the situation in which maximal protein adsorption occurs at intermediate plasma concentration (13). This effect implies that some proteins are more effective at competing for adsorption sites and that proteins with greater surface activity, although present at lower concentrations, play a greater role in determining the composition of the film (14-16). Normally, proteins that are found in greater abundance will adsorb first (13) and over a period of time be displaced by proteins with greater surface affinity (14, 15, 17).

Typically, competitive adsorption is studied by radiolabeling one protein and examining its adsorption from a multiprotein solution (15, 18, 19). This method can be tedious and simultaneous monitoring of multiple proteins is difficult. Chromatographic separation techniques have also been used to study competitive adsorption without labeling (12, 16, 20). SFM is able to produce both topographic and compositional maps of protein films on a microscopic scale in solution (5, 8, 11, 21). It is believed that a technique that can examine multi-component protein films locally will be an important complement to those discussed above.

Differentiation between species in multi-component protein films is a major challenge in the development of SFM as a tool for the analysis of protein adsorption on biomaterials. Toward this end, this chapter will examine a dual component film formed from the sequential adsorption of bovine serum albumin (BSA) and bovine fibrinogen (BFG) on highly oriented pyrolytic graphite (HOPG). Friction force imaging will be used to produce maps based on film composition (22, 23) in an attempt to differentiate between the two proteins. While the surface of HOPG is atomically smooth and ideal for SFM studies, it also serves as a model surface for more complex carbon biomaterials, such as low-temperature isotropic carbon (LTIC), a common artificial heart-valve material

(24). The goal here is to study the interaction of BFG with a pre-adsorbed layer of BSA and observe any displacement as a result of competitive adsorption.

Experimental

Reagents and Materials: Fraction I, type IV bovine fibrinogen (BFG) with 95% clottable protein and fraction V (99%) bovine serum albumin (BSA) was obtained from Sigma (St. Louis, MO) and used as received. Distilled/deionized water from a Nanopure (Barnstead, Dubuque, IA) purification system was used in all solution preparations and solutions were allowed to equilibrate to room temperature before each experiment. Protein concentrations were determined based on dry weight and diluted using phosphate buffered saline (PBS), prepared with reagent grade 0.2 mM KH_2PO_4 and 0.8 mM Na_2HPO4, 1 mM KCl and 10 mM NaCl. All solutions that were to be introduced into the microscope were filtered with 0.22 μm millex-GV, low protein-binding filter (Millipore, Bedford, MA) just before use. HOPG was a gift from Dr. Arthur Moore (Advanced Ceramics). HOPG was cleaved with adhesive tape to create a fresh surface before each experiment.

SFM Imaging: SFM images were obtained with a Nanoscope III (Digital Instruments, Santa Barbara, CA) equipped with a fluid cell. Contact mode silicon nitride cantilevers (k $\approx$ 0.06 N/m) were used, and the imaging force was $\leq$ 10 nN. The procedure for calculating the normal applied force has appeared elsewhere (11). Software flattening and planefitting of images were used where necessary.

Each experiment began with the addition of PBS into the fluid cell, which was permitted to equilibrate for 30 minutes to reduce drift. Images were then collected in PBS to ensure the surface was clean and that a smooth area on the substrate was selected before protein was added. Filtered protein solutions were then added to the cell and allowed to adsorb to the surface for 30 minutes. Images were taken with the protein in the cell and after subsequent flushing with PBS. The images showed few noticeable differences with protein solution or PBS in the

cell. In some cases, BFG was added to a PBS stream flowing across the substrate and imaged in real-time (5). Protein adsorption to the tip did not diminish the quality of the images at the resolution of interest (micron scale).

Modified Tips: Regular Digital Instruments silicon nitride tips were coated with 2 nm of chromium and 10 nm of gold. Tips were modified in 1 mM solutions of either octadecanethiol, $HS(CH_2)_{17}CH_3$ (ODT) (Aldrich, Milwaukee, WI) or 16-mercaptohexadecanoic acid, $HS(CH_2)_{15}CO_2H$ (MHA) (Dr. Marc Porter, Ames Lab, Iowa State) in punctilious ethanol (Quantum Chemical Co, Newark, NJ).

Results and Discussion

In the following sections, the topography of single component films of bovine serum albumin (BSA) and bovine fibrinogen (BFG) on HOPG will be examined. The approach in evaluating dual component protein films involves the initial adsorption of a partial monolayer of BSA followed by the adsorption of BFG. This sequential adsorption experiment will allow us to probe the effect of a pre-adsorbed layer of protein on the adsorption of BFG and examine any displacement or co-adsorption processes.

Single component films. The structure of plasma protein films is known to depend on the concentration of the protein in bulk solution (25). Figure 5.01 is 5 × 5 μm^2 topographic SFM images, collected in pH 7.4 PBS, detailing the concentration-dependent morphology of BSA films on HOPG. Figure 5.01A corresponds to an HOPG substrate after 30 minutes exposure to 50 μg/mL BSA in PBS (pH 7.4). The film morphology is comprised of many apparently spherical aggregates that measure between 6 and 13 nm in height. These structures are stable to imaging at normal forces of <10 nN in PBS.

Figure 5.01A shows that from a 50 μg/mL solution of BSA, intermolecular disulfide crosslinked BSA (IDC-BSA) covers greater than 80% of the surface. Assuming that these aggregates form in solution and that less than 3% of BSA can exist in this form, it is interesting that IDC-BSA cover much more than 3% of the
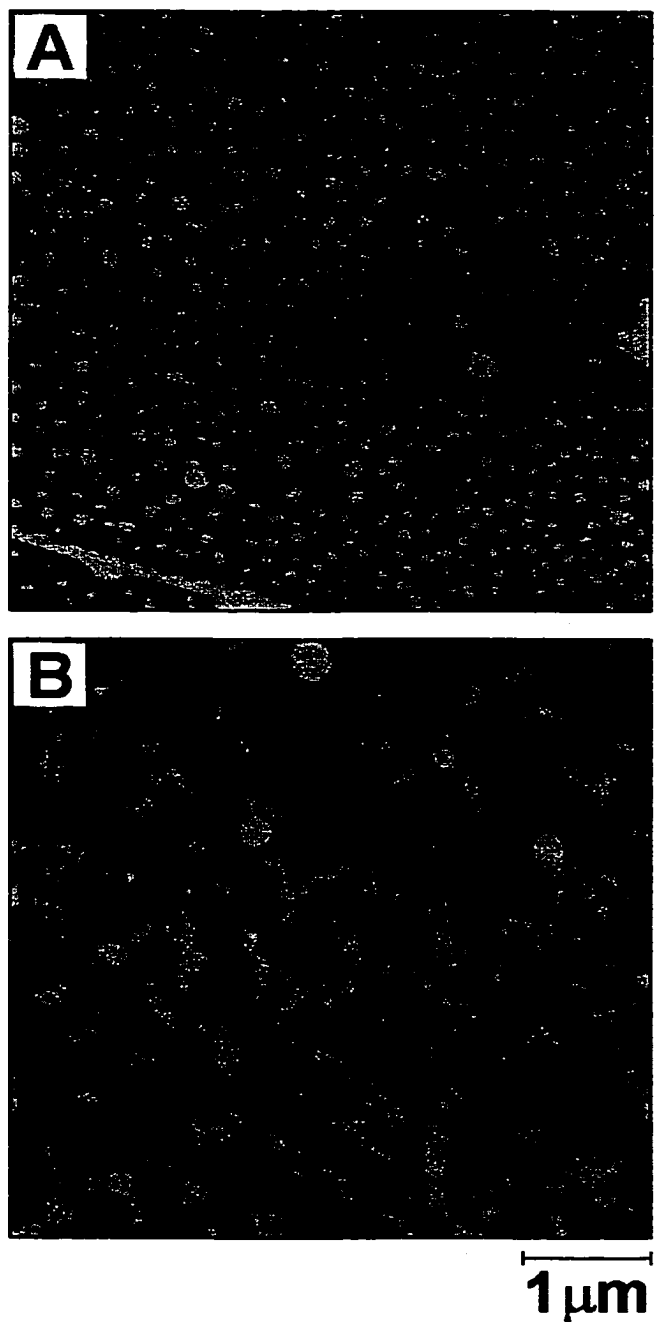
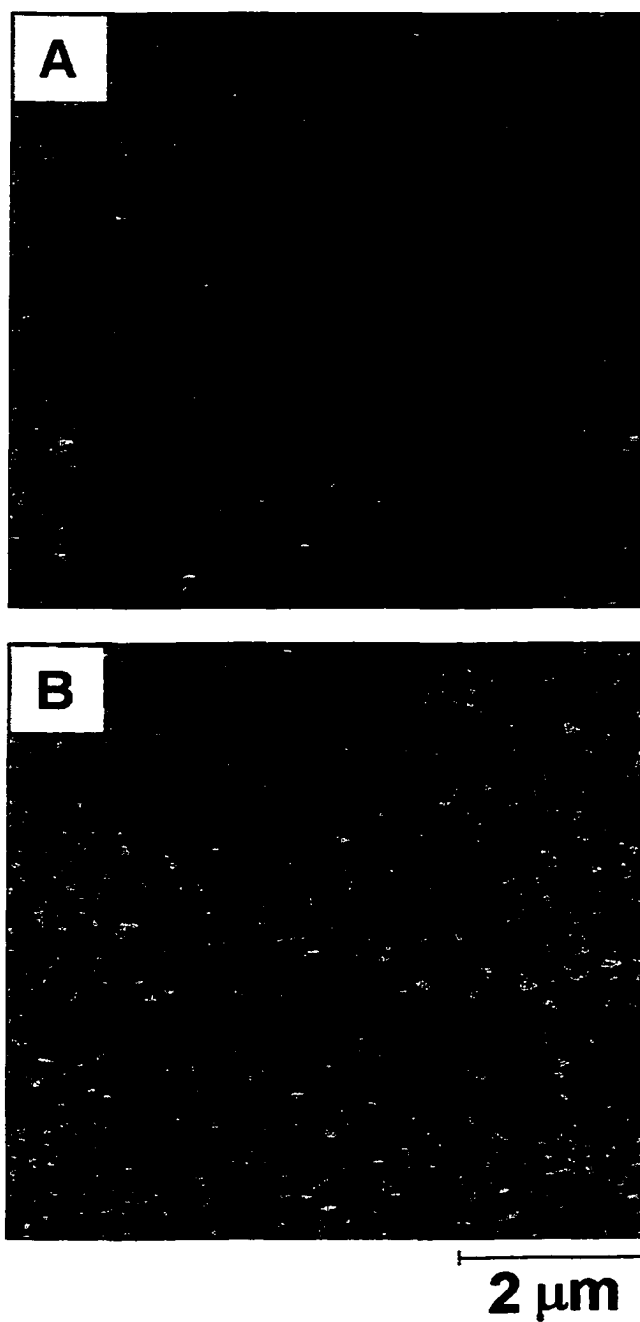**Figure 5.01.** 5 × 5 μm² topographic SFM images of bovine serum albumin (BSA) films on HOPG formed from 30 min. exposure of the substrate to A) 50 μg/mL BSA (Z-scale = 20 nm) and B) 10 μg/mL solutions of BSA (Z-scale = 5 nm). Images were collected in PBS containing the BSA.

surface. Aggregates of human albumin have also been observed on methyl-terminated hydrophobic monolayers (31). Furthermore, IDC-BSA adsorption was not observed on hydrophilic mica surfaces from 50 μg/mL solutions of BSA, as shown in the topographic image in Figure 5.02A. These observations imply that albumin aggregates preferentially adsorb on hydrophobic substrates. It is believed that the hydrophobic outer core of IDC-BSA gives it greater surface activity toward HOPG than individual BSA molecules. As a result, these aggregates can be found in high density as observed in Figure 5.01A.

Figure 5.01B depicts the topography of a film following 30 minutes adsorption from a 10 μg/mL solution of BSA. In this case, BSA coverage is incomplete and segregated domains separated by bare basal plane HOPG characterize the film topography. The observed partial layer suggests that a 10 μg/mL solution concentration is in a transition region of the adsorption isotherm before maximum surface coverage is achieved. The type of structure that is observed in Figure 5.01B is useful for measurement of film thickness. Analysis of cross-sectional profiles yields a height of 1.7 ± 0.3 nm for the domains in Figure 5.01B. This measurement is inconsistent with the crystallographic dimensions of BSA (8 nm × 3 nm) (32, 33). A plausible cause for this discrepancy is that the BSA molecules denature and spread upon adsorption to the hydrophobic graphite surface to increase the strength of the protein-surface interactions (34). A similar morphology was observed by Sheller, *et al.* for BSA films adsorbed to hydrophobic monolayers (31). These authors reported a thickness of ~3.6 nm with tapping mode SFM in ambient conditions. This suggests that operating in contact mode SFM may lead to compression of the BSA film resulting in low measured heights. In order to minimize tip perturbation of adsorbed protein layers, the images shown here were collected with low normal forces (<5 nN).

Other factors have been reported to account for inconsistent height measurements in SFM images of biomolecules. Marchant, *et al.* have stressed that

Figure 5.02. 7 × 7 μm² topographic (Z-scale = 5 nm) SFM images of protein films on mica substrates formed from 30 min. exposure to A) 50 μg/mL BSA and B) 1 mg/mL BFG. Images collected in PBS.

heights measured by SFM are affected by the degree of hydration of the protein (8). They reported a thickness for human fibrinogen (HFG) molecules much smaller than the dimensions obtained via electron microscopy. The lower height of the proteins imaged in solution was attributed to the spreading of globular domains facilitated by the existence of a hydration layer. In addition, work by Engel, *et al.* has shown that electrostatic interactions between the SFM tip and sample play a role in the height of biomolecules measured with SFM (35, 36). However, BSA and the SFM probe tip will both exhibit a nominal negative charge at pH 7.4. It was expected that repulsive electrostatic interactions unscreened by the electrolyte would result in a measured height greater than expected. This argument may not be necessary because any BSA adsorption to the tip may mask the tip's negative charge. Nevertheless, it is believed that the thickness measured in Figure 5.01B is due to the spreading of the domains of BSA upon adsorption. This spreading serves to increase interactions with the HOPG substrate.

A similar analysis on the topography of bovine fibrinogen (BFG) films adsorbed to HOPG was carried out. Figure 5.03 contains topographic images of BFG films adsorbed for 30 min. from solution concentrations of 50 and 10 μg/mL. Figure 5.03A shows that, similar to BSA, the topography of BFG films formed from 50 μg/mL is dominated by spherical aggregates. This is consistent with a previous report that involved the analysis of BFG adsorption in real-time (4). This work also showed that the regions between the aggregates in Figure 5.03A consist of a more uniform BFG layer that serves to embed the aggregates. The heights of the structures in Figure 5.03A range from 8 nm to 25 nm above the film. Aggregates in fibrinogen films have been observed previously with SEM (37) and have been designated as macromolecular protein complexes (MPC) (29). MPCs are likely formed via disulfide crosslinking similar to IDC-BSA. Solution concentrations >50 μg/mL were examined and an increase in density of adsorbed complexes was observed. This suggests that the aggregation takes place in
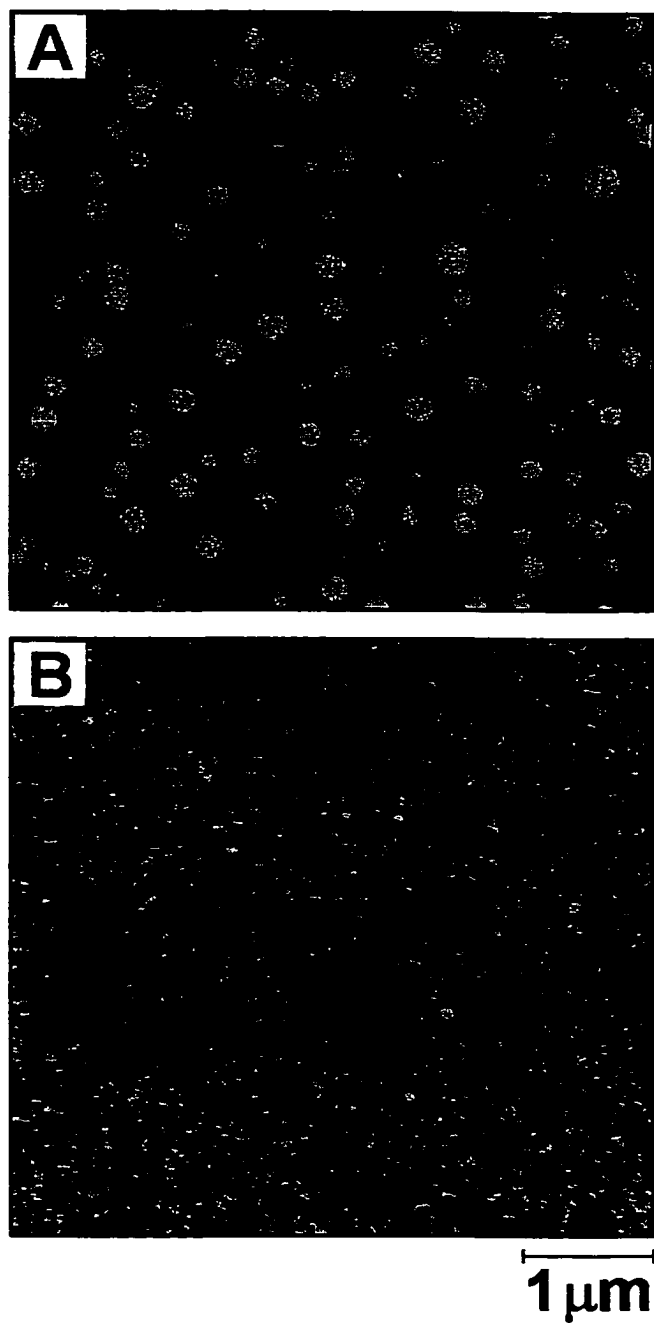
Figure 5.03. 5 × 5 μm² topographic SFM images of bovine fibrinogen (BFG) films on HOPG formed from 30 min. exposure of the substrate to A) 50 μg/mL BFG (Z-scale = 20 nm) and B) 10 μg/mL solutions of BFG (Z-scale = 5 nm). Images were collected in PBS containing the BSA.

solution and is consistent with the observed behavior of MPCs. Also, similarly to the case of BSA, MPC do not absorb on mica surfaces as indicated in Figure 5.02B.

Figure 5.03B shows that BFG forms a laterally uniform film, without aggregation, from lower concentrations (10 μg/mL). This observation is in contrast to the BSA case where a partial coverage results from 10 μg/mL solutions (Figure 5.01B). BFG is a highly surface active protein that adsorbs to most surfaces in high coverage regardless of its bulk concentration (19, 38). Feng and Andrade reported that, when adsorbed from solutions with similar bulk concentration, human fibrinogen adsorbs to LTIC at 2.5 times higher coverage than human albumin (16). The adsorption isotherm for fibrinogen on polystyrene begins to plateau at solution concentrations of 10 μg/mL (39). SFM images are consistent with these observations.

Sequential Adsorption of BSA and BFG. In Chapter IV, SFM operated in the friction force mode was demonstrated to be sensitive to the state of non-specifically adsorbed protein (11). Based on that conclusion, it was believed that frictional contrast could be used to differentiate two different adsorbed proteins. Thus, the goal is to use friction imaging to monitor processes that occur when a protein in solution interacts with a surface containing a pre-adsorbed layer of a different protein. A previous study suggests that fibrinogen will adsorb on top of and inside any voids in a pre-adsorbed albumin layer (16). From the analysis of single component films described above, BSA was pre-adsorbed from 10 μg/mL solutions. The unique morphology of BSA films formed under these conditions (Figure 5.01B) will allow us to probe co-adsorption and/or displacement by BFG in solution.

Images obtained after exposure of HOPG to 10 μg/mL BSA are shown in parts A and B of Figure 5.04. Similar to Figure 5.01B, the topography in Figure 5.04A is characterized by domains of adsorbed albumin separated by regions of
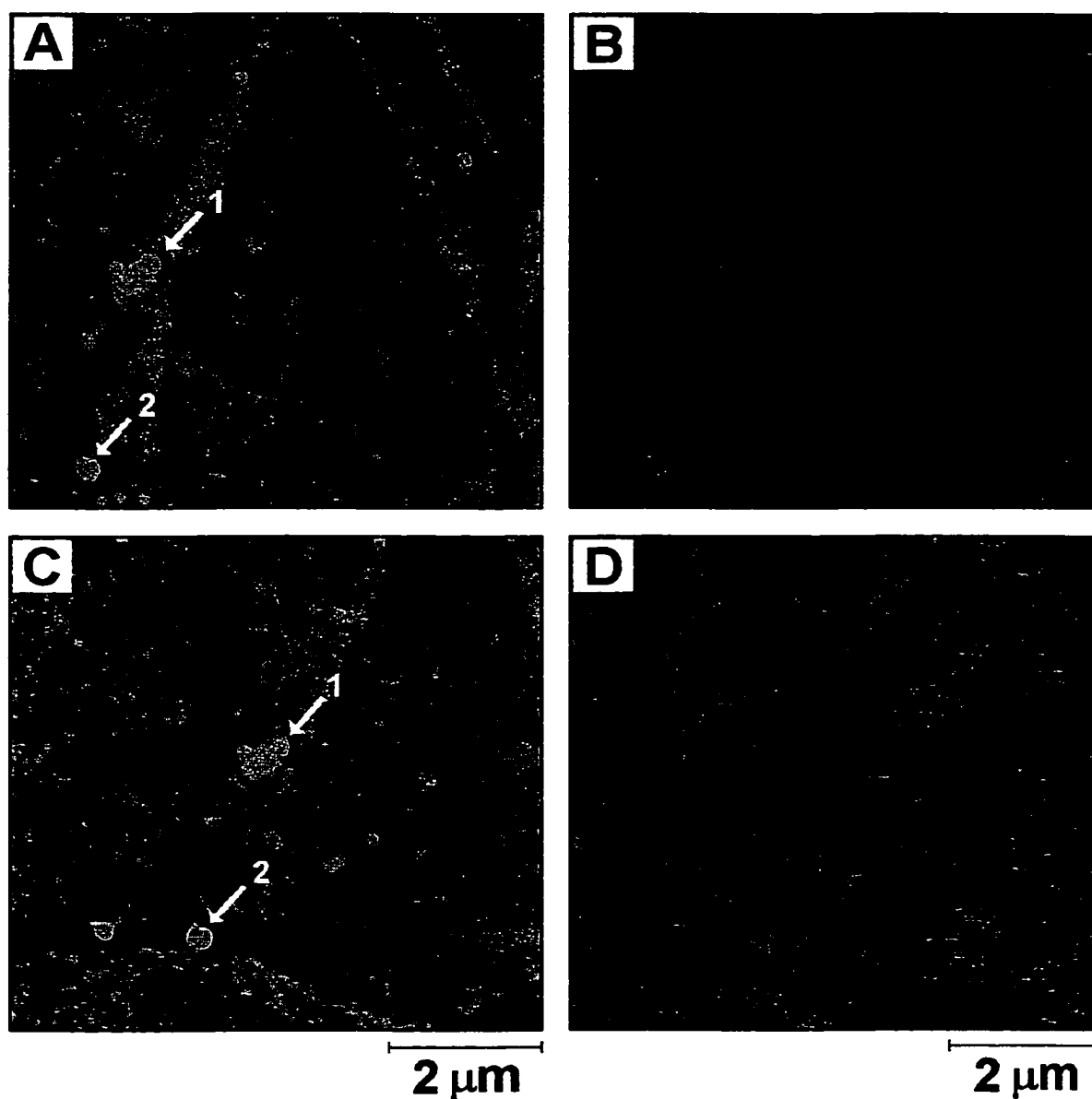
Figure 5.04. A) 7 × 7 μm² topographic (Z-scale = 5 nm) image of a BSA film on HOPG formed from 10 μg/mL of BSA. B) Friction image corresponding to A (Z-scale = 0.05 V). C) 7 × 7 μm² topographic (Z-scale = 7 nm) image after exposure of the surface shown in Figure 5.03A and 3B to 50 μg/mL BFG for 1 h. D) Friction image corresponding to A (Z-scale = 0.05 V). Images were collected in PBS.

exposed graphite. Figure 5.04B is the corresponding friction image. Using the shapes of the BSA domains in Figure 5.04A as a spatial reference, the exposed graphite exhibits a slightly higher friction than the adsorbed BSA. This observation is somewhat surprising in that SFM measured friction at basal plane HOPG is generally low relative to other surfaces (5, 40). A recent report has shown that the adhesive interactions between a BSA coated SFM tip and an adsorbed BSA film is much lower than that between a BSA coated tip and a polystyrene substrate (4). This observation is due to the weakness of the interaction between the BSA layer adsorbed to the substrate and BSA adsorbed to the tip surface. In pH 7.4 buffer, both of these surfaces will exhibit a net negative charge that will prevent significant adhesion. On the other hand, the interaction between the protein coated tip and the hydrophobic polystyrene would be strong. Although coating of the SFM probes with BSA was not purposely performed in this work, we believe that the protein will adsorb to the tip surface during each experiment. The frictional contrast observed in Figure 5.04B is consistent with the previously reported adhesion results.

The surface shown in Figure 5.04A and B was then exposed to 50 µg/mL BFG. Parts C and D of Figure 5.04 were collected in roughly the same location as Figure 5.04A and B one hour after BFG was introduced. Some features of the original BSA layer remain following BFG exposure. For example, two IDC-BSA structures, highlighted by arrows 1 and 2, are visible in Figure 5.04B. These same structures are also present in Figure 5.04C after 1 h exposure to BFG. However, the domain structure observed in Figure 5.04B is transformed by the adsorption of BFG to a more uniform topography. Despite the transformation in topography, a pattern of contrast remains in the friction image (Figure 5.04D) that resembles that observed for the BSA domains in Figure 5.04B.

As an aid in comparing the two friction images, each is re-plotted in Figure 5.05. Parts A and B of Figure 5.05 are identical to parts B and D of Figure 5.04,
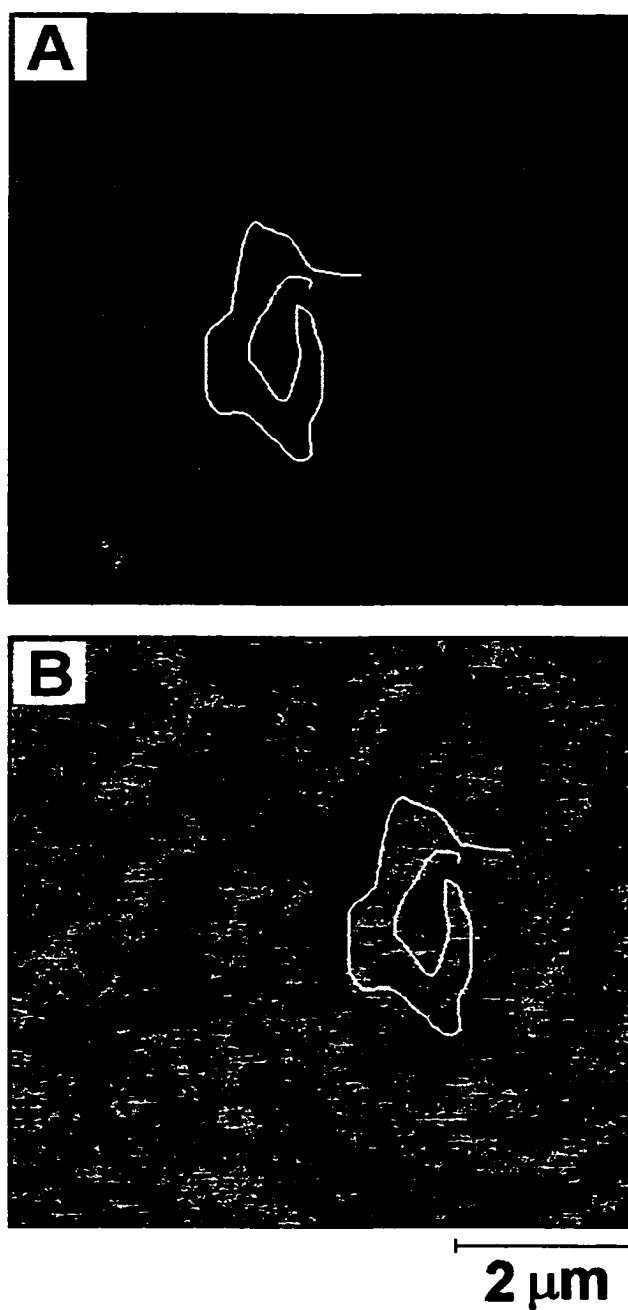
Figure 5.05. A) and B) are re-plots of parts B and D of Figure 4, respectively. The white outline highlights a domain shape similar to both images (see text).

respectively. In Figure 5.05A, a high friction domain, corresponding to an area of exposed graphite in part A of Figure 5.04, has been outlined. This outline was then transferred to a high friction region of part B of Figure 5.05. The domain shape in Figure 5.05B matches well with that in Figure 5.05A. Careful inspection reveals other identical domains in each image. The contrast observed in Figure 5.04D can be attributed to one of two scenarios: i) BFG adsorbs directly to the HOPG through the voids in the pre-adsorbed BSA film and the frictional contrast results from the difference between the two proteins; or ii) BFG adsorbs both in the voids and on top of the pre-adsorbed BSA film in different states such that the result is an overall uniform topography but with observed differences in the SFM measured friction.

To address these two possibilities, an experiment was designed to test whether BFG does adsorb on top of the BSA domains. The experiment is similar to that used for Figure 5.04, but employs a reduced concentration of BFG. The use of a lower concentration of BFG reduces the rate of adsorption, allowing images to be captured in real-time as the BFG adsorbs onto the surface. The results are shown in the topographic images of Figure 5.06. Figure 5.06A is an image showing again the domain structure that forms from 30 min adsorption of BSA from a 10 μg/mL solution. The cross-sectional profile reveals a film thickness of 1.3 nm. Part B of Figure 5.06 is an image of the same area as Figure 5.06A collected while a 10 μg/mL BFG solution flowed through the SFM fluid cell. Thus, Figure 5.06B is a snapshot of the BFG adsorption process. At this point in the experiment, domains are still observed with roughly the same shape as the original BSA domains in Figure 5.06A. However, as shown by the cross-sectional profile, the height of the domains has increased to ~4.3 nm. Further exposure of the surface to the flowing BFG solution results in adsorption to the exposed graphite with a final topography similar to that observed in Figure 5.04C.
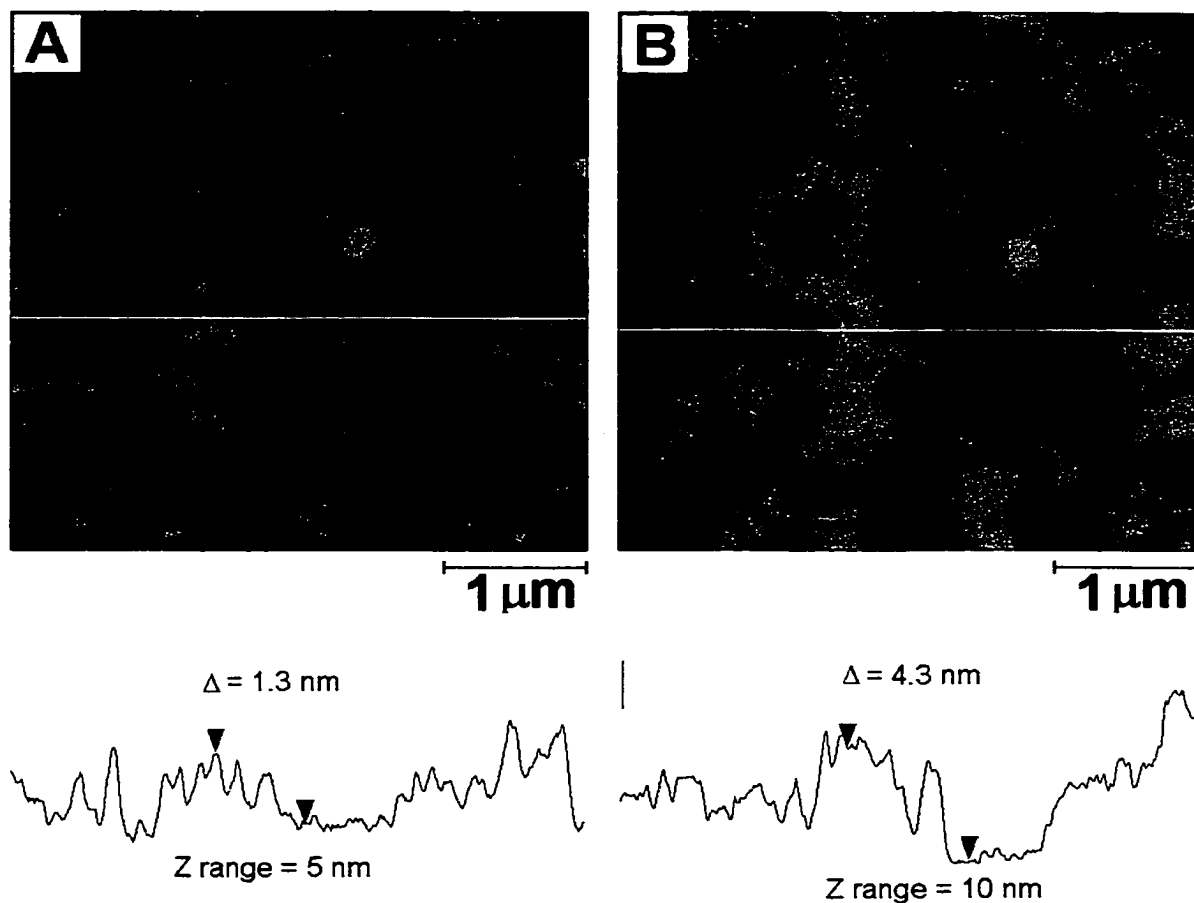
Figure 5.06. A) 4 × 4 μm² topographic image (Z-scale = 5 nm) of BSA adsorbed on HOPG from 10 μg/mL solution captured under flowing PBS solution. The cross-sectional profile below the image corresponds to the white line. B) The same area as in (A) collected while 10 μg/mL BFG solution was added to the flowing buffer stream (Z-scale = 10 nm). The cross-sectional profile below each image corresponds to the white line through the image.

Two important conclusions can be drawn from Figure 5.06. The first is that the 3 nm increase in the height of the domains is strong evidence that BFG does indeed adsorb to the top of the pre-adsorbed layer of BSA. Furthermore, the frictional contrast observed in Figure 5.04D can now be attributed to two different adsorbed states of BFG, consistent with Chapter IV. One adsorbed state results from adsorption directly to the graphite and the other results from the interaction with the pre-adsorbed BSA layer. Secondly, BFG preferentially adsorbs to a pre-adsorbed layer of BSA over exposed graphite. Adsorption of fibrinogen to an albumin layer has been indicated in a previous report (16). Although this may be the initial step in a displacement process, no displacement during the time-scales examined (30–60 min) was observed.

Mechanism of frictional contrast. The friction at a SFM tip-sample junction depends on the normal force (*i.e.*, load), the interfacial work of adhesion (W_{ts}) and the tip-sample contact area. Since SFM images are collected at constant load, frictional contrast is thus generated by spatial variations in the chemistry of the surface, which govern W_{ts} and/or mechanical properties (*i.e.*, viscoelasticity), influence contact area. Chemically modified SFM probes were employed to identify which of these effects is the most important in governing the frictional contrast observed for different adsorbed protein states. Gold-coated Si_3N_4 tips were modified via self-assembly of alkanethiolate monolayers with different tail groups. To produce tips with vastly different chemical properties, octadecanthiol (ODT, $HS(CH_2)_{17}CH_3$) and mercaptohexadecanoic acid (MHA, $HS(CH_2)_{15}COOH$) were chosen precursors. The working theory here is that if the mechanical properties of the protein layers were the main contributor to the observed frictional contrast in Figure 5.04D, then the chemistry of the tip should not influence the contrast.

Figure 5.07 contains 6 × 6 μm^2 SFM images of protein films prepared by the adsorption of 10 $\mu g/mL$ BSA followed by the adsorption of 50 $\mu g/mL$ BFG.
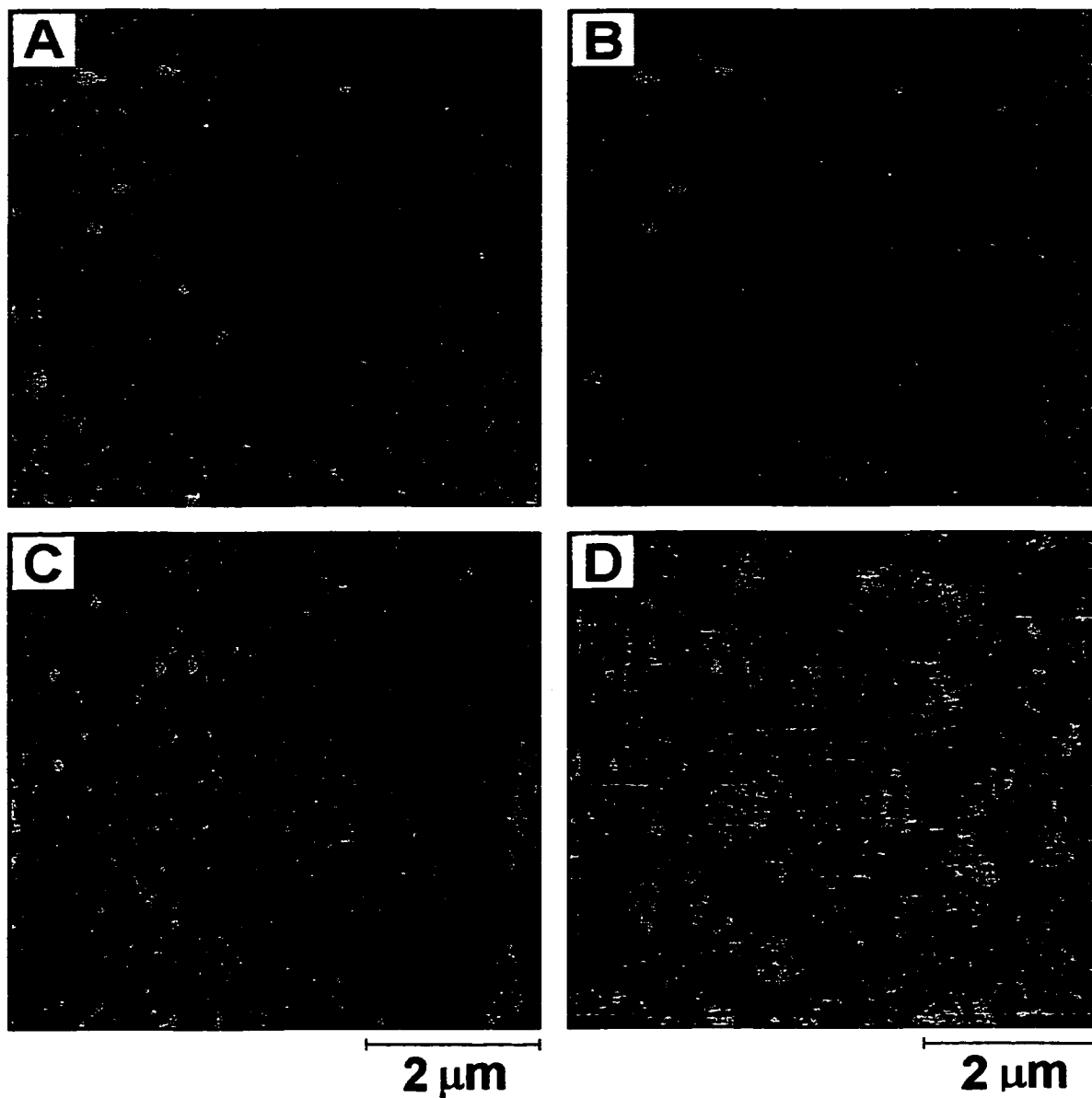
Figure 5.07. Protein films on HOPG formed by 30 min. adsorption of 10 μg/mL BSA and subsequent adsorption of 50 μg/mL BFG. A) 6 × 6 μm² topographic image (Z-scale = 7 nm) collected using $HS(CH_2)_{17}CH_3$ modified tip. B) Friction image (Z-scale = 0.05 V) corresponding to part (A). C) 6 ×6 μm² topographic image (Z-scale = 7 nm) collected using $HS(CH_2)_{15}CO_2H$ modified tip. B) Friction image (Z-scale = 0.05 V) corresponding to part (C).

Parts A and B of Figure 5.07 are respective topographic and friction images collected with the hydrophobic ODT modified tip while parts C and D were collected with the hydrophilic MHA modified tip. Similar to Figure 5.04C, a uniform topography is observed with both tip chemistries (parts A and C of Figure 5.07). However, while the methyl-terminated tip does not yield any significant frictional contrast in Figure 5.07B, a contrast pattern is observed with the carboxylate-terminated tip (Figure 5.07D) that corresponds to the initial domains of the pre-adsorbed BSA layer. Based on my previous work on BFG adsorption to alkanethiolate monolayers (11) it is likely that a layer of adsorbed protein exists on both the methyl- and carboxylate modified tips during imaging. It is also likely that the conformation of the layers is different on each tip. Although this complicates a complete interpretation, it's believe that the dependence of the frictional contrast on tip chemistry shown in Figure 5.07 indicate that interfacial chemistry is more important than mechanical properties in determining the frictional contrast at adsorbed protein films. Specifically, the interaction between the amino acid groups exposed to the interface on the protein layers at both the substrate and the tip determines the contrast. Concerns on protein adsorption to the probe tip and its possible effect on friction contrast will be address further in the conclusions and future works chapter (Chapter VII).

Conclusions

SFM was employed in the analysis of a dual component protein layer adsorbed to HOPG. Initial analysis was directed toward single component BSA and BFG layers where we found that the morphology of the protein films on HOPG depend on the concentration of the bulk protein solutions. Aggregates were prevalent in films formed from high solution concentrations of both BSA and BFG. These structures are highly effective in competing for adsorption sites. Next, adsorption of BFG to a pre-adsorbed partial layer of BSA was analyzed.

BSA was not displaced by the BFG after 1 h incubation time. BFG adsorbs to the top of the BSA layer as well as in the voids in distinct conformations. Importantly, different adsorbed protein states were detected with friction force imaging. The observed frictional contrast depends on the chemistry of the SFM probe tip indicating that chemical effects are more important than mechanical properties of the protein layer in determining the conformational sensitive contrast. These studies have extended the use of SFM for the characterization of the interactions between biological fluids and biomaterials.

References

(1)   Cullen, D. C.; Lowe, C. R. *J. Colloid Interface Sci.* **1994**, *166*, 102-108.

(2)   You, H. X.; Lowe, C. R. *J. Colloid Interface Sci.* **1996**, *182*, 586-601.

(3)   Droz, E.; Taboraelli, M.; Descouts, P.; Wells, T. N. C. *Biophys. J.* **1994**, *67*, 1316-1323.

(4)   Chen, X.; Davies, M. C.; Roberts, C. J.; Tendler, S. J. B.; Williams, P. M.; Davies, J.; Dawkes, A. C.; Edwards, J. C. *Langmuir* **1997**, *13*, 4106 - 4111.

(5)   Ta, T. C.; Sykes, M. T.; McDermott, M. T. *Langmuir* **1998**, *14*, 2435-2443.

(6)   Ortega-Vinuesa, J. L.; Tengvall, P.; Lundstrom, I. *J. Coll. Inter. Sci.* **1998**, *207*, 228-239.

(7)   Patel, N.; Davies, M. C.; Heaton, R. J.; Roberts, C. J.; Tendler, S. J. B.; Williams, P. M. *Appl Phys. A* **1998**, *66*, S569 - S574.

(8)   Marchant, R. E.; Barb, M. D.; Shainoff, J. R.; Eppel, S. J.; Wilson, D. L.; Siedlecki, C. A. *Thromb. Haemost.* **1997**, *77*, 1048-1051.

(9)   Chen, X.; Patel, N.; Davies, M. C.; Roberts, C. J.; Tendler, S. J. B.; Williams, P. M.; Davies, J.; Dawkes, A. C.; Edwards, J. C. *Appl. Phys. A.* **1998**, *66*, S631-S634.

(10)   Sit, P. S.; Marchant, R. E. *Thromb. Haemost.* **1999**, *82*, 1053-1060.

(11)   Ta, T. C.; McDermott, M. T. *Anal. Chem.* **2000**, *72*, 2627- 2634.

(12)   Andrade, J. D.; Hlady, V.; Feng, L.; Tingey, K. In *Interfacial Phenomena and Bioproducts*; Brash, J. L., Wojciechowski, P. W., Eds.; Marcel Dekker: New York, 1996, pp 19-55.

(13)   Brash, J. L.; Horbett, T. A. In *Proteins at Interfaces II : Fundamentals and Applications*; Brash, J. L., Horbett, T. A., Eds.; American Chemical Society: Washington, DC, 1995, pp 1 - 23.

(14)   Brash, J. L.; Uniyal, S. J. *J. Polym. Sci.* **1979,** *66*, 377.

(15)   Wojciechowski, P.; ten Hove, P.; Brash, J. L. *J. Colloid Interface Sci.* **1986,** *111*, 455 - 465.

(16)   Feng, L.; Andrade, J. D. *Biomaterials* **1994,** *15*, 323 - 333.

(17)   Vroman, L.; Adams, A. L. *J. Biomed. Mater. Res.* **1969,** *3*, 43.

(18)   Fabrizius-Homan, D. J.; Cooper, S. L. *J. Biomed. Mater. Res.* **1991,** *25*, 953-971.

(19)   Chinn, J. A.; Phillips, R. E. J.; Lew, K. R.; Horbett, T. A. *J. Colloid Interface Sci.* **1996,** *184*, 11-19.

(20)   Feng, L.; Andrade, J. D. *Colloids surf. B: Biointerfaces* **1995,** *4*, 313-325.

(21)   Fritz, M.; Radmacher, M.; Cleveland, J. P.; Allersma, M. W.; Stewart, R. J.; Gieselmann, R.; Janmey, P.; Schmidt, C. F.; Hansma, P. K. *Langmuir* **1995,** *11*, 3529-3535.

(22)   Frisbie, C. D.; Rozsnyai, L. F.; Noy, A.; Wrighton, M. S.; Lieber, C. M. *Science* **1994,** *265*, 2071.

(23)   Green, J. B. D.; McDermott, M. T.; Porter, M. D.; Siperko, L. M. *J. Phys. Chem.* **1995,** *99*, 10960 - 10965.

(24)   Brash, J. L. In *Blood Compatible Materials and Devices*; Sharma, C. P., Ed.; Technomic: Lancaster, 1991, pp 3 - 24.

(25)   Ramsden, J. J. *Phys. Rev. Lett.* **1993,** *71*, 295.

(26) Kshirsagar, B.; Wilson, B.; Wiggins, R. C. *Clini. Chim. Acta.* **1984**, *143*, 265.

(27) Lipinski, B. *J. Prot. Chem.* **1995**, *14*, 259.

(28) Lipinski, B.; Egyud, L. G. *Bioorg. Medic. Chem. Lett.* **1992**, *2*, 919.

(29) Lipinski, B.; Federman, S. M.; Krdewski, A. *Thrombosis Res.* **1995**, *78*, 461.

(30) Kurat, R.; Prenosil, J. E.; Ramsden, J. J. *J. Colloid Interface Sci.* **1997**, *185*, 1.

(31) Sheller, N. B.; Petrash, S.; Foster, M. D.; Tsukruk, V. V. *Langmuir* **1998**, *14*, 4535-4544.

(32) Suttipaisit, P. J.; Krisdhasma, V. J.; McGure, J. J. *J. Colloid Interface Sci.* **1992**, *154*, 316.

(33) Liebmann-Vinson, A.; Lander, L. M.; Foster, M. D.; Brittain, W. J.; Vogler, E. A.; Majkrzak, C. F.; Satifja, S. *Langmuir* **1996**, *12*, 2256.

(34) Norde, W.; Haynes, C. In *Proteins at Interfaces II: Fundamentals and Applications*; Horbett, T. A., Brash, J. L., Eds.; American Chemical Society: Washington, DC, 1995, pp 26 - 40.

(35) Muller, D. J.; Engel, A. *Biophys. J.* **1997**, *73*, 1633-1644.

(36) Muller, D. J.; Fotiadis, D.; Scheuring, S.; Muller, S. A.; Engel, A. *Biophys. J.* **1999**, *76*, 1101-1111.

(37) Nygren, H.; Stenberg, M. *J. Biomed. Mater. Res.* **1988**, *22*, 1.

(38) Feng, L.; Andrade, J. D. In *Proteins at Interfaces II: Fundamentals and Applications*; Horbett, T. A., Brash, J. L., Eds.; American Chemical Society: Washington, DC, 1995, pp 66 - 79.

(39) Moskowitz, K. A.; Bohdan, K.; Coller, B. S. *Thromb. Haemost.* **1998**, *79*, 824-831.

(40) McDermott, M. T.; McCreery, R. L. *Langmuir* **1994**, *10*, 4307 - 4314.

CHAPTER VI

DEVELOPMENT OF IRRAS AS A PROBE FOR ADSORBED PROTEIN CONFORMATION/ORIENTATION

Introduction

In Chapter III and IV, fibrinogen was adsorbed onto single component and patterned surfaces of methyl and carboxylate terminated groups. Antibody binding studies by infrared reflectance absorbance spectroscopy (IRRAS) and surface plasmon resonance (SPR) initially suggested that the protein adsorbed state was a function of surface chemistry. Topographic images on single component monolayers and friction contrasts observed for fibrinogen films on patterned surfaces confirmed those suppositions. IRRAS was instrumental in providing information with regards to the amount of protein present at the interface. In this chapter, we explore the possibility of obtaining conformational information directly from IRRAS spectral analysis.

Spectroscopic methods such as circular dichroism (1,2) and infrared spectroscopy in various configurations (*i.e.* attenuated total reflectance, reflectance adsorption) have been shown to be invaluable tools for the examination of films at solid-liquid and solid-gas interfaces. Absorption band frequency, intensity and shape can reveal information regarding protein conformation, including type and amount of various secondary structures (3-9). For example, the interaction of proteins with a surface can shift absorbance frequencies to higher energy as a result of protein denaturation (10, 11). The intensity of amide II bands has been used to quantify the amount of protein present at the interface (4, 10) and peak shape analysis of amide I has been used for assigning protein secondary structure or conformation (12).

Traditionally, ascertaining protein conformation from peak shape involve complex deconvolution or decomposition methods using extensive mathematical modeling (6, 13, 14). Deconvolution involves deconstructing a broad absorption

band into smaller component peaks which, when added together, will form the original peak shape and intensity. Also, it is possible to improve peak resolution by taking the first and second derivative of these peaks (7, 13, 15). The goal of both methods is to resolve individual peaks constituting the broader band. Both methods require appropriate software, and even after the method is applied, meaningful results may not be achieved. Thus there is a need for simple and quick procedures that can be performed on infrared absorbance peaks to estimate protein conformation or at least relative adsorbed protein conformation. This chapter will present data to demonstrate that the ratio of the amide I to amide II peaks can be used as an indicator of differences in protein conformation. This method is simple and universal because many type of proteins can be analyzed.

Experimental

Reagents and Materials: Phosphate-buffered saline (PBS) was prepared as described in previous chapters. PBS was used to prepare 20 μg/mL of human fibrinogen (HFG, fraction I, Sigma) by dry protein weight. Antibody to HFG (anti-HFG) from goat serum and bovine IgG (ICN biomedical, OH) solutions were prepared fresh with PBS just before each experiment to achieve concentrations of 160 μg/mL. PBS and protein solutions were filtered with a 22 μm millex-GV, low-protein binding filter (Millipore, Bedford, MA). Octadecanethiol $HS(CH_2)_{17}CH_3$ (ODT) was purchased from Aldrich (Milwaukee, WI) and mercaptohexadecaneoic acid, $HS(CH_2)_{15}CO_2H$ (MHA) was a gift from Dr. Marc Porter (Ames Lab, Iowa State). Mercaptoundecanoic acid, $HS(CH_2)_{10}COOH$ (MUA) was prepared as outlined by Aherne, et al. (16) and used to prepare the esters mercaptoundecanoic acid methyl ester [$HS(CH_2)_{10}CO_2CH_3$] (MET) and mercaptoundecanoic acid ethyl ester [$HS(CH_2)_{10}CO_2CH_2CH_3$] (EET). To prepare MET, enough MUA was dissolved in methanol to achieve a concentration of ~1 mM, and a few drops of concentration HCl was added to catalyze the conversion of MUA to MET. EET was prepared similarly to MET, however, ethanol was the

solvent. The conversion of MUA to MET or EET is a relatively quick process. However, Au coated glass slides prepared as discussed in Chapter IV, were immersed in these solutions 2 h after they were prepared.

Infrared Reflectance Absorbance Spectroscopy (IRRAS): Glass/Ti/Au substrates were immersed in thiol solutions (0.1-1 mM) for 30 min in the case of MHA, 60 min for MET and EET, and overnight for ODT. After substrate modification, they were immersed into 20 μg/mL HFG solutions for 1 h, rinsed with PBS and dried with argon. After drying, spectra of the HFG-coated slides were obtained in a Mattson Infinity FTIR spectrometer equipped with a low-noise MCT-A detector cooled with liquid N_2. A reflection accessory and a home built sample holder were housed in an external, auxiliary bench. Fibrinogen coated slides were then incubated with 160 μg/mL anti-HFG or Bovine IgG (bIgG) for 2 h. Slides were removed, rinsed with PBS and dried with argon prior to obtaining spectra. Amide II intensities were monitored amount of HFG adsorbed and estimate specific binding of anti-HFG to adsorbed HFG. After incubation of the HFG-coated slides with antibody, increase in amide II intensity was due to antibody interaction with HFG-coated surface. However, the increase signal may be the result of both specific binding and non-specific adsorption. To correct for non-specific adsorption, the percentage increase in intensity due to anti-HFG was substracted from the percentage increase from bIgG non-specific adsorption. For evaluating the effect of surface chemistry on HFG conformation, amide I to amide II ratio was calculated, and plotted against amount of specific binding to HFG on ODT, MHA, EET, and MET modified substrates.

Results and Discussion

Differential antibody binding to antigen proteins has become a standard measure for determining variations in protein conformation. In Chapter III and IV, antibody binding using goat anti-HFG data revealed differential binding to HFG protein adsorbed on MHA and ODT modified surfaces. This evidence

suggested that HFG conformation was controlled by surface chemistry. Similar measurements have been made on other chemical functionalities, namely methyl ester ($-CO_2CH_3$) and ethyl ester ($-CO_2CH_2CH_3$). Figure 6.01 is a bar plot of corrected specific binding as a function of surface chemistry onto which HFG was pre-adsorbed. Amount of adsorbed HFG, specific and non-specific binding was based on intensities of the amide II bands generated by IRRAS. Bars 1 and 2 of Figure 6.01 were shown earlier in Figure 3.11 (C bars). Percent increase of amide II intensity due to specific binding was 45 ± 9 % and 67 ± 9 % for ODT and MHA surfaces, respectively. The percentage of specific binding to HFG adsorbed on EET and MET modified surfaces are shown in bars 3 and 4 respectively. EET and MET surfaces showed similar corrected percent increase from specific anti-HFG binding, EET (55 ± 5 %), and MET (53 ± 9 %). This finding is not unexpected both functional groups are esters, and thus adsorbed HFG is likely to adopt similar conformations.

Protein conformation from the ratio of amide I to amide II. Without extensive treatments of infrared spectra, it is possible to determine relative protein conformations from simple calculations based on amide intensities. Figure 6.02 is an IRRAS spectrum, in the amide region, from HFG adsorbed on ODT surfaces. Intensities of amide I and amide II peaks were determined and amide I/amide II (A_{aI}/A_{aII}) ratio was calculated. Ratios were determined for HFG adsorbed on ODT, MHA, MET and EET surfaces. These ratios were then plotted against specific antibody binding from Figure 6.01, and are shown in Figure 6.03. Figure 6.03 indicates that for the same protein (i.e., HFG), A_{aI}/A_{aII} varies depending upon the surface chemistry to which HFG was adsorbed. Ratios were 1.70 ± 0.05, 1.92 ± 0.07, 1.88 ± 0.02, and 1.83 ± 0.03 for ODT, MHA, EET and MET surfaces respectively. A linear correlation analysis revealed a promising correlation (r = 0.9) between antibody binding and amide ratio determined from adsorbed HFG. This plot suggests it is possible ascertain relative protein conformations based only
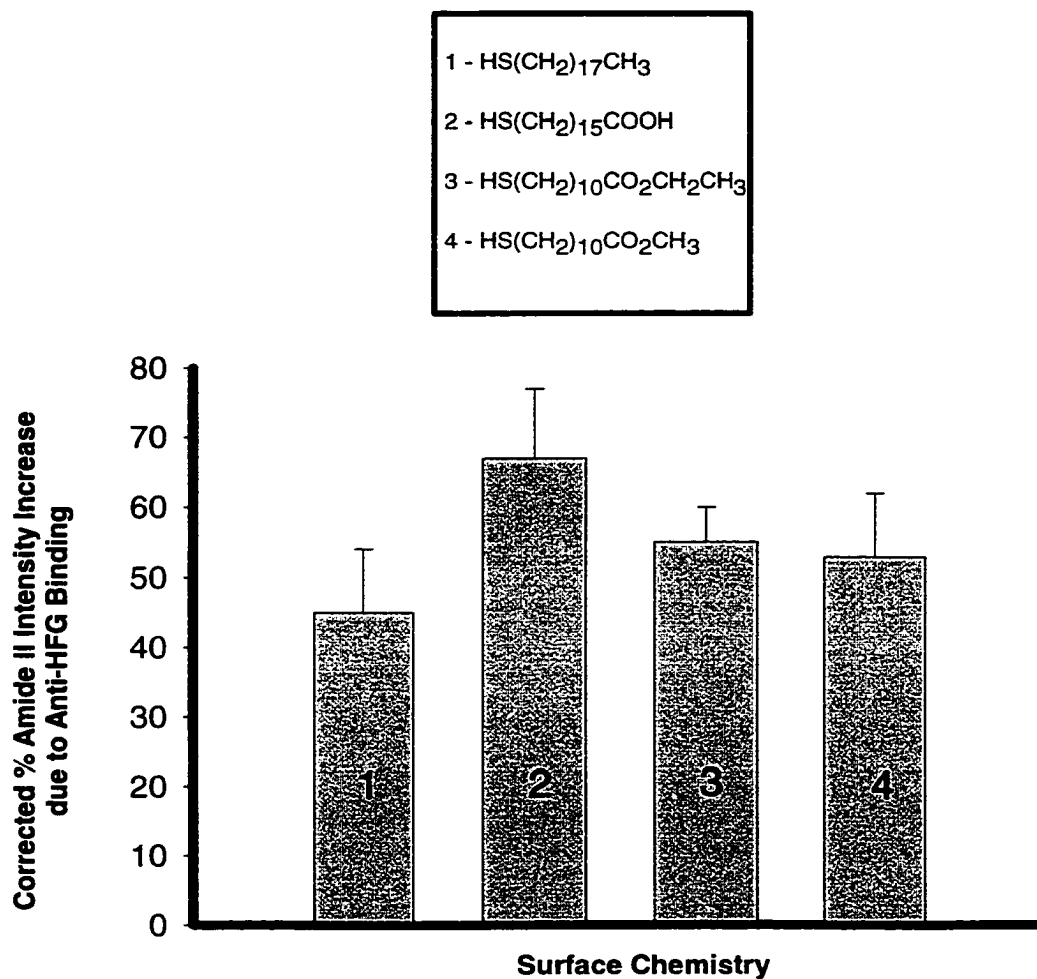
Figure 6.01. Bar graph depicting surface chemistry effect on amount of corrected specific binding of anti-HFG to adsorbed HFG.
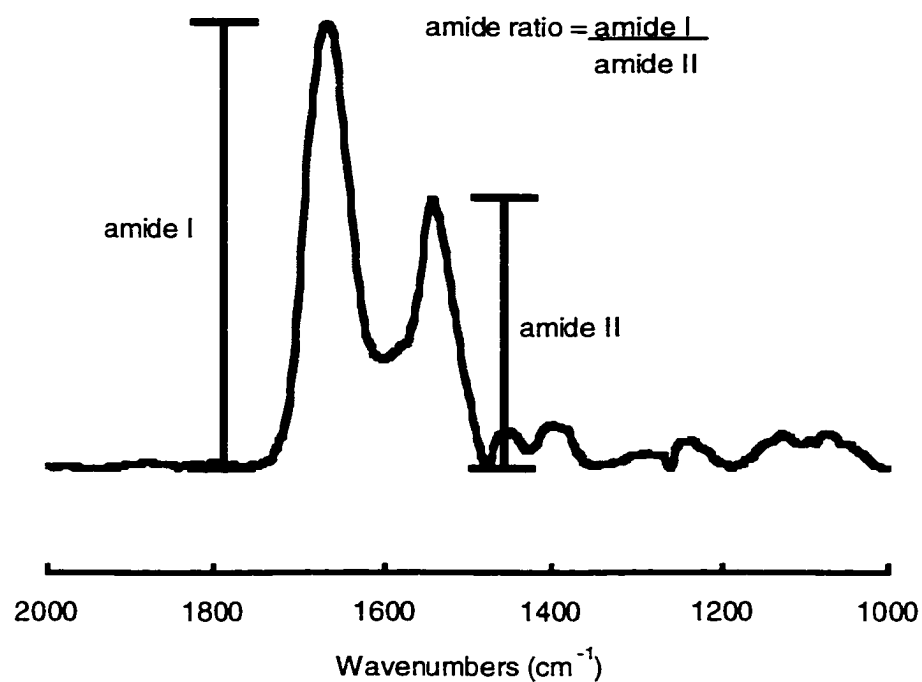
Figure 6.02. IRRAS spectrum of HFG adsorbed on ODT modified Au glass slides. Amide ratios were calculated from the absorbance intensities of amide I and II. Similar calculations were performed on MHA, MET and EET surfaces.
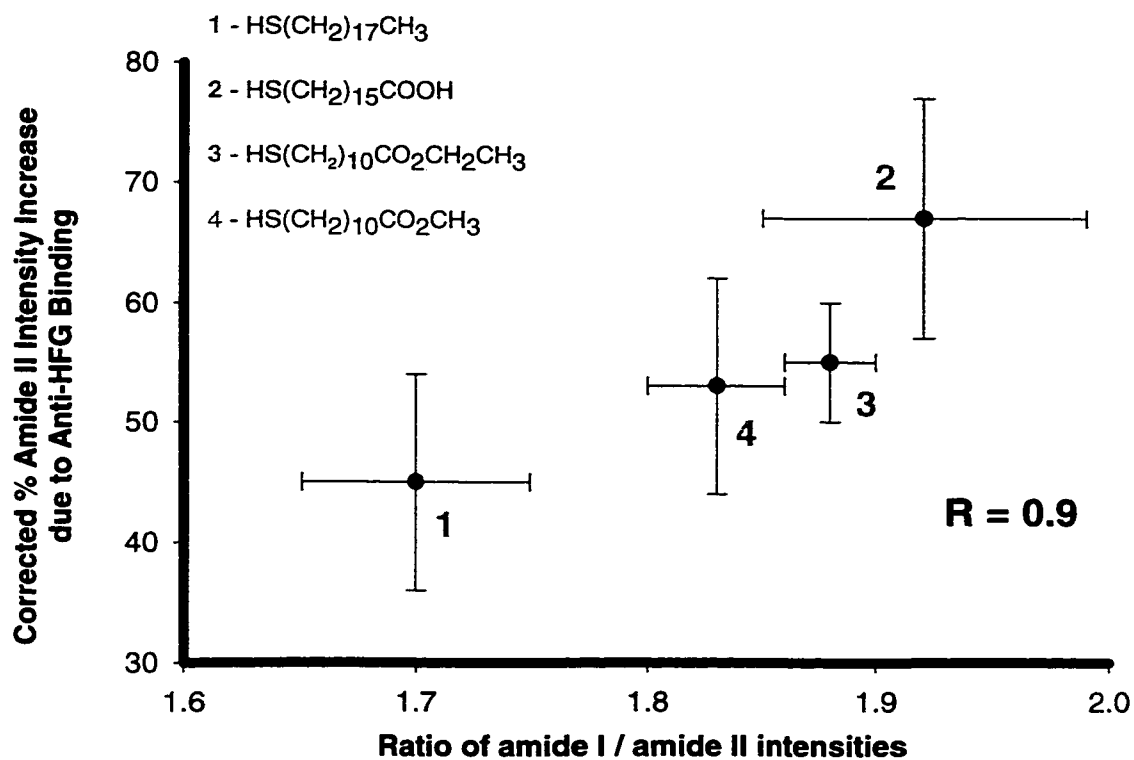
Figure 6.03. Plot of corrected amide II intensity increase due to specific anti-HFG binding versus amide I/amide II ratio for four different surface chemistries. Errors were based on four measurements.

on the A_{aI}/A_{aII} measurement, without going through complex deconvolution steps. However, the ratio itself cannot assign type or quantity of various protein secondary structure elements. Determination of α-helix, β-sheets, β-turns and random secondary structure elements still requires spectra decomposition.

<u>Amide ratio of HFN, BSA, LYS and bIgG on MHA and ODT surfaces.</u> In Chapter IV, friction contrast was observed on human fibronectin (HFN), bovine albumin (BSA), lysozyme (LYS) and bovine IgG (bIgG) protein films. It was asserted in Chapter IV that friction contrast was the direct result of differences in protein conformations, which were controlled by surface chemistry. As determined in this chapter, relative adsorbed protein conformations can be ascertained from A_{aI}/A_{aII}. Table 6.1 lists A_{aI}/A_{aII} for each protein adsorbed to CH_3 and COOH terminated monolayers, as well as whether a frictional contrast is observed on a substrate patterned with these two groups. Generally, a larger difference in A_{aI}/A_{aII} correlates with observed contrast.

In the cases of BSA and LYS, amide ratios for each protein were significantly different on the two surface chemistries. These differences are believed to be the result of varied adsorbed protein state, generating the friction contrast that were observed in Figure 4.13B and C. For HFN, the ratios are less differentiated, however friction contrast was observed in Figure 4.13A. At this point it is not clear what magnitude in amide ratio separation is necessary in order that friction contrast may be observed. However, amide ratio differences of 0.2 from HFN and HFG were detectable. In the case of bIgG, no friction contrast was observed (Figure 4.13D), even with an amide ratio separation of 0.2. Reasons for this observation are still uncertain, but it may be the result of bIgG's relatively large values of A_{aI}/A_{aII}. On the ODT and MHA surfaces, the amide ratio was 2.3 and 2.5 respectively. In all cases, the amide I/II ratio is smaller on the ODT surfaces than on the MHA surfaces. A smaller ratio may be the result of greater protein denaturation due to protein unfolding to maximize hydrophobic interaction

Amide I / Amide II Ratios for Various Serum Proteins				
	Human Fibronectin	Bovine Albumin	Chicken Lysozyme	Bovine IgG
$HS(CH_2)_{17}CH_3$	1.9 ± 0.1	1.2 ± 0.1	1.5 ± 0.1	2.3 ± 0.1
$HS(CH_2)_{15}CO_2H$	2.1 ± 0.1	1.8 ± 0.2	2.4 ± 0.1	2.5 ± 0.1
Friction Contrast	Yes	Yes	Yes	No

Table 6.1. Tabulated amide ratios of different proteins adsorbed on ODT and MHA modified substrates.

with the ODT surface. Thus, for bIgG, a relatively large amide I/II ratio on ODT may suggest only minor conformational differences from bIgG adsorbed on MHA surfaces.

Conclusions

A quick and simple method for determining relative protein conformational differences was demonstrated which was based solely assessing the amide I to amide II ratio. A linear correlation coefficient of r = 0.9 determined from a plot of specific antibody binding versus amide ratio supported this conclusion. Amide ratios were determined for HFN, BSA, LYS and bIgG on ODT and MHA surfaces. Different ratios were found at each functional group for each protein, providing evidence to support conclusions made in Chapter IV, that friction contrast observed in Figure 4.13 was generated as a result of different protein adsorbed states on the patterned surface.

References

(1)   McMillin, C. R.; Walton, A. G. *J. Colloid Interface Sci.* 1974, *48*, 345-349.

(2)   Sarver, R. W.; Krueger, W. C. *Anal. Biochem.* 1991, *199*, 61 - 67.

(3)   Chittur, K. K.; Fink, D. J.; Hutson, T. B.; Gendreau, R. M.; Jakobsen, R. J.; Leininger, R. I. In *Proteins at Interfaces: Physicochemical and Biochemical Studies*; Brash, J. L., Horbett, T. A., Eds.; American Chemical Society: Washington DC, 1987, pp 362 - 377.

(4)   Barbucci, R.; Magnani, A. *Biomaterials* 1994, *15*, 955-962.

(5)   Magnani, A.; Busi, E.; Barbucci, R. *J. Mater. Sci. Mater. Med.* 1994, *5*, 839-843.

(6)   Boulkanz, L.; Balcar, N.; Baron, M.-H. *Appl. Spectr.* 1995, *49*, 1737-1746.

(7)   Buijs, J.; Norde, W.; Lichtenbelt, J. *Langmuir* 1996, *12*, 1605-1613.

(8)   Chittur, K. K. *Biomaterials* 1998, *19*, 357-369.

(9)   Oberg, K. A.; Fink, A. L. *anal. Biochem.* 1998, *256*, 92-106.

(10)   Liedberg, B.; Ivarsson, B.; Lundstrom, I.; Salaneck, W. R. *Prog. Coll. Polym. Sci.* 1985, *70*, 67 - 75.

(11)   Caruso, F.; Furlong, D. N.; Ariga, K.; Ichinose, I.; Kunitake, T. *Langmuir* 1998, *14*, 4559-4565.

(12)   Liedberg, B.; Ivarsson, B.; Lundstrom, I. *J. Biochem. Biophys. Met.* 1984, *9*, 233-243.

(13)   Bentaleb, A.; Abele, A.; Haikel, Y.; Schaaf, P.; Voegel, J. C. *Langmuir* 1998, *14*, 6493 - 6500.

(14)   Heimburg, T.; Schunemann, J.; Weber, K.; Geisler, N. *Biochemistry* 1999, *38*, 12727-12734.

(15)   Fang, Y.; Dalgleish, D. G. *Food Hydrocolloids* 1998, *12*, 121-126.

(16)   Aherne, D.; Rao, S. N.; Fitzmaurice, D. *J. Phys. Chem. B* 1999, *103*, 1821-1825.

CHAPTER VII

CONCLUSIONS AND FUTURE WORKS

Overall Conclusions

In the preceding chapters, experimental results were presented to establish that research objectives as set forth in Chapter I were fulfilled. I believe the works presented in this thesis demonstrate that scanning force microscopy (SFM) and friction force microscopy (FFM) are powerful techniques for probing protein films. Initially, studying the adsorption characteristics of anthraquinone on highly oriented pyrolytic graphite (HOPG) afforded the opportunity to develop skills for imaging solid-liquid interfaces (Appendix A). In addition, SFM was able to deduce the structure of the anthraquinone film responsible for the interesting voltage-current voltammogram (1).

Development of flow imaging methodology allowed for mechanistic studies of protein adsorption in real-time (Chapter II). It was discovered that bovine fibrinogen (BFG) adsorption to mica and HOPG surfaces was facilitated through different mechanisms. Fibrinogen adsorption to HOPG was proposed to occur through the D domains, leaving the αC domain to interact laterally. On the mica surfaces, binding was considered to be the result of the interaction of the αC domain with the surface. Washing of BFG films on both surfaces with sodium dodecylsulfate (SDS) showed that films on HOPG were more resistant to desorption; thus it is believed that films on HOPG are stronger due to αC domain interactions (2). SFM imaging of equilibrated fibrinogen and albumin films also showed that surface properties influence film composition (Chapter V). Aggregates of fibrinogen and albumin were seen to adsorb to HOPG, while at mica surfaces, the film was uniform and smooth in texture. These aggregates are believed to have a hydrophobic outer shell formed as a result of intermolecular interactions of sulfur containing amino acid side chains (3, 4). The driving force

behind adsorption is likely hydrophobic in origin. These observations indicated that surface chemistry played an important role in determining film structure. The role of surface chemistry was explored further using self-assembled monolayers (SAM) on Au substrates (Chapter III).

Application of real-time imaging to study fibrinogen adsorption on different surface chemistries (ODT and MHA surfaces) revealed that after immersion in 20 μg/mL fibrinogen solution, films produced were complete and robust (Chapter III). Surface coverage probed by FTIR and SPR showed that slightly more fibrinogen adsorbed to MHA surfaces than ODT surfaces. Heights measured from images on the initial stages of adsorption indicated fibrinogen clusters adsorbed on ODT (1-1.5 nm) were much lower in topography then for fibrinogen adsorption to MHA surfaces (4-4.5 nm). Using SAMs, it was shown that surface chemistry had an effect on protein adsorption. Height variations provided early evidence that BFG had different conformations on -CH$_3$ and -COOH terminated monolayers. Antibody binding to human fibrinogen revealed that more antibodies were binding to fibrinogen adsorbed on MHA surfaces, and SPR indicated that approximately two antibody molecules bound to one molecule of pre-adsorbed fibrinogen (Chapter III). On ODT, one antibody molecule bound to each molecule of adsorbed fibrinogen.

Work presented in Chapter IV demonstrated for the first time the ability of FFM to compositionally map protein-liquid interfaces. Frictional contrast was observed for bovine and human fibrinogen adsorption to ODT and MHA patterned Au substrates. *Friction contrast was attributed to variation in adsorbed protein conformation* (5). Differences in adsorbed conformation were established in Chapter III for the same systems. Other origins of frictional contrast such as structural variation in the SAM, protein adsorbed to the tip and electrostatic interaction from the monolayer underneath the protein film have been addressed. These artifacts were found not to be determining factors. Studies of other protein

films showed different directions of friction contrast as would be expected for different proteins (Figure 4.12), thus removing doubts that friction contrast was a result of an imaging artifact. In Chapter VI, the ratio of amide I to amide II intensities was shown to be a promising indicator of adsorbed conformation and tested with HFG, albumin, lysozyme, IgG and fibronectin at ODT and MHA monolayers.

FFM was used to image films that were more complex (*i.e.*, multi-protein film). HOPG surfaces were pre-absorbed with BSA of low concentration (10 μg/ml) to produce a partial BSA film. This surface was then exposed to fibrinogen solution. Unexpectedly, fibrinogen was seen to adsorb both to the BSA covered regions and directly to the HOPG surface. Friction contrast was observed after fibrinogen was added and since fibrinogen was covering the surface completely, contrast was the result of the adsorbed state of fibrinogen. Friction resulting from viscoelastic properties was eliminated as a factor contributing to the contrast using modified probe tips.

Proposals for Future Works

To develop FFM as tools for biomaterials research, it must be demonstrated that FFM can map protein adsorbed conformation on real biomaterial surfaces. These surfaces can include polymers or other metals such as titanium. Polymers can be spin-coated onto mica to create smooth surfaces on which protein can be adsorbed. Real-time imaging may provide insight into the initial stages of adsorption, and also mechanisms of adsorption may be ascertained. Patterning of surfaces to contain two polymers can be used to produce different adsorbed states. This may be possible without lithographic patterning by merely using polymer blends. Higher resolution imaging may provide greater detail about film composition on a more localized scale.

To further address the issue of protein adsorption onto a tip and its influence on friction contrast, I propose studies similar to those performed in Chapter IV on

patterned monolayers. However a differently configured scanning force microcope called a Bioscope (Digital Instruments) will be used. This instrument allows the tip to be held above the aqueous media in which a sample surface is submerged. Therefore, a surface can be immersed in a protein solution, then rinsed with buffer before the tip is lowered into contact with the surface. This procedure will reduce the amount of protein adsorbed to the tip and the sample is kept under aqueous conditions at all times. Friction contrast is monitored.

Stemming from my research, numerous projects are currently being undertaking by other students. One project includes using tapping-mode SFM (TM-SFM) to map protein conformation. In TM-SFM, an AC input causes a cantilever to oscillate at a certain frequency and phase. One interesting way to generate an image of a surface is to monitor the phase shift of the cantilever as the tip interacts with the surface. The amount of phase shift has been correlated with surface chemistry (6). This technique is much gentler than contact mode SFM and thus less damaging to delicate biological samples. TM-SFM will be used to map fibrinogen adsorption in similar experiments to those carried out in Chapter IV. Preliminary results have been very promising.

Another project involve patterning surfaces to contain poly(ethylene) glycol (PEG) regions that resist protein adsorption (7) and vary the chemistry of adjacent areas to study the effect of chemistry on antibody orientation. The PEG regions serve as a baseline for measuring height changes as proteins and antibodies are added. In immunoassays, microtiter wells are often coated with protein A to promote the interaction of the F_c regions with the protein A layer (8), thus orienting the antibody to have the F_{ab} regions expose to the interface. Studies are underway to determine how surface chemistry will affect the protein A film and whether its properties can be correlated to the orientation of antibodies. Topographic SFM will be used to monitor antibody orientation.

Using enzyme digestion and mass spectrometry for detection, it may be possible to determine what part of fibrinogen is exposed to the solution interface when adsorbed to ODT and MHA SAMs. The assumption here is that if fibrinogen was adsorbed in a different conformation, digestion will occur at different sites. The resulting fragments from each surface type can be qualitatively compared from the mass spectra.

References

(1)   Ta, T. C.; Kanda, V.; McDermott, M. T. *J. Phys. Chem. B* **1999**, *103*, 1295.

(2)   Ta, T. C.; Sykes, M. T.; McDermott, M. T. *Langmuir* **1998**, *14*, 2435-2443.

(3)   Lipinski, B. *J. Prot. Chem.* **1995**, *14*, 259.

(4)   Lipinski, B.; Federman, S. M.; Krdewski, A. *Thrombosis Res.* **1995**, *78*, 461.

(5)   Ta, T. C.; McDermott, M. T. *Anal. Chem.* **2000**, *72*, 2627- 2634.

(6)   Finot, M. O.; McDermott, M. T. *J. Am. Chem. Soc.* **1997**, *119*, 8564 - 8565.

(7)   Prime, K. L.; Whitesides, G. M. *J. Am. Chem. Soc.* **1993**, *115*, 10714.

(8)   Gouda, H.; Shiraishi, M.; Takahashi, H.; Kato, K.; Torigoe, H.; Arata, Y.; Shimada, I. *Biochemistry* **1998**, *37*, 129.

APPENDIX A

VOLTAMMETRIC AND SCANNING FORCE MICROSCOPIC INVESTIGATION OF ANTHRAQUINONE FILMS SPONTANEOUSLY ADSORBED ON ORDERED GRAPHITE*

Introduction

Optimization of instrumental parameters is crucial for obtaining meaningful results with any instrument, and this may be even more so for scanning probe microscopy. The learning curve is initially steep and even after the initial learning stages, obtaining quality images of the solid-liquid or solid-gas interface can be an involved process. Results to be presented in this chapter were obtained very early in my graduate research career, and enabled me to gain valuable troubleshooting skills and microscopy experience. In addition, the substrate-adsorbate system described here is very interesting, and has been studied by others in the past. Scanning force microscopy was able to provide answers to an adsorption phenomenon, which other methods were unable to convincingly address.

Spontaneously adsorbed organic films play a key role in a variety of applications involving the use of carbon materials in electrochemistry. For example, many schemes to chemically modify the surfaces of solid electrodes have been developed to systematically control the rates and/or selectivity of heterogeneous electron transfer reactions (1-3). One of the first approaches involved the physical adsorption (physisorption) of electroactive organic molecules to graphite electrodes (4-6). The spontaneous adsorption of redox species to graphite electrode surfaces is simpler and more rapid than procedures

---

* A form of this chapter was published as "Ta, T. C., Kanda, V., and McDermott, M. T. *J. Phys. Chem B* **1999**, 103, 1295-1302".

involving covalent attachment and remains to be widely utilized as a pathway for immobilization and analysis (7).

The ease by which organic species adsorb to graphite may also limit the use of these materials in electrochemistry. A physisorbed layer of adventitious impurities can govern the reactivity of a carbon electrode, and reports have stressed the importance of an impurity-free carbon surface (8, 9). For example, adsorbed layers of organic molecules have been shown to influence electron transfer rates at glassy carbon (GC) electrodes (10, 11). In applications involving biological components, it has been demonstrated that an adsorbed protein film decreases observed currents at GC electrodes (12, 13). Thus, it is clear that the spontaneous adsorption of thin films can have a significant impact on the design and application of carbon electrodes.

Crucial to interpreting the electrochemical response of a modified carbon surface is a thorough understanding of how the final structure of the interface influences reactivity. Some of the more important parameters that define the interfacial architecture of a physisorbed layer include the coverage, molecular orientation, and two-dimensional arrangement of the immobilized species. Insights into the structure and coverage of electroactive adsorbed layers can be inferred from their voltammetric signature (5, 14). Vibrational spectroscopic techniques such as infrared (15, 16) and Raman spectroscopy (17-19) can provide chemical identification as well as orientation information. The details provided by these and other methodologies have advanced our understanding of modified electrochemical interfaces, but in a somewhat limited sense because they only describe the general population or average behavior of the adsorbed layer. A more complete picture can be obtained by combining macroscopic characterizations with techniques that probe the surfaces on a molecular scale. The family of techniques comprising scanning probe microscopy (SPM) has been widely utilized to examine the nanometer-scale structure of thin organic films on electrode

surfaces (20). Described in this chapter is a combine electrochemical and in situ scanning force microscopic (SFM) study of anthraquinone 2,6-disulfonate (2,6-AQDS) films adsorbed to ordered graphite electrodes.

Several recent reports have described the electrochemistry of adsorbed 2,6-AQDS layers (21-25). Anomalous, yet interesting, voltammetry consisting of multiple waves and a sharp spike was reported for 2,6-AQDS layers adsorbed to both Hg and pyrolytic graphite (PG) electrodes. Faulkner and co-workers proposed an intermolecular hydrogen-bonded structure as being responsible for the sharp voltammetric feature on Hg (21). In a combined electrochemical and infrared spectroscopic investigation, Zhang and Anson proposed that 2,6-AQDS initially adsorbs in a flat orientation on PG and reconfigures with increasing time or bulk solution concentration (23). A more recent report describes the adsorption of 2,6-AQDS to a variety of different carbon electrodes and suggests that surface carbon-oxygen functionality serve as adsorption sites (26). Due to interest in the interfacial architecture of modified carbon electrodes, these previous studies were further investigated. For 2,6-AQDS spontaneously adsorbed on highly oriented pyrolytic graphite (HOPG) surfaces, voltammetric responses will be correlated with film architectures determined by *in situ* SFM imaging.

Experimental

Reagents and Materials: Disodium anthraquinone 2,6-disulfonate (2,6-AQDS) was obtained from Aldrich (Milwaukee, WI) and was twice recrystallized from ethanol. All concentrations of 2,6-AQDS were prepared in 1 M $HClO_4$ (Caledon, Georgetown, Ontario). Water used for rinsing and preparation of all solutions was from a Nanopure (Barnstead, Dubuque, IA) water filtration system. Solutions of pH 4 were prepared by adjusting the pH of a 1 M $NaClO_4$ (Anachemia) solution with drops of 1 M $HClO_4$. Highly oriented pyrolytic graphite (HOPG) was either purchased from Advanced Ceramics Corp.

(Lakewood, OH) (ZYB grade) or obtained as a gift from Dr. Arthur Moore at Advanced Ceramics (ungraded).

Electrochemistry: Cyclic voltammetry (CV) experiments were performed using a standard three-electrode cell. A Ag/AgCl (saturated KCl) electrode and a platinum wire were used as the reference and the counter electrode, respectively. HOPG was the working electrode and was cleaved with tape to produce a clean, flat surface before each experiment. The radius of an inert o-ring defined the area of the working electrode ($\sim$0.5 cm^2). Voltammograms were obtained by sweeping the potential between +0.4 and -0.1 V vs Ag/AgCl at a scan rate of 100 mV/s using a PAR Model 270 potentiostat. Solutions of higher concentration (>100 μM) produce currents arising from both solution and surface-bound species. For these solution concentrations, 2,6-AQDS was allowed to adsorb for $\sim$30 min. The cell was then rinsed with 1 M HClO$_4$, and the experiments were conducted in 1 M HClO$_4$. Similar results were obtained from experiments performed in the microscope's electrochemical fluid cell.

SFM Studies: *In situ* SFM experiments were carried out in the electrochemical fluid cell of a Nanoscope III Multi-Mode system (Digital Instruments, Santa Barbara, CA). Contact mode topographic and lateral force images were collected simultaneously. Typically, the fluid cell was filled with 1 M HClO$_4$ and allowed to equilibrate for at least 30 min. The 2,6-AQDS solutions were then flushed through the fluid cell and allowed to equilibrate with the surface for 30 min. Imaging was performed with minimal load applied to the surface. This was achieved by using a cantilever with a low force constant ($k \sim$ 0.06 N/m, Digital Instruments) and imaging at normal forces < 2 nN.

Molecular Modeling: To approximate the molecular dimensions of 2,6-AQDS, tabulated van der Waal's radii (27) were incorporated into a commercial modeling software (MacroModel 5.5, MacroModel Development Group, Columbia University).

Results and Discussion

As noted above, several previous reports have described the cyclic voltammetry for 2,6-AQDS adsorbed at various electrode materials (21-25). Although support for our conclusions here derives mainly from SFM analysis, examples of the voltammetry of 2,6-AQDS adsorbed on cleaved basal plane HOPG from 1 M $HClO_4$ are presented for completeness. In all cases, the voltammetry presented was collected after the adsorbed layer had reached equilibrium with the contacting solution (~30 min). Figure 8.01A is the current-potential curve collected in a solution of 1.0 μM 2,6-AQDS, a concentration where solution phase species are undetectable by cyclic voltammetry. The voltammetric waves centered at 0.090 V vs. Ag/AgCl exhibit a full-width-at-half-maximum (FWHM) of 54 mV and a peak separation (ΔE_p) of 7 mV. The peak current of these waves increases linearly with the voltammetric scan rate. These observations indicate that 2,6-AQDS behaves as a near ideal, quasi-reversible, surface-bound redox species when adsorbed to HOPG from micromolar concentrations (28). In addition, the position of the waves in Figure 8.01A is ~0.05 V more positive than the $E_{1/2}$ for diffusing 2,6-AQDS ($E_{1/2} = 0.040$ V vs Ag/AgCl), implying that the reduced hydroquinone form is more strongly adsorbed. The wave shape and position in Figure 8.01A are generally observed for 2,6-AQDS adsorbed from solutions of concentrations <10 μM in 1 M $HClO_4$.

Integration of the area under the cathodic wave in Figure 8.01A yields a charge of 4.5×10^{-6} C/cm^2, which corresponds to an observed surface coverage (Γ_{obs}) of 2.3×10^{-11} mol/cm^2. On the basis of a saturation coverage of 1.32×10^{-10} mol/cm^2, which assumes that the aromatic rings of adsorbed 2,6-AQDS are oriented parallel with the graphite surface (molecular area = 128 $Å^2$), this coverage reflects ~17% of a fully-packed monolayer (29). Submonolayer quantities of quinones adsorbed to HOPG have been previously detected by voltammetry. It has been concluded that either 2,6-AQDS adsorbs solely to the area near a defect
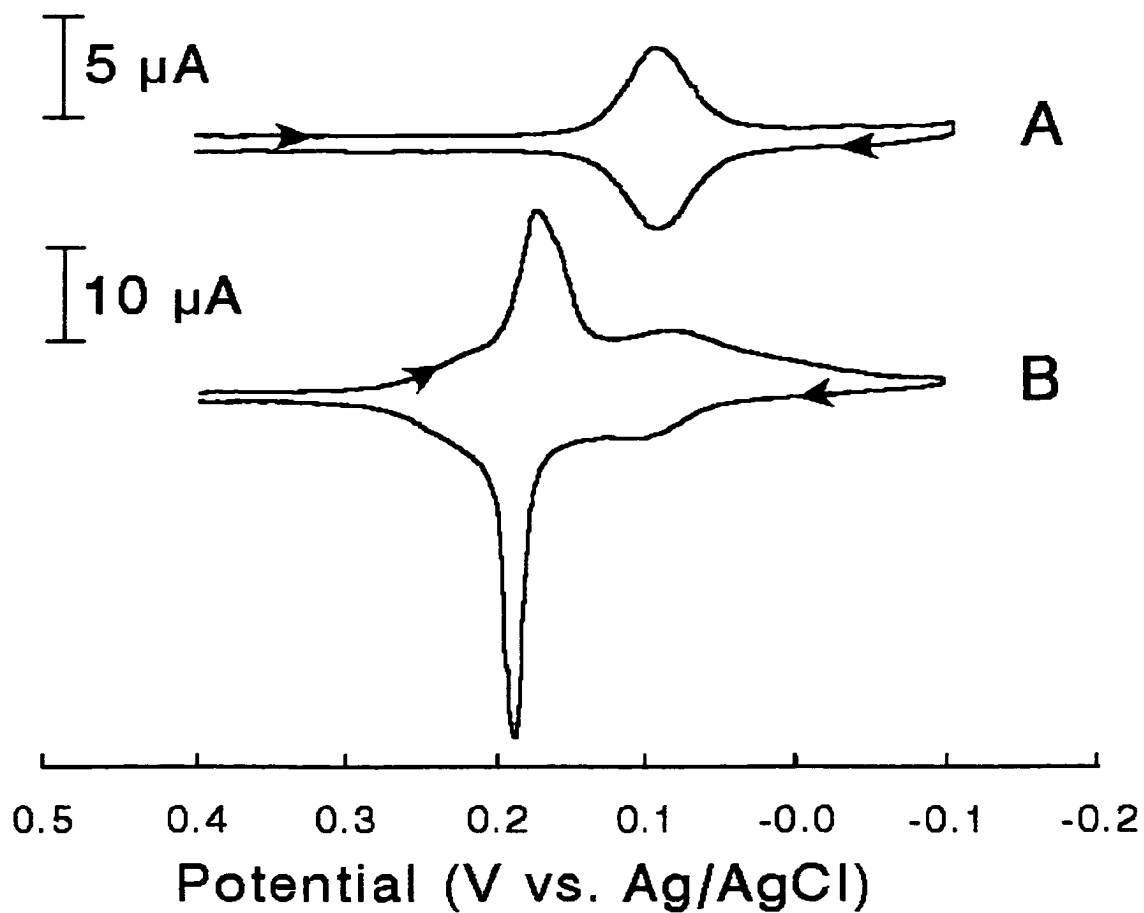
Figure 8.01. Cyclic voltammetry (CV) of 2,6-AQDS adsorbed on HOPG for 30 min. from different solution concentrations. (A) CV in 1 μM 2,6-AQDS (1 M HClO₄) (B) CV in 1 M HClO₄ after adsorption from 1 mM 2,6-AQDS (1 M HClO₄). v=100 mV/s for both voltammograms.

or adsorbed 2,6-AQDS is electroactive only at defects (22, 24). As described below, SFM data suggests that the second explanation is more reasonable.

Figure 8.01B shows the cyclic voltammetry of 2,6-AQDS collected in supporting electrolyte after adsorption to HOPG from a 1.0 mM solution. In addition to the waves at 0.09 V, a second set of peaks develops at 0.19 V vs Ag/AgCl. These spike-shaped peaks are similar to those observed on Hg (21) and PG (23) electrodes and are not observed for bulk solution concentrations less than 10 μM. It is noted that in a previous report, Anson, *et al.* observed three waves in the voltammetry of 2,6-AQDS on PG electrodes (23). A third wave was observed in ~30% of experiments performed at potentials slightly more negative than the one at 0.09 V. Because of this irreproducibility, there will be no further comment made about this third wave (see note 44).

The presence of multiple waves in Figure 8.01B argues that 2,6-AQDS adsorbs to HOPG in distinct states. One state, characterized by the well-behaved waves at 0.09 V, appears to be that of a model surface-bound redox species. The FWHM of the spikes in Figure 8.01B are 37 mV for the cathodic wave and 23 mV for the anodic. These narrow voltammetric waves imply a second adsorbate state exhibiting significant intermolecular interactions (30). Theoretical treatments by Laviron suggest that the location of the spike as a pre-wave on the potential axis is also attributable to energy effects arising from the interactions between adsorbed molecules (31). Integration of the cathodic waves in Figure 8.01B yields charges of 2.5 × 10^{-6} C/cm^2 for the wave at 0.09 V and 1.2 × 10^{-5} C/cm^2 for the spike at 0.19 V. The similarity of the charges for the waves at 0.09 V in both voltammograms of Figure 8.01 suggests that the second adsorbed state does not exist at the expense of the first. Taken together, the voltammetry in Figure 8.01 illustrates that the structure of spontaneously adsorbed films of 2,6-AQDS on HOPG is governed by the initial bulk concentration. Changes in adsorbed orientation as a function of bulk concentration have been reported for other

adsorbate/electrode combinations including 2,6-AQDS on PG (23) and various aromatic molecules on Pt (32, 33).

The two-dimensional architecture of 2,6-AQDS layers adsorbed to HOPG was investigated with in situ contact-mode SFM to better determine the nature of the differences in the cyclic voltammetry observed in Figure 8.01. The images in Figure 8.02 are that of unmodified HOPG in 1 M $HClO_4$ and serve to characterize our substrate. The $5.0 \times 5.0 \ \mu m^2$ topographic (Figure 8.02A) and lateral (friction) force (Figure 8.02B) images reveal regions of an atomically flat basal plane separated by step defects created in the cleavage process (24, 34). These steps, which generally exhibit heights corresponding to the interplane distance of graphite (0.33 nm), cause the SFM probe to "trip", resulting in a transient twisting of the cantilever and the observed high lateral force signal at these sites (Figure 8.02B) (35). A high lateral force signal was observed while scanning both up and down a step. This has previously been observed for HOPG and was attributed to the meniscus forces present between the tip and sample when imaging in air (35). Our images were collected in 1 M $HClO_4$, where meniscus forces are minimized. The increase in the lateral force signal while scanning down a step observed in Figure 8.02B was attributed to an increase in contact area or an imaging artifact resulting from the transient normal deflection of the cantilever at the step (*i.e.* error signal). The images in Figure 8.02 agree with what was expected on the basis of previous STM (34) and SFM (35) studies of HOPG and provide a signature of the substrate for comparisons with images of 2,6-AQDS layers.

Exposure of a freshly cleaved HOPG surface to solutions of 2,6-AQDS results in the images contained in Figure 8.03. Parts A and B of Figure 8.03 are respective $2.7 \times 2.7 \ \mu m^2$ topographic and lateral force images collected in a 10 μM 2,6-AQDS solution at an imaging force of ~2 nN. Figure 8.03A reveals topography that is distinct from the unmodified substrate shown in Figure 8.02A. An apparent overlayer covers approximately 90% of the surface. This type of
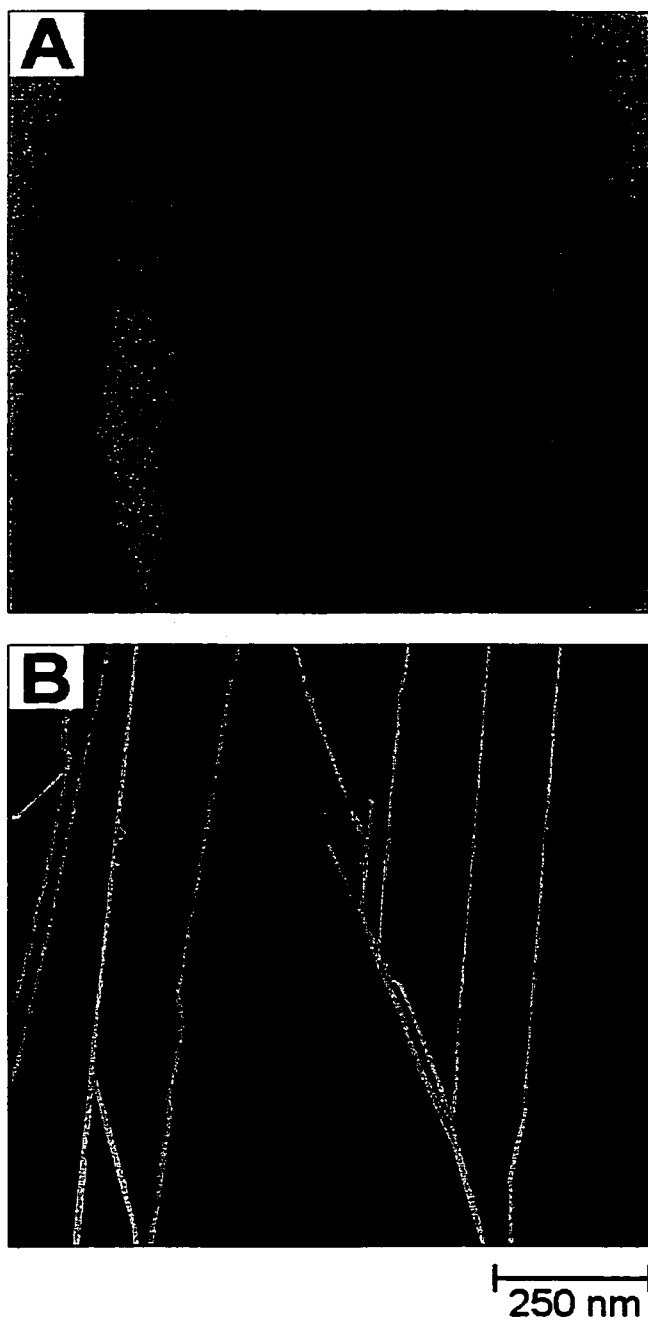
Figure 8.02. 5 × 5 μm^2 SFM images of unmodified HOPG obtained in 1M $HClO_4$. (A) Topography (Z-scale = 5 nm) and (B) lateral force (Z-scale = 0.3 V).

layer was observed only when imaging under $HClO_4$ solution. Images of HOPG collected in air following exposure to 2,6-AQDS solutions reveal adsorbate only at defect sites. This implies that the interaction of 2,6-AQDS with basal plane graphite is weak relative to the force applied by the scanning probe tip (10-50 nN in air). The film topography in Figure 8.03A appears discontinuous, containing a high density of pinhole defects. In most cases, the diameter of these pinholes is insufficient to allow the SFM tip to probe the HOPG substrate. The tip contacts the edge of the defect, resulting in a high lateral force at these sites due to tripping (Figure 8.03B). Also apparent are several 100-250 nm diameter defects, which display the characteristic low friction (darker contrast) of exposed basal plane in Figure 8.03B. High-resolution images reveal no observable molecular order in the film structure. Several cleavage steps are present on the right side of Figures 8.03A,B. There were no differences observed in film structure near these sites. After examination of a number of such samples, it was concluded that the voltammetric wave at 0.09 V in Figure 8.01A corresponds to the film structure observed in Figures 8.03A,B.

Consistent with the voltammetry in Figure 8.01, the structure of 2,6-AQDS films as revealed by SFM varies as a function of bulk concentration. Topographic and lateral force images of basal plane HOPG collected in 1 mM 2,6-AQDS solution are shown in parts C and D of Figure 8.03, respectively. The topography consists of a pattern of intersecting, elongated domains that are 0.3-0.7 nm higher than the surrounding background. These domains range in length from 100 to 700 nm and in width from 35 to 100 nm. Interestingly, in Figure 8.03D the domains exhibit a significantly lower friction relative to the topographically recessed background. It is not likely, then, that the background consists of basal plane HOPG, which generally displays relatively low friction. The presence of the wave at 0.09 V in Figure 8.01B suggests that a portion of the overall 2,6-AQDS film structure formed from 1 mM solutions is similar to that in Figure 8.03A. Thus the
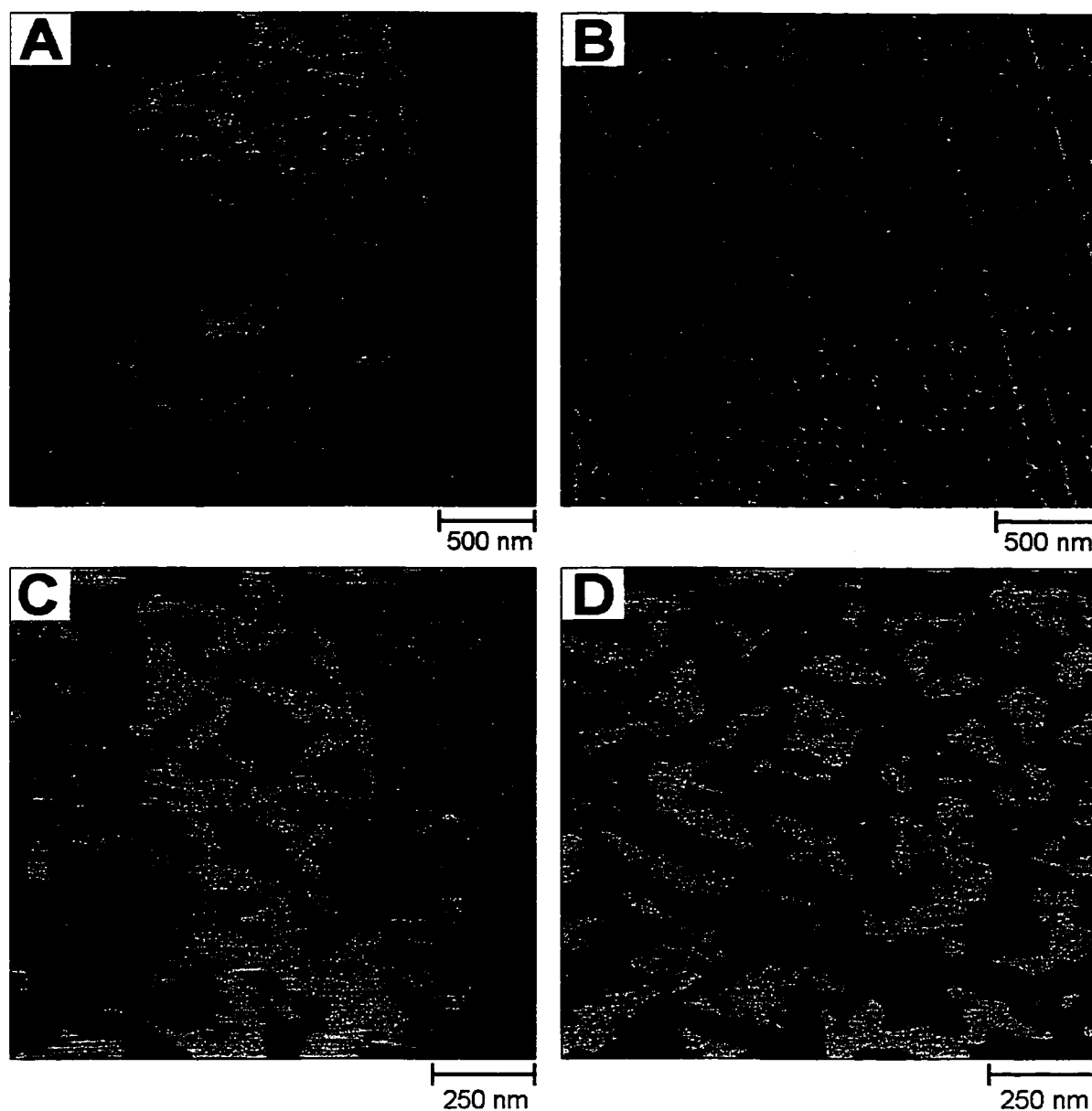
Figure 8.03. A and B are respective 2.7 × 2.7 μm² topographic (Z - scale = 10 nm) and lateral force (Z - scale = 0.2 V) SFM images of an equilibrated 2,6-AQDS film on HOPG. Images were collected in 10 μM AQDS (1 M HClO₄). C and D are respective 1.6 × 1.6 μm² topographic (Z - scale = 2 nm) and lateral force (Z - scale = 0.5 V) SFM images collected in 1 mM 2,6-AQDS (1 M HClO₄) solution.

recessed background in Figures 8.03C,D is believed to consist of this type of structure.

Separate experiments support this supposition and indicate that the domains apparent in parts C and D of Figure 8.03 are located on top of the initial disordered layer of 2,6-AQDS. A freshly cleaved HOPG surface was exposed to a 1 μM solution in the SFM fluid cell. Images of the resulting layer were very similar to those in Figures 8.03A,B. A solution of 1 mM 2,6-AQDS was then injected into the cell, resulting in the formation of domains shown in Figure 8.04A that are similar to those shown in Figures 8.03C,D. Furthermore, application of a slightly higher imaging force (~5 nN) causes the domain structures to be swept away, leaving behind the initial disordered layer as shown in Figure 8.04B. These results imply that the observed pattern of domains in Figure 8.03C is adsorbed on top of the initial, disordered 2,6-AQDS layer observed in Figures 8.03A,B.

Upon initial inspection, the domains in Figures 8.03C,D appear to intersect at common angles. Angles of 60 or 120 would imply a communication with the underlying graphite lattice. However, analysis of domains in several images does not yield a prevalent angle between domains, which is consistent with a model whereby the domains are separated from the basal plane by another adsorbate layer. Furthermore, on the basis of the combined evidence from the cyclic voltammetry and SFM images, the spiked voltammetric wave at 0.19 V was assigned to the domains that appear only at higher concentrations (>10 μM).

In order to further confirm this assignment, voltammetry and SFM structure of 2,6-AQDS layers formed from 1 mM solutions as a function of pH were examined. The cyclic voltammogram in Figure 8.05A was collected under identical conditions and is very similar to that in Figure 8.01B. Figure 8.05B is the voltammogram of the same layer after the pH of the electrolyte solution was raised to a value of 4. As expected for an electrochemical reaction involving protons, all waves are shifted to more negative potentials (28). In addition, the
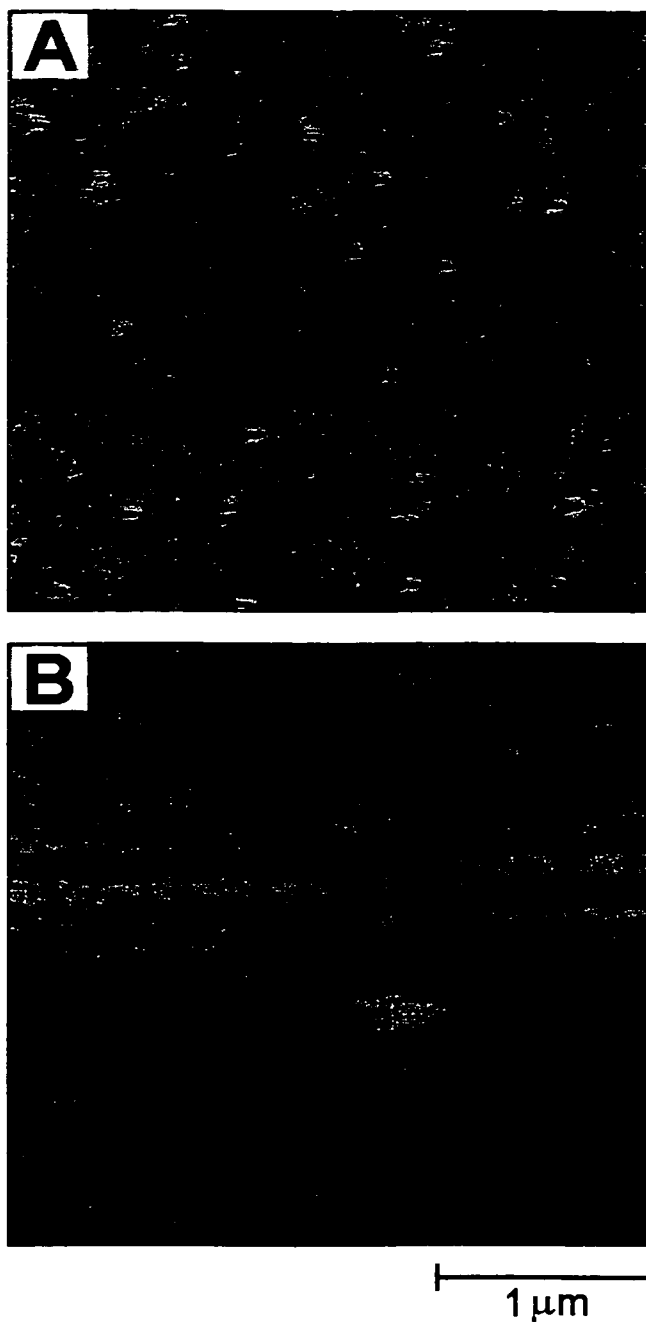
Figure 8.04. 3 × 3 μm² friction images. (A) HOPG was initial incubated with 1 μM 2,6-AQDS in 1 M HClO₄ for 30 min. and subsequently exposed to the 100 μM 2,6-AQDS in 1 M HClO₄. (B) 2,6-AQDS film formed from 1 mM 2,6-AQDS in 1 M HClO₄. Lower right corner was purposely scratched using the SFM tip.
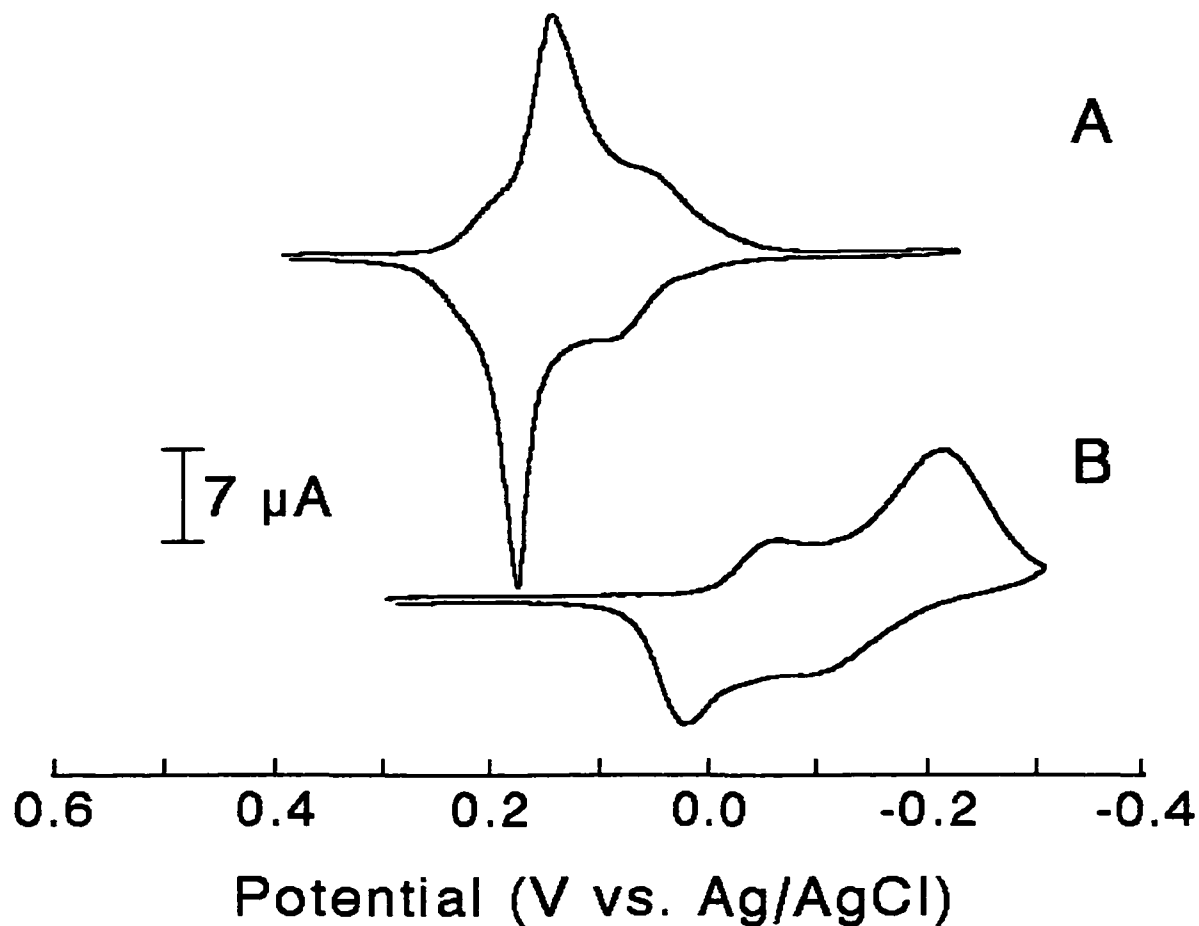
Figure 8.05. Cyclic voltammetry of 2,6-AQDS films formed from 1 mM AQDS (1M HClO₄) at different pH. (A) 1 M HClO4, pH ~ 0. (B) 1 M NaClO₄ adjusted to pH = 4 with HClO₄. v = 100 mV/s for both voltammograms.

overall charge under the waves in Figure 8.05B decreases by ~25% relative to that in Figure 8.05A. This decrease is likely the result of desorption due to the change in pH or rinsing. Importantly, the sharp voltammetric feature observed at lower pH disappeared, consistent with results from a previous report (23).

A similar experiment was performed in the SFM fluid cell. A cleaved HOPG electrode was exposed to a 1 mM 2,6-AQDS solution, and the resulting film was comparable to that shown in Figures 8.03C,D. After flushing and filling the cell with pH 4 electrolyte solution, the images in Figure 8.06 were obtained (44). As illustrated in the topography (Figure 8.06A) and particularly in the lateral force image (Figure 8.06B), the density of the domains appears lower and the structures present are much smaller than those in Figure 8.03C. The disordered, lower layer appears intact, as evidenced by its relatively high friction in Figure 8.06B. Considering both the voltammetry in Figure 8.05B and the images in Figure 8.06, it is clear that the disappearance of the voltammetric spike correlates with the disassembly of the linear domains. This observation provides strong evidence that the spike is the voltammetric signature of the linear domain structures.

The images in Figure 8.03, and others that I have obtained during this work, indicate that the vast majority of the cleaved HOPG surface is covered with a layer of 2,6-AQDS when adsorbed from solution concentrations from 1 μM to 1 mM. This observation is inconsistent with the measured voltammetric coverage in Figure 8.01 (e.g., 17% of a monolayer for Figure 8.01A) and reported previously (22, 25). In fact, for solution concentrations of 1-10 μM, full monolayer coverage of 2,6-AQDS adsorbed to cleaved basal plane HOPG electrodes were never measured voltammetrically. It has been demonstrated that the amount of adsorbed 2,6-AQDS on HOPG correlates with the density of edge plane defects (25). The SFM results presented here suggest that these types of adsorbates may only be electroactive at defects, leading to the above-mentioned correlation. Results from
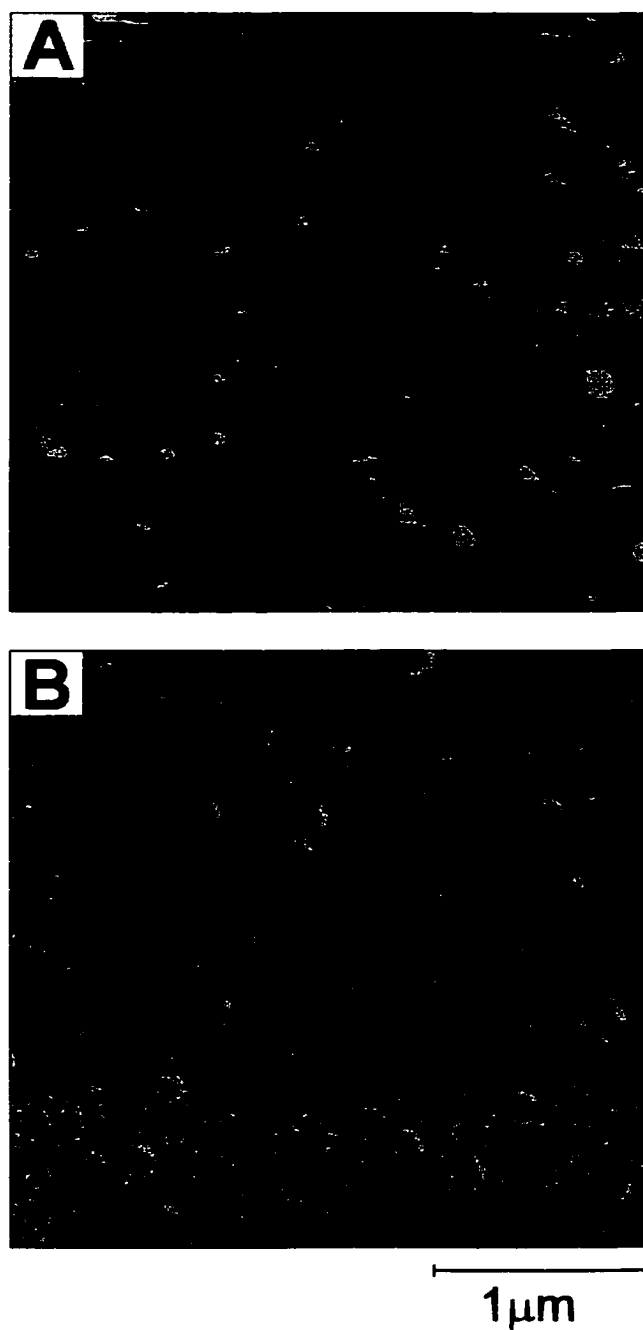
Figure 8.06. 3 × 3 μm² SFM images of 2,6-AQDS film formed from 1 mM 2,6-AQDS (1 M HClO4) collected in 1 M NaClO₄ adjusted to pH = 4 with HClO₄. (A) Topography (Z - scale = 3 nm) (B) Friction (Z - scale = 0.1 V).

a recent study indicate that surface oxygen groups act as sites for the adsorption of 2,6-AQDS on carbon surfaces (26). It may be that these functionalities are necessary for electron transfer to these adsorbates. In any case, it is clear from the images in Figure 8.03 that the amount of 2,6-AQDS actually adsorbed to HOPG electrodes does not agree with the amount determined electrochemically. This discrepancy needs further investigation. Adsorbate-covered step defects under potential control were imaged. While scanning the potential of the HOPG through the voltammetric wave at 0.09 V vs Ag/AgCl, no discernable variation in the topography or friction of the 2,6-AQDS layer at the defect was observed.

Insights into the molecular structure of the domains formed from higher concentration solutions of 2,6-AQDS (>10 μM) begin to develop from careful consideration of the lateral force image in Figure 8.03D. The measured friction in these regions is significantly lower than in the underlying film. Based on recent studies, this observation implies either a variation in chemical composition between the two regions (36-39) or a difference in molecular packing (40). As mentioned above, the reduced width of the voltammetric wave corresponding to the domains is indicative of significant intermolecular interactions, which adds weight to the latter of the two scenarios. High-resolution images of the layer depicted in Figures 8.03A,B reveal no molecular order and are consistent with a greater measured friction and a near ideal voltammetric wave shape. The lower friction and sharp voltammetric signature of the domains argues that significant intermolecular interactions exist and that these regions may be composed of a more ordered array of molecules.

High-resolution SFM images further detail the molecular scale architecture of 2,6-AQDS domains. Parts A and B of Figure 8.07 are 300 × 300 nm^2 topographic and lateral force images that reveal molecular-scale order in the domains. The domains appear to be composed of parallel, linear rows or stripes. These rows are more apparent in the lateral force image (Figure 8.07B), likely due
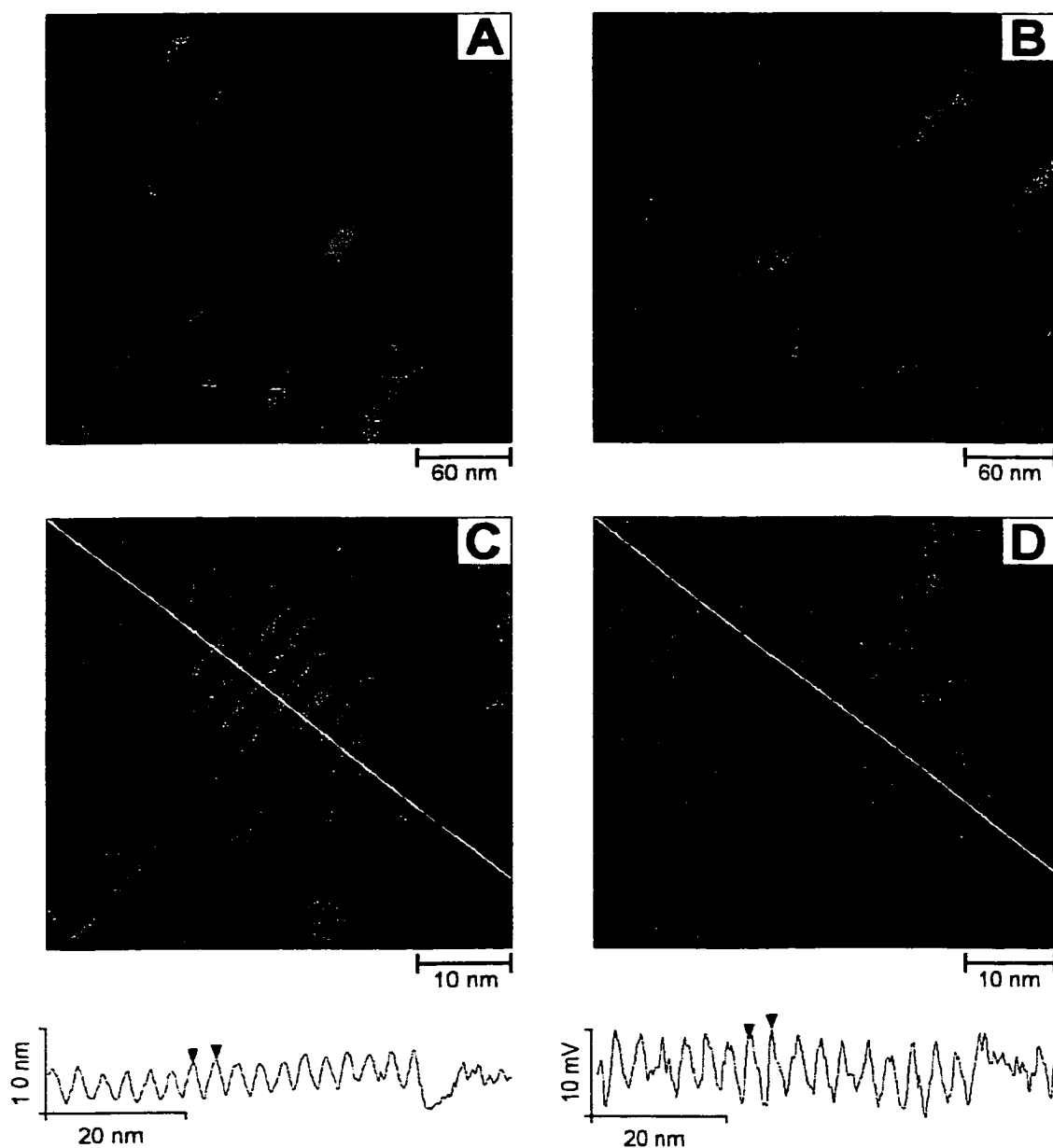
Figure 8.07. (A) 300 × 300 nm² topographic (Z - scale = 2 nm) and (B) lateral force (Z - scale = 0.05 V) SFM images of the domains formed from 1 mM 2,6-AQDS solutions. (C) 50 × 50 nm² topographic (Z - scale = 2 nm) and (D) lateral force (Z - scale = 0.05 V) of these domains showing a row type structure. The cursors in the cross-sectional profiles of C and D are 3.3 nm apart. All images were collected in 1 mM AQDS (1 M HClO₄).

to the higher sensitivity of a laser-reflection based SFM to the torsional motion of the cantilever (41). The stripes are oriented with the long axis of the domains and traverse each domain without interruption. The termination of the stripes occurs either at a free-standing domain edge, at a cleavage defect, or at the boundary between two (or more) domains. The intersection of several domains is illustrated near the center of Figures 8.07A,B. The boundaries between intersecting domains are well-defined with clean termination of the stripes of one domain into the stripes of another. These boundaries are reminiscent of grain boundaries observed in scanning tunneling microscopy images of liquid crystal monolayers on HOPG (42, 43). Importantly, the stripe structure observed in Figures 8.07A,B strongly argues that the domains are ordered on a molecular scale. This conclusion is consistent with the observed low friction and sharp voltammetric wave.

The stripe structure is depicted in greater detail in the 50×50 nm^2 images of Figures 7C,D. From the cross-sectional profile in Figure 8.07C, the periodicity between the stripes measures 3.3 nm with a corrugation amplitude of 0.35 nm. Interestingly, the rows themselves exhibit lower friction than the surrounding layer and it is the combined effect of the group of stripes that produces overall lower friction of the entire domain. I did not observe any significant variations in the friction of the domains as a function of domain orientation relative to the scan direction. Although our SFM images reveal nanometer-scale periodicity, they do not display the resolution necessary to predict the molecular packing scheme responsible for the observed row structure. A hydrogen-bonded structure, originally predicted by Faulker, *et al.* (21) and shown in Figure 8.08A, would produce rows of interacting molecules. Using van der Waals radii, our modeling efforts yield a maximum sulfonate-sulfonate distance in 2,6-AQDS of 14 Å. On the basis of this distance, the adjacent row spacing for flat-lying molecules would be ~1 nm (Figure 8.08B), which is much smaller than our measured inter-row distance of 3.3 nm. An edgewise orientation would exhibit an even smaller row-
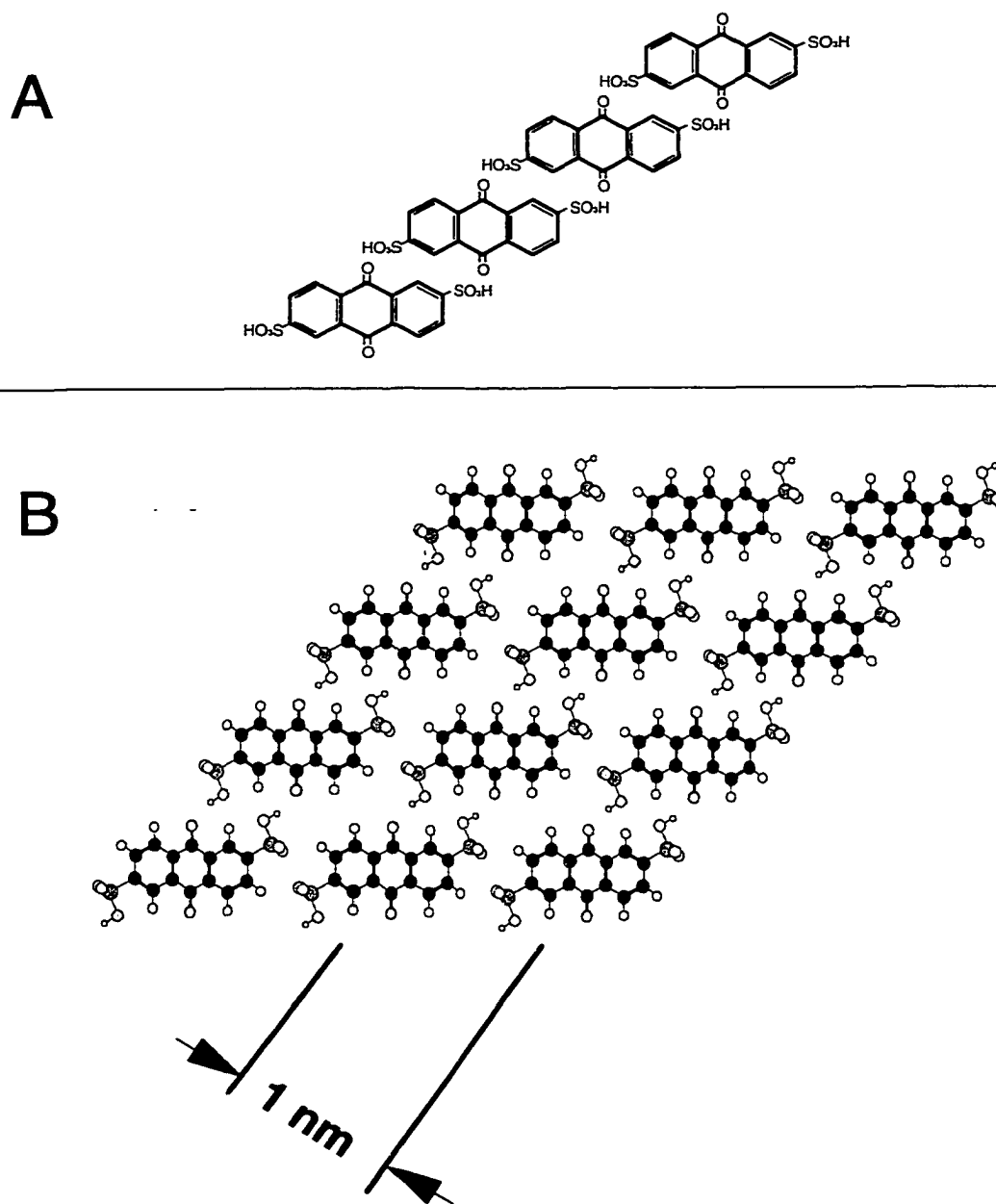
Figure 8.08. (A) Linear structure originally proposed by He, Crooks and Faulkner (*J. Phys. Chem.* 1990, 94, 1135). (B) Predicted row spacing of this structure based on van der Waals radii of 2,6-AQDS.

row periodicity. Thus, the large periodicity relative to the dimension of individual 2,6-AQDS molecules suggests that a simple structure involving a string of interacting single molecules is unlikely. In addition, a flat lying structure like that depicted in Figure 8.08 to exhibit the low friction observed in our experiments cannot be envisioned. It is believed that the low friction of each row reflects a crystalline architecture where the cross-section of each row is composed of a densely packed group of molecules, likely packed via hydrogen bonding. This crystal structure then extends linearly.

Conclusions

It is clear from our experiments that the two-dimensional structure of 2,6-AQDS films spontaneously adsorbed to HOPG is governed by the solution concentration from which the films are formed. The different film architectures are reflected both in the voltammetric response of the films and in SFM images. When 2,6-AQDS is adsorbed from solutions of 10 μM or less, a near complete, disordered monolayer exhibits near ideal cyclic voltammetry for a surface-bound redox system. This layer apparently adsorbs to the basal plane of the HOPG electrode with no predisposition for binding solely to cleavage defects. An array of molecular domains forms on top of the original disordered layer from solutions of higher concentration (10 μM to 1 mM). The appearance of these domains correlates with the development of a sharp spike in the voltammetry. The width of the spike as well as its location on the potential axis suggests a structure exhibiting significant intermolecular interactions. Two characteristics revealed by SFM imaging confirm this type of structure. First, lateral force images show that the domains exhibit an overall lower friction than the initial disordered film, implying a crystalline architecture. Secondly, high-resolution images reveal that each domain is composed of a series of parallel rows, again pointing to a well-defined, organized structure.

The full coverage of adsorbed 2,6-AQDS observed in SFM image does not correlate with the coverage determined voltammetrically here (~17%) and elsewhere (22). This suggests that adsorbed 2,6-AQDS is electroactive only at certain sites, likely cleavage defects. The different 2,6-AQDS film architectures reported here can only be observed when imaging under solution. Images collected in ambient air reveal adsorbate only on the cleavage defects. This points to a stronger binding of 2,6-AQDS to edge plane graphite relative to the basal plane and is consistent with preferential electroactivity at these sites. The combination of voltammetric measurements and in situ SFM imaging in this work has provided a powerful correlation relating the electrochemical reactivity and two-dimensional structure of spontaneously adsorbed 2,6-AQDS films on graphite.

References

(1)   Murray, R. W. *Electroanalytical Chemistry*; Marcel Dekker: New York, 1984.

(2)   Hubbard, A. T. *Chem. Rev.* **1988**, *88*, 633.

(3)   Bard, A. J. *J. Phys. Chem.* **1993**, *97*, 771.

(4)   Brown, A. P.; Koval, C.; Anson, F. C. *J. Electroanal. Chem.* **1976**, *72*, 379.

(5)   Brown, A. P.; Anson, F. C. *Anal. Chem.* **1977**, *49*, 1589.

(6)   Brown, A. P.; Anson, F. C. *J. Electroanal. Chem.* **1977**, *83*, 203.

(7)   Shi, M.; Anson, F. C. *Anal. Chem.* **1998**, *70*, 1489.

(8)   McCreery, R. L. In *Electroanalytical Chemistry*; Bard, A. J., Ed.; Marcel Dekker: New York, 1991; Vol. 17, pp 221-374.

(9)   McCreery, R. L.; Kneten, K. R.; McDermott, C. A.; McDermott, M. T. *Coll. Surf. A* **1994**, *93*, 211.

(10)   Chen, P.; Fryling, M. A.; McCreery, R. L. *Anal. Chem.* **1995**, *67*, 3115.

(11)   Chen, P.; McCreery, R. L. *Anal. Chem.* **1996,** *68,* 3958.

(12)   Downard, A. J.; Roddick, A. D. *Electroanal.* **1994,** *6,* 409.

(13)   Downard, A. J.; Roddick, A. D. *Electroanal.* **1995,** *7,* 376.

(14)   Laviron, E. In *Electroanalytical Chemistry*; Bard, A. J., Ed.; Marcel Dekker: New York, 1982; Vol. 12, pp 53-157.

(15)   Porter, M. D.; Bright, T. B.; Allara, D. L.; Kuwana, T. *Anal. Chem.* **1986,** *58,* 2461.

(16)   Porter, M. D. *Anal. Chem.* **1988,** *60,* 1143A.

(17)   Zhao, J.; McCreery, R. L. *Langmuir* **1995,** *11,* 4036.

(18)   Kagan, M. R.; McCreery, R. L. *Langmuir* **1995,** *11,* 4041.

(19)   Liu, Y.-C.; McCreery, R. L. *J. Am. Chem. Soc.* **1995,** *67,* 3115.

(20)   Green, J.-B.; McDermott, C. A.; McDermott, M. T.; Porter, M. D. In *Frontiers in Electrochemistry: Imaging of Surfaces and Interfaces*; Lipkowski, J., Ross, P. N., Eds., 1999, pp. 249-342.

(21)   He, P.; Crooks, R. M.; Faulkner, L. R. *J. Phys. Chem.* **1990,** *94,* 1135.

(22)   McDermott, M. T.; Kneten, K.; McCreery, R. L. *J. Phys. Chem.* **1992,** *96,* 3124.

(23)   Zhang, J.; Anson, F. C. *J. Electroanal. Chem.* **1992,** *331,* 945.

(24)   Forster, R. J. *Langmuir* **1995,** *11,* 2247.

(25)   McDermott, M. T.; McCreery, R. L. *Langmuir* **1994,** *10,* 4307.

(26)   Xu, J.; Chen, Q.; Swain, G. M. *Anal. Chem.* **1998,** *70,* 3146.

(27)   *CRC Handbook of Chemistry and Physics,* 66th ed ed.; CRC Press: Boca Raton, Fl., 1985.

(28)   Bard, A. J.; Faulkner, L. R. *Electrochemical Methods*; Wiley: New York, 1980.

(29) Soriaga, M. P.; Hubbard, A. T. *J. Am. Chem. Soc.* **1982**, *104*, 3937.

(30) Laviron, R. *Electroanal. Chem.* **1974**, *52*, 395.

(31) Laviron, E. *Electroanal. Chem.* **1975**, *63*, 245.

(32) Soriaga, M. P.; Wilson, P. H.; Hubbard, A. T.; Benton, C. S. J. *Electroanal. Chem.* **1982**, *142*, 317.

(33) Soriaga, M. P.; Stickney, J. L.; Hubbard, A. T. *Electroanal. Chem.* **1983**, *144*, 207.

(34) Chang, H.; Bard, A. J. *Langmuir* **1991**, *7*, 1143.

(35) Baselt, D. R.; Baldeschwieler, J. D. *J. Vac. Sci. Technol. B* **1992**, *10*, 2316.

(36) Overney, R. M.; Meyer, E.; Frommer, J.; D., B.; Luthi, R.; Howald, L.; Guntherodt, H.-J.; Fujihira, M.; Takano, H.; Gotoh, Y. *Nature* **1992**, *359*, 133.

(37) Frisbie, D. D.; Rozsnyai, L. F.; Noy, A.; Wrighton, M. S.; Lieber, C. M. *Science* **1994**, *265*, 2071.

(38) Wilbur, J. L.; Biebuyck, H. A.; MacDonald, J. C.; Whitesides, G. M. *Langmuir* **1995**, *13*, 2504-2510.

(39) Green, J.-B.; McDermott, M. T.; Porter, M. D.; Siperko, L. M. *J. Phys. Chem.* **1995**, *99*, 10960.

(40) McDermott, M. T.; Green, J.-B.; Porter, M. D. *Langmuir* **1997**, *13*, 2504-2510.

(41) Meyer, G.; Amer, N. M. *Appl. Phys. Lett.* **1990**, *57*, 2089.

(42) Frommer, J. *Angew. Chem. Int. Ed. Engl.* **1992**, *31*, 1298.

(43) Patrick, D. L.; Cee, V. J.; Purcell, T. J.; Beebe, T. B. J. *Langmuir* **1996**, *12*, 1830.

(44) Also observed in Figure 8.07A,B are several circular features measuring ~0.9 nm in height that exhibit lower friction than the domains. These

structures were observed in ~30% of the images collected in this work and believe that they are three-dimensional aggregates of 2,6-AQDS. These structures are also believed to be responsible for a third voltammetric wave that was observed occasionally.